UNIVERSITY OF BIRMINGHAM

COMPUTATIONAL FLUID DYNAMICS MODELLING OF COMPLEX FLUID FLOW IN STIRRED VESSELS

by

LI LIU

A thesis submitted to
The University of Birmingham
for the degree of
DOCTOR OF PHILOSOPHY

School of Chemical Engineering
College of Engineering and Physical Sciences
The University of Birmingham
November 2013

ABSTRACT

Fluid mixing in stirred vessels is widely encountered in a number of industries. In this work, different experimental techniques and the CFD modelling approach are used to measure the mixing of a wide range of fluids in stirred vessels. As the detailed validation is essential for CFD modelling, CFD predictions are compared in detail with different experimental measurements. The capability of CFD modelling of the 3D spatial distribution of velocity and solid concentration within opaque concentrated solid-liquid suspensions with the mean solid concentration up to 40 wt% is assessed by comparing with the experimental data obtained from positron emission particle tracking (PEPT) measurements. Because the impeller configuration is of significant importance to the flow pattern, the performance of different impellers for single-phase mixing of Newtonian and non-Newtonian fluids in stirred vessels is compared. CFD predictions of flow fields generated from different impellers are compared with those measured by the well-established particle image velocimetry (PIV) technique.

It is well-known that the mixing feature of non-Newtonian fluids in stirred vessels presents significant difference with that of Newtonian fluids due to the viscosity dependence on shear-rate. The formation of pseudo-cavern and cavern is the typical mixing characteristic of shear-thinning and viscoplastic fluids, respectively. The capability of CFD modelling of different mixing features of non-Newtonian fluids in stirred vessels are verified by comparing with experimental data obtained from PIV, PEPT, and planar laser induced fluorescence (PLIF) measurements. Flow fields generated in different mixing conditions, e.g. single phase mixing of Newtonian and non-Newtonian fluids under transitional and turbulent regimes, and solid-

liquid suspensions under turbulent regimes, are well predicted by the CFD modelling. However, due to the complex flow mechanism and inadequacy of some CFD models, local solid concentrations under the impeller and close to the tank base are significantly overestimated.

Solids suspended in non-Newtonian fluids, though widely encountered in industries, have not been well studied. Using PEPT and CFD modelling, detailed 3D distributions of velocity of both phases and solid concentration are investigated. Solid suspensions in non-Newtonian fluids have shown significant difference with solid suspensions in water.

ACKNOWLEDGEMENTS

Firstly, I would like to express my gratitude to my supervisor Prof. Mostafa Barigou for his valuable guidance during my PhD research. It has been a great pleasure to work with him, and I have learned a lot from him, especially his precise attitude toward research.

I would like to thank Dr Muhammd Eesa, Dr Luke Adams, and Dr Julia Hofinger for their kind introduction and advice with using a CFD simulation package. I would like to thank Dr Antonio Guida for his guidance in using the PEPT technique and his help in analysing PEPT data using Matlab. I would like to thank Dr Andreas Tsoligkas for his training and advice with PIV experiments, Professor Mark Simmons and Federico Alberini for their advice with PIV and PLIF experiments. Also, I would like to thank Dr. Joseph Gargiuli for his assistance with PEPT experiments.

I genuinely appreciated the support from people in General Office, especially Lynn Draper and Elizabeth Kent. I would also like to thank the staff from the Mechanical Engineering workshop, especially David Boylin and Thomas Eddleston, for their help in building experimental rig.

I want to thank Sara Ghorbanian Farah Abadi, Zainab Alsharify, and Shuai Tian for their friendship and support. It has been great pleasure to work with them in the same group.

Last but not least, I would like to thank my parents, and my friends Mary Hudson and Samantha Asbury for their support and encouragement.

TABLE OF CONTENTS

Chapter I INTRODUCTION 1
1.1. Motivation 1
1.2. Objective 2
1.3. Layout of thesis 3
Chapter II LITERATURE REVIEW 5
2.1. Introduction 5
2.2. Mechanically agitated vessels 7
2.2.1. Impeller type 7
2.2.2. Impeller bottom clearance and impeller geometrical parameters 9
2.3. Fluid rheology 10
2.3.1. Shear-thinning fluids 10
2.3.2. Viscoplastic fluids 12
2.3.3. Solid-liquid suspensions 15
2.4. Flow mechanisms 19
2.4.1. Turbulent regime 19
2.4.2. Laminar and transitional regimes 20
2.5. Experimental techniques 22
2.5.1. Particle Image Velocimetry 23
2.5.2. Positron Emission Particle Tracking 24
2.5.3. Planar Laser Induced Fluorescence 26
2.6. Computational fluid dynamics modelling 26
2.6.1. Modelling approach 29
2.6.2. Turbulence models in the RANS approach 30
2.6.3. Modelling approach for the rotating impeller 32
Chapter III NUMERICAL MODELLING OF SINGLE PHASE FLUID MIXING UNDER DIFFERENT FLOW REGIMES AND AGITATED BY VARIOUS IMPELLERS 36
3.1. Introduction 37
3.2. Experimental setup 40
3.2.1. Mixing vessel 40
3.2.2. Materials 41

3.2.3. PIV setup 43
3.3. CFD simulation 43
3.4. Results and discussion 46
3.4.1. Azimuthally resolved CFD predictions compared with PIV and PEPT 46
3.4.2. CFD predicted velocities at different azimuthal positions compared with PIV and PEPT 48
3.4.3. Effect of impeller type on highly turbulent flow field 50
3.4.4 Effect of impeller type on the flow fields of CMC solutions 55
3.4.5. Effect of rheology on the flow fields of CMC solutions 64
3.4.6 Effects of rheological properties and Re_{imp} on the discharge angle 70
3.4.7 Reynolds number similarity 72
3.5. Conclusion 75
Chapter IV NUMERICAL MODELLING OF VELOCITY FIELD AND PHASE DISTRIBUTION IN DENSE MONODISPERSE SOLID-LIQUID SUSPENSIONS UNDER DIFFERENT AGITATION REGIMES 77
4.1. Introduction 78
4.2. Materials and methods 81
4.3. Numerical modelling 83
4.4. Results and discussion 87
4.4.1. Velocity distributions 88
4.4.2. Particle-fluid slip 94
4.4.3. Flow number 96
4.4.4. Solid distribution 99
4.4.5. Uniformity of suspension 102
4.4.6. Effects of solids on liquid flow field 104
4.5. Effect of drag model 107
4.5.1. Effect of drag models on velocity distributions 110
4.5.2 Effect of drag models on solid distribution 114
4.6. Effects of non-drag forces 117
4.6.1. Effects of non-drag forces on the velocity distribution and solid distributions 117
4.7. Effects of “SG” and “MFR” 120

4.7.1. Effects of “SG” and “MFR” on the velocity distribution and solid distributions ..
…….120
4.8. Conclusions....123
Chapter V NUMERICAL MODELLING OF MULTI-COMPONENT HYDRODYNAMICS AND SPATIAL PHASE DISTRIBUTION IN MECHANICALLY AGITATED DENSE BINARY AND POLY SUSPENSIONS 127
5.1. Introduction....128
5.2. Experimental and modelling apparatus....129
5.3. Numerical modelling 130
5.4. Results and discussion 131
5.4.1. Binary disperse 131
5.4.1.1. Distribution of local velocity components 132
5.4.1.2. Reynolds number similarity 136
5.4.1.3. Spatial distribution of solid components....137
5.4.1.4. Impeller pumping capacity....141
5.4.1.5. Distributions of particle-fluid slip velocities....143
5.4.1.6. Uniformity of suspension 146
5.4.1.6.1. Binary suspensions....146
5.4.1.6.2. Comparison of binary and mono-disperse suspensions 147
5.4.1.7. Verification of mass continuity....148
5.4.2. Poly disperse....149
5.4.2.1. Distributions of local velocity components....150
5.4.2.2. Spatial distributions of solid components 154
5.5. Conclusions....160
Chapter VI NUMERICAL STUDY OF HERSCHEL-BULKLEY FLUID MIXING IN STIRRED VESSELS COMPARED WITH DIFFERENT TECHNOLOGICAL MEASUREMENTS 163
6.1. Introduction....164
6.2. Materials and methods 166
6.2.1. Mixing vessel and fluid rheology 166
6.2.2. PEPT and PIV measurements....168
6.3. Numerical modelling 169

6.4. Results and discussion 172
6.4.1. CFD predicted velocity field compared with PEPT 172
6.4.2. CFD predicted tracer distribution within cavern compared with PLIF 175
6.4.3. Verification of PEPT and CFD methods by comparing with PIV measurements 179
6.4.4. Effect of locations of interfaces between rotating and stationary domains on the CFD predicted cavern size and shape 182
6.4.5. Effect of impeller type and rotating mode on the cavern size and shape 186
6.4.6. Cavern upward growth for PBTD, PBTU and RDT 188
6.4.7. Effects of impeller size on the cavern size and shape 189
6.4.8. Effects of rheological parameters on the cavern size and shape 191
6.4.9. Effects of impeller bottom clearance on the cavern size and shape 194
6.4.10. Effects of impeller bottom clearance on the flow field within cavern 196
6.4.11. Ability of CFD modelling to capture the effects of different stirred tank configurations on the mixing of viscoplastic fluids 197
6.4.12. Power number 200
6.5. Conclusion 201
Chapter VII EXPERIMENTAL AND NUMERICAL MODELLING OF SOLID SUSPENSIONS IN VISCOPLASTIC FLUIDS 204
7.1. Introduction 205
7.2. Materials and methods 207
7.2.1. Mixing vessel and solid-liquid systems 207
7.2.2. Positron emission particle tracking 208
7.3. Numerical modelling 209
7.4. Results and discussion 211
7.4.1. Velocity distributions 211
7.4.2. Effect of the presence of solid phase on the flow field of the liquid phase 213
7.4.3. Flow number 215
7.4.4. Particle-fluid slip 216
7.4.5. Solid distributions 218
7.4.6. Uniformity of suspension 219
7.4.7. Mass continuity 221

7.4.8. Comparison of velocity distributions from CFD and PEPT 222
7.4.10. Comparison of solid distributions from CFD and PEPT 228
7.4.10. Numerical study of the effect of solids on mixing of viscoplastic fluids with higher apparent yield stress 230
7.5. Conclusions 236
Chapter VIII CONCLUSIONS AND FUTURE WORK 239
8.1. Conclusions 239
8.1.1. CFD modelling of mixing of Newtonian and shear-thinning fluids 239
8.1.2. CFD modelling of solid-liquid suspensions 240
8.1.3. CFD modelling of mixing of viscoplastic fluids 240
8.1.4. CFD modelling of mixing of solid suspension in viscoplastic fluids 241
8.2. Suggestions for future work 242
REFERENCES 244

LIST OF TABLES

Table 3.1. Dimensions of impeller configurations.

Table 3.2. Range of PIV measurements and CFD simulations.

Table 3.3. Rheological properties of CMC solutions.

Table 3.4. Comparison of Power number from CFD and experiments.

Table 3.5. The values of ($\frac{u_r}{u_z}$).

Table 4.1. Literature CFD studies of dilute solid-liquid systems.

Table 4.2. Literature CFD studies of moderate to dense solid-liquid systems.

Table 4.3. Range of PEPT measurements and CFD simulations.

Table 4.4. Mesh Independency study.

Table 4.5. Comparison of CFD predictions of flow number with PEPT measurements.

Table 4.6. Effects of solids presence on volume-average turbulent properties of the liquid phase.

Table 5.1. Range of PEPT measurements and CFD simulations.

Table 5.2. Comparison of CFD predictions of flow number with PEPT measurements.

Table 6.1. Dimensions of stirred vessels used in PLIF, PIV, PEPT measurements and CFD simulations.

Table 6.2. Rheological parameters in PEPT measurements and CFD simulations.

Table 7.1. Rheological parameters and experimental conditions for solid-liquid suspension.

LIST OF FIGURES

Figure 2.1. Configuration and dimensions of a mechanically agitated vessel.

Figure 2.2. Typical flow patterns generated by the radial impeller and the axial impeller in stirred vessels (Edwards, 1997): (a) axial impeller; (b) radial impeller.

Figure 2.3. Rheological properties of Newtonian and non-Newtonian fluids (Paul et al., 2004).

Figure 2.4. Degree of solid suspension (Paul et al., 2004): (a) Partial suspension; (b) Complete suspension; (c) Uniform suspension.

Figure 2.5. Trailing vortices behind a blade of a 45° PBT in down-pumping mode (Schäfer et al., 1998).

Figure 2.6. Mixing structure of a high viscosity fluid (99.7% pure glycerin) agitated by a RDT at Re = 25 measured by PLIF (Alvarez et al., 2002).

Figure 2.7. Example of cavern formation around the impeller in the mixing of viscoplastic fluids in a stirred tank.

Figure 2.8. Schematic illustration of rotating and stationary domains.

Figure 3.1. Configurations and computational mesh for the stirred tank and various impellers.

Figure 3.2. Variation of viscosity with shear rate for CMC solution at different concentrations.

Figure 3.3. Azimuthally-averaged distribution of the velocity components in PBTD mode at N = 220 rpm (Re_{imp} =40,041) – CFD and PIV compared.

Figure 3.4. Azimuthally-averaged distribution of the velocity components of water in PBTD mode at N = 220 rpm (Re_{imp} =40,041): CFD, PIV, and PEPT compared.

Figure 3.5. Distribution of the velocity components in PBTD mode at different planes at N = 220 rpm (Re_{imp} =40,041) – CFD and PIV compared.

Figure 3.6. PIV measurements of the mean radial-axial velocity fields in water at plane of $\theta = 85^{o}$ at N = 220 rpm (Re_{imp} =40,041).

Figure 3.7. Distribution of the velocity components at plane of $\theta = 85^{o}$ at N = 220 rpm (Re_{imp} =40,041) – CFD and PIV compared.

Figure 3.8. PIV measurements of the mean radial-axial fields of 0.2 wt% CMC solutions at plane of $\theta = 85^{o}$.

Figure 3.9. Distribution of the velocity components at plane of $\theta = 85^{o}$ in 0.2 wt% CMC solutions – CFD and PIV compared.

Figure 3.10. PIV measurements of the mean radial-axial fields of CMC solutions at $\theta = 85^{o}$.

Figure 3.11. Distribution of the velocity components at plane of $\theta = 85^{o}$ in 0.5 wt% and 0.7 wt% CMC solutions – CFD and PIV compared.

Figure 3.12. Effects of fluid rheology and Reynolds number on the discharge angle of different impellers.

—○— PBTD, —△— A310D, —▽—A340: 0.2 wt% CMC solution
○ PBTD, △ A310D, ▽ A340: 0.5 wt% CMC solution
● PBTD, ▲ A310D, ▼ A340: 0.7 wt% CMC solution

Figure 3.13. Power numbers of different impellers against the Reynolds number.

—□— RDT, —○— PBTD, —△— A310D, —▽—A340: 0.2 wt% CMC solution
□ RDT, ○ PBTD, △ A310D, ▽ A340: 0.5 wt% CMC solution

■ RDT, ● PBTD, ▲ A310D, ▼ A340: 0.7 wt% CMC solution
Figure 3.14. Demonstration of Reynolds number similarity in the 0.2 wt% CMC solution.

Figure 4.1. Computational grid section in the 45° plane between two baffles.

Figure 4.2. Azimuthally-averaged distributions of the velocity components of the liquid phase in suspension at *Njs* – CFD and PEPT compared: *dp* = 1 mm; *X* = 5.2 wt%; *Njs* = 360 rpm.

Figure 4.3. Azimuthally-averaged distributions of the velocity components of the solid phase in suspension at *Njs* – CFD and PEPT compared: *dp* = 1 mm; *X* = 5.2 wt%; *Njs* = 360 rpm.

Figure 4.4. CFD-predicted liquid flow pattern generated by a down-pumping PBT in a solid-liquid suspension at *Njs*: *dp* = 1 mm; *X* = 5.2 wt%; *Njs* = 360 rpm.

Figure 4.5. Azimuthally-averaged distributions of the velocity components of the liquid phase in suspension at *Njs* – CFD and PEPT compared: *dp* = 1 mm; *X* = 20 wt%; *Njs* = 490 rpm.

Figure 4.6. Azimuthally-averaged distributions of the velocity components of the solid phase in suspension at *Njs* – CFD and PEPT compared: *dp* = 1 mm; *X* = 20 wt%; *Njs* = 490 rpm.

Figure 4.7. Azimuthally-averaged distributions of the velocity components of the liquid and solid phase in suspension at *N* = 2*Njs* – CFD and PEPT compared: *dp* = 1 mm; *X* = 5.2 wt%; *Njs* = 360 rpm.

Figure 4.8. Azimuthally-averaged maps of time-averaged slip velocity from PEPT measurements at *Njs* and *N* = 2*Njs*: *dp* = 1 mm; *X* = 5.2 wt%.

Figure 4.9. Azimuthally-averaged distributions of solid volume concentration in suspension at *Njs* (*dp* = 1 mm).

Figure 4.10. Azimuthally-averaged distributions of solid volume concentration in suspension at $N > Njs$ (dp = 1 mm).

Figure 4.11. Azimuthally-averaged distributions of solid volume concentration in suspension at $N > Njs$ (dp = 3 mm).

Figure 4.12. Variation of uniformity index and volumetric power consumption as a function of impeller speed for all conditions investigated (see Table 3):

—○— ξ; ····○···· P/V: dp = 1 mm; X = 5.2 wt%;
—●— ξ; ····●···· P/V: dp = 1 mm; X = 20 wt%;
—□— ξ; ····□···· P/V: dp = 3 mm; X = 5.2 wt%;
—*— ξ; ····*···· P/V: dp = 3 mm; X = 10.6 wt%;
—■— ξ; ····■···· P/V: dp = 3 mm; X = 20 wt%.

Figure 4.13. Effects of solids presence on the azimuthally-averaged velocity distributions of the liquid phase at Njs: dp = 1 mm, 3 mm; X = 20 wt%; Njs = 490 rpm.

Figure 4.14. Contours of energy dissipation rate ε in the 45° plane between two baffles.

Figure 4.15. Azimuthally-averaged distributions of the velocity components of the liquid and solid phase in suspension at $N = N_{js}$ = 360 rpm, d_p = 3 mm, X = 5.2 wt%: — Gidaspow model; --- Pinelli model; ··· modified Brucato model; O PEPT.

Figure 4.16. Azimuthally-averaged distributions of the velocity components of the liquid and solid phase in suspension at $N = N_{js}$ = 410 rpm, d_p = 3 mm, X = 10.6 wt%: — Gidaspow model; --- Pinelli model; ··· modified Brucato model; O PEPT.

Figure 4.17. Azimuthally-averaged distributions of the velocity components of the liquid and solid phase in suspension at $N = N_{js}$ = 490 rpm, d_p = 3 mm, X = 20 wt%: — Gidaspow model; --- Pinelli model; ··· modified Brucato model; O PEPT.

Figure 4.18. Azimuthally-averaged distributions of the velocity components of the liquid and solid phase in suspension at $N = N_{js}$ = 590 rpm, d_p = 3 mm, X = 40 wt%: — Gidaspow model; --- Pinelli model; ⋯ modified Brucato model; O PEPT.

Figure 4.19. Azimuthally-averaged distributions of the velocity components of the liquid and solid phase in suspension at $N = 1.5N_{js}$ = 735 rpm, d_p = 3 mm, X = 20 wt%: — Gidaspow model; --- Pinelli model; ⋯ modified Brucato model; O PEPT.

Figure 4.20. Azimuthally-averaged distributions of solid volume concentration in suspension at N_{js} (d_p = 3 mm): — Gidaspow model; --- Pinelli model; ⋯ modified Brucato model; O PEPT.

Figure 4.21. Azimuthally-averaged distributions of solid volume concentration in suspension at $N > N_{js}$ (d_p = 3 mm): — Gidaspow model; --- Pinelli model; ⋯ modified Brucato model; O PEPT.

Figure 4.22. Azimuthally-averaged distributions of the velocity components of the liquid and solid phase in suspension at $N = N_{js}$ = 360 rpm, d_p = 3 mm, X = 5.2 wt%: — Gidaspow model only; ⋯ adding lift force and virtual mass force; O PEPT.

Figure 4.23. Azimuthally-averaged distributions of the velocity components of the liquid and solid phase in suspension at $N = N_{js}$ = 590 rpm, d_p = 3 mm, X = 40 wt%: — Gidaspow model only; ⋯ adding lift force and virtual mass force; O PEPT.

Figure 4.24. Azimuthally-averaged distributions of the velocity components of the liquid and solid phase in suspension at $N = 1.5N_{js}$ = 735 rpm, d_p = 3 mm, X = 20 wt%: — Gidaspow model only; ⋯ adding lift force and virtual mass force; O PEPT.

Figure 4.25. Azimuthally-averaged distributions of solid volume concentration in suspension, d_p = 3 mm: — Gidaspow model only; ⋯ adding lift force and virtual mass force; O PEPT.

Figure 4.26. Azimuthally-averaged distributions of the velocity components of the liquid and solid phase in suspension at $N = N_{js}$ = 360 rpm, d_p = 3 mm, X = 5.2 wt%.

Figure 4.27. Azimuthally-averaged distributions of the velocity components of the liquid and solid phase in suspension at $N = N_{js}$ = 590 rpm, d_p = 3 mm, X = 40 wt%.

Figure 4.28. Azimuthally-averaged distributions of the velocity components of the liquid and solid phase in suspension at $N = 1.5N_{js}$ = 735 rpm, d_p = 3 mm, X = 20 wt%.

Figure 4.29. Azimuthally-averaged distributions of solid volume concentration in suspension (d_p = 3 mm).

Figure 5.1. Computational grid section in the 45° plane between two baffles.

Figure 5.2. Azimuthally-averaged axial distributions of the normalised velocity components of the liquid and solid components at N_{js}: X = 5 wt%; N_{js} = 380 rpm.

Figure 5.3. Azimuthally-averaged radial distributions of the normalised velocity components of the liquid and solid components at N_{js}: X = 5 wt%; N_{js} = 380 rpm.

Figure 5.4. Azimuthally-averaged axial distributions of the normalised velocity components of the liquid and solid components at N_{js}: X = 10 wt%; N_{js} = 450 rpm.

Figure 5.5. Azimuthally-averaged axial distributions of the normalised velocity components of the liquid and solid components at N_{js}: X = 20 wt%; N_{js} = 510 rpm.

Figure 5.6. Azimuthally-averaged axial distributions of the normalised velocity components of the liquid and solid components at N_{js}: X = 40 wt%; N_{js} = 610 rpm.

Figure 5.7. Azimuthally-averaged axial distributions of the normalised velocity components of the liquid and solid components at $N = 2N_{js}$: $X = 10$ wt%; $N = 800$ rpm.

Figure 5.8. Demonstration of Reynolds number similarity – Azimuthally-averaged radial distributions of the normalised velocity components of the three mixture components based on PEPT measurements: — $X = 5$ wt%; --- $X = 10$ wt%; -·-·-· $X = 20$ wt%; ··· $X = 40$ wt%; $N = N_{js}$; $Re_{imp} = 1.5\times10^5 – 2.4\times10^5$ (see Table 1).

Figure 5.9. Azimuthally-averaged axial distributions of normalised solid volume concentration in suspension at N_{js}.

Figure 5.10. Azimuthally-averaged radial distributions of normalised solid volume concentration in suspension at N_{js}.

Figure 5.11. Azimuthally-averaged axial distributions of normalised solid volume concentration in suspension at $N > N_{js}$.

Figure 5.12. Azimuthally-averaged radial distributions of normalised time-average slip velocity based on PEPT measurements at different solid concentrations and agitation speeds.

Figure 5.13. Measure of global difference in slip velocity between the two solid components in the vessel as a function of mean solid concentration.

Figure 5.14. Variation of suspension uniformity index as a function of impeller speed for different particle sizes in binary- and mono-disperse suspensions.

Figure 5.15. Comparison of azimuthally-averaged axial and radial distributions of normalised solid volume concentration based on PEPT measurements in binary- and mono-disperse suspensions at N_{js}.

Figure 5.16. Normalised radial and axial velocities averaged on surfaces S_r (of diameter $0.5T$) and S_h ($0.3H$ off the base), respectively, showing excellent verification of mass continuity by both PEPT (Guida et al., 2011) and CFD.

Figure 5.17. Azimuthally-averaged axial distributions of the normalised velocity components of the liquid and solid components at N_{js}: $X = 5$ wt%; $N_{js} = 380$ rpm.

Figure 5.18. Azimuthally-averaged axial distributions of the normalised velocity components of the liquid and solid components at N_{js}: $X = 10$ wt%; $N_{js} = 450$ rpm.

Figure 5.19. Azimuthally-averaged axial distributions of the normalised velocity components of the liquid and solid components at N_{js}: $X = 20$ wt%; $N_{js} = 510$ rpm.

Figure 5.20. Azimuthally-averaged axial distributions of the normalised velocity components of the liquid and solid components at N_{js}: $X = 40$ wt%; $N_{js} = 610$ rpm.

Figure 5.21. Azimuthally-averaged radial distributions of normalised solid volume concentration in suspension at N_{js}: $X = 5$ wt%; $N_{js} = 380$ rpm.

Figure 5.22. Azimuthally-averaged radial distributions of normalised solid volume concentration in suspension at N_{js}: $X = 10$ wt%; $N_{js} = 450$ rpm.

Figure 5.23. Azimuthally-averaged radial distributions of normalised solid volume concentration in suspension at N_{js}: $X = 20$ wt%; $N_{js} = 510$ rpm.

Figure 5.24. Azimuthally-averaged radial distributions of normalised solid volume concentration in suspension at N_{js}: $X = 40$ wt%; $N_{js} = 610$ rpm.

Figure 5.25. Azimuthally-averaged local volume concentration maps for the poly disperse systems at varying X: yellow, $d_p \sim 1$ mm; red, $d_p \sim 1.7$ mm; green, $d_p \sim 2.2$ mm; blue, $d_p \sim 2.7$ mm; black, $d_p \sim 3$ mm.

Figure 6.1. Computational grid section in the 45° plane between two baffles: (a) smaller tank with the smallest impeller; (b) smaller tank with the medium impeller.

Figure 6.2. Azimuthally-averaged velocity field at N = 200 rpm (Re = 76.3) from PEPT measurement (Guida, 2010).

Figure 6.3. Azimuthally-averaged distributions of velocity components – CFD and PEPT compared: N = 200 rpm (Re = 76.3): (a) radial positions; (b) axial positions within the impeller blade width; (c) axial positions below the impeller; (d) axial positions above the impeller.

Figure 6.4. Distribution of tracer over time from PLIF measurement at N = 200 rpm (Re = 76.3) (Guida, 2010).

Figure 6.5. Distribution of tracer over time from CFD prediction at N = 200 rpm (Re = 76.3).

Figure 6.6. Cavern development over time.

Figure 6.7. Comparison of velocity distributions from PEPT, PIV and CFD at N = 65 rpm.

Figure 6.8. Comparison of velocity distributions from PEPT, PIV and CFD at N = 125 rpm.

Figure 6.9. Comparison of velocity distributions from PEPT PIV and CFD at N = 180 rpm.

Figure 6.10. Different arrangements of the rotating domain and stationary domain in CFD modelling of a stirred vessel: (a) arrangement in the work of Adams and Barigou (2007); (b) conventional arrangement; (c) arrangement in present study.

Figure 6.11. Comparison of cavern shape and size at different Reynolds numbers from PLIF measurement (Adams and Barigou, 2007) and CFD predictions using three definitions.

Figure 6.12. Cavern shape and size for PBTU and RDT from CFD predictions using the three definitions: --- $u_\theta = 0.01u_{tip}$; -.-.- $u_{rz} = 0.01u_{tip}$; — $u = 5\times10^{-4}$ $m\ s^{-1}$.

Figure 6.13. Cavern growth upward under PBTD, PBTU and RDT rotating modes.

Figure 6.14. Effects of rheological properties and impeller bottom clearance on the cavern size and shape generated by PBT of $D = T/2$ in the down-pumping mode and measured by PEPT.

Figure 6.15. CFD predicted cavern shape and size under PBTU and RDT rotating modes: $C = 0.5T$.

Figure 6.16. Comparison of cavern size and shape from PEPT measurement and CFD prediction: - - -, $u_{rz} = 0.01u_{tip}$; ·····, $u_\theta = 0.01u_{tip}$; —, $u = 5\times10^{-4}$ $m\ s^{-1}$; ♦ PEPT measurement.

Figure 6.17. Azimuthally-averaged velocity fields from PEPT measurement.

Figure 6.18. Azimuthally-averaged radial velocity profiles of axial velocity components u_z.

Figure 6.19. Azimuthally-averaged radial velocity profiles of radial velocity components u_r.

Figure 6.20. Azimuthally-averaged radial velocity profiles of radial velocity components u_θ.

Figure 6.21. Effect of yield stress on the cavern shape and size.

Figure 6.22. Effect of flow consistency coefficient on the cavern shape and size.

Figure 6.23. Effect of flow behavior index on the cavern shape and size.

Figure 6.24. Power number as a function of Reynolds number.

Figure 7.1. Computational grid section in the 45° plane between two baffles.

Figure 7.2. Azimuthally-averaged velocity maps of the liquid and solid phases at varying X and $N = N_{js}$.

Figure 7.3. Effect of solid phase on the velocity distribution of the liquid phase at N_{js}.

Figure 7.4. Effect of the mean mass concentration of the solid phase on the flow number.

Figure 7.5. Azimuthally-averaged maps of time-averaged slip velocity from PEPT measurements.

Figure 7.6. Normalized azimuthally-averaged maps of spatial distribution of the local solid concentration at varying X and $N = N_{js}$.

Figure 7.7. Variation of the suspension uniformity index as a function of the mean solid mass concentration.

Figure 7.8. Normalized radial and axial velocities averaged on surface S_r (of diameter $0.53T$) and S_z ($0.2H$ off the base), respectively.

Figure 7.9. Azimuthally-averaged axial distributions of the velocity components of the liquid and solid components at N_{js}: $X = 2.4$ wt%; $N_{js} = 495$ rpm.

Figure 7.10. Azimuthally-averaged radial distributions of the velocity components of the liquid and solid components at N_{js}: $X = 2.4$ wt%; $N_{js} = 495$ rpm.

Figure 7.11. Azimuthally-averaged axial distributions of the velocity components of the liquid and solid components at N_{js}: $X = 11.5$ wt%; $N_{js} = 600$ rpm.

Figure 7.12. Azimuthally-averaged radial distributions of the velocity components of the liquid and solid components at N_{js}: $X = 11.5$ wt%; $N_{js} = 600$ rpm.

Figure 7.13. Azimuthally-averaged axial distributions of the velocity components of the liquid and solid components at N_{js}: X = 21.6 wt%; N_{js} = 750 rpm.

Figure 7.14. Azimuthally-averaged radial distributions of the velocity components of the liquid and solid components at N_{js}: X = 21.6 wt%; N_{js} = 750 rpm.

Figure 7.15. Radial profiles of azimuthally-averaged solid volume concentration.

Figure 7.16. Azimuthally-averaged radial distributions of the velocity components of the liquid and solid components at N_{js}: X = 2.4 wt%; N_{js} = 495 rpm.

Figure 7.17. Azimuthally-averaged radial distributions of the velocity components of the liquid and solid components at N_{js}: X = 11.5 wt%; N_{js} = 600 rpm.

Figure 7.18. Azimuthally-averaged radial distributions of the velocity components of the liquid and solid components at N_{js}: X = 21.6 wt%; N_{js} = 750 rpm.

Figure 7.19. Comparison of azimuthally-averaged radial distributions of solid volume concentration in different viscoplastic fluids.

Figure 7.20. Comparison of azimuthally-averaged radial distributions of liquid velocity with and without presence of solids at N = 200 rpm.

Figure 7.21. Comparison of azimuthally-averaged radial distributions of solid concentration with and without presence of solids: – N = 200 rpm; --- $N = N_{js}$ = 495 rpm; ⋯ $N = N_{js}$ = 600 rpm.

Chapter I

INTRODUCTION

1.1. Motivation

Mixing in stirred vessels has become one of the most widely encountered industrial processes. Mixing efficiency plays an important role in improving product quality and industrial profitability. With high quality products becoming more and more desirable in the market, mixing efficiency is greatly required to be improved.

However, due to the complex hydrodynamics of fluid mixing in stirred vessels, a number of challenging problems still exist for improving the mixing quality and to properly design the stirred vessel configuration. It has been reported that the lack of fundamental knowledge of the mixing process in stirred vessels has caused losses of several billion dollars a year (Smith, 1991). Using global parameters such as the power input per unit mass as the design principle of stirred vessels is far from enough to provide the critical information. Local properties throughout the stirred vessel have been desired by industry, because localized hydrodynamics and phase distributions inside the stirred vessel are more informative for proper design of stirred vessels.

A lot of efforts have been devoted to the understanding of fundamental concepts. The well-established experimental techniques such as Laser Doppler anemometry (LDV) and particle image velocimetry (PIV) have made significant contributions to the understanding of complex hydrodynamics in stirred vessels. However, they have presented their own limitations to investigate complex mixing systems in modern process industries. For example, one of the challenges using conventional experimental techniques is the opacity of the majority of fluids

in many industries such as slurries and highly concentrated solid-liquid suspensions. Techniques which are not restricted to transparent mixing systems have been attempted by researchers, like Positron Emission Particle Tracking (PEPT) and the computer automated radioactive particle tracking (CARPT).

Computational fluid dynamics (CFD) has been developed fast with the development of computer resources. Due to its advances, for example, it is cost effective, and it is capable of providing comprehensive fundamental conceptions which are experimentally expensive or unobtainable. CFD has drawn a lot of attention and has been widely used for analysing fluid flows in stirred vessels. In single-phase systems, CFD modelling of mixing of various fluids in stirred vessels of different configurations has been widely validated. However, due to the lack of experimental data because of the limitations of the well-established techniques as mentioned above, CFD modelling of opaque systems, like condensed solid-liquid systems, and mixing of most non-Newtonian fluids have not been well validated.

Therefore, the aim of this work is using CFD to investigate the complex fluid mixing in stirred vessels and to provide detailed descriptions of the localized hydrodynamics and phase distributions. The capability of CFD modeling of various mixing systems is assessed by comparing in detail with different experimental measurements.

1.2. Objective

1. The ability of CFD modeling for predicting the solid-liquid suspensions at high solid loadings will be verified. Various CFD approaches and models will be tested through comparison with the spatial distribution of velocity and solid concentration comprehensively, given the local velocity and phase distribution from the PEPT measurement.

2. The ability of CFD modeling for predicting the mixing of complex non-Newtonian fluids in stirred vessels, and solid suspensions in non-Newtonian fluids will be examined by comparing the CFD simulations with experimental data obtained from different measurement techniques, including PIV, PEPT and planar laser-induced fluorescence (PLIF).
3. Detailed parametric studies and optimization studies will be carried out using the well validated CFD approaches and CFD models. Effects of fluid rheology and stirred tank configuration on the mixing efficiency will be investigated, which could provide proper guidelines for the stirred tank design.

1.3. Layout of thesis

This thesis is structured as follows. The background and review of relevant literature are given in Chapter II. Detailed descriptions of different experimental techniques and CFD modelling are discussed. In Chapter III, single phase mixing of Newtonian and shear-thinning fluids in a stirred vessel is investigated. The predicted fluid flows in turbulent and transitional regimes are compared with PIV and PEPT measurements. The performances of different types of impellers for mixing of Newtonian and non-Newtonian fluids are presented. In Chapter IV, monodisperse solid-liquid suspensions at duifferent concentrations are investigated by CFD modeling. The detailed 3-D distribution of local velocity and solid concentration are compared with PEPT measurements. Effects of modelling approaches and CFD models on the simulations are investigated. Subsequently, similar numerical investigations are carried out for binary- and poly-disperse systems in Chapter V. CFD modeling of mixing of viscoplastic fluids in stirred vessels are presented in Chapter VI, where the predicted cavern formation around the impeller and velocity distribution within cavern are

compared with PIV, PEPT and PLIF measurements. Effects of the stirred tank configuration including impeller type, impeller diameter, impeller clearance on the cavern size and shape as well as fluid velocity within the cavern are investigated. Study of solid suspensions in viscoplastic fluids using PEPT and CFD is reported in Chapter VII. Finally, Chapter VII presents the conclusion of the work and suggestions for future work.

This research has led to the following journal publications:

1. Liu, L., Barigou, M., 2013, Numerical modeling of velocity field and phase distribution in dense monodisperse solid-liquid suspensions under different regimes of agitation: CFD and experiment, Chemical Engineering Science, doi: 10.1016/j.ces.2013.05.066 (Chapter IV).

2. Liu, L., Barigou, M., 2013, Experimentally validated CFD simulations of multi-component hydrodynamics and phase distribution in agitated high solid fraction binary suspensions, Industrial&Engineering Chemistry Research, doi: 10.1021/ie3032586 (Chapter V).

Chapter II

LITERATURE REVIEW

2.1. Introduction

Fluid mixing is commonly encountered in a wide range of processes in chemicals, biochemicals, polymer, crystallization, mineral, food and pharmaceutical industries. Concerning the wide range of process objectives in industries, fluid mixing takes place in a range of equipment such as in-line static mixers, rotor-stator mixers, and stirred vessels. Mechanically agitated vessels, among these diverse mixers, are the most common fluid mixing devices in the process applications used, for example, for the blending of miscible liquids, gas dispersion or solid suspension in a liquid, and optimization of chemical reactions. The general purpose of fluid mixing in stirred vessels is to reduce inhomogeneity in order to achieve a desired process result (Paul et al., 2004), for instance, the reduction of non-uniformity of solid distributions in solid-liquid systems.

Fig. 2.1 illustrates the typical configuration of a baffled-tank consisting of a centrally positioned shaft, an impeller (a pitched blade turbine in this figure), and four baffles. Compared with unbaffled-tanks, baffled-tanks have received more attention for fluid mixing under turbulent regime due to the capability of preventing the formation of a central vortex in the turbulent flow and also promoting fluid mixing in the axial direction. Unbaffled-tanks are usually used for the mixing of high viscosity fluids where the vortexing seldom occurs and close-clearance impellers, at 85 to 95% of the tank diameter including helical-ribbon impeller, helical screw impeller, and anchor impeller are usually required (Paul et al., 2004). Fluid in a stirred vessel is pumped by a rotating impeller, and is then transported to other regions of the

stirred vessel. The flow pattern of fluid mixing in stirred vessels varies widely, and is significantly affected by both fluid rheology and configuration of stirred tanks. Fig. 2.2 illustrates two typical flow patterns of fluid mixing under turbulent regime, agitated by the radial impeller and the axial impeller, respectively. It can be observed that two circulation loops (one above and one below the radial impeller) are generated by the radial impeller, while one circulation loop is generated by the axial impeller. The circulation loop is required to be large enough to transport the material to all parts of the stirred vessel so that effective mixing could be achieved.

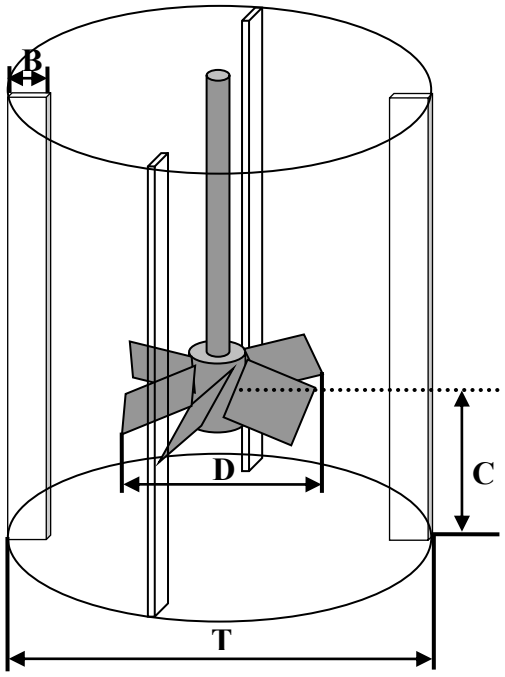

Figure 2.1. Configuration and dimensions of a mechanically agitated vessel.

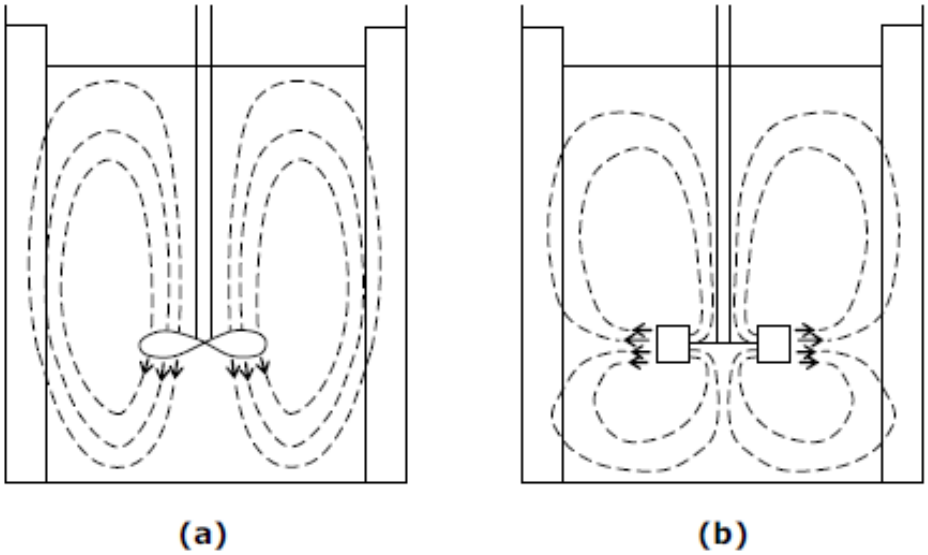

Figure 2.2. Typical flow patterns generated by the radial impeller and the axial impeller in stirred vessels (Edwards, 1997): (a) axial impeller; (b) radial impeller.

2.2. Mechanically agitated vessels

The local hydrodynamics and phase distributions in a stirred vessel are not only affected by the above mentioned fluid rheology but also significantly influenced by the configuration of the stirred vessel, e.g. tank base shape, impeller type and geometry, and impeller position. Understanding the effect of these geometrical parameters on mixing performance is considerably important to the proper design of the stirred vessel for achieving various mixing purposes.

2.2.1. Impeller type

A wide variety of impellers are available in industry. The impellers are generally classified into three groups considering the discharge direction of the fluid in a stirred vessel: 1) radial impellers such as RDT that discharge the fluid in the radial direction towards the tank wall; 2) axial impeller such as marine propeller (MP) that discharge the fluid in the axial direction, upward or downward, depending on the impeller rotating direction; 3) mixed impellers such

as PBT with the blade pitch angle varying in the range of 10°- 90° from the horizontal with 45° being the most commonly used. The radial impellers are generally used for gas dispersion due to a higher shear characteristic, whereas the mixed and axial impellers are considered to be suitable for the solid particle suspensions because of their high pumping efficiencies.

Using the RDT and PBT in various applications usually meets the requirements, therefore, are the most widely used impellers in most industries, and numerous studies have focused on characterizing their mixing performances (Lee and Yianneskis, 1998; Revstedt et al., 2000; Javed et al., 2006). However, in some applications such as gas-liquid systems and fermentations where stirred vessels of high aspect ratio are commonly used, multiple impellers are required (Bujalski et al., 2002 (a); Montante et al., 2001; Montante and Magelli, 2005; Taghavi et al., 2011). Furthermore, for mixing of high viscosity fluids, close-clearance types of impellers such as helical-ribbon impeller, helical screw impeller, and anchor impeller are recommended (Brito de la Fuente et al., 1997; Aubin et al., 2000; Peixoto et al., 2000). The guidelines for the impeller selection can be found in the work of Paul et al. (2004).

The mixing performance of different types of impellers in single-phase mixing has been extensively studied (Galindo and Nienow, 1993; Zhou and Kresta, 1996; Thakur et al., 2004; Kumaresan and Joshi, 2006), and research on the performance of various impellers in multiphase flow has been reviewed by Kasat and Pandit (2005). In these studies, *Po*, of various impellers has been extensively investigated because of the simplicity of measurements (Hemrajani and Tatterson, 2004). The flow pattern and velocity field generated by different impellers have also been extensively reported (Zhou and Kresta, 1996; Kumaresan and Joshi, 2006). The flow pattern under the turbulent regime has been reported to be significantly affected by the impeller type. However, the impeller type has a negligible effect on the flow

pattern in the mixing of highly viscous fluids in stirred vessels at low *Re* where the tangential flow is predominant (Elson, 1990; Moore and Cossor, 1995). Most recently, Patel et al. (2011) investigated the performance of 7 axial impellers and 4 radial impellers in the mixing of viscoplastic fluids, and they found that the impellers with high solidity ratio give better mixing efficiency.

2.2.2. Impeller bottom clearance and impeller geometrical parameters

Studies on the effect of the impeller bottom clearance, i.e. the distance from the vessel base to the impeller central line, on the mixing of various fluids show different intendancy depending on the mixing system. Some studies found that moving the impeller from the standard position ($T/3$) to a higher position ($T/2$) can generate better flow pattern and larger fluid motion volume in the mixing of high viscosity fluids (Jaworski et al., 1991; Kresta and Wood, 1993; Amannullah et al., 1997; Fangary et al., 2000; Ochieng et al., 2008; Ein-Mozaffari and Upreti, 2009).

On the contrary, low impeller position has been found to more efficient for the RDT to lift particles from the tank bottom in the solid-liquid suspensions due to greater energy transfer to particles (Nienow, A. W., 1968; Armenante and Nagamine, 1998; Montante et al., 1999).

Impeller geometrical parameters such as impeller diameter, blade width and thickness, and the number of impeller blades have also been reported widely to significantly affect the fluid mixing (Rutherford et al., 1996; Prajapati and Ein-Mozaffari, 2009; Ein-Mozaffari and Upreti, 2009; Ameur et al., 2011; Ameur and Bouzit, 2012). Moreover, the effect of the blade angle of PBT (e.g. 60°, 45°, 30°) on the flow pattern has been studied by Murthy and Joshi (2008) and Ranade and Joshi (1989).

2.3. Fluid rheology

Fluids in many industries such as food, polymer, catalyst, oil and mining exhibit non-Newtonian rheological properties, like plasticity, elasticity, yields stress, and thixotropy. The greater the non-Newtonian behaviour of the fluids the more complex the fluid mixing in stirred vessels is. Non-Newtonian fluids with viscosities that are shear-rate dependent but time-independent are most commonly encountered in industry. Based on the relationship between the fluid viscosity and shear rate, non-Newtonian fluids have been generally classified into four groups, i.e. shear-thinning, shear-thickening, Bingham and viscoplastic fluids (Paul et al., 2004). Their non-Newtonian flow behaviours are shown in Fig. 2.3. The shear-thinning and viscoplastic fluids are relevant to this thesis, and their rheological characteristics are discussed in more detail below.

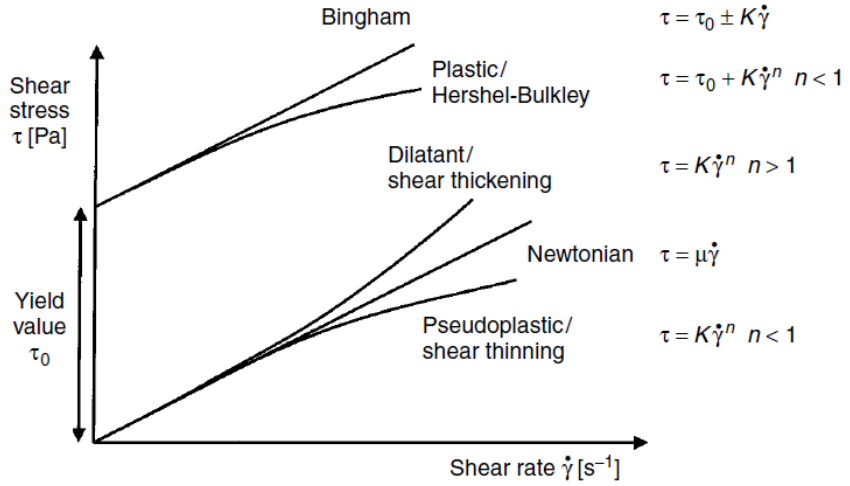

Figure 2.3. Rheological properties of Newtonian and non-Newtonian fluids (Paul et al., 2004).

2.3.1. Shear-thinning fluids

Shear-thinning fluids (also termed power-law fluids or pseudoplastic fluids) show a decrease in viscosity with increasing shear rate and comprise an important class of the non-Newtonian

fluid group. The rheological properties of shear-thinning fluids can be described by differnet constitutive laws, and power-law model is usually used for shear-thinning behavior:

$$\tau = k\dot{\gamma}^n \tag{2.1}$$

where, τ is the shear stress, $\dot{\gamma}$ is the shear rate, k is the fluid consistency coefficient and n is the flow behaviour index, less than 1 for shear-thinning fluids.

The viscosity of shear-thinning fluids reduces significantly near the impeller due to the high shear rate, and is relatively high in the low shear regions away from the impeller. Therefore, the fluid mixing is constrained in the region around the impeller, termed a pseudo-cavern. The fluid has been found to be generally well mixed within the pseudo-cavern, while beyond it the shear-thinning fluids move with very small velocity ($<< 1\% u_{tip}$) (Amanullah et al., 1998; Adams and Barigou, 2007, Adams, 2009). The shape and size of the pseudo-cavern generated by various impellers have been widely investigated (Amanullah et al., 1998; Alvarez et al., 2002; Arratia et al., 2006). In order to conveniently assess the size of the pseudo-cavern in the stirred vessel, different theoretical models have been developed to correlate the size of pseudo-caverns with the power draw and the configuration of stirred vessels. The most commonly used spherical and toroidal models (Amanullah et al., 1998) are shown below,

the spherical model,

$$r_c^{[1-(2/n)]} = v_0\left[\left(\frac{2}{n}-1\right)\left(\frac{4\pi k}{F}\right)^{1/n}\right] + b^{[1-(2/n)]} \tag{2.2}$$

where r_c is the radius of the pseudo-cavern; b = T/2, v_0 is the velocity at the pseudo-cavern boundary, and F is the body force at the pseudo-cavern boundary,

and the toroidal model,

$$r_c^{[1-(2/n)]} = v_0\left[\left(\frac{2}{n}-1\right)\left(\frac{4\pi^2 k}{F}\right)^{1/n}\right] + b^{[1-(2/n)]} \tag{2.3}$$

where $r_c = D_c / 4$ $b = T/4$.

Besides the theoretical analysis, different experimental techniques have been used to measure the pseudo-cavern, moreover, the detailed dynamic behaviours within the pseudo-caverns have also been measured. Photography method was used in the early studies to capture the cavern formation (Galindo and Nienow, 1992; Galindo et al., 1996). The chaotic characteristics such as stretching, folding, as shown in Fig. 2.4, measured by the planar laser-induced fluorescence (PLIF) have been reported in some work (Zalc et al., 2001; Alvarez et al., 2002; Arratia et al., 2006). Laser Doppler anemometry (LDV), particle image velocimetry (PIV), and Computational fluid dynamics (CFD) have been used to measure the flow fields of mixing of shear-thinning fluids in stirred vessels (Lamberto et al., 1999, 2001; Adams and Barigou, 2007; Adams, 2009). It has been reported that the rheology of shear-thinning fluids has significant effect on the size of pseudo-cavern and the fluid velocity within the pseudo-cavern.

2.3.2. Viscoplastic fluids

Apparent yield stress is an important characteristic of viscoplastic fluids (also is termed as yield stress fluids). As a consequence, it is essential for the external forces to overcome the apparent yield stress for the viscoplastic fluids to flow, or they behave like a solid.

The rheological behavior of viscoplastic fluid is generally described as,

$$\tau = \tau_y + k\dot{\gamma}^n \tag{2.4}$$

where τ_y is the yield stress, k is the fluid consistency coefficient and n is the flow behaviour index. Fluid is called Bingham fluid if $n = 1$, and is called Herschel-Bulkley fluid if $n < 1$. Because Bingham fluid is not investigated in this work, the term of viscoplastic fluid means the same with Herschel-Bulkley fluid.

Viscoplastic fluids show similar mixing features to shear-thinning fluids, whereby fluid mixing is constrained around the impeller. However, with viscoplastic liquids there is a fixed boundary due to the apparent yield stress, and there is no fluid motion beyond the cavern boundary (Galindo and Nienow, 1992; Adams and Barigou, 2007, Adams, 2009). The term cavern was first used by Wichterle and Wein (1975) to describe the mobile zone around the impeller. Cavern formation around the impeller is a unique characteristic of mixing of viscoplastic fluids.

Due to the detrimental effect of cavern on mixing efficiency, numerous efforts have been made on measuring the cavern size in order to eliminate the dead zone beyond the cavern. The cavern size and shape have been described by different mathematical models, and three most widely used models are shown below,

cylindrical model (Elson and Cheesman, 1986),

$$\left(\frac{D_c}{D}\right)^3 = \frac{P_0}{\left[\left(H_c / D_c\right)+1/3\right]\pi^2}\left(\frac{\rho N^2 D^2}{\tau_y}\right) \tag{2.5}$$

spherical model (Solomon, 1981),

$$\left(\frac{D_c}{D}\right)^3 = \left(\frac{4P_0}{3\pi}\right)\left(\frac{\rho N^2 D^2}{\tau_y}\right) \tag{2.6}$$

toroidal model (Amanullah et al., 1998),

$$\left(\frac{D_c}{D}\right)^2 = \frac{1}{\pi}\left(\frac{\rho N^2 D^2}{\tau_y}\right)\sqrt{N_f^2 + \left(\frac{4P_0}{3\pi}\right)^2} \tag{2.7}$$

The cavern size and shape resolved from above mentioned models have been widely compared in literature (Nienow and Elson, 1988; Amanullah et al., 1998; Adams and Barigou, 2007). The cylindrical model has been reported to predict better cavern shape and size generated from radial impellers than the spherical model (Nienow and Elson, 1988). However, neither spherical nor cylindrical model could provide accurate cavern generated from axial impellers, but the torus model gave good predicted cavern shape (Amanullah et al., 1998; Adams and Barigou, 2007).

Considering the experimental investigation, the cavern size and shape as well as velocity distributions within the cavern have not been well studied, though being of importance to estimate the mixing quality. This is because most viscoplastic fluids are opaque, and the conventional experimental techniques used to measure the velocity distributions, like LDV and PIV, require transparent systems. Attempts to obtain the flow field inside cavern have been made by some researchers. The velocity distributions inside the cavern in the mixing of carbopol solution agitated by a RDT and PBT were measured using LDV by Moore and Cossor (1995). The flow patterns generated by these two impellers at low Reynolds numbers were reported to be identical due to the predominant tangential flow. Ultrasonic Doppler velocimetry (UDV) has been used to measure the flow field generated from different types impellers including PBT, Lightnin A310 and Scaba 6SRGT in some studies (Ihejirika and Ein-Mozaffari, 2007; Pakzad et al., 2007; Saeed et al., 2008; Ein-Mozaffari and Upreti, 2009).

Though the understanding of mixing of non-Newtonian fluids in stirred vessels has made progress with the development of both experimental technique and computational modelling,

a wide range of challenges have not been resolved, e.g. wide variations in the spatial distributions of the fluid viscosity throughout the stirred vessel result in significant difficulties in controlling the mixing process of non-Newtonian fluids.

2.3.3. Solid-liquid suspensions

Apart from the above mentioned classification, i.e. laminar, transitional and turbulent regime, fluid mixing in stirred vessels has also been generally classified into the single phase flow and multi-phase flow concerning the number of mixing phases. General information about the single phase flow in stirred vessels has been discussed above, and as it is widely encountered in a variety of industries, it is necessary to introduce briefly the multiphase flow in stirred vessels, e.g. solid/liquid, gas/liquid, and solid/gas/liquid. Due to the additional effects associated with the discrete phase, e.g. interactions between particle-fluid and particle-particle collisions, considerable complexity of the turbulent (time-dependent) flow structure is induced in the multi-phase mixing in stirred vessels (Nienow, 1997b).

Solid suspensions in liquids find a wide range of industrial applications in chemical reaction, pharmaceuticals, catalytic, crystallization, sterilization, and mineral industries. Depending on the density of solid particles, the solid particles may settle at the tank base ($\rho_d > \rho_l$), or float on the liquid surface ($\rho_d < \rho_l$). In order to achieve good heat and mass transfer, or chemical reaction between the liquid phase and solid particles, the settling or floating solid particles need to be lifted off the tank base or be drawn down from the liquid top surface. The particles are then distributed to different regions within the stirred vessel. Either inadequate or overmixing of solid suspensions in liquids causes poor product quality or poor energy efficiency.

Considering the suspension of settling particles, three levels have been classified in terms of the degree of solid suspensions: 1) on-bottom motion; 2) just complete suspension; 3) uniform suspension (Paul et al., 2004), as shown in Fig. 2.4. The just complete suspension (impeller speed of N_{js},) is a critical state which could satisfy the requirement in most industrial applications, because under this condition the total surface of solid particles is sufficiently exposed to the liquid phase. The uniform solid distribution which requires much higher impeller speed of above N_{js} are desirable in some industries such as crystallizers and polymerization reactors, and non-uniform solid distribution may lead to unacceptably high local supersaturating levels and subsequent non-uniformity in crystal growth (Atiemo-Obeng et al., 2004).

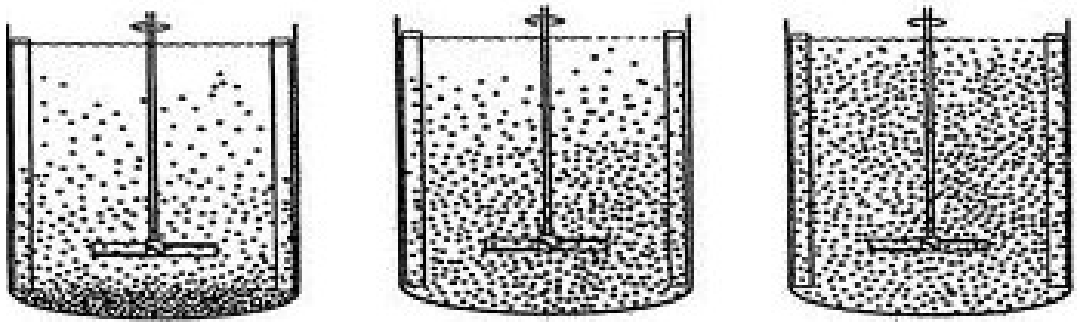

(a) **(b)** **(c)**

Figure 2.4. Degree of solid suspension (Paul et al., 2004): (a) Partial suspension; (b) Complete suspension; (c) Uniform suspension.

Extensive studies on characterizing the value of N_{js} have been carried out since the empirical correlation for N_{js} was proposed in the pioneering work of Zwietering (1958), and these studies have been reviewed by Jafari et al. (2012) and Tadhavi et al. (2011). However, none of the developed correlations are universally applicable, as the values of N_{js} from different theoretical models vary over a wide range (Bohnet and Niesmak, 1980). The Zwietering

criterion, i.e. no particle remains stationary on the bottom of the tank for longer than 1-2 s, is still the most widely used criterion.

Comparing with the theoretical models for the values of N_{js}, a localized hydrodynamic approach provides a more efficient basis for design since it enables a detailed description of the multiphase flow structures. The dilute solid suspensions, with the solid loading ranging from 0.02 vol% to 2.5 vol%, have been widely investigated using the well-established optical techniques such as LDV and PIV (Nouri and Whitelaw, 1992; Guiraud et al., 1997; Micheletti and Yianneskis, 2004; Montante et al., 2012). However, these techniques cannot be applied to dense solid concentrations due to the opacity of the systems. Solid dynamics at low solid concentrations have little effect on the liquid phase and hence, the liquid flow in dilute solid-liquid suspensions presents high similarity to the flow field of the single phase (Mersmann et al. 1998; Montante, G., 2012). However, with increasing solid particles, the effect of solid particles on the liquid phase is no longer negligible. Large drop in liquid velocities in the presence of particles of 2.5 vol% has been reported (Nouri and Whitelaw, 1992; Micheletti and Yianneskis, 2004).

So far, attempts at local measurements have been mainly limited to the investigation of mean axial solid-concentration profiles at low to medium solid loadings using intrusive conductivity or capacitance probes (Godfrey and Zhu, 1994; Brunazzi *et al.*, 2004; Špidla et al., 2005). Both the radial and axial solid distributions at solid loading of 20 vol%, using the probe method, were measured by Yamazaki and Miyanami (1986). The probe methods, however, give limited information and cannot be used to probe the local hydrodynamics of suspensions in detail or to measure the 3-D distribution of both liquid and solid. Recently, the radioactive particle tracer method has been used to measure the flow fields of both phases; solid

distributions at high solid loadings of up to 40 wt% were reported by Guida et al. (2009, 2010) using the Positron Emission Particle Tracking (PEPT) measurement, and the Computer Automated Radioactive Particle Tracking (CARPT) technique based on gamma-ray emissions has been developed (Rammohan et al., 2001; Guha et al., 2007). CFD modelling has been widely employed for simulating the solid-liquid suspensions in stirred vessels, as reviewed by Sommerfeld and Decker (2004) and Sardeshpande and Ranade (2012). Direct Numerical Simulations (DNS), Large Eddy Simulations (LES), and Eulerian-Lagrangian approches were used to handle dilute systems (~ 5 vol%) in a limited range of works due to computationally expensive cost (Derksen, 2003; Sbrizzai et al., 2006). The multi-fluid Eulerian-Eulerian model has been most widely used to model high solid concentrations (Tamburini et al. 2011; Khopkar et al., 2006). However, validations reported in the literature have been restricted to dilute systems (Montante and Magelli, 2005; Khopkar et al., 2006; Micale et al., 2004; Altway et al., 2001).

Mixing features become more complicated concerning solid suspensions in liquids exhibiting non-Newtonian behaviour, for example, in the process of particulate food mixtures such as fruit particles in yoghurt. This area has been scarcely investigated in the previous research. The just suspended impeller speed, N_{js}, for solid suspensions in shear-thinning liquids was measured in few studies (Kushalkar and Pangarkar, 1995; Wu and Pullum, 2001; Ibrahim and Nienow, 2010). Attempt at the detailed local information of solid suspensions in a Bingham liquid has been made numerically by Derksen (2009) using a Lattice-Boltzmann method. However, due to the lack of experimental data for the solid suspensions in viscoplastic liquids in stirred vessels, a one-dimensional single phase planar channel flow was performed instead to validate the CFD predictions. In summary, there are still outstanding issues that have not

been addressed concerning the accurate CFD modelling of solid-liquid suspensions due to the complex interactions between the phases and within the solid particles.

2.4. Flow mechanisms

The Reynolds number, *Re*, has been widely used to characterize fluid flows. *Re* is also useful to describe the fluid mixing in stirred vessels. In the situation of fluid mixing in stirred vessels, the impeller Reynolds number is defined as,

$$\mathrm{Re}_{imp} = \frac{\rho N D^2}{\mu} \tag{2.8}$$

where ρ is fluid density, N is impeller rotating speed, D is impeller diameter, and μ is fluid dynamic viscosity. The fluid flow is in laminar regime when $Re_{imp} < 10$ and is in turbulent regime when $Re_{imp} > 10^4$, with the transitional regime in between, i.e. $10 < Re_{imp} < 10^4$.

2.4.1. Turbulent regime

In industrial practices, mixing of low viscosity fluids (less than about 10 mPa s) in stirred vessels usually falls in the turbulent regime. A number of turbulent eddies of different length scales and intensities exist throughout the stirred vessels in the turbulent flow. The motion of the turbulent eddies play a significant role in promoting the fluid mixing rate, therefore, the turbulent regime is generally desirable for fluid mixing in stirred vessels. The mixing characteristics under turbulent regime in stirred vessels have been investigated in many studies, and the turbulence field has been reported to exhibit three-dimensional velocity fluctuations, anisotropic turbulence dissipations, and periodic hydrodynamics in the literature (Yianneskis et al., 1987; Wu and Patterson, 1989; Escudié and Liné, 2006). The turbulent intensity close to the impeller has been found to be significantly stronger than that in other

regions in the stirred vessel, and large proportion of the energy is dissipated close to the impeller (Cutter, 1966). Fluctuating turbulent trailing vortices are usually generated behind the impeller blades (Yianneskis et al., 1987; Schäfer et al., 1998; Escudié et al., 2004; Roy et al., 2010), with an example as illustrated in Fig. 2.5.

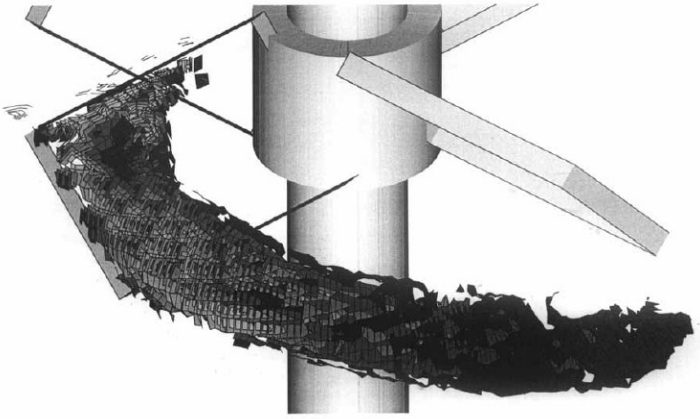

Figure 2.5. Trailing vortices behind a blade of a 45° PBT in down-pumping mode (Schäfer et al., 1998).

2.4.2. Laminar and transitional regimes

In most situations in the mixing of high viscosity fluids (more than about 10 Pa s) such as pastes, creams and paints, it is fairly difficult to achieve the turbulent state, and instead the laminar or transitional regimes usually predominate. In comparison with the mixing mechanism in the turbulent regime, lack of turbulent eddy dissipation in laminar and transitional regimes results in less efficient transportation. Due to the high viscosity, the energy input quickly diminishes away from the impeller, therefore, poor mixing is likely to occur, especially in the regions close to the tank wall and liquid free surface. Even though the complex turbulence eddy dissipation is absent in the laminar and transitional regimes, the mixing of high viscosity fluids is still accompanied by complex mixing phenomena. Fluid elements close to the impeller are highly sheared and are consequently, stretched, elongated and folded, with an example as shown in Fig. 2.4. These mixing features are of importance

for fluid mixing in the laminar regime (Edwards, 1997; Zalc et al., 2001; Alvarez et al., 2002; Arratia et al., 2006). The majority of high viscosity fluids exhibit non-Newtonian behaviour. Non-Newtonian fluids often show complex rheologies (e.g. viscosity dependence on shear rate or time dependent behaviour) and ultimately this makes the mixing mechanism more complicated. Fig. 2.6 shows two examples of the typical cavern formation in the viscoplastic fluid mixing, agitated by two types of impellers in the transitional regime.

Figure 2.6. Mixing structure of a high viscousity fluid (99.7% pure glycerin) agitated by a RDT at *Re* = 25 measured by PLIF (Alvarez et al., 2002).

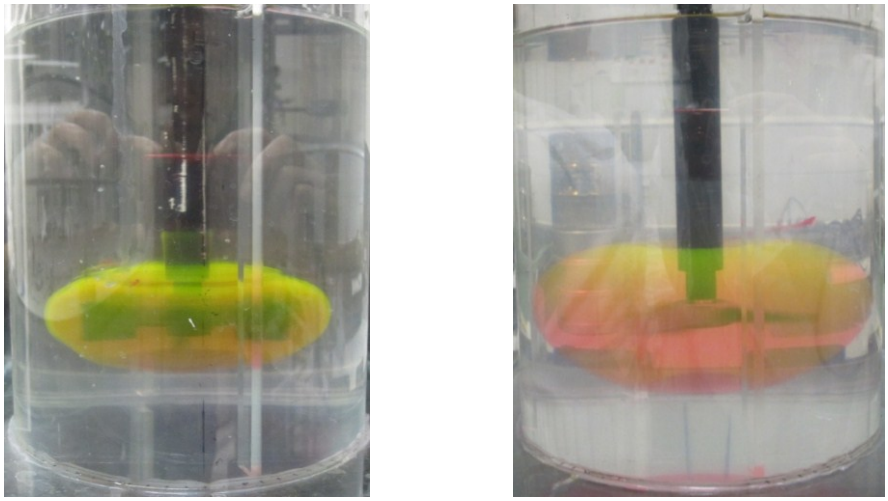

RDT (*Re* = 55) **A310-down pumping (*Re* = 260)**

Figure 2.7. Example of cavern formation around the impeller in the mixing of viscoplastic fluids in a stirred tank.

An important dimensionless parameter which has been applied widely to assess the mixing efficiency under above mentioned flow regimes is the power number, *Po*, expressed as a function of Reynolds number, Re_{imp}. The slope of the curves (*Po* vs. Re_{imp}) for various types of impellers in the laminar regime have been found to be -1, *Po* has been found to have complex relationship with Re_{imp} in the transitional regime, and *Po* is independent of the Reynolds number in turbulent regime (Metzner et al., 1961; Galindo and Nienow, 1992; Brito-de la Fuente et al., 1997; Aubin et al., 2000; Paul et al., 2004).

This brief introduction indicates that fluid mixing in stirred vessels exhibits considerable complexity regardless of flow regime, and the fluid rheology has a significant effect on the flow patterns and mixing quality. Therefore, a good understanding of the rheological properties, especially of complex non-Newtonian fluids, are fundamental in the study of fluid mixing in stirred vessels. The rheological behaviour of various non-Newtonian fluids and their mixing characteristics are given in more detail in the following section.

2.5. Experimental techniques

Because of the relative simplicity, *Po* as a function of *Re* for various types of impellers have been widely measured and used as the guideline for the stirred vessel design (Rushton et al., 1950; Holmes, et al., 1964; Hemrajani and Tatterson, 2004), though this information does not provide any insight into the detailed mixing within stirred vessels. With the increased requirement of more detailed local information for proper design, the intrusive conductivity or capacitance probes were introduced for testing the local information, like the local velocity and solid concentration (Günkel et al. 1971; Khopkar et al., 2006). However, the information from this method is still limited, meanwhile, the accuracy is subjected to the disturbance of the local flow by the probes. Non-intrusive optical methods such as Laser Doppler

Velocimetry (LDV) and Particle Image Velocimetry (PIV) were introduced after the invention of laser in the 1960s. The optical methods have been extensively used by a number of researchers and substantial improvement of the understandings of fluid mixing in stirred vessels has achieved over the last four decades. Meanwhile, the performance of the optical methods has improved rapidly with the development of laser and camera techniques, and LDA and PIV are currently the most widely used techniques. However, the optically-based experimental measurements are constrained to transparent systems resulting in limited practical use for many industries, so alternative techniques are desirable for most non-Newtonian fluids and multiphase systems which are opaque. The Lagrangian tracking techniques such as the Positron Emission Particle Tracking (PEPT) and Computer Automated Radioactive Tracking (CARPT) are two promising techniques to investigate the localized information for the opaque systems. The Ultrasonic Doppler Velocimetry (UDV) technique has also been used to measure the velocity field in stirred vessels. The wide use of experimental measurements has been extensively reviewed by Mavros (2001). The following discussed and reviewed experimental techniques are relevant to this work.

2.5.1. Particle Image Velocimetry

PIV is a well-established non-intrusive optical technique used for measuring the instantaneous flow in translucent systems, which has made significant contribution to the studies of complex hydrodynamics in stirred vessels. PIV provides the 2-D Eulerian data by measuring the velocities on a laser plane going through the stirred vessel.

The PIV equipment consists of laser emission unit and camera for image recording. The laser emission and camera capture are controlled by a synchronizer. A small amount of buoyant seeding particles used to follow fluid flow are introduced into the system prior to experiments.

Tracer particles are illuminated by the very thin laser sheet. The positions of the seeding particles are recorded in the images captured by the camera located perpendicular to the laser sheet. The images are divided into many small interrogation areas (IA). The displacement of particles in each interrogation area is determined using the Fast Fourier Transform (FFT) cross correlation.

Extensive information on the single phase flow fields in stirred vessels have been obtained from the PIV measurements (Bakker et al., 1996; Sheng et al., 1998; Zalc et al, 2001; Kukura et al., 2002; Aubin et al., 2004). The local energy dissipation rate, ε_l, investigated by the PIV measurements have also been reported in the literature (Zhou and Kresta, 1996; Sharp and Adrian, 2001; Khan et al., 2006). The trailing vortices have been constructed using the 3-D angle resolved PIV measurement (Baldi and Yianneskis, 2003; Khan et al., 2004; Chung et al., 2007). PIV has also been used to measure the multiphase flow by some researchers, but only limited to very dilute systems (Virdung and Rasmuson, 2003; Montante et al., 2010). Aubin et al. (2004) studied gas-liquid flows at low aeration rates. However, its utilities is constrained to the transparent systems and cannot be applied to fluids and slurries which are opaque (Micheletti and Yianneskis, 2004; Unadkat et al., 2009; Montante et al., 2012).

2.5.2. Positron Emission Particle Tracking

PEPT is a non-intrusive Lagrangian technique which has been widely used to study the particle characteristics (Parker et al., 1993, 2002). A radioactive particle tracer is used in the PEPT measurement to track the fluid flow, therefore, it can be applied to both transparent and opaque systems. PEPT consists of two face-to-face gamma camera heads, between which the operating system is mounted. A single positron-emitting particle used as the flow tracer is tracked in 3-D space and time to reveal its full Lagrangian trajectory. The tracer is labelled

with a positron-emitting nuclide, and two back-to-back 511 keV γ-rays are emitted once a positron annihilates with an electron. Only coincidence events in which γ-rays are simultaneously detected by both detectors of 59×47 cm^2 are recorded, and the tracer is located at the intersection of the γ-rays by using a location algorithm.

The tracing quality of the positron-emitting particle tracer is of significant importance to the accuracy of the Lagrangian trajectory tracking. The tracking quality is affected by three primary factors, i.e. the match of the density of the tracer and the fluid being tracked, the tracer size and its mechanical resistance. Ideally, the density of the radioactive tracer is the same as that of the tracked fluid. The mechanical resistance of the particle tracer can be characterised by the Stokes number, which is the ratio of the particle response time, τ_p and fluid response time, τ_f. To track the fluid motion faithfully, $St = \tau_p / \tau_f < 0.1$ is essential (Schetz and Fuhs, 1996). The Stokes numbers of particle tracer, i.e. resin of 250-600 μm, has been examined and reported by Chiti (2008) that the maximum value of *St* was 0.092 indicating good tracking of the fluid streamlines.

The three Cartesian coordinates, *x*, *y*, *z*, at the corresponding time, can be analysed in two different ways: a Lagrangian-statistical analysis exploiting concepts such as residence time, circulation time and trajectory length distribution, or a Lagrangian-Eulerian analysis used to extract local Eulerian quantities from the purely Lagrangian information contained in the tracer trajectory such as the three velocity components (u_z, u_r, u_θ) of each phase, the local phase occupancy or time-average concentration.

PEPT measurement of turbulent water flow in a stirred vessel has been validated by comparing with the well-established PIV measurement and has been shown to be an accurate and reliable technique (Pianko-Oprych et al., 2009). The feasibility of PEPT for studying the

agitation of non-Newtonian fluids with and without solid particles within a stirred vessel was assessed by Fangary et al. (1999, 2000, 2002). The Lagrangian information including the trajectory-length distribution and circulation time was investigated in their studies. The Eulerian information for the shear-thinning and viscoplastic fluids from the PEPT measurements was reported by Adams et al. (2008, 2009). Furthermore, the Lagrangian information and the Eulerian information including the three velocity components (u_z, u_r, u_θ) of both the liquid and solid phases as well as the solid concentration distribution obtained from the PEPT measurements for the solid-liquid suspensions in stirred vessel have been analysed (Fishwick et al., 2003; 2005; Guida et al., 2009; 2010; 2012).

2.5.3. Planar Laser Induced Fluorescence

PLIF is also a non-intrusive optical technique, which is typically used to measure the mixing time through recording the distribution of the fluorescent dye as a function of time (Szalai et al. 2004). PLIF set up is similar to the PIV measurement. The fluorescent dye is illuminated by a thin laser sheet passing through the stirred vessel, and the process of tracer distribution is captured by a CCD camera located perpendicularly to the laser sheet.

PLIF has been widely used to measure the flow pattern and mixing time of various fluid mixing in stirred tanks including the turbulent fluid mixing (Sano and Usui, 1985; Nienow, 1997a; Guillard et al., 2000), and the laminar or transitional fluid flows (Kukura et al., 2002; Szalai et al., 2004; Adams and Barigou, 2007).

2.6. Computational fluid dynamics modelling

The principle of CFD technique is analysing the fluid flow phenomena by solving a set of governing equations that describe the fluid dynamics (Versteeg and Malalasekera, 1996). CFD was firstly used in the aerospace, and thereafter with the development of computer

resources and CFD models, CFD technique has become a most commonly used tool and has been widely used in studying fluid dynamics in numerous engineering applications during the past three decades (Bakker et al., 2001). CFD modelling has significant advances, for example, its ability to provide the comprehensive fundamental conceptions which are experimentally expensive or unobtainable such as the local hydrodynamics, phase distribution, and heat and mass transfer. In addition, CFD can be helpful to the scale-up problem which has caused substantial uncertainties in the design of stirred vessels. Sommerfeld and Decker (2004) reviewed the developments and described the trends in the CFD for studying the single phase and multiphase flows in stirred tanks. A large amount of efforts has been devoted to develop the CFD models for studying fluid mixing in stirred tanks over the past two decades, and attempts of using the CFD modelling for more complex mixing systems has recently drawn attention. A number of numerical investigations on solid suspensions in water have been reported in the last decades: some dealt with dilute suspension (Guha et al., 2008; Montante and Magelli, 2007; Fan et al., 2005), and some dealt with more industrially relevant moderate to dense solids loadings (Yamazaki et al., 1986; Barresi and Baldi, 1987; Shamlou and Koutsakos, 1989). The ability of CFD to simulate the mixing of complex non-Newtonian fluids in stirred vessels has also been assessed in the literature (Kelly and Gigas, 2003; Pakzad et al. 2008; Adams and Barigou, 2007). Concerning the validation of CFD modelling, the predicted single phase flow in stirred vessels agitated by different types of impellers has been well validated using the well-established LDV or PIV measurements in a large number of works (Jaworski et al., 1997; Jaworski et al., 2000). However, CFD modelling of more complicated mixing systems including dense solid-liquid suspensions have not been well validated.

As the main technique used in this thesis, an introduction of necessary theory background of CFD modelling is given below.

The governing equations (Navier-Stokes equations) which form the basis of the model are the continuity equation:

$$\frac{\partial(\rho_q \phi_q)}{\partial t} + \frac{\partial(\rho_q u_{iq} \phi_q)}{\partial x_i} = 0 \tag{2.9}$$

and the momentum equation,

$$\frac{\partial(\rho_q u_{iq} \phi_q)}{\partial t} + \frac{\partial(\rho_q u_{iq} u_{jq} \phi_q)}{\partial x_i} = -\phi_q \frac{\partial P}{\partial x_i} + \frac{\partial}{\partial x_i}\left[\phi_q \mu_{qeff}\left(\frac{\partial u_{iq}}{\partial x_j} + \frac{\partial u_{jq}}{\partial x_i} - \frac{2}{3}\frac{\partial u_{kq}}{\partial x_k}\delta_{ij}\right)\right] + \rho_q \phi_q F_g + F_B \tag{2.10}$$

where ρ is density, ϕ is volumetric fraction (for single phase, $\phi = 1$), u is velocity vector, t is time, P is pressure, μ_{eff} is effective viscosity, δ_{ij} is the Kronecker delta ($\delta_{ij} = 1$ when $i = j$; $\delta_{ij} = 0$ when $i \neq j$), and i, j, k are the three coordinate directions; note that for solid-liquid suspension systems, $q \equiv d$ denotes the dispersed phase, and $q \equiv c$ denotes the continuous phase (van Wachem and Almstedt, 2003). The gravitational force is denoted by F_g. The term F_B is the body force, for example, the Coriolis and centrifugal forces induced by impeller rotating.

Apart from the solving the continuity and momentum equations, additional equations may be required for solving specific mixing problems. For example, the interaction between the phases needs to be calculated for modelling solid-liquid systems, therefore, a drag force mode is required to be solved simultaneously. The effect of non-drag forces such as lift force and virtual mass force have been investigated and have been found to be negligible (Ljungqvist

and Rasmuson, 2001; Sha et al., 2001). For CFD modelling of mixing of non-Newtonian fluids, due to the viscosity dependence on shear-rate, additional models needs to be implemented in the CFD modelling to describe the fluid rheology, e.g. the power-law model and Herschel-Bulkley model.

2.6.1. Modelling approach

Three approaches have been widely used for modelling the mixing in stirred vessel, i.e. direct numerical simulation (DNS), large eddy simulation (LES) and Reynolds Averaged Navier-Stokes equations (RANS). DNS resolves the whole scales of turbulence, so the numerical grid is required to be smaller than the Kolmogorov scale. Consequently, a large number of grids are needed which causes the DNS approach to be far too computationally expensive. Moreover, DNS is restricted to low to moderate Reynolds numbers (up to Re ~8,000), indicting little practical meaning for most industrial processes, where the fluid flows are in high turbulent regime ($Re \geq 10^4$).

LES, on the other hand, resolves the large-scale turbulent eddies explicitly and hence, allows coarser grid. The small eddies are modelled by a sub-grid scale (SGS) model. LES was firstly used by Eggels (1996) for investigating the detailed flow in the impeller region. The use of LES for studying the fluid mixing in stirred tanks has been summarized by some researchers (Squires and Simonin, 1996; Murthy and Joshi, 2008).

RANS is the most widely used modelling approach, which is capable of providing adequate predictions for the engineering accuracy with much less computational resource requirement (Coroneo et al., 2011). Detailed description of RANS is given in the following section.

Studies that compare the performance of the three modelling approaches have showed that the difference between the flow fields from the three methods is negligible. However, LES and

DNS had superiority for predicting the turbulent quantities, though at a great expense of computational resources (Yeoh et al., 2004; Hartmann et al., 2004b; Verzicco et al., 2004; Guha et al., 2008).

Concerning solid-liquid suspensions, DNS and LES have been employed in very few studies (Derksen, 2003), and RANS is more suitable and has received extensive attention. In the RANS approach, the Eulerain-Lagrange approach (Decker and Sommerfeld, 1996; Zhang and Ahmadi, 2005) simulates the solid phase as a discrete phase and so allows particle tracking, in addition, the physical effects such as the particle-turbulence interaction on the particle motion can be modelled. However, the number of particles that can be tracked is currently very limited, thus restricting the applicability of the model to dilute mixture (up to ~5%). The multi-fluid Eulerian-Eulerian model (Montante et al., 2001; Sha et al., 2001; Micale et al., 2004; Montante et al., 2005; Špidla et al., 2005; Khopkar et al., 2006; Micale et al., 2000) which treats both liquid and solid phases as continua is capable of predicting high solid concentrations, therefore, has been most widely used and developed.

2.6.2. Turbulence models in the RANS approach

The conservation equations can be resolved without additional models for modelling laminar flow. Due to the fluctuating velocity in the turbulent flow, which has been described in section 2.2.1, additional turbulence models are necessary. In the RANS method, the instantaneous velocity is decomposed into a mean velocity component, $\overline{u}$, and a fluctuating component, u' , i.e. $u = \overline{u} + u'$. Taking the Navier-Stokes momentum equation for the single phase flow for an example (i.e. $\phi = 0$ in equation (2.10)), equation (2.11) is obtained by substituting $\overline{u} + u'$ for u and re-arranging,

$$\frac{\partial(\rho\overline{u}_i)}{\partial t}+\frac{\partial(\rho\overline{u}_i\overline{u}_j)}{\partial x_i}=-\frac{\partial(P)}{\partial x_i}+\frac{\partial}{\partial x_j}\left[\mu\left(\frac{\partial(\overline{u}_i)}{\partial x_j}+\frac{\partial(\overline{u}_j)}{\partial x_i}-\frac{2}{3}\frac{\partial(\overline{u}_k)}{\partial x_k}\delta_{ij}\right)\right]+\frac{\partial}{\partial x_j}\left(-\rho\overline{u_i'u_j'}\right)+\rho F_g+F_B \tag{2.11}$$

The additional term on the right hand side that include the fluctuation components, $\rho\overline{u_i'u_j'}$, is the Reynolds stress, so additional turbulent models are required in order to close the equations. The k-ε turbulence model (Launder and Spalding, 1974) has been the most widely used turbulent model for modelling turbulent flow in stirred tanks in the literature. The transport equations for the turbulence kinetic energy, k, and the energy dissipation rate, ε, are,

$$\frac{\partial}{\partial t}(\rho k)+\nabla(\rho u_i k)=\nabla\left(\left(\mu+\frac{\mu_T}{\sigma_k}\right)\frac{\partial k}{\partial x_i}\right)+\rho(P_k-\varepsilon) \tag{2.12}$$

$$\frac{\partial}{\partial t}(\rho\varepsilon)+\nabla(\rho u_i\varepsilon)=\nabla\left(\left(\mu+\frac{\mu_T}{\sigma_\varepsilon}\right)\frac{\partial\varepsilon}{\partial x_i}\right)+\rho\frac{\varepsilon}{k}(C_1P_k-C_2\varepsilon) \tag{2.13}$$

where P_k is a generation term of turbulence; C_1=1.44 , C_2=1.92 , $\sigma_k=1$, $\sigma_\varepsilon=1.314$, and $\mu_T=\rho C_\mu\frac{k^2}{\varepsilon}$ is the turbulent viscosity, $C_\mu=0.09$.

The ability of k-ε turbulence model for predicting the velocity field, especially of single phase mixing, has been widely validated through comparison with various experimental measurements such as PIV and LDV (Ranade et al., 1992; Brucato et al., 1998; Aubin et al., 2004). The k-ε turbulence model, however, is acknowledged to under- or over-estimate the turbulence quantities (Abujelala and Lilley, 1984; Lee and Yianneskis, 1998; Jenne and Reuss, 1999; Rammohan, 2002; Escudié and Liné, 2006; Deglon and Meyer, 2006). Most studies have attributed this inaccuracy to the inherent isotropic turbulence assumption of the k-ε turbulence model, knowing that the turbulence field in a stirred vessel is anisotropic. On the

other hand, Deglon and Meyer (2006) attributed the poor predictions to the numerical errors rather than the inadequacies of the k-ε model.

For the sake of improving the CFD prediction, other turbulence models, for example, the modified k-ε turbulence models (e.g. RNG k-ε turbulence model), and the anisotropic based turbulence model (e.g. Reynolds stress model (RSM) and Algebraic Stress Model (ASM)), have been used by some researchers (Armenate and Chou, 1996; Sheng et al., 1998). As every turbulence model has its own inherent deficiencies due to the simplifying assumptions, many studies have compared the performance of various turbulent models for modelling fluid mixing in stirred vessels (Jaworski et al., 1997; Sheng et al., 1998; Montante et al., 2001; Jaworski and Zakrzewska, 2002; Aubin et al., 2004; Gunyol and Mudde, 2009; Chtourou et al., 2011). All these studies have shown that the predicted mean velocities from all turbulent models present slight differences, and the predictions agree fairly well with the experimental data. The turbulence quantities, especially in the impeller region, however, have been found to be affected by the turbulence model, though the conclusions on the optimal turbulent model in different studies are not unanimous. Montante et al. (2000), and Jaworski and Zakrzewska (2002) concluded that the k-ε model gave a better result than the RNG k-ε model and RSM model. However, the RNG k-ε model is stated to be the most appropriate model in the work of Chtourou et al. (2011). Aubin et al. (2004) found little difference of the predicted turbulent kinetic energy, k, from different turbulent models.

2.6.3. Modelling approach for the rotating impeller

The relative motion between the rotating impeller and the stationary baffles requires a special treatment. In the earliest work, the impeller rotation was not modelled explicitly, instead, the available experimental data was imposed as the boundary condition at the cylindrical surface

of the impeller swept region, so-called the "black-box" method (Gosman et al., 1992; Bakker, 1992; Bakker and Van den Akker, 1994; Venneker, 1999; Barrue et al., 2001). As a consequence, the flow detail within the impeller region is not available. Also, because highly accurate experimental data is required for this approach, it is restricted to specific stirred vessel geometry where the experimental data was obtained. In the 1990s, three approaches, namely the Input-Output (IO) (Brucato et al., 1994), Sliding Grid (SG) (Luo et al., 1993), and Multiple Frames of References (MFR) (Luo et al., 1994) methods were developed to deal with the interaction between the rotating impeller and stationary baffles. Thereafter, the fluid flow in stirred tanks can be simulated fully explicitly without any experimental data as the boundary condition.

The whole stirred vessel, in all the three approaches, is divided into two regions, i.e. a cylindrical rotating domain including the rotating impeller and shaft, and a stationary domain including the baffles and tank walls, as illustrated in Fig. 2.8. The two sub-domains are non-overlapping in the SG and MFR methods, and are partially overlapping in the IO method. The MFR and IO are steady-state simulations where the rotating region does not actually move but the effect of the movement is added within the rotating region through a rotating reference frame, while the SG method is a transient simulation in which the grids of the inner domain rotates, hence, requires significantly higher computational time. The extent of the rotating domain is not arbitrary, but has to be selected appropriately in order to insure that the flow at the interfaces is almost steady, and does not change in the azimuthal direction or with time.

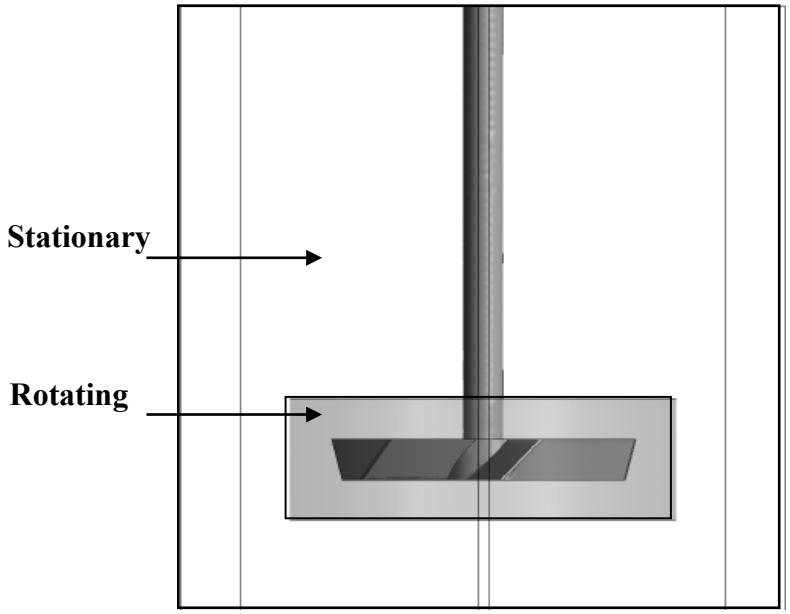

Figure 2.8. Schematic illustration of rotating and stationary domains.

The SG has been reported to provide better results because it can resolve the unsteady nature of the fluid flow which is more releastic (Brucato et al., 1998; Micale et al., 1999). However, the three approaches have been found to have little effect on the flow fields in some studies (Montate et al., 2001; Aubin et al., 2004).

Concerning the boundary condition in the CFD simulations of fluid mixing in stirred vessels, top liquid surface needs special treatment. Free-slip or the symmetry plane boundary condition are usually set for the free surface for fully baffled tanks for simplification, because the central vortex is much reduced. However, due to the significant centre vortex in the un-baffled tanks, the free surface shape needs to be modelled in order to account for its effect on the flow field (Serra et al., 2001; Torré et al., 2006; Lamarque et al., 2010).

The above mentioned various equations are partial differential equations (PDE) which could be not resolved by the computer programme. A discretization scheme is used to transfer these equations into the numerical format. The most commonly used discretization schemes are the higher order schemes in terms of the accuracy. Investigations on the effects of the

discretization scheme on the CFD predictions of the mixing in stirred vessels showed that higher order schemes provided similar accurate results, while the accuracy of the results from the first order method was not adequate (Marshall and Bakker, 2004; Aubin et al., 2004; Deglon and Meyer, 2006; Coroneo et al., 2011).

Chapter III

NUMERICAL MODELLING OF SINGLE PHASE FLUID MIXING UNDER DIFFERENT FLOW REGIMES AND AGITATED BY VARIOUS IMPELLERS

Abstract

The mixing of low viscosity Newtonian fluids in highly turbulent flow and the mixing of high viscosity shear-thinning fluids in the transient regime in a stirred vessel agitated by different types of impellers in both the down-pumping and up-pumping modes have been studied, using CFD modelling. Differences of fluid average velocity of low viscosity Newtonian fluids in highly turbulent flow at different angular position in stirred vessel due to the effect of baffles are well captured by CFD modelling, and CFD predictions agree very well with PIV and PEPT measurements. The numerical predictions of ensemble-averaged velocity distributions of shear-thinning fluid are compared with PIV measurements. In the CFD modelling, the SG and MFR approaches are employed for modeling the turbulent flow and transitional flow, respectively. Both the turbulent and transitional fluid flows generated by different impellers are well predicted by CFD modelling. The Reynolds number and fluid rheology have significant effects on the discharge angle of the axial and mixed impellers in the mixing of highly viscous fluids. The fluids are discharged increasingly more radially with an increase in viscosity or decrease in Reynolds number. However, the discharge angle of the wide-blade Lightinin A340 is only slightly affected. The normalized velocities increase with *Re*, but become independent of *Re* at high Reynolds number.

3.1. Introduction

Since commercial CFD codes were first released, they have been fast developed both in the research area and as a cost effective engineering tool over the past decades. CFD modelling has been widely used for analysing fluid flows, heat and mass transfers in complex geometries such as stirred tanks which are widely used in various industrial processes, from simple mixings to emulsifications, solid dispersions, fermentations and homogeneous/heterogeneous chemical reactions. CFD offers an alternative way to understand the complex flow fields inside stirred tanks, since the well-established measurement techniques, such as the optical non-intrusive PIV and LDA, are restricted to transparent systems. Though the intrusive approach such as hot wire anemometry (HWA) could be applied in opaque fluids, however, they provide limited information and the local velocity field may be altered. Dramatic increase in computing power has reduced the computational time, therefore, has significantly promoted the widespread application of CFD modelling.

The validations of CFD predictions of flow fields in various stirred vessels against experimental data (generally LDA or PIV data) have been carried out intensively for water in fully turbulent flow (Re > 10,000) (Jaworski et al., 1998; Ng et al., 1998; Montante et al., 2001; Jaworski et al., 2002; Murthy and Joshi, 2008). For turbulent flow, the standard k-ε turbulence model (Launder and Spalding, 1974) is the most popular turbulence model. The standard k-ε turbulence model has been reported to give reasonably accurate predictions of mean velocity fields, although the turbulence field is usually under- or over-predicted due to its isotropic Reynolds stress assumption based on the Reynolds Averaged Navier-Stokes (RANS) equations (Ng et al., 1998; Montante et al., 2001). On the other hand, Deglon and Meyer (2006) and Coroneo et al. (2011) reported that the turbulent quantities could be well predicted by the standard k-ε turbulence model with much finer computational cells. The

mesh density is 1509 grids/cm^3 in the study of Deglon and Meyer (2006) and is 2490 grids/cm^3 in the study of Coroneo et al. (2011). However, the mesh density varies in a range of 10 – 600 grids/cm^3 is usually used in the majorty of numerical studies, as summarized by Utomo (2009).

In the previous studies, the capability of CFD modelling for low viscosity Newtonian fluids in turbulent regime are usually assessed by comparing with PIV and LDV measurements in the 45° plane between two baffles based on the assumption of axial symmetry. The effect of the angular position relative to the baffle on the flow field in a fully baffled tank has been reported in literature (Aubin et al., 2004; Guida et al., 2010), velocities in other parts of the stirred vessel, therefore, are necessary to be validated. Due to the intrinsic 2-D technique of PIV and LDV, the tangential velocity component could be obtained using special treatment, like stereoscopic PIV which requires 2 cameras (Hinsch, 2002) and reconstruction of multiple 2-D planes (Chung et al., 2008). As a 3-D Lagrangian tracking technique, PEPT has been used conveniently to provide the 3-D information of flow fields in stirred vessels and is very useful for the CFD validation.

On the other hand, the capability of CFD modelling of mixing of non-Newtonian fluids in stirred vessels has received less attention despite the fact that most of industrial processes deal with non-Newtonian fluids (Zalc et al., 2001; Kelly and Gigas, 2003). Non-Newtonian fluids are usually much more viscous than water, therefore, the mixing of non-Newtonian fluids in stirred vessels is difficult to achieve turbulent flow, but is usually in the laminar or transitional regime. Due to the complexity of transitional flow, no specific CFD model has been developed for modelling the transitional flow. The turbulence model has been reported not to be appropriate for modelling the low transitional flow. The utility of laminar model for

modeling low transitional flow (Re < 1,000) has been assessed and has been widely accepted to be capable of giving reasonable CFD predictions (Zalc et al., 2001; Letellier et al., 2002; Kelly and Gigas, 2003; Pakzad et al. 2007)

In addition, because of more and more impellers of different geometries becoming used in industries, the capability of CFD modelling of the performance of different impellers in various fluids is worthy being examined.

In this chapter, the CFD predictions of high turbulent flow fields and flow fields of shear-thinning fluids (i.e. CMC solutions of various concentrations) in transitional regime agitated by Rushton disc turbine (RDT), 45^{o} pitched blade turbine (PBT), a hydrofoil impeller Lightnin A310, and wide-blade Lightnin A340 in a stirred vessel are validated against the experimental data from different techniques. Moreover, both down-pumping and up-pumping modes are investigated when the fluids are agitated by the PBT and Lightnin impellers. The range of PIV experiments and CFD studies conducted are summarized in Table 3.2. It needs to be noted that the velocities under different conditions were measured in the plane at 85 degree on the windward side of the baffle.

In order to investigate the effect of angular position on the fluid velocity, the CFD prediction of the velocity distribution in three planes, i.e. 5° on the leeward side of the baffle, 45° in the mid-way between two baffles, 85° on the windward side of the baffle, under the condition of high turbulent flow agitated in the PBTD mode were validated by comparing with PIV and PEPT measurements reported by Guida (2010). Moreover, the predicted tangential velocity components in these three planes were also validated.

Table 3.1. Dimensions of impeller configurations.

Impeller	T (mm)	H	D	B	C	W (mm)
PBT	190	T	0.55T	0.1T	0.33T	23
RDT	190	T	0.53T	0.1T	0.33T	20
A310	190	T	0.53T	0.1T	0.33T	12
A340	190	T	0.60T	0.1T	0.33T	44

Table 3.2. Range of PIV measurements and CFD simulations.

	PIV			
Liquids	Re_{imp} (N (rpm))			
	PBTD&PBTU	RDT	A310D&A310U	A340D&A340U
Water	40,041 (220)	36,667 (220)	36,667 (220)	52,800 (220)
CMC (0.2 wt%)	115.5 (60)	105.8 (60)	105.8 (60)	152.3 (60)
	303.3 (120)	277.8 (120)	277.8 (120)	400 (120)
	705.5 (220)	646.1 (220)	646.1 (220)	930.3 (220)
	1086.7 (300)	995.1 (300)	995.1 (300)	1433 (300)
CMC (0.5 wt%)	259.6 (220)	237.7 (220)	237.7 (220)	342.3 (220)
CMC (0.7 wt%)	116.6 (220)	106.8 (220)	106.8 (220)	153.7 (220)

3.2. Experimental setup

3.2.1. Mixing vessel

Both the numerical and PIV measurements were carried out in a standard flat-bottom cylindrical glass tank of diameter T = 190 mm, fitted with four baffles of 0.1T spaced at 90° degrees. The cylindrical tank was placed inside a square glass tank filled with water to minimize the optical distortion in the PIV experiments. The stirred vessel was filled with the working liquids to a height $H = T$, and was agitated by four impeller: a six-blade RDT, a six-blade 45° PBT, an axial impeller Lightnin A310, and a wide-blade Lightnin A340. The impellers were set at the off-bottom clearance of T/3. The configurations and mesh of the stirred tank and four impellers are shown in Fig. 3.1, and the dimensions of the four impellers are listed in Table 3.1. The transition "sliding-grid" (SG) method (Luo et al., 1993) and

steady state "multiple-frames of reference" (MFR) method (Luo et al., 1994) both take into account the interaction between the rotating impeller and stationary baffles are used in the turbulent and transitional flows, respectively.

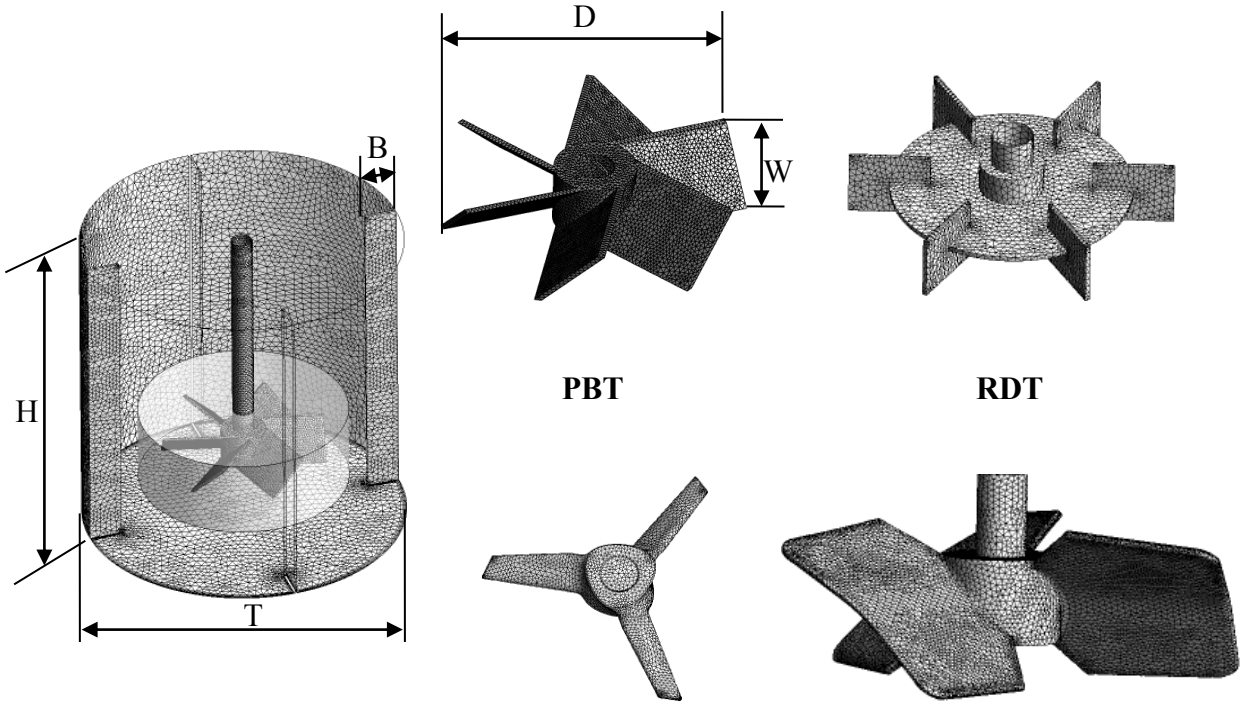

Figure 3.1. Configurations and computational mesh for the stirred tank and various impellers.

3.2.2. Materials

Shear-thinning Carboxymethyl cellulose (CMC) solutions with concentrations of 0.2 wt%, 0.5 wt% and 0.7 wt% were used in the PIV measurements. The shear-thinning behavior of the CMC solutions described by the power law model was used in the CFD modeling,

$$\tau = k\dot{\gamma}^{n} \tag{3.1}$$

where, $\dot{\gamma}$ is the shear rate, k is fluid consistency coefficient and n is the flow behaviour index.

The rheological parameters of CMC solutions, as listed in Table 3.3, were tested by a 2° 60 mm cone and plate geometry using a stress controlled rheometer (AR-1000, TA Instruments) with the shear rate over the range of 0.01 to 1000 s^{-1}. The measured rheology of CMC solutions of different concentrations are shown in Fig. 3.2. The Reynolds numbers were calculated using the well-known Metzer and Otto correlation (Metzner and Otto, 1957):

$$\mathrm{Re} = \frac{\rho N^{2-n} D^2}{k k_s^{n-1}} \tag{3.2}$$

where k_s is the Metzner-Otto constant. The value of k_s was set as 11 for all impellers investigated, as it is generally recommended and only slightly dependent on the impeller type (Adams and Barigou, 2007).

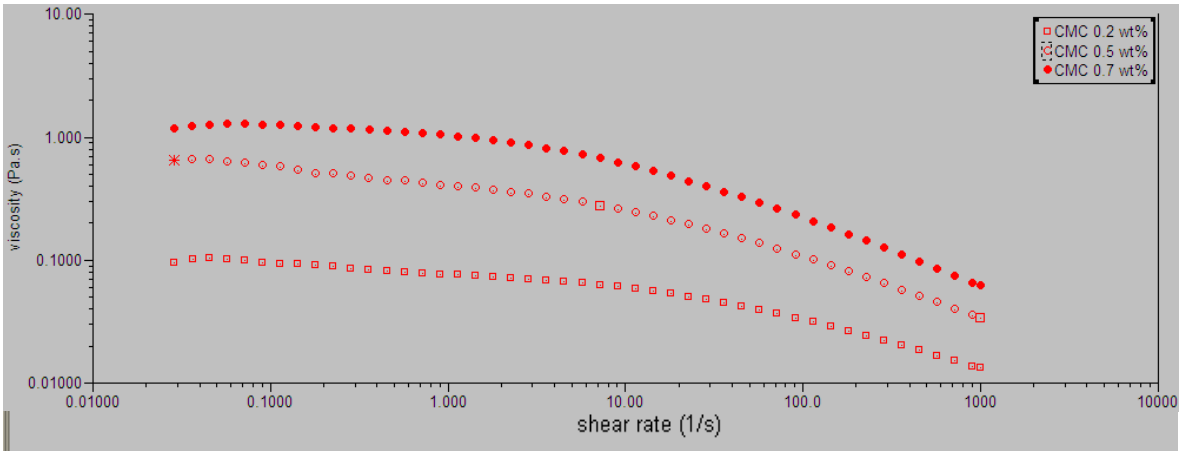

Figure 3.2. Variation of viscosity with shear rate for CMC solution at different concentrations.

Table 3.3. Rheological properties of CMC solutions.

CMC	k (Pa s^n)	n
0.2 wt%	0.2424	0.6073
0.5 wt%	0.867	0.533
0.7 wt%	2.413	0.4727

3.2.3. PIV setup

In the PIV measurement, the liquid were seeded using 10μm hollow silver coated particles. The seeding particles were illuminated using a dual head Nd: YAG 532 nm pulsed laser with the thickness, ~ 1 mm (New Wave Research Inc. USA). A single frame-straddling CCD camera (PowerView Plus 4MP, TSI Inc., USA) capable of capturing 7 images pairs per second with a resolution of 2048×2048 pixels was used to record simultaneous images. The synchronization of the laser and camera frame were controlled by a TSI Laserpulse 610035 synchronizer. The captured images were divided into small interrogation areas (IA) of 16×16 pixels^2 (0.92×0.92 mm^2) and processed by a recursive Nyquist grid. TSI Insight software was used to interrogate the pairs of images using the Fast Fourier Transform (FFT) cross-correlation.

The effect of the number of PIV images on the flow field measurement has been tested by Guida et al. (2010), and 200 image pairs were stated to be enough to obtain the converged average velocities. 500 pairs of PIV images were recorded in each experiment. The laser sheet was set at 85° which is on the windward side of the baffle to avoid light obstruction by the baffle in front of the camera (Chung et al., 2007; Guida et al., 2010).

3.3. CFD simulation

Numerical simulations were performed using the commercial CFD code ANSYS CFX 12.0.

The governing equations (Navier-Stokes equations) which form the basis of modelling single phase turbulent flow are the continuity equation:

$$\frac{\partial(\rho)}{\partial t}+\frac{\partial(\rho u_i)}{\partial x_i}=0 \tag{3.3}$$

and the momentum equation,

$$\frac{\partial(\rho u_i)}{\partial t}+\frac{\partial(\rho u_i u_j)}{\partial x_i}=-\frac{\partial(P)}{\partial x_i}+\frac{\partial}{\partial x_j}\left[\mu\left(\frac{\partial(u_i)}{\partial x_j}+\frac{\partial(u_j)}{\partial x_i}-\frac{2}{3}\frac{\partial(u_k)}{\partial x_k}\delta_{ij}\right)\right]+\rho g_i+F_B \tag{3.4}$$

where ρ is fluid density, u is velocity vector, μ is the fluid viscosity, P is pressure, δ_{ij} is the Kronecker delta ($\delta_{ij}=1$ when $i = j$; $\delta_{ij}=0$ when $i \neq j$). The term F_B is the body force which includes the Coriolis and centrifugal forces induced by using the SG or MFR approach. It is noted that the transient terms in the continuity and momentum equations were omitted using the steady state MFR method. The code is based on the finite-volume method, and the so-called "High Resolution Advection Scheme" was used to discretise the governing equations.

For modelling the turbulent flow, the above system of differential equations was closed by employing the well-known mixture $k-\varepsilon$ turbulence model (Launder and Spalding, 1974). The two-equation turbulence model consists of the differential transport equation (3.5) for the turbulent kinetic energy, k, and equation (3.6) for its dissipation rate, ε, thus:

$$\frac{\partial}{\partial t}(\rho k)+\nabla(\rho u_i k)=\nabla\left(\left(\mu+\frac{\mu_T}{\sigma_k}\right)\frac{\partial k}{\partial x_i}\right)+\rho(P_k-\varepsilon) \tag{3.5}$$

$$\frac{\partial}{\partial t}(\rho \varepsilon)+\nabla(\rho u_i \varepsilon)=\nabla\left(\left(\mu+\frac{\mu_T}{\sigma_\varepsilon}\right)\frac{\partial \varepsilon}{\partial x_i}\right)+\rho\frac{\varepsilon}{k}(C_1 P_k-C_2\varepsilon) \tag{3.6}$$

where P_k is a generation term of turbulence; $C_1=1.44$, $C_2=1.92$, $\sigma_k=1$, and $\sigma_\varepsilon=1.314$.

The Reynolds numbers of the highly turbulent flow agitated by different impellers, as listed in Table 3.2 are ≥ 36,667. Such high rotational speed with the innate feature of periodic, time-dependent flow in the stirred tank cause the calculation to be difficult to converge using the steady-state simulation, i.e. MFR method. Therefore, the fully transient SG method is

necessary to calculate the turbulent flow field. The transient run was initialised from the steady-state result obtained using the MFR approach, since it has been reported that using the steady-state result as the initialisation can significantly reduce the number of revolutions needed before a quasi-steady state is reached (Li et al., 2005). The final flow field obtained from the SG approach is only a snapshot at the last time step, therefore, the number of impeller revolutions which was used to calculate the numerical time-averaged velocity fields was gradually increased until the time-averaged velocities reach the convergence state at 12 revolutions.

On the other hand, the MFR method was employed instead in the CFD simulations of mixing of CMC solutions in transitional regime, as listed in Table 3.2, since it requires much less computational resource than the SG approach, and the laminar model was used. The power law model, i.e., equation (3.1) was used to compute the local apparent viscosity of the fluid and was implemented with the expression language feature in the ANSYS CFX 12.0. In order to avoid the shear rate dropping to zero where it happens in the regions away from the impeller, a lower limitation value of shear rate of 10^{-8} s^{-1} was employed which was taken if the shear rate is smaller than it.

The computational domain, as a consequence of either using the SG or MFR methods, is necessary to be divided into two regions, as shown in Fig. 3.1: one domain containing all of the rotating elements (hub, blades and shaft), and the other containing the stationary parts (baffles, tank wall and base) separated by three interfaces, a vertical cylindrical interface at r = 68 mm, and two plane horizontal interfaces at z = 15 mm and 15 mm above the higher edge and lower edge of different impellers, respectively. The interfaces were set sufficiently

remote from the impeller to minimize the effects on the results. The free surface was modeled as a free-slip boundary.

The various stirred tank configurations were divided by non-uniformly distributed unstructured tetrahedral elements. The grids used in the rotating domain are much finer considering the high velocity and turbulent gradient. Inflation boundary layers were generated on the solid surfaces such as impeller blades, shaft, baffles and tank walls to cover the high velocity gradients because of no slip wall boundary conditions. The mesh independence study was carried out prior to the CFD case studies, and the total grid number of 701,527, 736,839, 843,805 and 1,104,143 were found to be sufficient and finally used for the stirred tank agitated by PBT, RDT, Lightnin A310 and Lightnin A340 were employed, respectively, as illustrated in Fig.3.1. Numerical convergence was assumed when the sum of all normalized residuals fell below 10^{-4} for all equations.

3.4. Results and discussion

3.4.1. Azimuthally resolved CFD predictions compared with PIV and PEPT

The azimuthally averaged velocity from the PIV measurement was obtained by averaging the velocities on the 17 planes between two adjacent baffles, as shown in Fig. 3.3. The details of obtaining the azimuthally averaged velocity from the PIV and PEPT measurements have been described in the work of Guida (2010). Fig 3.4 shows the CFD simulated azimuthally averaged velocity distributions of water agitated in the PBTD compared with the PIV and PEPT measurements (Guida, 2010) at various locations within the stirred vessel. It can be seen that the agreement between the CFD prediction and the two sets of experimental data are excellent overall.

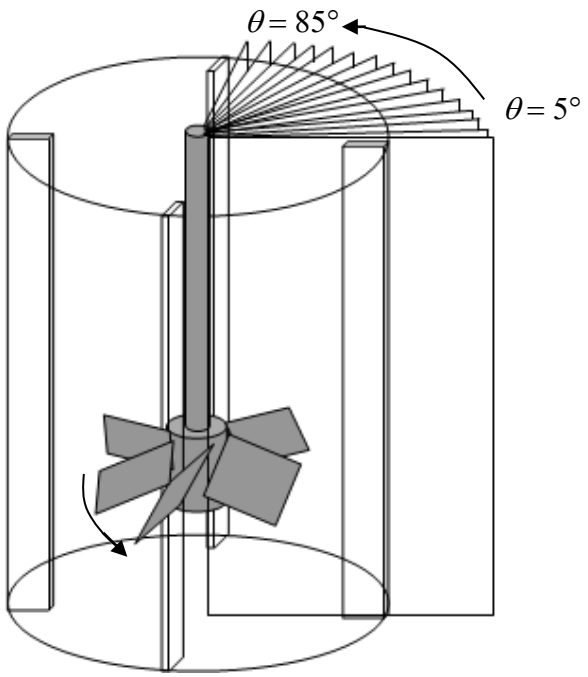

Figure 3.3. Azimuthally-averaged velocity obtained from 17 planes between two adjacent baffles in PIV measurements.

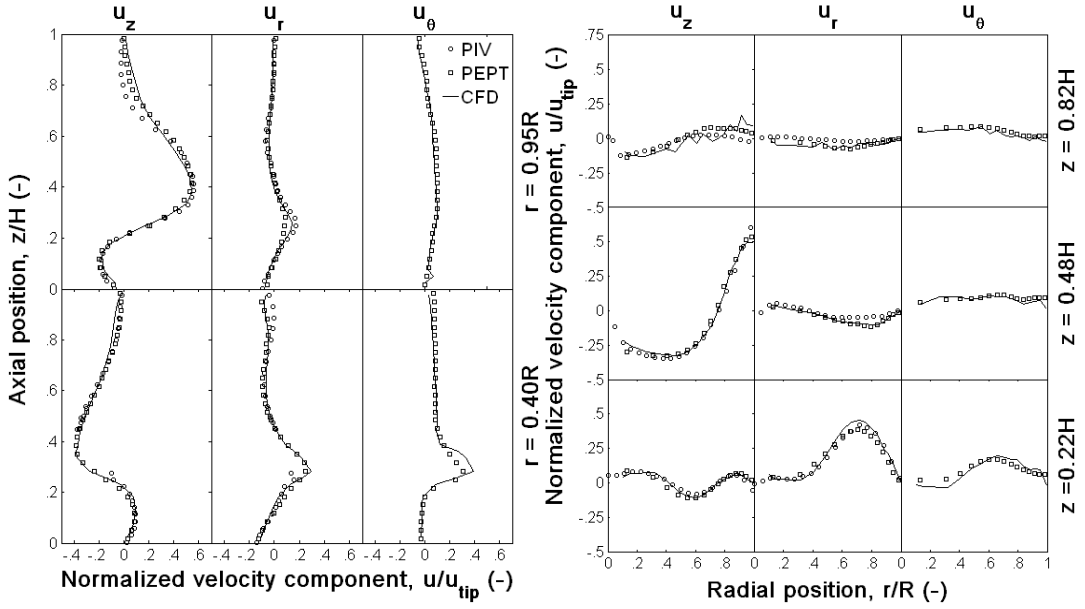

Figure 3.4. Azimuthally-averaged distribution of the velocity components of water in PBTD mode at N = 220 rpm (Re_{imp} =40,041): CFD, PIV, and PEPT compared.

All three axial velocity components, i.e. u_z , u_r , u_θ reach their local maxima within the impeller region with u_z being predominant. u_r , u_θ reduce significantly, while, u_z reaches the

local maximum (~ 0.4 u_{tip}) at r = 0.95R where all of the fluid has to flow upwards due to the effect of the baffles.

Considering the radial profiles, above the impeller at z = 0.48H, the maximum downward velocity is 0.35 u_{tip} representing the inlet stream to the impeller. At the bottom of the circulation loop (i.e., z = 0.22H, r = 0.7R), the radial component, u_r , reaches the local maximum, 0.42 u_{tip} ,where the axial component, u_z , however, reduces to ~ 0.13 u_{tip} .

3.4.2. CFD predicted velocities at different azimuthal positions compared with PIV and PEPT

Fig 3.5 shows the comparisons of axial and radial velocity distributions in planes of θ = 5°, 45°, and 85° shown in Fig 3.3, from the three sets of data. The effect of baffles is well predicted by CFD as the predicted velocities at different angular positions agree very well with the PIV and PEPT measurements.

At r = 0.95R, the magnitudes of velocities, especially the axial component, u_z , at different angular positions show significant difference suggesting that the strong effect of baffles on the flow field. In the plane of θ = 85°, the maximum magnitude of u_z is ~ 0.6 u_{tip} , whereas the maximum magnitude of u_z is ~ 0.4 u_{tip} in the plane of θ = 5°. On the contrary, far away from the baffles, e.g. at r = 0.4R, the effect of baffles on the flow field reduces significantly, as it can be seen that the velocity profiles are highly similar at various angular positions at r = 0.4R.

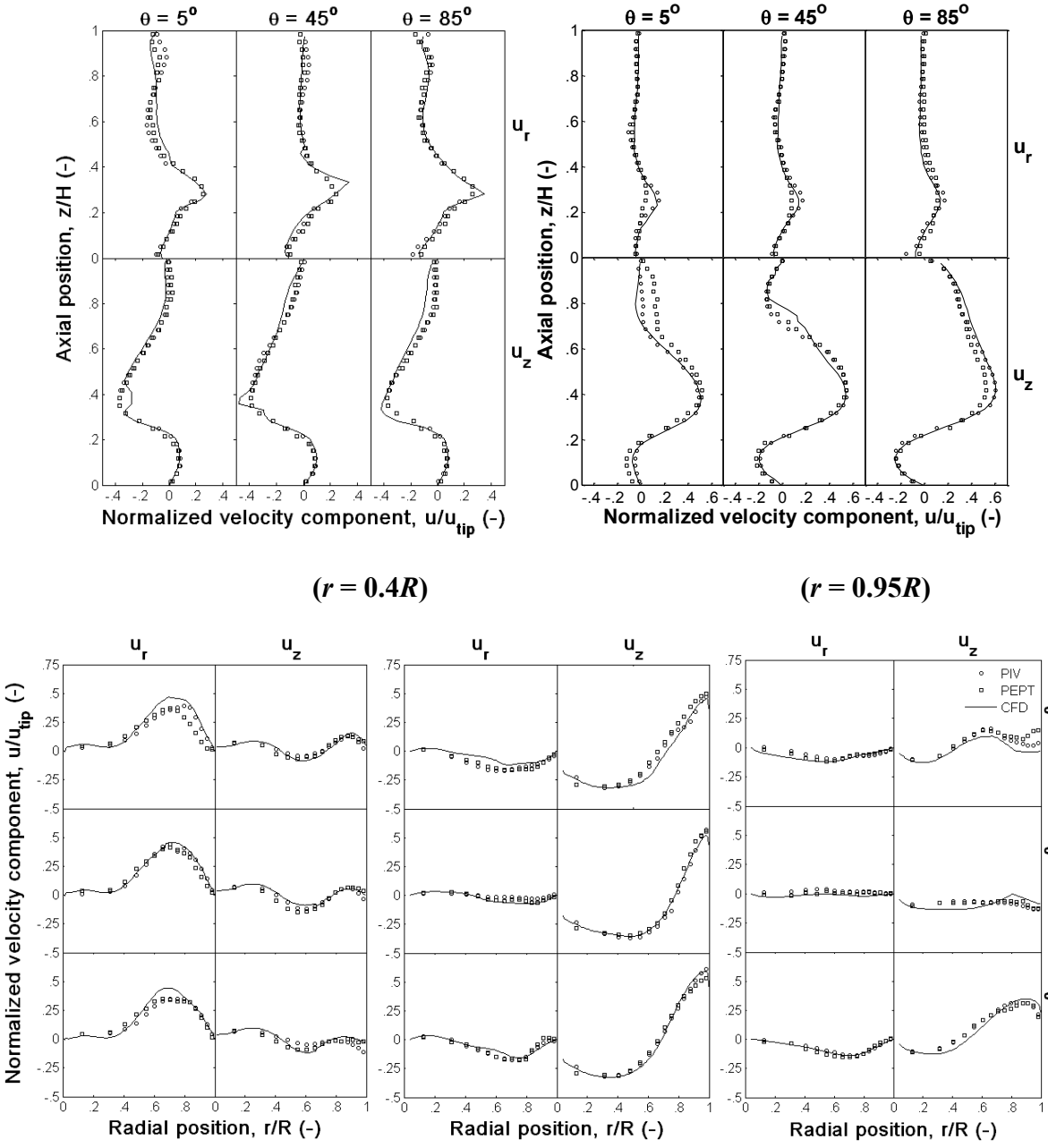

Figure 3.5. Distribution of the velocity components of water in PBTD mode at different planes at N = 220 rpm (Re_{imp} =40,041): CFD, PIV, and PEPT compared.

Radially, the velocity distributions in different planes are similar, except near the free surface (z = 0.82H) where the differences are apparent, especially the axial component, u_z. The profile of u_z is fairly flat in the 45° plane, whereas, there is sharp variation in the other two

planes close to the baffle. It can be seen that the velocity profile in the 5° plane and 85° plane are significantly different.

3.4.3. Effect of impeller type on highly turbulent flow field

The flow patterns of water agitated by four impellers, i.e. RDT, PBT, Lightnin A310, and Lightnin A340 impeller, and in both down- and up-pumping for the PBT, Lightnin A310, and Lightnin A340 impeller, measured by PIV in plane of θ = 85° at N = 220 rpm (the corresponding values of Re_{imp} are listed in Table 3.2) are shown in Fig 3.6.

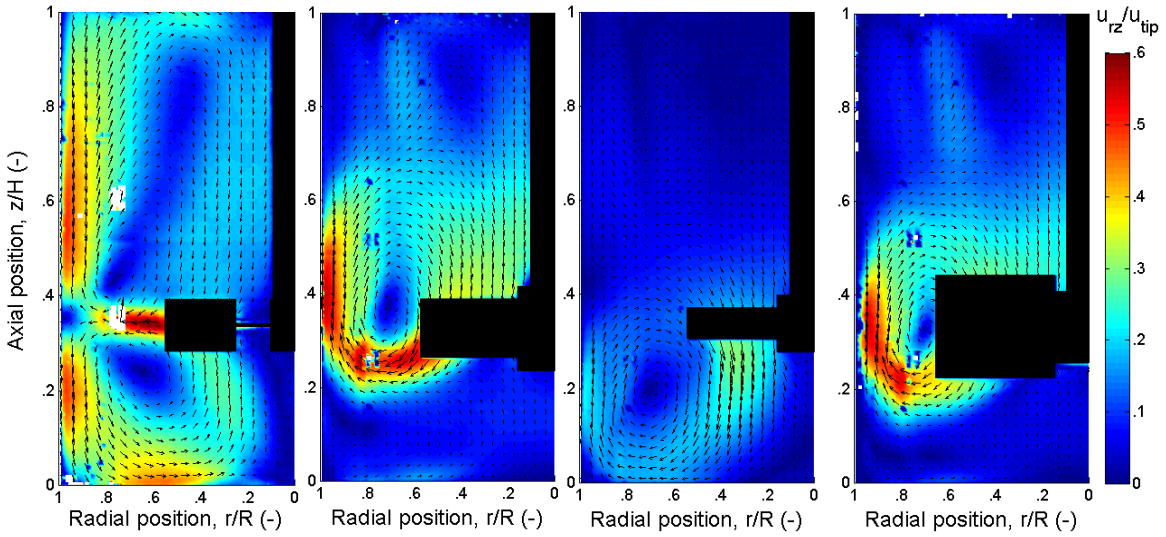

(RDT) **(PBTD)** **(A310-D)** **(A340-D)**

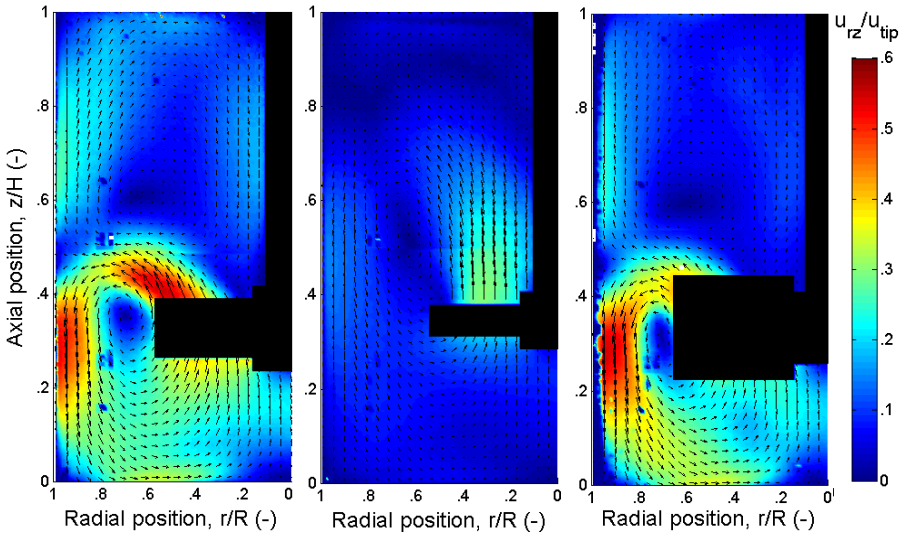

(PBTU) **(A310-U)** **(A340-U)**

Figure 3.6. PIV measurements of the mean radial-axial velocity fields in water at plane of $\theta = 85^{o}$ at $N = 220$ rpm (Re_{imp} =40,041).

The RDT, PBT and Lightnin A310 produce radial, oblique and vertical discharge streams, respectively, as typically reported in the literature. The discharge stream of the wide blade hydrofoil impeller, Lightnin A340, is similar to that of PBT. The discharge streams in either up- or down-pumping mode of PBT, Lightnin A310 and Lightnin A340 present high

similarity. The RDT creates two main circulation loops above and below the impeller, while A310 effectively only create a single main circulation loop below or above the impeller when operated in down- or up-pumping mode, respectively. The discharge streams of PBT and Lightnin A340 do not reach the bottom of the vessel when operated in down-pumping mode, and a secondary circulation loops are introduced, though much weaker than the primary ones. On the other hand, the primary circulation loops of PBT and Lightnin A340 reach the bottom of the vessel when operated in up-pumping mode, and the secondary circulation loops reach the free surface. This may suggest that PBTU mode is more effective to disperse solid at the bottom of the vessel than PBTDmode at impeller clearance of $C = T/3$.

Very similar flow patterns are generated from the PBT and Lightnin A340 in both the down- and up-pumping modes, as shown in Fig 3.6. However, in the impeller discharge region, the flow intensity in the discharge stream for Lightnin A340 is much weaker compared with that for the PBT, though it has wider blades (Geometrical parameters are listed in Table 3.1). Another characteristic of the Lightnin A340, as can be observed in Fig 3.6, is that it creates high velocity intensity at the tank wall in the up-pumping mode, which is useful for enhancing the heat transfer from the tank wall to the liquid. This is consistent with the design purpose in practice (Lightnin Company).

The quantitative comparisons between the CFD predictions and the PIV measurements in the discharge stream are shown in Fig 3.7. The positions chosen for plotting the velocity profiles are 4 mm below the the lower edge in the down-pumping mode or 4 mm above higher edge of different impellers in the up-pumping mode. Choosing the positions at the same distance from the blade edge of different impeller is due to the blades of different impellers having different width (as listed in Table 3.1). Modelling the velocities at these positions so close to

the impeller blade edge in fact poses a great challenge with regards to the high intensity and gradient of both the velocity and turbulence. In general, the agreement between CFD modelling and PIV data is very good, except for the Lightnin A340 in the up-pumping mode where the velocities are overestimated. This may be due to the difference between the blade curvature of the Lightnin A340 in the CFD modeling and that used in the PIV experiments, which is caused by the difficulty of measuring the curvature accurately.

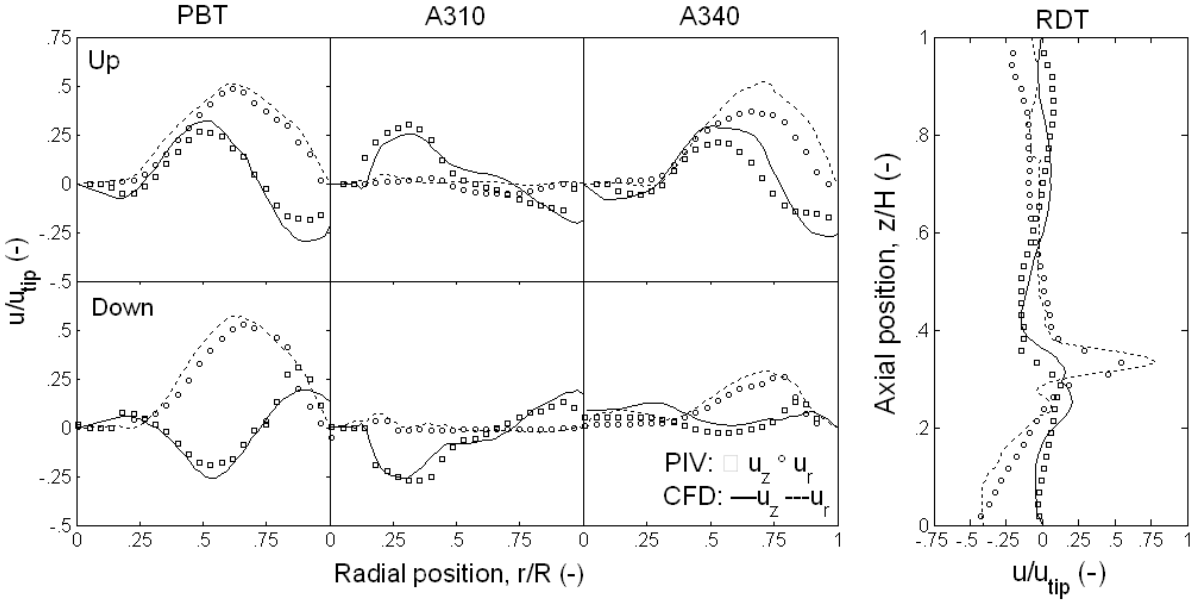

Figure 3.7. Distribution of the velocity components of water at plane of $\theta = 85^{o}$ at N = 220 rpm (Re_{imp} =40,041): CFD and PIV compared.

The fluid is discharged strongly by the RDT in the radial direction. The profile of the axial velocity component shows that within the RDT discharge region, the values of u_z is not zero indicating that the discharge stream is not 100% in the radial direction but with an upward inclination of the outflow, which is consistent with the reports in the literature (Yianneskis et al., 1987). The maximum radial velocity in the discharge stream of RDT measured by PIV is ~ $0.6\,u_{tip}$ at z = $0.33T$, while the value predicted by CFD is ~ $0.76\,u_{tip}$. Both values are within the range of values reported in the literature between 0.5 – $0.85\,u_{tip}$ (Van der Molen

and Van Maanen, 1978; Wu and Patterson, 1989; Kemoun et al., 1994; Zhou and Kresta, 1996; Ranade et al., 2001).

Concerning the flow field in the discharge region of PBT, the maximum magnitude of the axial component, u_z, in both down- and up-pumping mode is $0.25\,u_{tip}$ occurring near the impeller tip (r = 0.55R), while the maximum radial component, u_r, is $0.57\,u_{tip}$ occurring beyond the impeller tip at r = 0.65R. This position is at the bottom or top of the primary circulation loop in the down- and up-pumping mode, respectively, as shown in Fig. 3.6.

The distributions of the radial velocity component, u_r of the Lightnin A310 are fairly flat in both the down- and up-pumping modes, while the axial component, u_z, varies sharply. This is consistent with the performance of the axial impeller. The sharp variance of the axial component, u_z, however, is constrained within the width of impeller blades. The maximum value of u_z is about $0.30\,u_{tip}$ occurring in the middle of impeller blade, which agrees very well with the value of ~ $0.28\,u_{tip}$ reported by Zhou and Kresta (1996).

Comparing the velocity distributions in the down- and up-pumping modes of the PBT and Lightnin A310 impeller, it can be seen that the distributions of u_r in the discharge streams are practically the same, while the distributions of u_z are the mirror of each other. However, this is not the case for the Lightnin A340, as shown in Fig 3.7. The mixing performance of A340U is much better than the A340D, which is consistent with the previous report of its utility of up-pumping in gas-liquid applications such as hydrogenations, or solids drawdown in stirred tanks (Khazam and Kresta, 2008).

The power numbers of different impellers predicted by CFD (based on torque) are 6.7, 1.9, 0.26 and 1.9 for RDT, PBT, Lightnin A310 and Lightnin A340, respectively, as shown in

Table 3.4. The values agree very well with those reported by Hemrajani and Tatterson (2004), except that for the RDT which is about 30% higher. The predicted power numbers of PBT and Lightnin A310 are also in good agreement with the literature values of ~ 2.0 and ~ 0.3 reported by Hemrajani and Tatterson (2004) and Zhou and Kresta (1996), respectively. The CFD predicted power numbers in down- and up-pumping modes are practically the same. The PBT and Lightnin A340 have the same power number, which may be due to the highly similar flow patterns generated by the two impellers.

Table 3.4. Comparison of Power number from CFD and experiments.

Power number (*Po*)	RDT	PBT	A310	A340
CFD	6.7	1.9	0.26	1.9
Experiment	5.0	2.0	0.3	-

3.4.4 Effect of impeller type on the flow fields of CMC solutions

The performance of impellers for the mixing of non-Newtonian fluids in stirred vessel has been found to be significantly different with that for the mixing of low viscosity Newtonian fluids. The impeller type has been shown to have little effect on the flow pattern because the tangential flow is usually predominant in the non-Newtonian fluid mixing at low Re ~ 50 reported by Moore and Cossor (1995).

The velocity vector maps of shear thinning fluids, i.e. 0.2 wt% CMC solutions (Re_{imp} = 100 – 1430, as listed in Table 3.2), agitated by all investigated impellers and measured by PIV are shown in Fig 3.8. It can be seen that at low Reynolds number, the pseudo-cavern is formed for each impeller. The formation of pseudo-cavern in shear thinning fluid has been reported in the literature (Amanullah et al., 1998; Adams and Barigou, 2007), beyond which the fluid is still moving, however, with very small velocities (<< 1% u_{tip}). The shape of the pseudo-cavern generated in the mixing of shear thinning fluids has been theoretically approximated

using the spherical or toroidal model. Amanullah et al. (1998) stated that the toroidal model predicted better cavern shape, and Adams and Barigou (2007) also found that the toroidal model agreed better with the CFD simulations. The toroidal model is,

$$r_c^{[1-(2/n)]} = v_0 \left[\left(\frac{2}{n} - 1 \right) \left(\frac{4\pi^2 k}{F} \right)^{1/n} \right] + b^{[1-(2/n)]} \tag{3.7}$$

Where r_c is the radius of the pseudo-cavern, $r_c = D_c / 4$, b = T/4, v_0 is the velocity at the pseudo-cavern boundary, and F is the body force at the pseudo-cavern boundary.

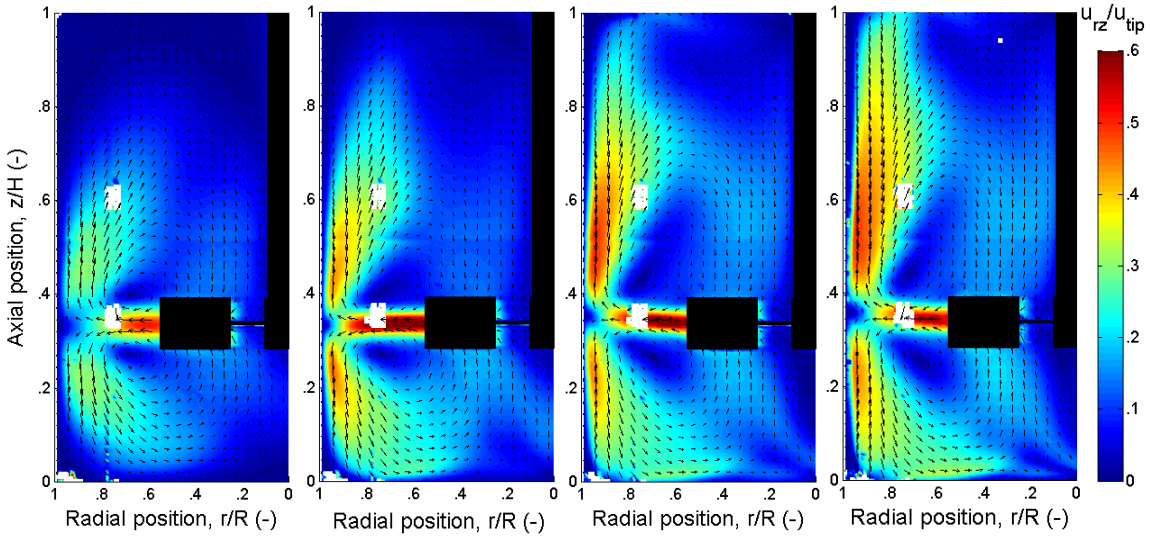

(RDT)

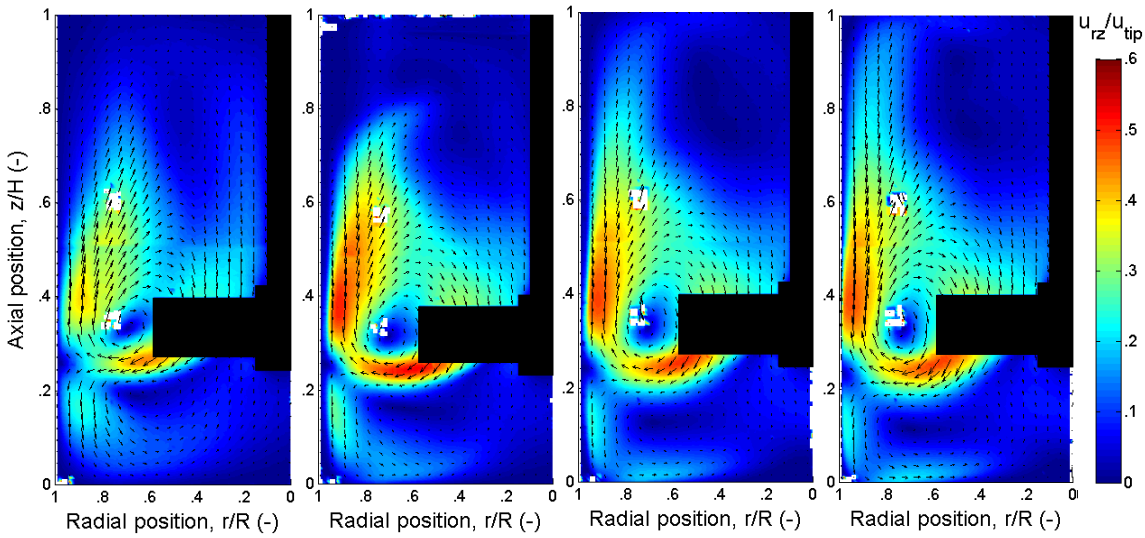

(PBTD)

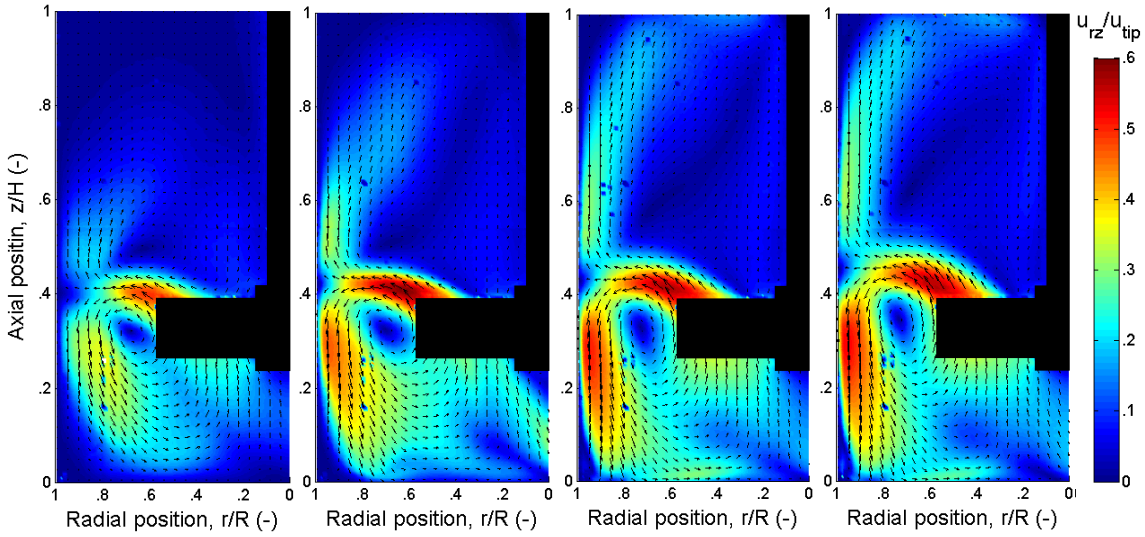

(PBTU)

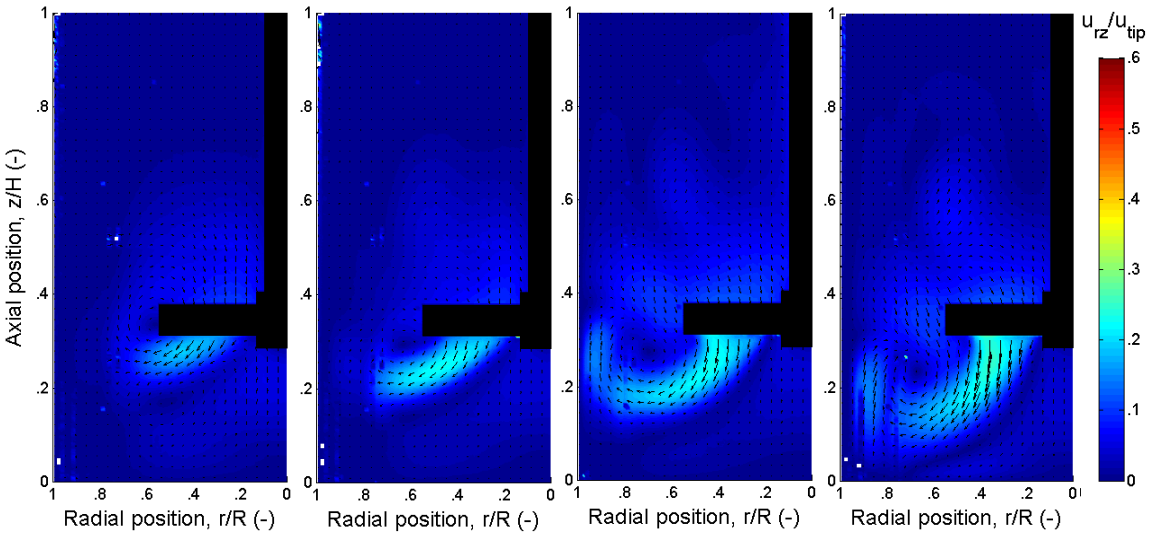

(A310-Down pumping)

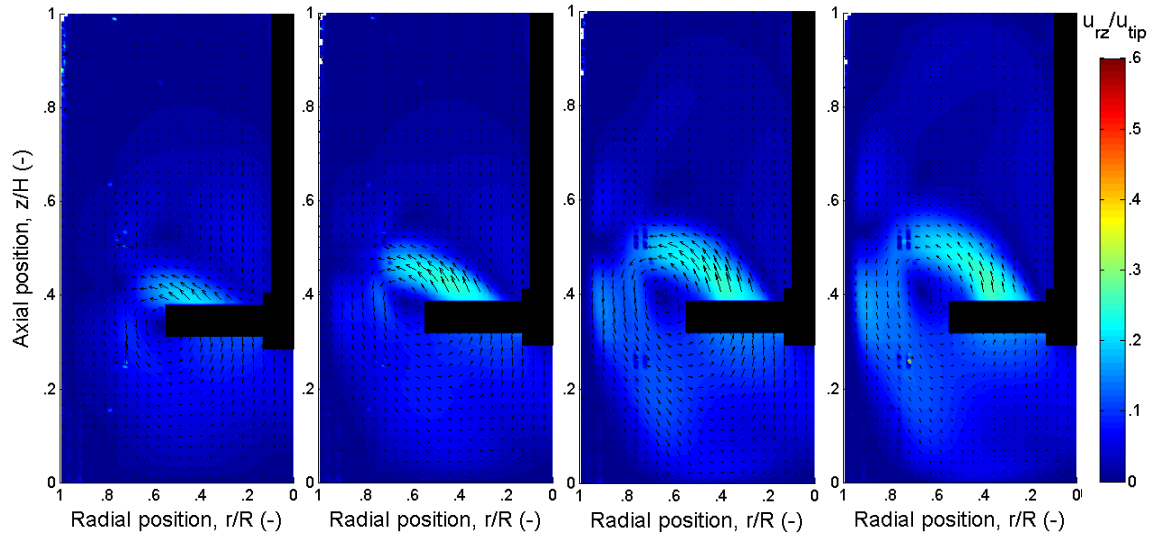

(A310-Up pumping)

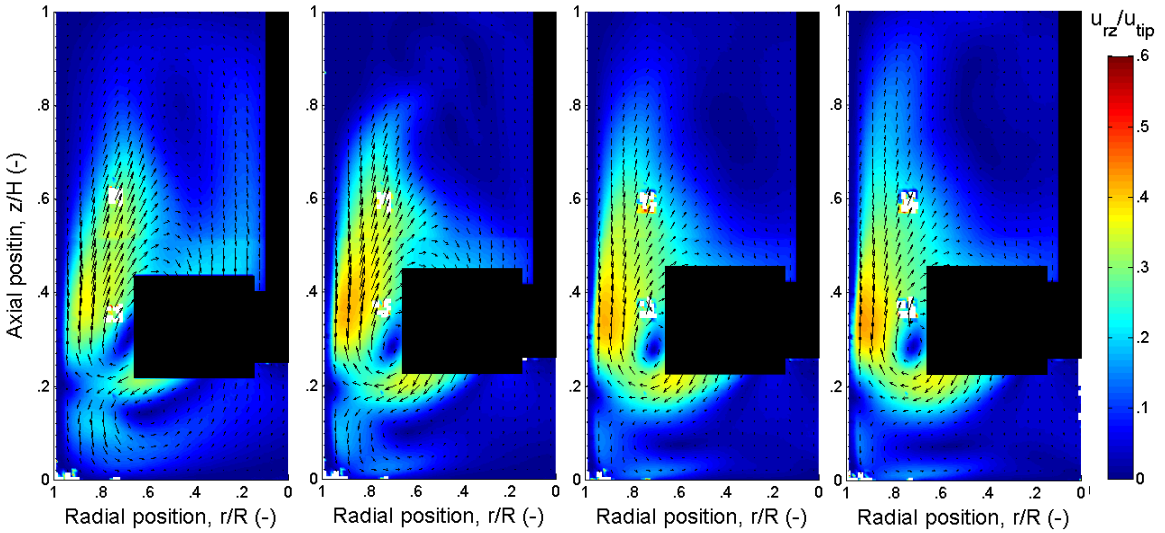

(A340-Down pumping)

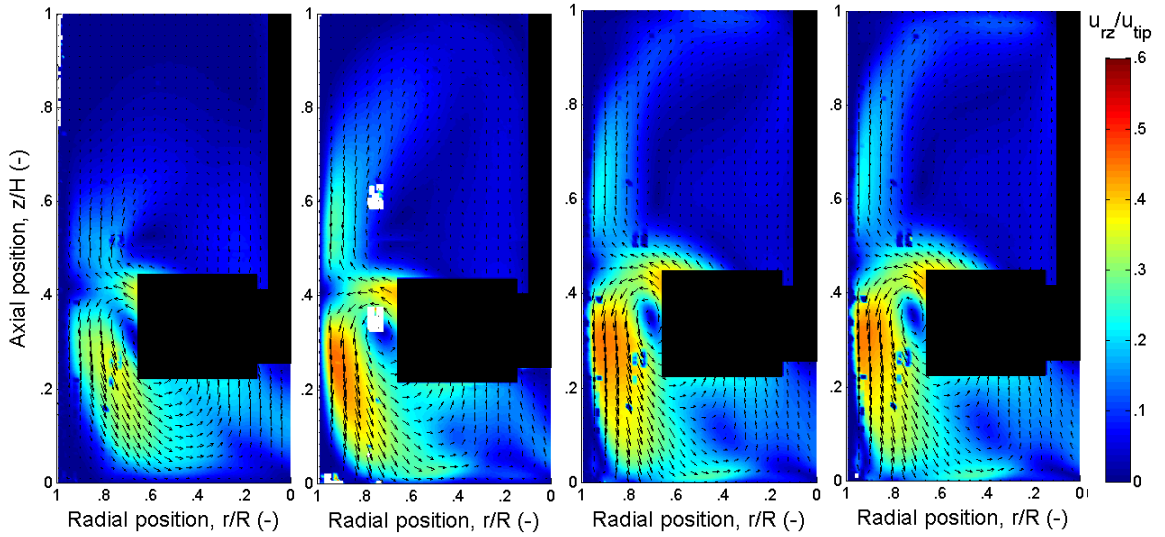

(A340-Up pumping)

(*N* = 60 rpm) **(*N* = 120 rpm)** **(*N* = 220 rpm)** **(*N* = 300 rpm)**

Figure 3.8. PIV measurements of the mean radial-axial fields of 0.2 wt% CMC solutions at plane of $\theta = 85^{o}$.

The impeller speeds, calculated based on the toroidal model, for the pseudo-caverns to reach the tank wall are 25, 30, 87 and 25 rpm for the RDT, PBT, Lightnin A310 and Lightnin A340, respectively. The PIV measurement in Fig 3.8 clearly shows that, except the Lightnin A310, the pseudo-caverns generated by all the other investigated impellers have reached the vessel wall at $N = 60$ rpm.

Once the pseudo-caverns reach the vessel wall, they grow vertically with increase in the impeller speed until they reach the surface of the stirred vessel. It can be seen that the pseudo-caverns grows fast as the impeller speed increasing from $N = 60$ rpm to $N = 220$ rpm. The pseudo-caverns in the 0.2 wt% CMC solution apparently have reached the top liquid surface at the impeller speed of $N = 220$ rpm using all investigated impellers, except the Lightnin A310.

The pseudo-cavern reaching the tank wall and the liquid free surface, however, does not necessarily mean that the liquid in the vessel is well mixed. Jaworski and Nienow (1994) reported that the poorly mixed region occurred in the centre of the circulation loop, since the liquid in this region does not go through the impeller region and consequently is not vigorously mixed. This problem could be mainly attributed to the absence of sufficient turbulence, and cannot be solved by simply increasing impeller speed, as shown in Fig 3.8, the flow fields generated by different impellers at N = 300 rpm is relatively the same as those at N = 220 rpm.

Reynolds number has significant effect on the discharge angle, which is more pronounced for the PBT and Lightnin A310. It is shown obviously in Fig 3.8 that the fluids is discharged by the PBT and Lightnin A310 mainly in the radial direction at low Reynolds numbers (Re_{imp} ~ 100 – 300), however, the axial discharge increases significantly with increasing Reynolds number. This effect can also be examined by the change of the height level of the primary flow loops from different impellers with increasing Reynolds number. The bottoms of the primary flow loops in the down-pumping mode move downward, and the top boundary of the primary flow loops in the up-pumping mode move upward, respectively, indicating the axial discharge becomes more and more significant with the increasing Reynolds number. The effect of Re_{imp} on the discharge angle is discussed in more details in section 3.4.6.

The detailed quantitative comparisons between the CFD predictions and PIV measurements in the discharge stream of four impellers in the different agitating modes and at various impeller speeds, are shown in Fig 3.9. The positions chosen for plotting the velocity profiles are 4 mm below the the lower edge in the down-pumping or 4 mm above the higher edge of different impellers in the up-pumping mode, and the reason has been discussed in section 3.4.3. The

CFD predictions of the velocity distribution agree very well with the PIV measurements, indicating that the laminar model can be used satisfactorily to predict the fluid mixing in the transition flow regime (Re_{imp} ~ 100 – 1500 in this study) in stirred vessels. The discrepancies between the two sets of data occur to the local maxima of different impellers, particular those of the RDT. This could be attributed to the local maximum flow intensity which could not be accurately predicted using the laminar model. As expected, with the increase in Re_{imp}, the discrepancies for the local maxima became worse due to the inadequacy of the laminar model. The relatively large discrepancy occurring with the Lightnin A340 could be attributed to the difference of the blade geometry in CFD modelling and in PIV measurements, as mentioned in section 3.4.3.

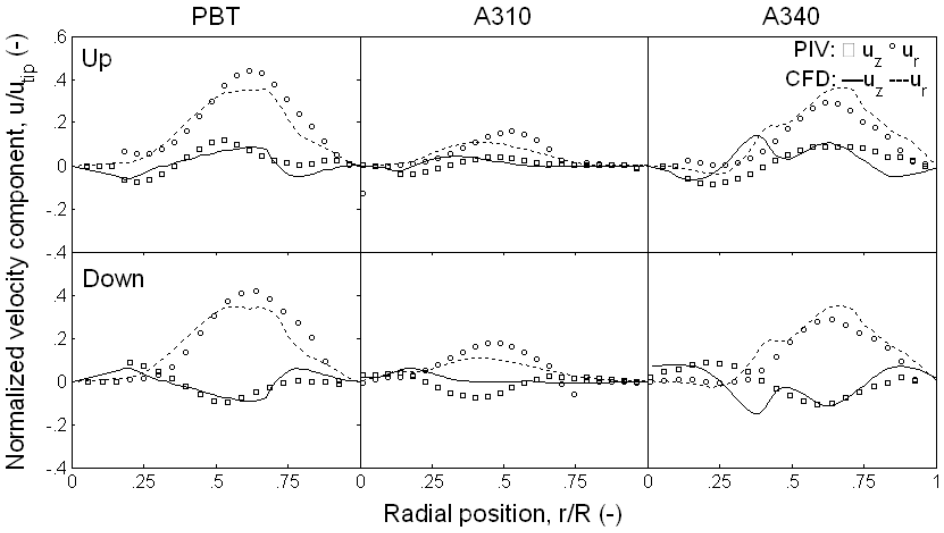

(N = 60 rpm)

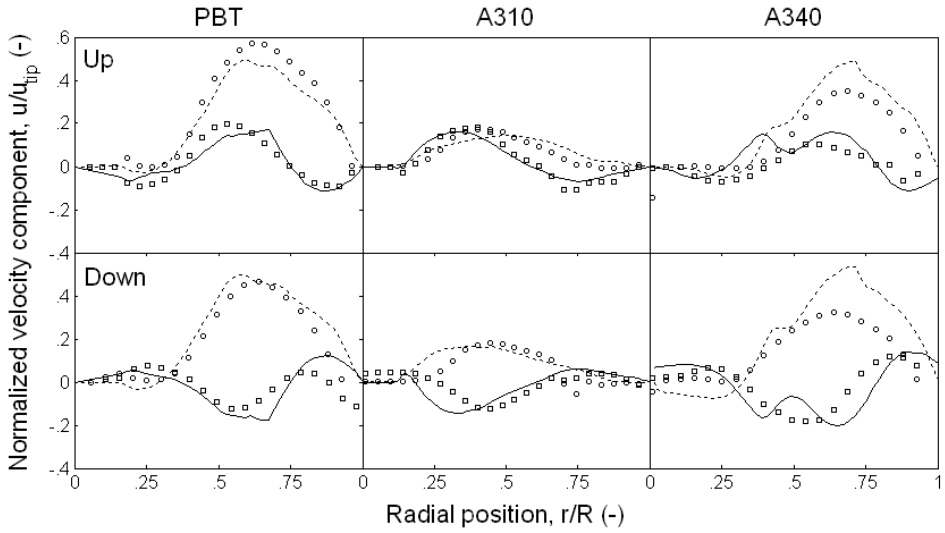

(*N* = 120 rpm)

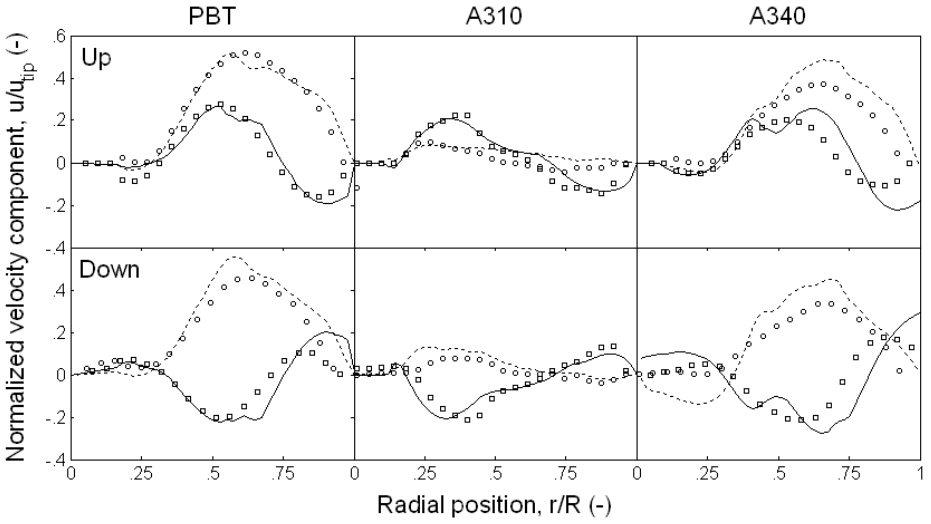

(*N* = 220 rpm)

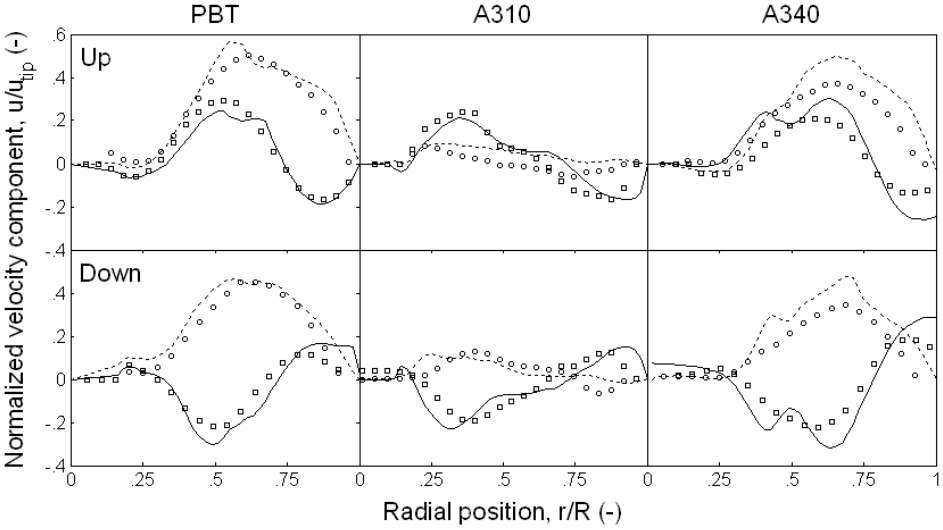

(*N* = 300 rpm)

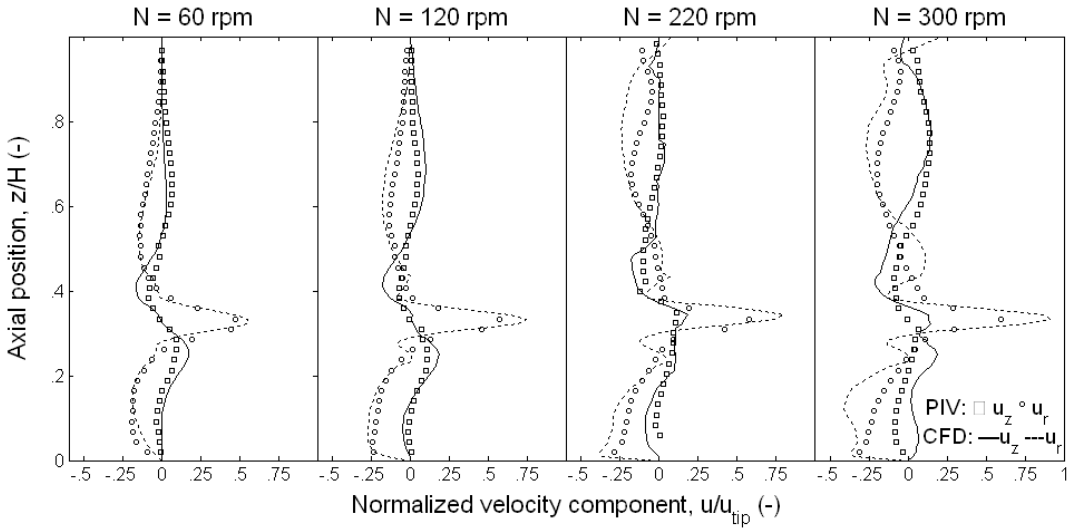

Figure 3.9. Distribution of the velocity components at plane of $\theta = 85^{o}$ in 0.2 wt% CMC solutions: CFD and PIV compared.

Comparing the local maxima of the radial velocities, u_r and axial velocities, u_z, in the discharge stream at low Reynolds number (Re_{imp} ~ 100), it can be found that, u_r is considerably predominant. However, the axial velocities, u_z, are very small, with nearly the same local maxima of only ~ 0.1 u_{tip} for the PBT, Lightnin A310, and Lightnin A340 in both the down- and up-pumping modes.

The axial velocities, u_z, increase significantly with Reynolds number, and the local maxima are ~ 0.2 u_{tip} for the PBT, Lightnin A310, and Lightnin A340 at N = 300 rpm, respectively. The radial velocities, u_r, however, present different trend with the increasing Reynolds number. It is interesting to find from the velocity profiles for Lightnin A310 that, the u_r reduces significantly at $N \geq 220$ rpm, while for the PBT and Lightnin A340, u_r only change slightly with the local maxima of u_r ~ 0.44 u_{tip}, and ~ 0.33 u_{tip}, respectively, at different Reynolds number. It has been discussed in section 3.4.3 that the mixing performance of

A340U is much better than the A340D in highly turbulent flow, as shown in Fig. 3.5. However, similar mixing performances of A340D and A340U can be seen in the mixing of 0.2 wt% CMC solution. The maximum discharge flow of RDT, measured by PIV, increases with increasing Reynolds number, however, it changes slightly at $N \geq 220$.

3.4.5. Effect of rheology on the flow fields of CMC solutions

It is well acknowledged that the fluid rheology has significant effect on the mixing of non-Newtonian fluids in stirred tank. The flow fields of CMC solutions of 0.2 wt%, 0.5 wt%, and 0.7 wt% at the same impeller speed of N = 220 rpm are investigated. The rheological parameters are listed in Table 3.3. The corresponding effective viscosities calculated based on the Metzner-Otto correlation (Metzner and Otto, 1957) are 57, 154 and 343 mPa.s for the 0.2 wt%, 0.5 wt%, and 0.7 wt% CMC solutions, respectively.

The minimum impeller speeds required for pseudo-caverns to reach the vessel wall in the 0.7 wt% CMC solution, based on toroidal model, equation (3.7) (Amanullah et al., 1998), are 105, 135, 408 and 111 rpm for RTD, PBTD, Lightnin A310 and Lightnin A340, respectively, which are about 4 – 5 times higher than those in the 0.2 wt% CMC solution.

The velocity vector maps of all investigated impellers in various CMC solutions at the same impeller speed of N = 220 rpm measured by PIV are shown in Fig 3.10. It needs to be noted that the rightmost velocity vector map of each impeller in Fig 3.10 illustrates the normalized velocity vectors of the 0.2 wt% CMC solutions agitated at N = 60 rpm, which has the same Reynolds number as that of agitating 0.7 wt% CMC solutions at N = 220 rpm.

The size of pseudo-caverns reduces considerably with the increase in the fluid effective viscosity. At the same *Re*, the normalized velocity fields in 0.7 wt% CMC are much lower than that in 0.2 wt% CMC solution. The discharge angle is significantly affected by the fluid

rheology, as the discharge stream becomes more radial inclined with the increase in the effective viscosity, which is discussed in more details in section 3.4.6.

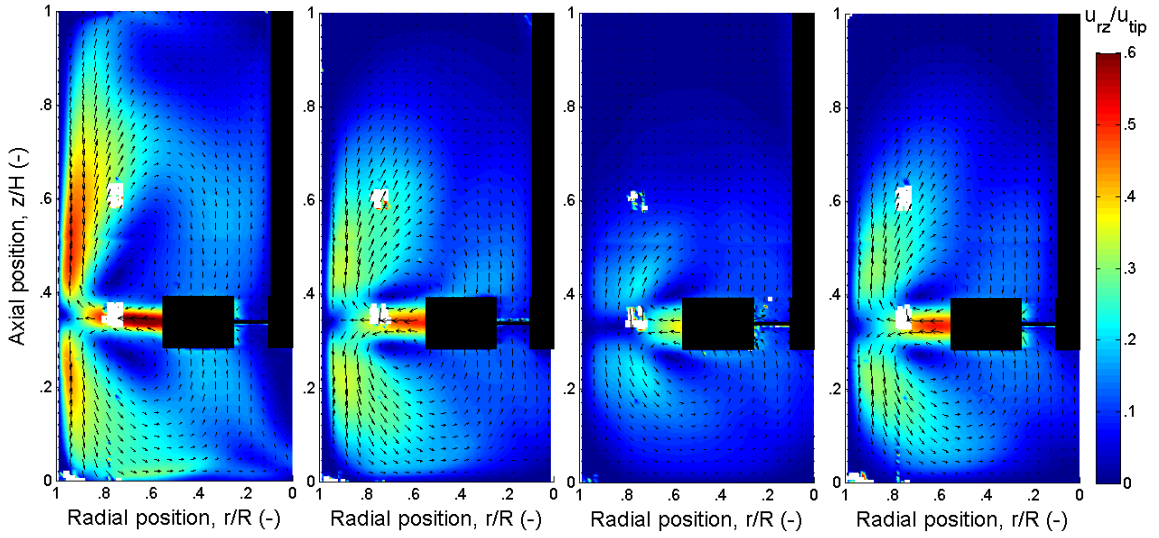

(RDT)

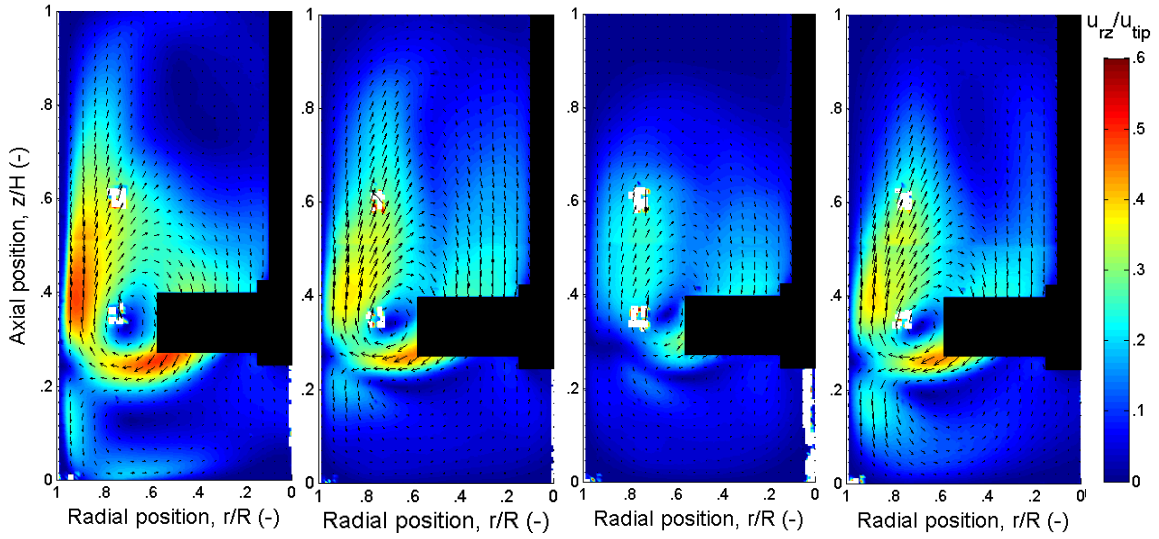

(PBTD)

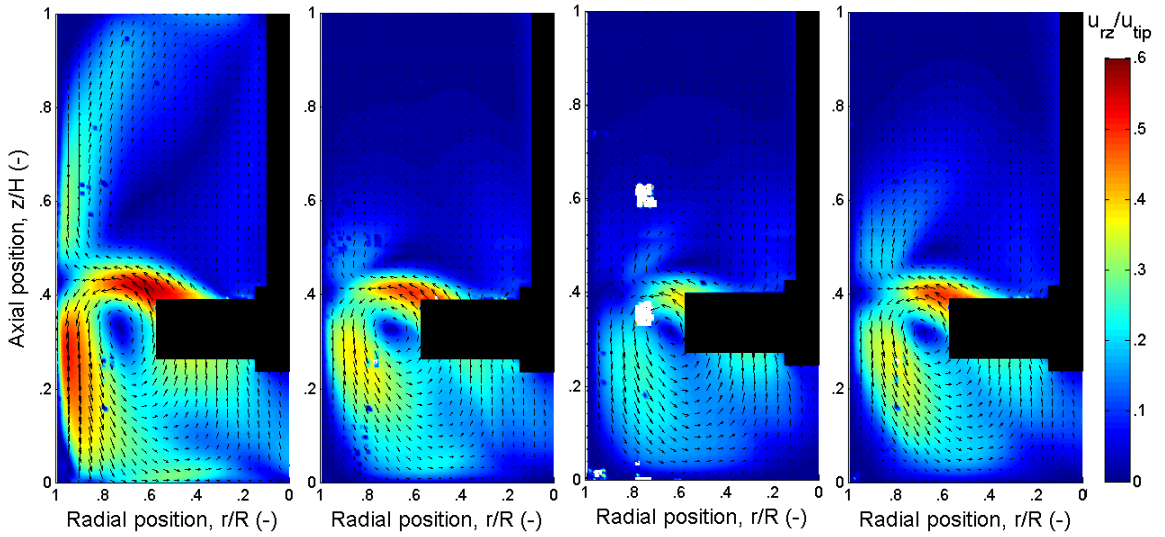

(PBTU)

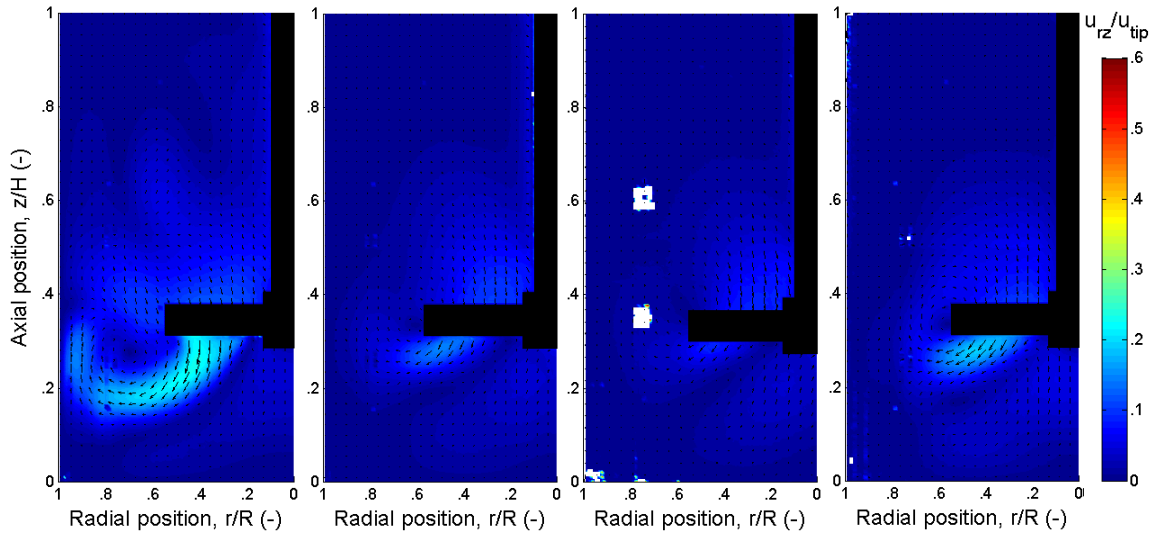

(A310-Down pumping)

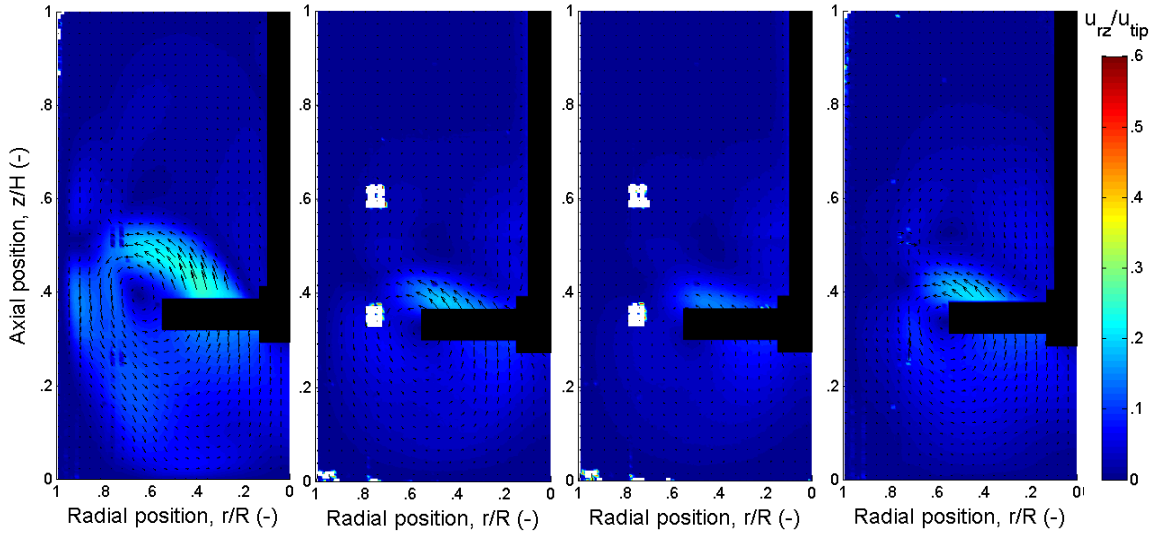

(A310-Up pumping)

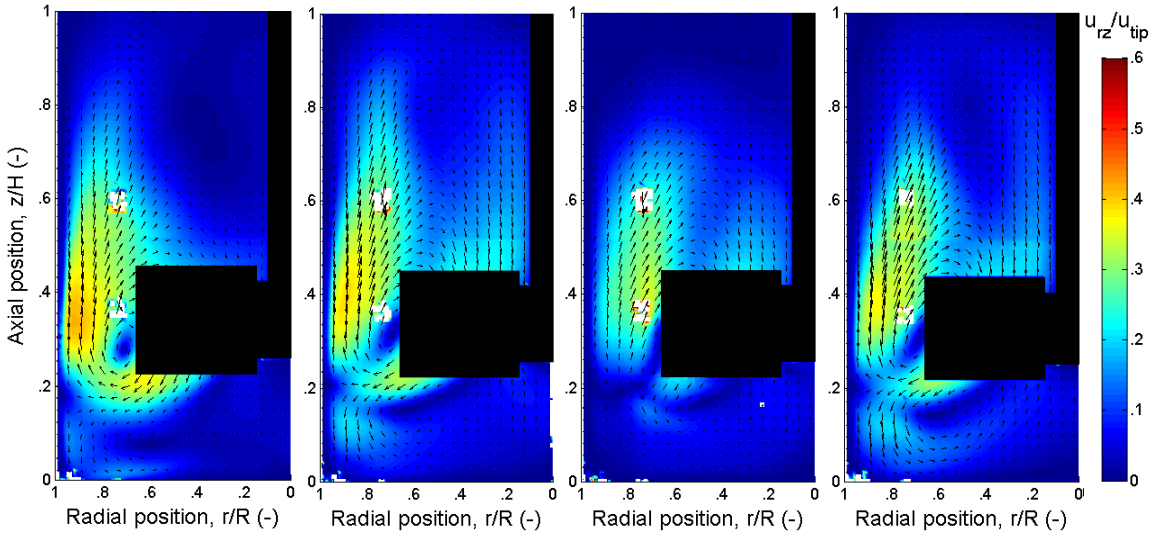

(A340-Down pumping)

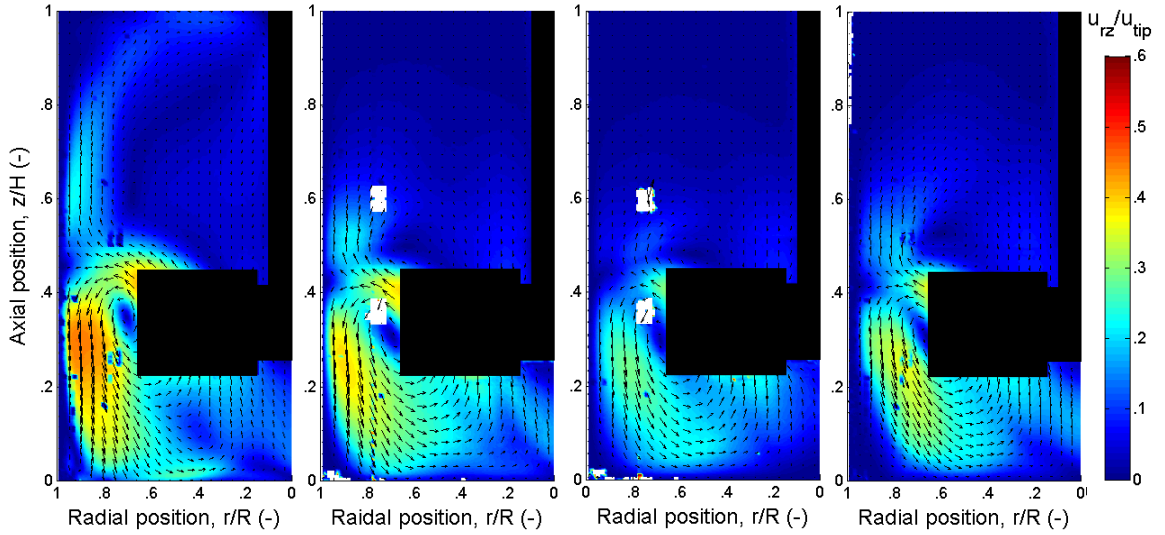

(A340-Up pumping)

(0.2 wt%) (0.5 wt%) (0.7 wt%) (0.2 wt%)

Figure 3.10. PIV measurements of the mean radial-axial fields of CMC solutions at θ= 85°.

The quantitative comparisons of the CFD predicted and PIV measured velocity distributions in the discharge streams of all investigated impellers in CMC solutions of 0.5 wt% and 0.7 wt% at a constant impeller speed, N = 220 rpm, are shown in Fig 3.11. The positions for these velocity profiles are the same as mentioned above. It can be seen that the velocity distributions are well captured by the CFD simulations except for the localised errors in u_r and u_z, as the reasons have been discussed above.

For mixing of non-Newtonian fluids in stirred vessels, the Lightnin A310 is the least effective impeller for generating efficient mixing area, which may be due to its very low solidity ratio (~ 0.67) as reported in the literature (Patel et al., 2011). Patel et al. (2011) investigated the performance of 7 axial impellers and 4 radial impellers in the mixing of viscoplastic fluids, and they have found that the impeller with high solidity ratio, i.e. $\frac{A_{imp}}{V_{imp}}$, where the A_{imp} is

the area of the impeller blades, and V_{imp} is the swept volume of the impeller blades, are more effective for mixing viscoplastic fluids.

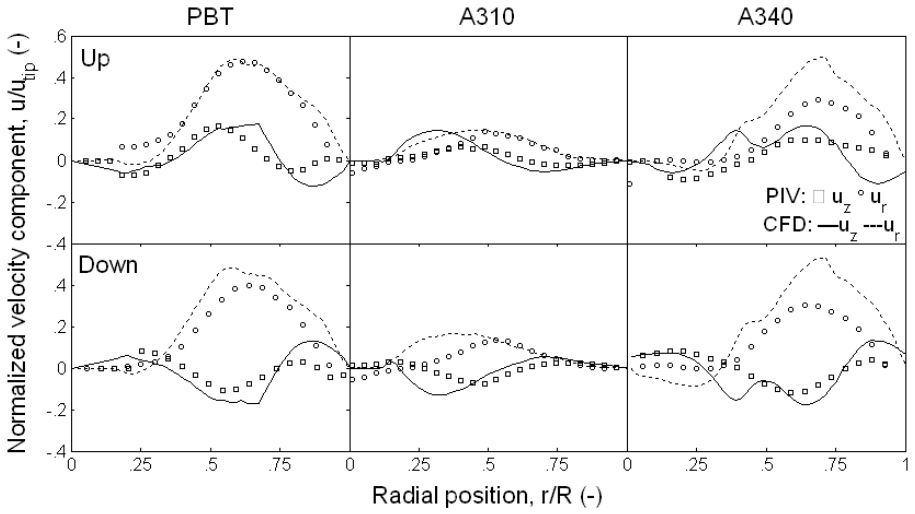

(0.5 wt%)

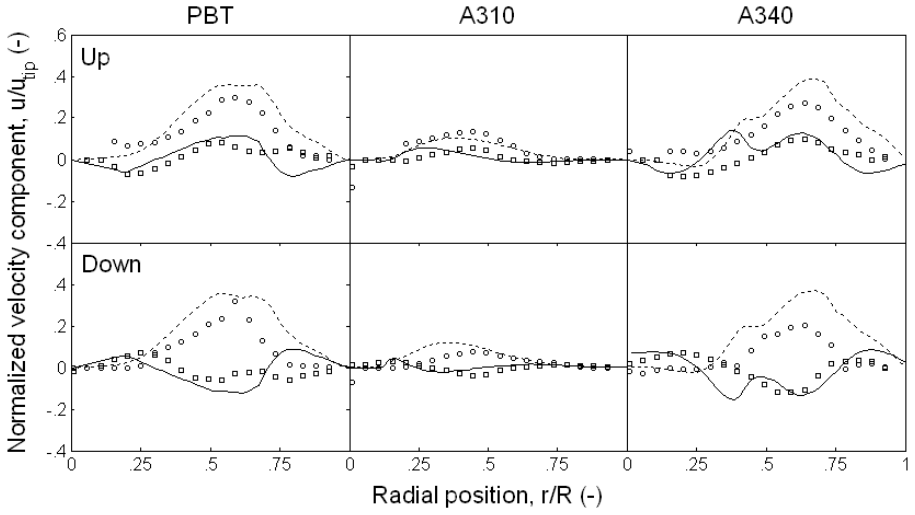

(0.7 wt%)

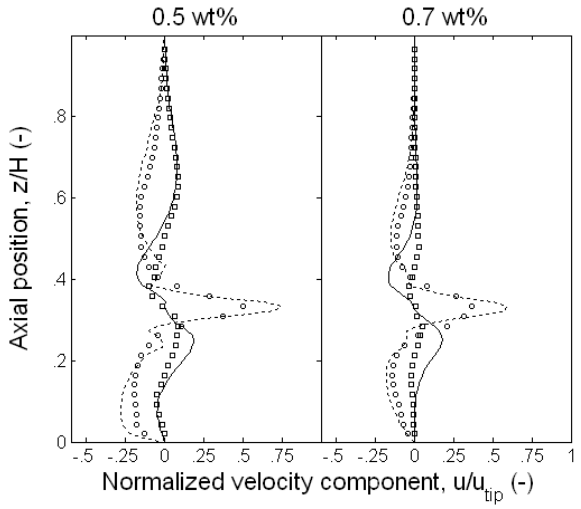

(RDT)

Figure 3.11. Distribution of the velocity components at plane of $\theta = 85^{o}$ in 0.5 wt% and 0.7 wt% CMC solutions: CFD and PIV compared.

3.4.6 Effects of rheological properties and Re_{imp} on the discharge angle

The rheological properties of mixing fluids and the Re_{imp} have no effect on the discharge angle of the radial impeller, RDT. However, it has been reported in the literature that the discharge angle of the mixed and axial impellers are significantly affected by the fluid rheology and the Re_{imp}. These effects have been studied for shear thinning fluids and yield stress fluids agitated by hydrofoil impellers (Jaworski and Nienow, 1994; Couerbe et al., 2008). Kelly and Gigas (2003) investigated the discharge angle of 0.1 wt% carbopol solution agitated by hydrofoil impeller A315, and they found that the axial pumping capacity reduced significantly with the decrease in *Re* or increase in fluid effective viscosity.

The effects of *Re* and fluid rheological parameters have been discussed briefly based on the velocity vector maps in Fig 3.8 and Fig. 3.10 in section 3.4.4 and section 3.4.5. The radial profiles in the vicinity of impeller in Fig 3.9 and Fig. 3.11 show that the ratios of the maxima

of the radial velocity component and axial velocity component, $\frac{u_r}{u_z}$, of the PBT, Lightnin A310 and Lightnin A340 reduce significantly with the increase in Reynolds number, whereas the ratios increase with the increasing the fluid effective viscosity. As presented in Table 3.5, the magnitudes of $\frac{u_r}{u_z}$ for the PBT, Lightnin A310 and Lightnin A340 in the down-pumping mode reduces from 4.2 to 2.3, from 2 to 0.38, from 2.73 to 1.54 with impeller speed increasing from N = 60 rpm to N = 300 rpm, respectively.

The variation of the discharge angles of investigated impellers with the *Re* is shown in Fig 3.12. It should be noted that only the discharge angles in the down-pumping mode are shown in Fig 3.11, as the flow patterns in the up-pumping seems to mirror those in the down-pumping mode. The discharge angle of PBT in 0.2 wt% CMC solution increases from about 10^o at Re_{imp} = 115, to about 30^o at Re_{imp} = 1090. The discharge angle of Lightnin A310 exhibits steepest increase, as the discharge angle increases from about 30^o to 80^o as Re_{imp} increases from 105 to 995. The discharge angle of A340 is only weakly affected by the Reynolds number, as it varies around 45^o. The discharge angles of PBT, Lightnin A310 and Lightnin A340 drop significantly for the mixing of higher CMC concentrations, i.e. 0.5 wt% and 0.7 wt% CMC solutions at the same Reynolds number.

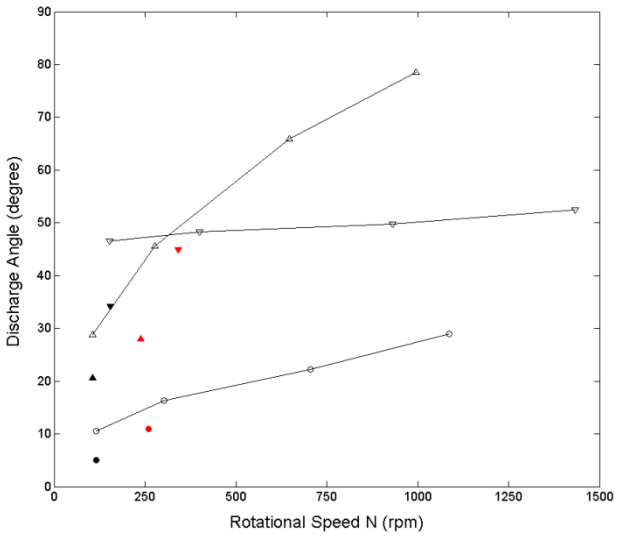

Figure 3.12. Effects of fluid rheology and Reynolds number on the discharge angle of different impellers.

—○— PBTD, —△— A310D, —▽—A340: 0.2 wt% CMC solution

● PBTD, ▲ A310D, ▼ A340: 0.5 wt% CMC solution

● PBTD, ▲ A310D, ▼ A340: 0.7 wt% CMC solution

Table 3.5. The values of ($\frac{u_r}{u_z}$).

Liquids	N (rpm)	$\frac{u_r}{u_z}$		
		PBT	A310	A340
Water		2.65	0.11	8.67
CMC (0.2 wt%)	60	4.2	2	2.73
	120	3.83	1.5	1.78
	220	2.3	0.38	1.62
	300	2.04	0.65	1.54
CMC (0.5 wt%)	220	3.64	2.12	2.73
CMC (0.7 wt%)	220	5.3	2.57	1.67

3.4.7 Reynolds number similarity

The flow structure at high Reynolds numbers has been reported to present similar characteristics, a phenomenon often referred to as Reynolds number similarity. In fully turbulent flow, viscosity effects vanish and dimensionless mean values such as velocities

normalised by the impeller tip speed should be independent of Reynolds number (Van der Molen and Van Maanen, 1978; Costes and Couderc, 1988; Venneker et al., 2010). Van der Molen and Van Maanen (1978) proposed a correlation of the normalized radial velocity component in the impeller center plane as a function of the radial position only,

$$\frac{u_r}{u_{tip}} = 0.85\left(\frac{r}{0.5D}\right)^{-7/6} \tag{3.8}$$

The Reynolds number similarity of the mixing of viscous Newtonian and non-Newtonian fluids in stirred vessels has drawn less attention. Dyster et al. (1993) reported that the flow number, *Fl*, was Reynolds number independent at $Re_{imp} > 500$ in viscous Newtonian fluids. Koutsakos et al. (1990) introduced a correlation parameter ξ on the right side of equation (3.8) for the mixing of non-Newtonian fluids. Jahangiri (2005) investigated the correlation parameters, ξ_θ and ξ_r for the mean tangential and radial velocities, respectively, for the shear-thinning fluids. Most recently, Venneker et al. (2010) investigated the Reynolds number similarity for both the mean velocities and RMS velocities in the shear-thinning fluids.

The power number of all investigated impeller in transitional regime calculated from CFD data (based on torque) are shown in Fig 3.13. CFD predicts that in the transitional flow, the power number of RDT increases, while those of PBT and Lightnin A310 decrease with increasing Reynolds number. The profile of the power number of Lightnin A340 is very close to that of PBT, and its power number only slightly changes by the Reynolds number. The profile of the power number of RDT does not level off in the range $Re_{imp} \leq 1{,}000$. Considering the other three impellers, however, the power numbers are independent of the Reynolds number at $Re_{imp} \geq 900$ for the PBT and Lightin A340. The power number of Lightin A310 becomes independent of the Reynolds number at much smaller Reynolds

number, Re_{imp} ~ 400. The constant values of power number for different impellers are very similar to those in the fully turbulent regime. For each investigated impeller, the predicted power number for CMC solutions with different rheological properties collapse into a single line when plotted against the Reynolds number suggesting that the power number only depends on the Reynolds number.

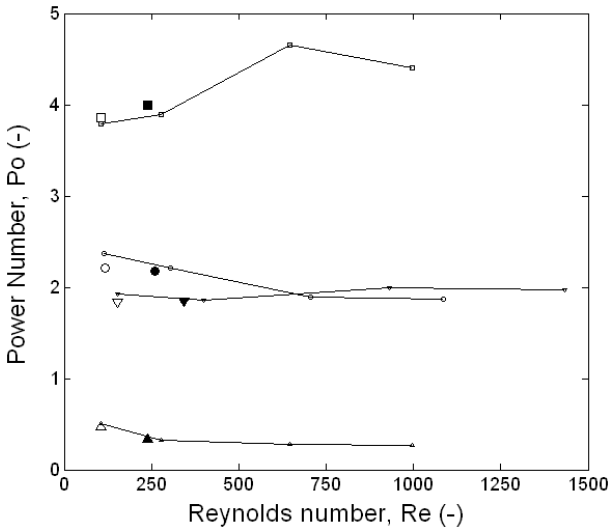

Figure 3.13. Power numbers of different impellers against the Reynolds number.

—□— RDT, —○— PBTD, —△— A310D, —▽—A340: 0.2 wt% CMC solution

□ RDT, ○ PBTD, △ A310D, ▽ A340: 0.5 wt% CMC solution

■ RDT, ● PBTD, ▲ A310D, ▼ A340: 0.7 wt% CMC solution

Fig. 3.14 shows the profiles of velocities of mixing of 0.2 wt% CMC solution in the discharge stream of the investigated impellers at N = 220 rpm and N = 300 rpm. It can be readily seen that the velocities at the two impeller speeds coincide with each other very well, except the axial velocities of the RDT which are still affected by the Re_{imp}.

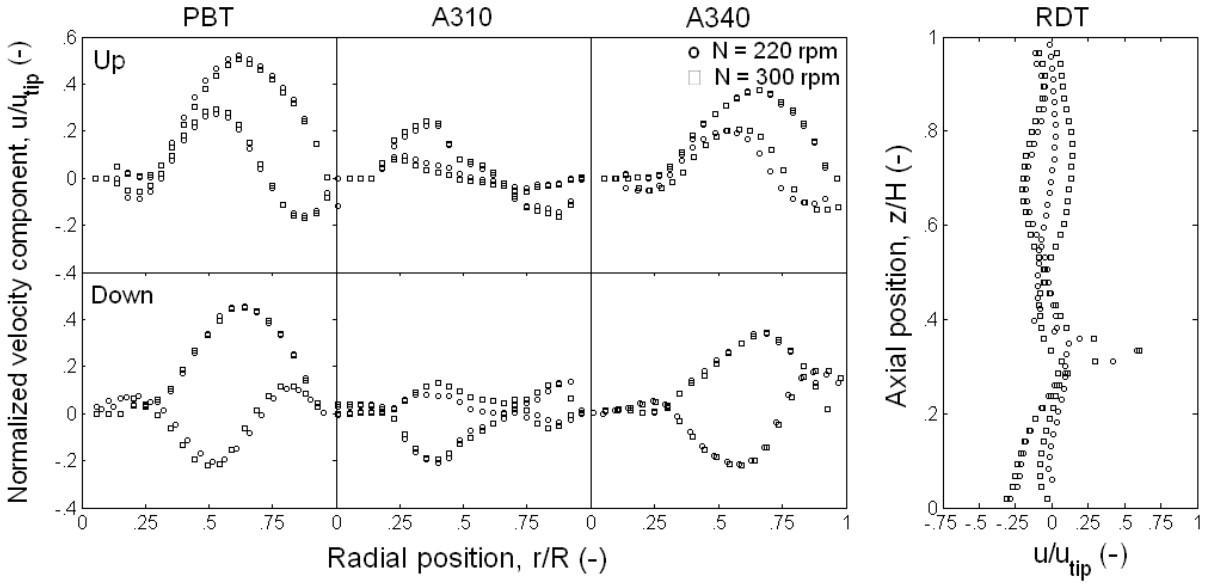

Figure 3.14. Demonstration of Reynolds number similarity in the 0.2 wt% CMC solution.

3.5. Conclusion

The highly turbulent flow fields of water and the flow fields of CMC solutions of different concentrations under the transitional regime, agitated by RDT, PBT, Lightnin A310 and Lightnin A340 in both down-and up- pumping modes in a stirred vessel have been successfully modelled by CFD. For the turbulent mixing of water, not only the azimuthally-averaged velocity distributions but also the velocity distributions in three planes, i.e. 5° on the leeward side of the baffle, 45° in the mid-way between two baffles, 85° on the windward side of the baffle degree can be well predicted by CFD modelling, as the agreement with the PIV and PEPT measurements is fairly good.

The time-averaged velocity distributions for turbulent water flow and CMC solutions of 0.2 wt%, 0.5 wt%, and 0.7 wt% in transitional flow, in the vicinity of the investigated impellers, and in the plane 85° on the windward side of the baffle, are also predicted very well by CFD

modelling in comparison with the PIV measurements, except the Lighnin A340, which could be due to the difference of the blade bending angle of the Lightnin A340 in the CFD modeling and that used in the PIV experiments.

The Reynolds number and fluid rheology have significant effects on the discharge angle, especially those of PBT and Lightinin A310. The radial discharge increases significantly either with decrease in Reynolds number or with increase in the fluid effective viscosity. The discharge angle of the wide-blade Lightinin A340 is significantly affected by the fluid rheology, however, is only slightly affected by the Reynolds number.

The power number of RDT does not level off in the range $Re_{imp} \leq 1{,}000$ in the present study, while the power numbers of all the other three impellers have become independent of the Reynolds number at $Re_{imp} \leq 1{,}000$, i.e. at $Re_{imp} \sim 900$ for the PBT and Lightin A340, and much smaller Reynolds number, $Re_{imp} \sim 400$ for Lightin A310. The normalized velocities in the discharge stream of the investigated impellers present Reynolds number similarity at high Reynolds number ($Re_{imp} \sim 1000$).

Notation

D	impeller diameter	m
H	height of suspension	m
N	impeller rotational speed	s^{-1}
r	radial distance	m
R	vessel radius	m
Re_{imp}	impeller Reynolds number	-
T	vessel diameter	m
u_{tip}	impeller tip speed	m s^{-1}
$u_r\ u_z\ u_\theta$	cylindrical velocity components	m s^{-1}
z	vertical distance	m

Chapter IV

NUMERICAL MODELLING OF VELOCITY FIELD AND PHASE DISTRIBUTION IN DENSE MONODISPERSE SOLID-LIQUID SUSPENSIONS UNDER DIFFERENT AGITATION REGIMES

Abstract

Turbulent suspensions of monodisperse coarse glass particles of 1 and 3 mm diameter in water were numerically simulated at their 'just-suspended' speed N_{js} and at speeds above it up to $2N_{js}$, in a vessel agitated by a down-pumping pitched-blade turbine. The solid concentration was in the range 5.2 – 40 wt%. The numerical results are compared to detailed 3-D distributions of the three local phase velocity components and solid concentration obtained by an accurate technique of positron emission particle tracking (PEPT). The predictions of flow number and mean velocity profiles for both phases are generally excellent both at N_{js} and above it. Predictions of the spatial solids distribution are good except near the base of the vessel and underneath the agitator where they are largely overestimated, however, they improve significantly with increasing solid concentration. At N_{js}, there are wide variations in the spatial distribution of the inter-phase slip velocity. The largest total slip velocities are of considerable magnitude, on the order of ~ $0.10u_{tip}$. Increasing the agitation speed up to $2N_{js}$, reduces the normalised slip velocities significantly. Results also indicate that there is no impact on the distributions of turbulent kinetic energy and Kolmogorov length scale. The eddy dissipation rate, however, is increasingly suppressed as solid concentration increases at N_{js}. Same velocity fields are obtained using the transient (SG) and steady state (MFR) simulations. Effects of non-drag forces on the predicted distributions of velocities of both phases and solid concentration are negligible. However, the drag model has significant influence.

4.1. Introduction

Solid-liquid suspension in stirred vessels is widely encountered in industry, for example, food, crystallization, catalysis, mineral, pharmaceuticals, and personal/home care products. Numerous difficult mixing problems are found with solid-liquid processing which pose a formidable challenge to industry. The methods generally used for designing stirred vessels for solid-liquid mixing tend to be based on global empirical data. A localized hydrodynamic approach provides a better more efficient basis for design since it enables a detailed description of the multiphase flow structure. However, few measurement techniques exist which can provide reliable data of this kind.

The well-established optical techniques such as LDV and PIV are at best only applicable to very dilute suspensions and cannot be applied to fluids and slurries which are opaque (Micheletti and Yianneskis, 2004; Unadkat et al. 2009; Montante et al. 2012). But, even at such low solid fractions and working in small tanks, it has still been difficult to obtain accurate measurements especially near the impeller. So far, attempts at local measurements have been mainly limited to the investigation of mean axial solid-concentration profiles at relatively low solid loadings using intrusive conductivity or capacitance probes (Brunazzi *et al.*, 2004). However, these methods give limited information and cannot be used to probe the local hydrodynamics of suspensions in detail or to measure the 3-D distribution of both liquid and solid.

More recent experimental studies using electrical resistance tomography (ERT) demonstrated, albeit mainly qualitatively, how visualization of gas, solid or liquid distribution can help improve understanding of mixing process (Wang et al., 2007). However, these methods give limited information and cannot be used to probe the local hydrodynamics of suspensions in

detail or to measure the 3-D distribution of both liquid and solid. On the other hand, a more sophisticated computer automated radioactive particle tracking (CARPT) technique based on gamma-ray emissions has been developed (Rammohan et al., 2001; Guha et al., 2007), and Guida et al. (2009, 2010) recently reported on the use of technique of positron emission particle tracking (PEPT) to measure the local hydrodynamics as well as the spatial phase distribution in mechanically agitated solid-liquid suspensions.

Numerically too, these multiphase systems, especially at high solid loadings, have not been adequately studied and are not well understood. This is partly due to the considerable complexity of the turbulent (time-dependent) flow structures induced by the interaction between the impeller and surrounding fluid, coupled with additional effects associated with the discrete phase. Indeed, there are still outstanding issues concerning the accurate modelling of particle-fluid and particle-particle interaction effects.

Direct or Large Eddy Simulations are still far too expensive computationally to deal with multiphase flows in stirred tanks and can only handle dilute systems (~ 5 vol%). Therefore, solution of the Navier-Stokes equations by means of Computational Fluid Dynamics (CFD) codes with the appropriate two-phase models incorporated seems to be the most advanced cost-effective method currently available to model such systems. However, this area is still in need of development. In particular, detailed and rigorous 'pointwise' experimental validation of such models, particularly at substantial solid concentrations of industrial relevance, has not been reported. There is, therefore, a clear need for further analysis and evaluation of the available models and codes.

A number of numerical investigations have been reported in the last decade: some dealt with dilute suspensions of little practical relevance and are summarized in Table 4.1, and some

dealt with more industrially relevant solids loadings (moderate to dense) and are summarized in Table 4.2. Such studies of solid-liquid mixing, especially those dealing with concentrated slurries, have been mainly concerned with predicting the solid concentration distribution but not distributions of phase velocities or slip velocities. The validation work reported in the literature has been very limited and has relied mostly on single-traverse probe measurements of axial solid distributions.

In this chapter, the flow of coarse glass particles in water is studied numerically by means of a CFD model in a mechanically agitated vessel under different regimes of particle suspension. Experimental results from PEPT measurements of suspensions of 3 mm particles in water at X = 5.2 – 40 wt% obtained using PEPT at $N = N_{js}$ reported by Guida et al. (2011), and new PEPT measurements of suspensions of 1 mm particles in water at X = 5.2, 20 wt% at $N = N_{js}$ as well as suspensions of monodisperse coarse glass particles of 1 and 3 mm diameter in water at speeds above N_{js} up to $2N_{js}$ carried out the author are used for validation of a number of suspension characteristics including most importantly the detailed 3-D velocity field of both the continuous and discrete phase, and the spatial phase distribution. Results are also analysed to infer local time-average particle-fluid slip velocities, phase flow number, suspension uniformity and the effects of particle addition on the liquid flow field.

Table 4.1. Literature CFD studies of dilute solid-liquid systems.

Reference	Solid concentration	Particle diameter (mm)	Validation method
Guha et al. (2008)	1 vol%	0.3	Three velocity components of solid at at $z = 0.075H$, $0.25H$, $0.34H$ and $0.65H$ from computer automated radioactive particle tracking
Ochieng and Onyango (2008)	1.33 vol% (10 vol % only CFD)	0.75	Axial solid concentration from optical attenuation technique
Shan et al. (2008)	0.5 vol% (10 vol % only CFD)	0.08	Local solid concentration at $z = 0.33H$, $0.48H$, $0.57H$, $0.67H$, $0.83H$ from fibre optic probe measurement
Montante and Magelli (2007)	1.5-3.6 g L^{-1}	0.33	Axial solid concentration from optical attenuation technique
Ochieng and Lewis	0.54 wt%, 1.33 wt% (above 5	0.23, 0.4, 0.75	Axial solid distribution from optical

(2006)	wt% only CFD)		attenuation technique
Fan et al. (2005)	0.02 vol%	0.16	Axial velocity component of liquid at $z = 0.27H$ from DPIV
Oshinowo and Bakker (2002)	0.5 vol%	0.253	Axial velocity of both liquid and solid phase at $r = 0.464R$ and $r = 0.961R$ from LDV
Montante et al. (2001)	1 to 5 g L^{-1}	0.13, 0.33, 0.79	Axial solid distribution from optical attenuation technique
Ljungqvist and Rasmuson (2001)	0.1- 2 vol%	0.075, 0.15, 0.45	Three velocity components of liquid phase at $z = 0.25H$ and $z = 0.034H$ from phase-Doppler anemometry

Table 4.2. Literature CFD studies of moderate to dense solid-liquid systems.

Reference	Solid concentration	Particle diameter (mm)	Validation method
Tamburini et al. (2011)	16.9-33.8 wt%	0.231, 055	Mass of suspended solids measured with pressure gauge technique
Sardeshpande et al. (2011)	1 vol%, 3 vol%, 7 vol%	0.25, 0.35	Axial velocity of the liquid and solid phase at $z= 0.18H$ from ultrasound velocity profiler measurement
Hosseini et al. (2010)	10 wt%	0.1-0.9	Cloud height and impeller torque
Tamburini et al. (2009)	21.5 wt%	0.231	Photography of solid suspension height and axial solid concentration at $r = 0.7R$ measured using a conductivity probe
Kasat et al. (2008)	10 vol%	0.264	Axial solid distribution from photo-electric method
Khopkar et al. (2006)	10-16 vol%	0.135-0.655	Axial solid distribution measured by optical fibre probe at $r = 0.7R$.
Montante and Magelli (2005)	4-6 vol%	0.137-0.675	Axial solid distribution measured by optical probe
Micale et al. (2004)	0.48-14.4 vol%	0.212-0.25	Photography of solid suspension height
Oshinowo and Bakker (2002)	12 vol %	0.39	Axial solid distribution from sampling probe measurement
Altway et al. (2001)	5-20 vol%	0.087	Axial solid distribution from photo-electric method

4.2. Materials and methods

The PEPT measurements were conducted in a standard cylindrical, flat-bottomed vessel made of Perspex. The diameter of vessels is T = 288 mm, and the height of the suspension in the vessel was set at $H = T$. The vessel was fitted with four wall baffles of $0.1T$ spaced at 90° degrees and was agitated by a down-pumping 6-blade 45º pitched-turbine (PBT) of diameter $D = T/2$, located $T/4$ from the tank base. The suspending liquid used was tap water with its density adjusted to 1150 kg m^{-3} by adding NaCl to make the PEPT particle tracer used to track the liquid phase neutrally buoyant. Nearly-monomodal and nearly-spherical glass beads of two different sizes (d_p = 1.00-1.25 mm or d_p = 2.85-3.30 mm) having a density of 2485 kg

m^{-3} were used to obtain a two-phase suspension with a mean solid mass concentration, X, varying in the range 0 to 40 wt%. These particles will be referred to as 1 mm and 3 mm particles.

The 3-D trajectories of the fluid phase and of the solid phase were resolved separately in distinct successive PEPT experiments. A radioactive neutrally-buoyant resin particle tracer (600 μm) was used to track the liquid phase, and an individual representative glass particle radioactively labelled in a cyclotron was used to track the solid phase trajectories. Based on the verification of ergodicity in a turbulent flow system by Guida et al. (2009; 2010; 2012), every experiment was run for 30 min, a sufficiently long runtime.

Experiments were conducted under different regimes of solid suspension corresponding to the minimum speed for particle suspension N_{js} and speeds above it up to $2N_{js}$. N_{js} was visually determined in the transparent vessel according to the well-known Zwietering criterion (Zwietering, 1958), i.e. no particle remains stationary on the bottom of the tank for longer than 1-2 s. The range of PEPT experiments and CFD studies conducted are summarized in Table 4.3. Suspensions of particles of 3 mm diameter in water at X = 5.2 - 40 wt% at their 'just-suspended' speed N_{js} reported by Guida et al. (2010) were also listed in Table 4.3, marked with *, since they were used for the validations of the CFD modellings.

Table 4.3. Range of PEPT measurements and CFD simulations.

d_p (mm)	X (wt%)	C (vol%)	N (rpm) ($Re_{imp} \times 10^{-5}$)			
			$N = N_{js}$	$N > N_{js}$		
1	5.2	2.5	360 (1.43)	450 (1.79)	540 (2.15)	720 (2.86)
	20	10.4	490 (1.91)	613 (2.44)	-	-
3	5.2	2.5	360 (1.43)*	450 (1.79)	540 (2.15)	720 (2.86)
	10.6	5.2	410 (1.61)*	520 (2.07)	-	720 (2.86)
	20	10.4	490 (1.91)*	613 (2.44)	-	735 (2.92)
	40	23.6	590 (2.34)*			

*PEPT measurements reported by Guida et al. (2010)

4.3. Numerical modelling

Numerical simulations were performed using the commercial CFD code ANSYS CFX 12.0. In simulating solid-liquid flows, the Eulerian-Lagrangian model would be a more realistic approach because it simulates the solid phase as a discrete phase and so allows particle tracking. However, the number of particles that can be tracked is currently very limited, thus restricting the applicability of the model to dilute mixtures. The multi-fluid Eulerian-Eulerian model was therefore used instead, whereby the liquid and solid phases are both treated as continua.

The governing equations which form the basis of the model are the continuity equation:

$$\frac{\partial(\rho_q \phi_q)}{\partial t} + \frac{\partial(\rho_q u_{iq} \phi_q)}{\partial x_i} = 0 \tag{4.1}$$

and the momentum equation

$$\frac{\partial(\rho_q u_{iq} \phi_q)}{\partial t} + \frac{\partial(\rho_q u_{iq} u_{jq} \phi_q)}{\partial x_i} = -\phi_q \frac{\partial P}{\partial x_i} + \frac{\partial}{\partial x_i}\left[\phi_q \mu_{qeff}\left(\frac{\partial u_{iq}}{\partial x_j} + \frac{\partial u_{jq}}{\partial x_i} - \frac{2}{3}\frac{\partial u_{kq}}{\partial x_k}\delta_{ij}\right)\right] + F_{iq} + \rho_q \phi_q \left(F_g + F_{lift,q} + F_{vm,q}\right) + F_B - \nabla P_s \tag{4.2}$$

where ρ is density, ϕ is volumetric fraction, u is velocity vector, t is time, P is pressure, μ_{eff} is effective viscosity, δ_{ij} is the Kronecker delta ($\delta_{ij} = 1$ when $i = j$; $\delta_{ij} = 0$ when $i \neq j$), and i, j, k are the three coordinate directions; note that $q \equiv d$ denotes the dispersed phase, and $q \equiv c$ denotes the continuous phase (van Wachem and Almstedt, 2003). The gravitational force is denoted by F_g and the inter-phase drag force is denoted by F_{iq}. The lift force, $F_{lift,q}$, and the virtual mass force, $F_{vm,q}$, were initially omitted as they did not significantly affect the results as previously reported by others (Ljungqvist and Rasmuson, 2001; Sha et al., 2001). The

effects of these non-drag forces on the flow fields of both phases are discussed in more detail in section 4.7. The term F_B is the body force which includes the Coriolis and centrifugal forces induced by using the Multiple Frames Reference (MFR) approach, as discussed further below,

Inclusion of the particle-particle interaction force was attempted through the solid pressure term (∇P_s) for the solid phase in equation (4.2). As inter-particle interactions increase with solid concentration, the inclusion of this term has been suggested particularly for highly concentrated suspensions ($C > 0.2$) (Gidaspow, 1994),. This solid pressure term is, therefore, a function of the solid concentration thus

$$P_s = P_s\,(C_s) \tag{4.3}$$

and hence,

$$\nabla P_s = G(C_s)\nabla C_s \tag{4.4}$$

The function $G\,(C_s)$ is referred to as the Elasticity Modulus, and is expressed as follows,

$$G(C_s) = G_0 e^{E(C_s - C_{sm})} \tag{4.5}$$

where G_0 is the reference elasticity modulus, E is the compaction modulus, and C_{sm} is the maximum packing parameter (maximum solid loading). There are no generally accepted values for these parameters; however, the values G_0 = 1 Pa, E = 20 – 600, have been suggested by Bouillard et al. (1989) The maximum packing parameter C_{sm} was determined by Thomas (1965) as 0.625 for spherical particles.

The inclusion of particle-particle interactions through the solid pressure model which is available in ANSYS-CFX, however, led to bad convergence due to linearisation problems in the software, and it was not possible to achieve convergence with residual levels below 10^{-3}.

In fact, at higher concentrations better predictions were obtained without inclusion of the solid pressure model which was subsequently removed from the simulations.

The code is based on the finite-volume method, and the so-called "High Resolution Advection Scheme" was used to discretise the governing equations.

The inter-phase drag force, F_{iq}, was modelled via the drag coefficient, C_D, as:

$$F_{iq} = \frac{3}{4}\frac{\phi_d \rho_d}{d_p} C_D |u_d - u_c|(u_d - u_c) \tag{4.6}$$

C_D was estimated using the Gidaspow drag model for densely distributed solid particles (Gidaspow, 1994):

for $\phi_d \le 0.2$ $$C_D = \phi_c^{-1.65} \max\left(\frac{24}{\mathrm{Re}'}\left(1 + 0.15\,\mathrm{Re}'^{0.687}\right),\ 0.44\right) \tag{4.7}$$

and $\phi_d > 0.2$ $$F_{iq} = 150\frac{(1-\phi_c)^2 \mu_c}{\phi_c d_p^2} + \frac{7}{4}\frac{(1-\phi_c)\rho_c}{d_p}|u_d - u_c| \tag{4.8}$$

where the particle Reynolds number Re′ is defined as $\mathrm{Re}' = \phi_c \frac{\rho_c |u_d - u_c| d_p}{\mu_c}$, and μ_c is the viscosity of the continuous phase. The model has been found to be particularly useful for higher solid loadings in pipes (Eesa and Barigou, 2008; 2009) and in stirred vessels (Ochieng et al., 2008).

The above system of differential equations was closed by employing the well-known mixture $k-\varepsilon$ turbulence model where the two phases are assumed to share the same k and ε (Montante and Magelli, 2005; Špidla et al., 2005). The two-equation turbulence model consists of the differential transport equation (4.9) for the turbulent kinetic energy, k, and equation (4.10) for its dissipation rate, ε, thus:

$$\frac{\partial\left(\rho_q\phi_q k\right)}{\partial t}+\frac{\partial\left(\rho_q\phi_q u_{iq} k\right)}{\partial x_i}=\frac{\partial}{\partial x_i}\left(\phi_q\left(\mu_q+\frac{\mu_{qeff}}{\sigma_k}\right)\frac{\partial k}{\partial x_i}\right)+\rho_q\phi_q\left(P_k-\varepsilon\right) \tag{4.9}$$

$$\frac{\partial\left(\rho_q\phi_q \varepsilon\right)}{\partial t}+\frac{\partial\left(\rho_q\phi_q u_{iq} \varepsilon\right)}{\partial x_i}=\frac{\partial}{\partial x_i}\left(\phi_q\left(\mu_q+\frac{\mu_{qeff}}{\sigma_\varepsilon}\right)\frac{\partial \varepsilon}{\partial x_i}\right)+\rho_q\phi_q\frac{\varepsilon}{k}\left(C_1P_k-C_2\varepsilon\right) \tag{4.10}$$

where P_k is a generation term of turbulence; C_1=1.44, C_2=1.92, σ_k =1, and σ_ε =1.314.

The geometry used was an exact replica of the experimental mixing vessel. As pointed out above, the Multiple Reference Frames (MFR) method was used to take into account the interaction between the stationary baffles and the rotating impeller blades. Consequently, the computational domain was divided into two regions, as shown in Fig. 4.1: one domain containing all of the rotating elements (hub, blades and shaft), and the other containing the stationary parts (baffles, tank wall and base) separated by three interfaces, a vertical cylindrical interface at *r* = 94 mm, and two plane horizontal interfaces at *z* = 37 mm and 107 mm from the bottom of the tank. The interfaces were set sufficiently remote from the impeller to minimize the effects on the results.

A mesh independence study was conducted, and the predicted powers using different number of grids are shown in Table 4.4. There were no significant improvements in the impeller torque beyond a mesh consisting of 1, 065858 cells. However, as the computational cost was not prohibitive, an even finer mesh was used to achieve a good prediction of turbulent quantities; this aspect has been discussed by Deglon and Meyer (2006) and Coroneo et al. (2011). Thus, the computational grid used, consisted of 1,504, 928 non-uniformly distributed unstructured tetrahedral cells, as illustrated in Fig. 4.1. A denser mesh is used in the rotating domain for better accuracy, because this region is characterized by high velocity gradients. Inflated boundary layers were used on the bottom of the tank, walls, baffles, blades and shaft

to cover the high velocity gradients in these regions of no slip. Numerical convergence was assumed when the sum of all normalized residuals fell below 10^{-4} for all equations; but most residuals were in fact usually below 10^{-6} by the end of the simulation.

Table 4.4. Mesh independency study.

Number of grid	Torque (N m)	Power (W)
589,434	0.725	27.3
1,065858	0.693	26.1
1,504,928	0.690	26.0

4.4. Results and discussion

A detailed quantitative comparison between the CFD predictions and PEPT data was conducted at the positions depicted in Fig. 4.1. For both the liquid and solid phases, the azimuthally-averaged distributions of the local velocity components (u_z , u_r , u_θ) were compared:

(i) axially along two radial positions: $r = 0.53R$, close to the tip of the impeller; and $r = 0.95R$, close to the tank wall; and

(ii) radially along five axial positions: $z = 0.016H$, close to the base of the vessel; $z = 0.08H$, approximately halfway between the base and the lower edge of the impeller; $z = 0.17H$, just under the lower edge of the impeller; $z = 0.33H$, just above the upper edge of the impeller; and $z = 0.83H$, in the upper part of the vessel. All the velocity plots presented have been normalized by the impeller tip speed ($u_{tip} = \pi DN$).

The azimuthally-averaged spatial distributions of the local solid concentration were also resolved both by PEPT and CFD, and compared at these two radial and five axial locations. The solid concentration profiles presented have been normalized by the overall mean volume solid concentration (C).

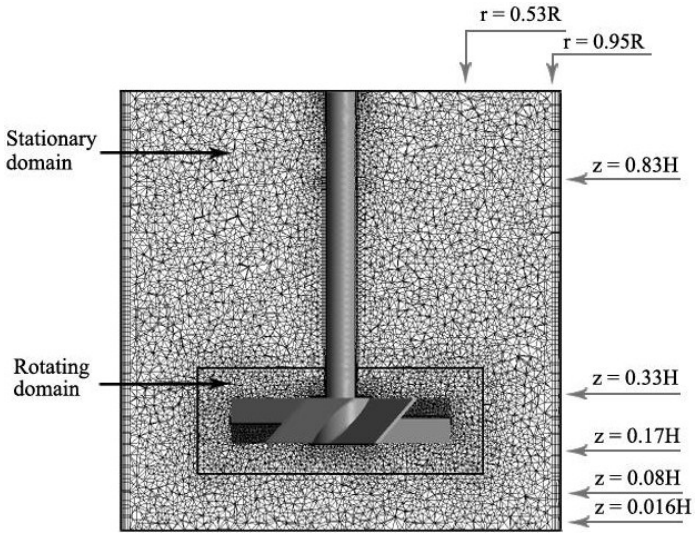

Figure 4.1. Computational grid section in the 45° plane between two baffles.

4.4.1. Velocity distributions

The experimental and numerically predicted velocity distributions for the liquid phase and solid phase are compared in Fig. 4.2 and Fig. 4.3, respectively, for the 1 mm particles at the solid concentration of 5.2 wt%. It can be readily seen that all three velocity components for both phases are very well predicted by CFD as the agreement with PEPT is overall excellent. Considering the radial profiles of the liquid in Fig. 4.2, the maximum discrepancy between the two sets of data is ~ $0.1\,u_{tip}$ and concerns u_z near the free surface (z = 0.83H). Such a significant error could be attributed to the small free vortex forming near the shaft which is not taken into account as the simulation assumes a flat free surface across the whole section of the vessel. There is also a similar underestimation in u_r near the base of the vessel which may be due to the overestimation of the amount of solids rolling along the bottom, as discussed later.

The vertical liquid velocity profiles are equally well predicted except for the localised errors in u_r and u_θ near the free surface, as discussed above. The axial profiles of u_z and u_r at r = 0.53R exhibit approximately equal local maxima of ~ $\left|0.30u_{tip}\right|$ in the impeller discharge at the level ~ 0.17H just below the impeller, which is consistent with the performance of a down-pumping mixed flow impeller. The maximum u_θ is significantly smaller (~ $0.20\,u_{tip}$) and occurs at the same position.

The tangential component u_θ reduces to zero everywhere at r = 0.95R where the effect of the baffles is probably close to its maximum. Here, the radial component u_r is also zero everywhere except near the base where the liquid is forced to follow the upward jet of the flow loop, as shown in Fig. 4.4 which illustrates the general flow pattern created by the down-pumping PBT. Because of the single flow loop generated, all of the fluid has to flow upwards near the wall and, thus, the entire u_z profile is positive and exhibits a local maximum (~ $0.40\,u_{tip}$) at r = 0.95R which is significantly greater than the maximum in the impeller discharge.

Similar observations to those noted above for the liquid phase can also be made about the solid phase, concerning the high accuracy of the CFD predictions as well as the salient features exhibited by the velocity profiles, as show in Fig. 4.3. Comparing the local maximum of the axial velocity component of the solids to that of the liquid near the impeller tip at r = 0.53R, the solids are discharged downwards at a significantly higher velocity than the liquid (~ $0.40\,u_{tip}$ compared to ~ $0.30\,u_{tip}$).

The radial velocity distributions of both phases are fairly flat in the upper parts of the vessel, but exhibit sharp variations in the impeller region, especially the u_z component. The maximum velocities in the vessel occur just below the impeller along the plane z/H = 0.17. On the basis of the PEPT measurements, in the range 5.2 wt% – 20 wt% solids, the maximum total velocity u for both the liquid and solid is ~ $0.50\,u_{tip}$ and occurs close to the impeller tip at r/R = 0.47 on this plane, and the agreement with CFD is excellent (see Fig. 4.2 and Fig. 4.3).

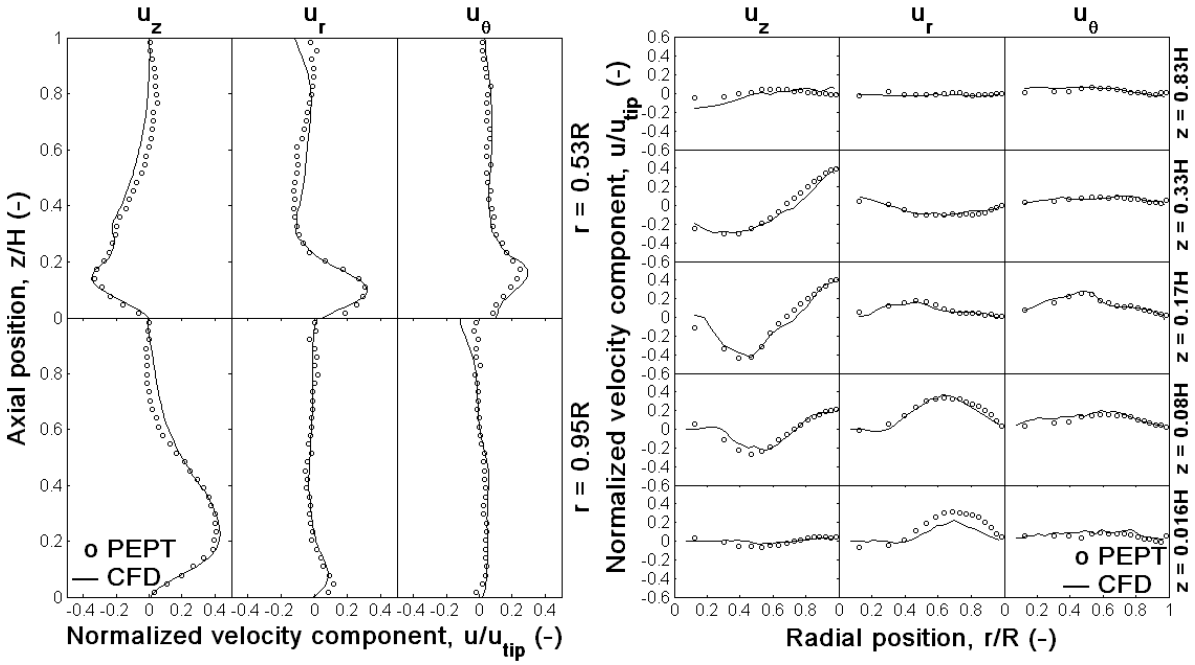

Figure 4.2. Azimuthally-averaged distributions of the velocity components of the liquid phase in suspension at N_{js} – CFD and PEPT compared: d_p = 1 mm; X = 5.2 wt%; N_{js} = 360 rpm.

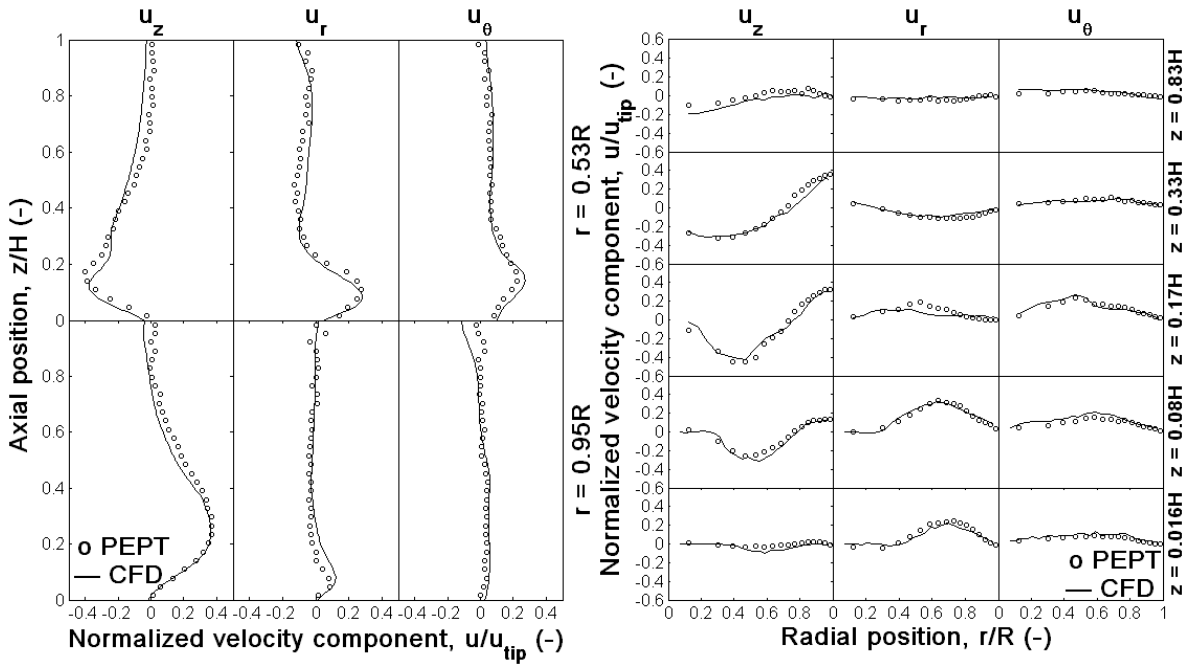

Figure 4.3. Azimuthally-averaged distributions of the velocity components of the solid phase in suspension at N_{js} – CFD and PEPT compared: d_p = 1 mm; X = 5.2 wt%; N_{js} = 360 rpm.

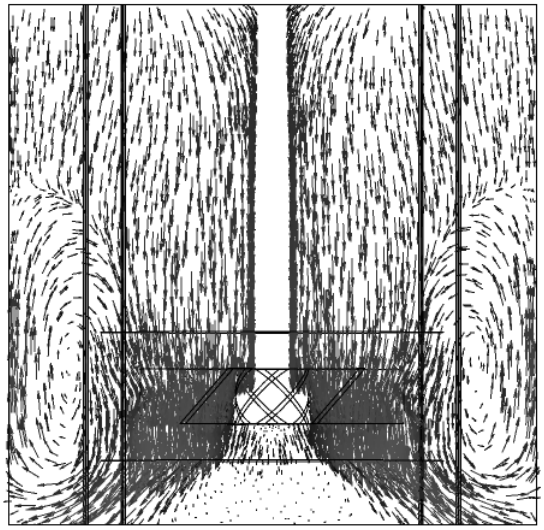

Figure 4.4. Liquid flow pattern generated by a down-pumping PBT in a solid-liquid suspension.

Near the wall, the upward moving particles lag the upward moving fluid by a significant margin as reported by other workers (Guiraud et al., 1997; Ljungqvist and Rasmuson, 2001;

2004); the maximum u_z being ~ $0.40\,u_{tip}$ for the fluid and ~ $0.33\,u_{tip}$ for the solid. Near the shaft, however, the falling particles move slightly faster (lead) than the fluid as reported by other researchers (Pianko-Oprych et al., 2009; Ljungqvist and Rasmuson, 2001; 2004).

At the greater solid concentration of 20 wt%, the accuracy of the CFD-predicted velocity fields remains high for both the liquid and solid phases, as shown in Fig. 4.5 and Fig. 4.6, respectively. The velocity profiles are qualitatively similar to those obtained at 5.2 wt% solids and display both qualitatively and quantitatively essentially the same features discussed above.

Increasing the rotational speed gradually above N_{js} alters the state of the suspension significantly. Sample results for $N = 2N_{js}$ corresponding to a nearly homogenous suspension are displayed in Fig. 4.7, and the CFD predictions remain excellent overall.

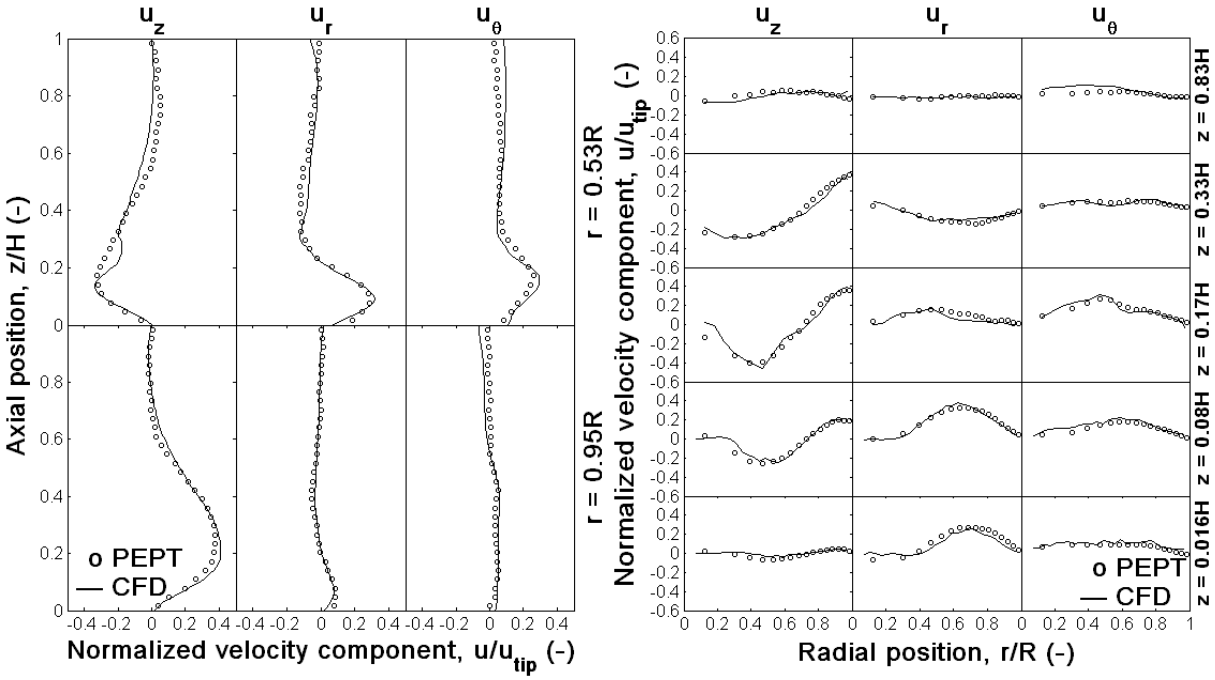

Figure 4.5. Azimuthally-averaged distributions of the velocity components of the liquid phase in suspension at N_{js} – CFD and PEPT compared: d_p = 1 mm; X = 20 wt%; N_{js} = 490 rpm.

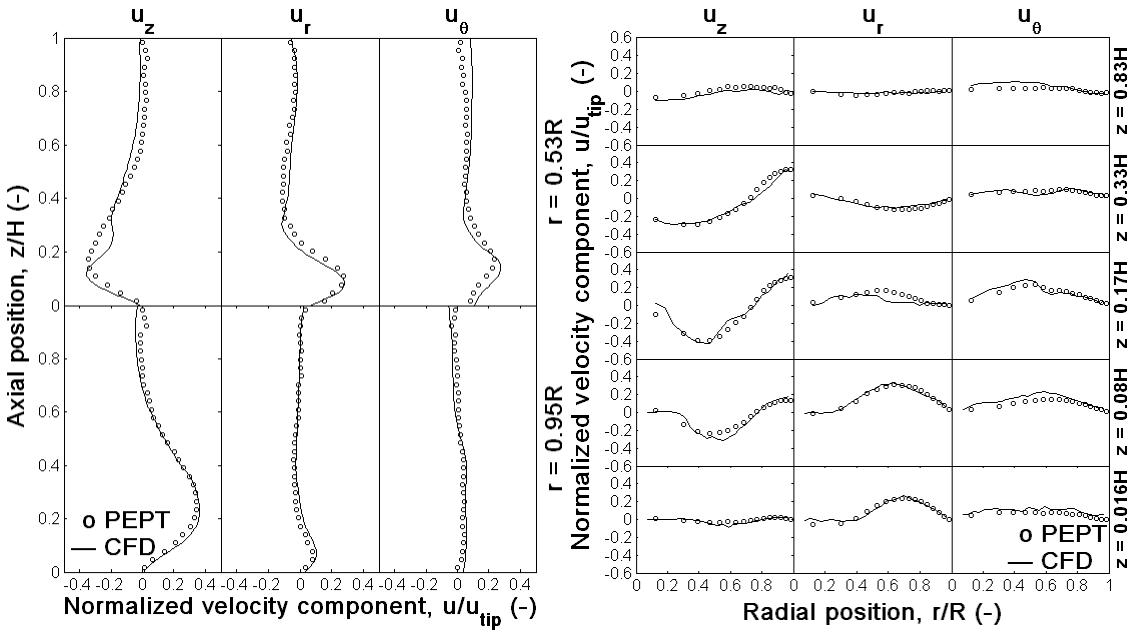

Figure 4.6. Azimuthally-averaged distributions of the velocity components of the solid phase in suspension at N_{js} – CFD and PEPT compared: d_p = 1 mm; X = 20 wt%; N_{js} = 490 rpm.

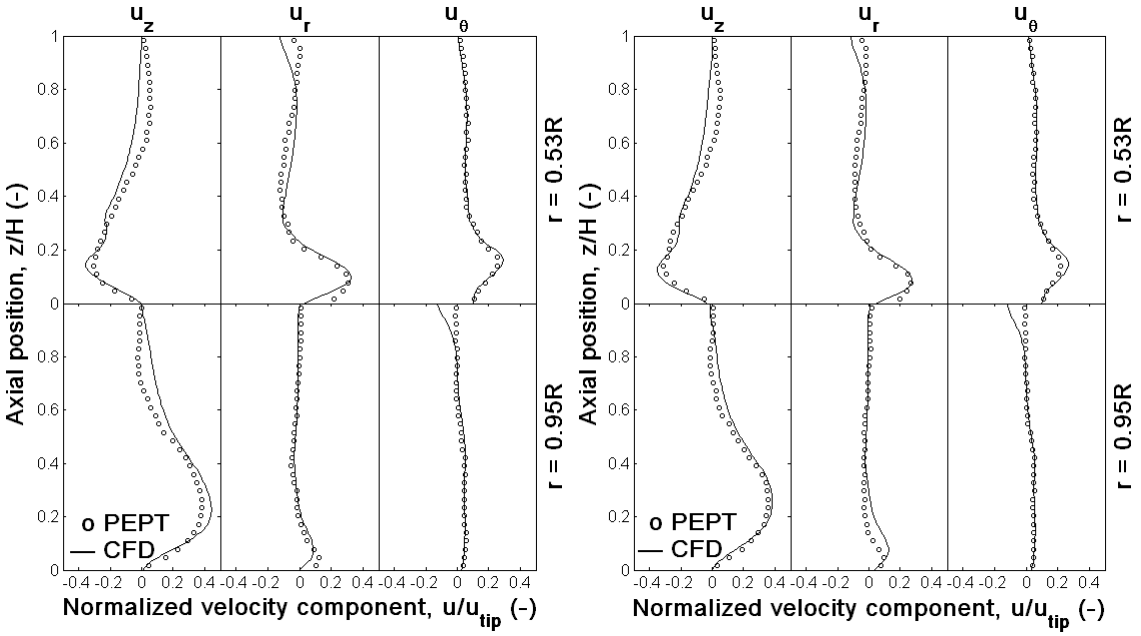

Liquid phase **Solid phase**

Figure 4.7. Azimuthally-averaged distributions of the velocity components of the liquid and solid phase in suspension at $N = 2N_{js}$ – CFD and PEPT compared: d_p = 1 mm; X = 5.2 wt%; N_{js} = 360 rpm.

4.4.2. Particle-fluid slip

Information on particle-fluid slip velocity is of significant importance to processing applications involving the inter-phase transfer of heat and mass. Usually the free terminal settling velocity of the particle is taken in practice as the mean slip velocity in stirred vessel, however, the local slip velocities vary vastly throughout stirred vessel (Atiemo-Obeng et al., 2004).

In 3-D the magnitude of the local time-average slip velocity vector can be estimated for the solid phase using PEPT (or CFD) data, thus:

$$s = \sqrt{\left(u_\theta^{(L)} - u_\theta^{(S)}\right)^2 + \left(u_r^{(L)} - u_r^{(S)}\right)^2 + \left(u_z^{(L)} - u_z^{(S)}\right)^2} \tag{4.11}$$

where the superscripts (L) and (S) refer to the liquid and solid phase, respectively. It should be noted, however, that whilst the estimations yielded by this method based on local velocity measurements by PEPT, or CFD predictions, are likely to be much more realistic and reliable than traditional practice suggests, it is currently difficult to be certain about their absolute accuracy given that information is missing on possible added slip arising from particle spin and turbulent velocity fluctuations of the two phases (including whether in or out of phase).

Spatial distributions of the normalised total local time-average slip velocity, s, obtained on the basis of PEPT measurements at $N = N_{js}$ and estimated using equation (4.11) are depicted in Fig. 4.8. The individual slip components in the r, z, and θ directions are also displayed. There are wide variations in the spatial distribution of s. The largest total slip velocities are observed in the vicinity of the impeller and are of the order of $\sim 0.10\,u_{tip}$ which are rather considerable because of the significant inertia of the particles. Considering the individual components of the slip velocity vector, by far the largest slip occurs in the z direction.

Nevertheless, some significant slip (~ $0.06\,u_{tip}$) is also observed in the r and θ directions in the impeller discharge region.

Compared to the measured particle terminal velocity of the 1 mm glass beads, the volume-average of the absolute values of s in the stirred vessel is about 30% smaller up to 20 wt%. Local values of s, however, vary from cell to cell and can be much smaller or much larger than the particle terminal velocity, and can be positive or negative. Guiraud et al. (1997) also reported slip velocities for 253 μm glass particles in a dilute suspension (~ 0.5 vol%) which were much smaller than the particle settling velocity.

Increasing the impeller speed much above N_{js}, reduces the normalised slip velocities significantly, as shown in Fig. 4.8. The volume-average slip based on the total velocity u drops by ~ 25% when N reaches $2N_{js}$. Such a reduction is essentially wholly related to slip reductions in the axial direction given that particles are better suspended in a nearly homogeneous mixture. Note, however, that the absolute slip velocities are more or less unaffected by the increase in N.

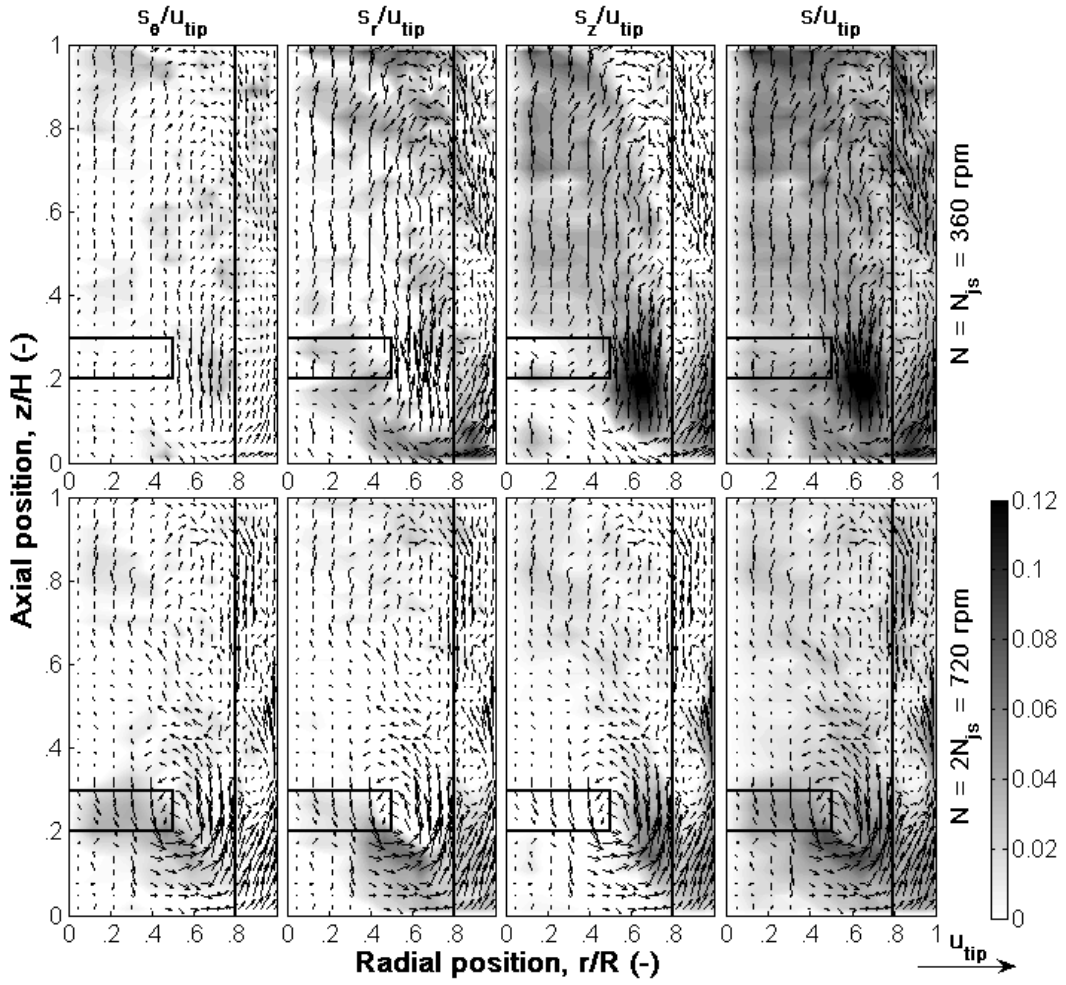

Figure 4.8. Azimuthally-averaged maps of time-averaged slip velocity from PEPT measurements at N_{js} and $N = 2N_{js}$: d_p = 1 mm; X = 5.2 wt%.

4.4.3. Flow number

Recently, Guida et al. (2010) extended the use of the usual definition of the flow number used to estimate the pumping effectiveness of impellers in single-phase systems to a two-phase problem. The flow number is computed using the following expression for the liquid phase:

$$Fl^{(L)} = \frac{Q^{(L)}}{ND^3} = \frac{1}{ND^3} \int_{PBT} (1-c) u_z^{(L)} dS \tag{4.12}$$

and for the solid phase:

$$Fl^{(S)} = \frac{Q^{(S)}}{ND^3} = \frac{1}{ND^3} \int_{PBT} cu_z^{(S)} dS \tag{4.13}$$

For each phase, $Q^{(L)}$ or $Q^{(S)}$ is calculated by integrating along the lower horizontal edge of the impeller blade the axial velocity profile weighted by the local phase volume concentration, i.e. by c for the solid phase and by $(1–c)$ for the liquid phase.

The sum of $Q^{(L)}$ and $Q^{(S)}$ represents the total volumetric discharge, Q, and introducing the two-phase flow number, Fl, it follows that:

$$Fl = \frac{Q}{ND^3} = \frac{Q^L + Q^S}{ND^3} = Fl^{(L)} + Fl^{(S)} \tag{4.14}$$

The experimental results including those reported by Guida et al. (2010) for suspensions of particles of 3 mm diameter in water at X = 5.2 - 40 wt%, and at their 'just-suspended' speed N_{js}, and the computational results are presented in Table 4.5. At low solid concentration, the solid flow number $Fl^{(S)}$ is only a small fraction of the liquid flow number $Fl^{(L)}$, but it increases proportionally to C. This is of course expected because in the calculation of the flow number, as pointed out above, the flowrate of each phase is weighted by its local volume concentration (see Eqs. (4.12) and (4.13)).

At low to moderate X values, CFD seriously underpredicts $Fl^{(S)}$ compared to PEPT probably because of its very low magnitude which makes it more prone to numerical error. Some of the discrepancy between $Fl^{(s)}_{PEPT}$ and $Fl^{(s)}_{CFD}$ is caused by the error in predicting the local particle concentration. At higher X values, the predictions improve greatly and, in fact, become very accurate, being only a few percent different from the experimental values. On the other hand, the predictions of $Fl^{(L)}$ are very good throughout. There are no published flow number data in solid-liquid suspensions, but in the absence of particles (X = 0) the single-

phase flow number obtained from PEPT ($Fl^{(L)} = 0.87$) agrees very well with published data for a 6-blade pitched turbine (e.g., $Fl^{(L)} = 0.86$ in Gabriele et al. (2009); and $Fl^{(L)} = 0.88$ in Hockey and Nouri (1996). Overall, therefore, because of the relatively large dominance of $Fl^{(L)}$ the predictions of the two-phase flow number Fl are also good at the lower solid concentrations (on average ~ 10-15% error); at the higher concentration, the error is ~ 5% which can be considered very good; see Table 4.5.

Table 4.5. Comparison of CFD predictions of flow number with PEPT measurements.

X (wt%)	N (rpm)	$Fl^{(S)}_{PEPT}$	$Fl^{(S)}_{CFD}$	$Fl^{(L)}_{PEPT}$	$Fl^{(L)}_{CFD}$	Fl_{PEPT}	Fl_{CFD}	$\frac{Fl_{CFD} - Fl_{PEPT}}{Fl_{PEPT}} \times 100\%$
d_p = 1 mm								
0	330	–	–	0.870	0.780	0.870*	0.780	-10.3
5.2	N_{js} = 360	0.027	0.013	0.886	0.770	0.913	0.783	-14.2
	450	0.025	0.012	0.911	0.779	0.936	0.791	-15.5
	540	0.024	0.013	0.877	0.777	0.901	0.790	-12.3
	720	0.020	0.015	0.876	0.772	0.896	0.787	-12.2
20	N_{js} = 490	0.093	0.075	0.760	0.701	0.853	0.776	-9.0
	613	0.091	0.070	0.773	0.706	0.863	0.776	-10.2
d_p = 3 mm								
5.2	N_{js} = 360	0.025*	0.031	0.878*	0.773	0.903*	0.804	-11.0
	450	0.025	0.009	0.858	0.770	0.883	0.779	-11.8
	540	0.022	0.009	0.853	0.779	0.875	0.788	-10.0
	720	0.020	0.014	–	0.773	–	0.787	–
10.6	N_{js} = 410	0.057*	0.033	0.851*	0.759	0.908*	0.792	-12.8
20	N_{js} = 490	0.082*	0.079	0.737*	0.727	0.819*	0.806	-1.6
	613	0.079	0.066	0.759	0.724	0.838	0.790	-5.7
	735	0.072	0.061	0.742	0.728	0.814	0.789	-3.1

*PEPT measurements reported by Guida et al. (2010) .

At zero solid concentration (i.e. single-phase fluid) Fl is ~ 0.87 and CFD underpredicts this value by ~ 10% compared to PEPT. The two-phase flow number, Fl, remains approximately constant at ~ 0.90 at low to moderate solid loadings up to ~ 10.6 wt%, however, reduces significantly at solid concentrations above ~ 10.6 wt%. This is because the compensation by

the increase in $Fl^{(S)}$ for the small reduction in $Fl^{(L)}$ at low at low to moderate fails to counterweight the steep reduction in $Fl^{(L)}$ at higher solid concentrations. For example, for d_p = 3 mm at N_{js}, this effect amounts to a reduction of ~ 10% when X rises from 10.6 wt% to 20 wt% and ~ 18% at 40 wt%, as reported in the experimental studies (Guida et al., 2010); for the same system a reduction of up to ~ 40 wt% was reported with the PBT pumping upwards.

4.4.4. Solid distribution

The azimuthally-averaged axial and radial distributions of the solid phase at N_{js} are presented in Fig. 4.9. Under this 'just-suspended' condition, the maximum solid area is exposed to the fluid but there are usually considerable concentration gradients in the vessel and, depending on the type of particles, there may be a significant region of clear liquid near the top. In fact, the axial profiles in Fig. 4.9 show that the solid concentration above the impeller reduces gradually upwards until it reaches zero close to the surface; for example, at z = 0.83H the concentration has dropped to about 0.45C. Overall, considering the axial solid distribution, there is a good agreement between the PEPT measurements and the CFD predictions, except near the base of the vessel.

Radially, the solids are nearly uniformly distributed except in the central region underneath the impeller where there is a clear mound of accumulated solids (Fig. 4.9), with PEPT measuring concentrations which are several times greater than the mean concentration. The worst CFD predictions occur close to the base (z = 0.016H and 0.08H) where the computed values exceed the experimental ones by several folds. This is to be expected because the flow near the base is very complex and the mechanics of particle settling and particle lift-off and resuspension are not implemented in the CFD model. However, even though the local solid

fraction is not well predicted in this region, it is important to note that the local velocities for both phases are very well predicted, as discussed above (see Figs. 4.2, 4.3, 4.5, 4.6).

The radial solid distributions just above ($z = 0.33H$) and just below ($z = 0.17H$) the impeller are also seriously underpredicted by CFD (a factor of ~ 2). In the upper region, away from the impeller, however, the agreement improves substantially and tends to be very good. It is noteworthy that the predictions around the impeller and close to the base improve significantly with an increase in mean solid concentration, as shown in Fig. 4.9. Similar observations were also made in the case of the 3 mm particle suspensions. As X increases, the assumption of a continuous solid phase built in the Eulerian model becomes less severe, which might explain some of the improvement in the CFD predictions.

Furthermore, the Gidaspow drag model used in the simulations was previously found to be particularly useful at higher solid loadings, and its improved performance may have been the main reason behind the better accuracy of prediction at the higher solid concentrations (Ochieng et al, 2008; Easa and Barigou, 2008 and 2009). On the other hand, however, as solid concentration increases, particle-particle collisions are expected to increase which trends to complicated the physics of the flow and, hence, it is difficult at present to suggest a completely satisfactory explanation.

At impeller speeds above N_{js}, as discussed in more detail below, the uniformity of the suspension improves significantly and the CFD predictions of solid distribution improve somewhat with it, notably near the base, as shown in Fig. 4.10 and Fig. 4.11 for the 1 mm and 3 mm systems, respectively. However, the still relatively high solid presence at the bottom of the vessel continues to be a challenge for the numerical code to provide an accurate estimation of the local solid concentration.

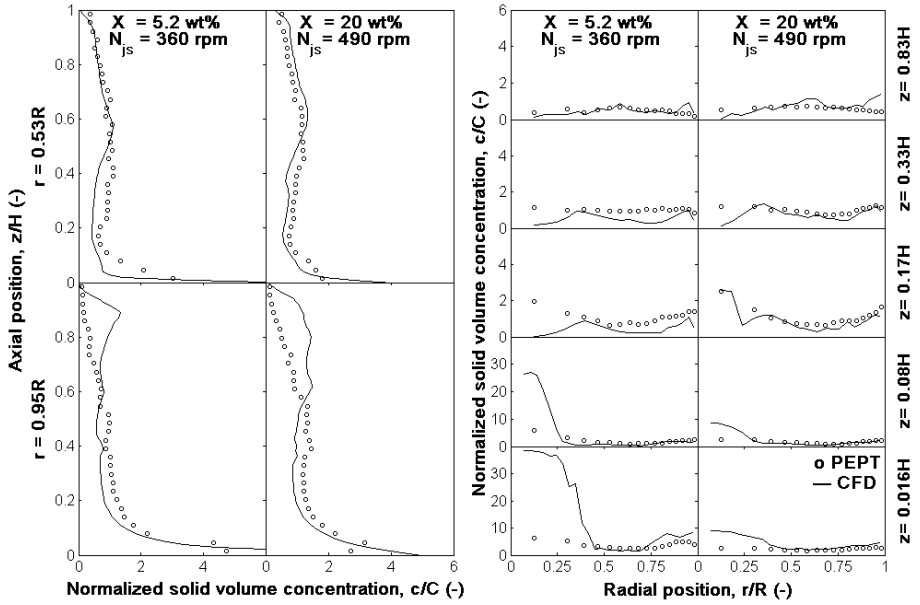

Figure 4.9. Azimuthally-averaged distributions of solid volume concentration in suspension at N_{js} (d_p = 1 mm).

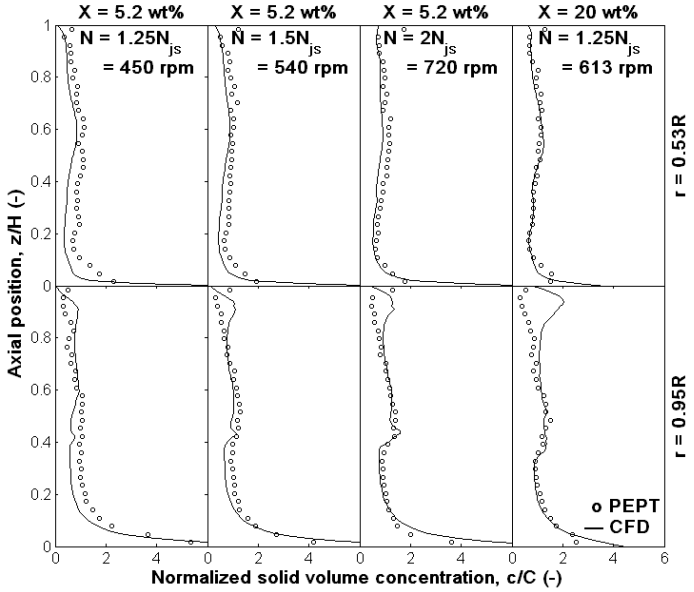

Figure 4.10. Azimuthally-averaged distributions of solid volume concentration in suspension at $N > N_{js}$ (d_p = 1 mm).

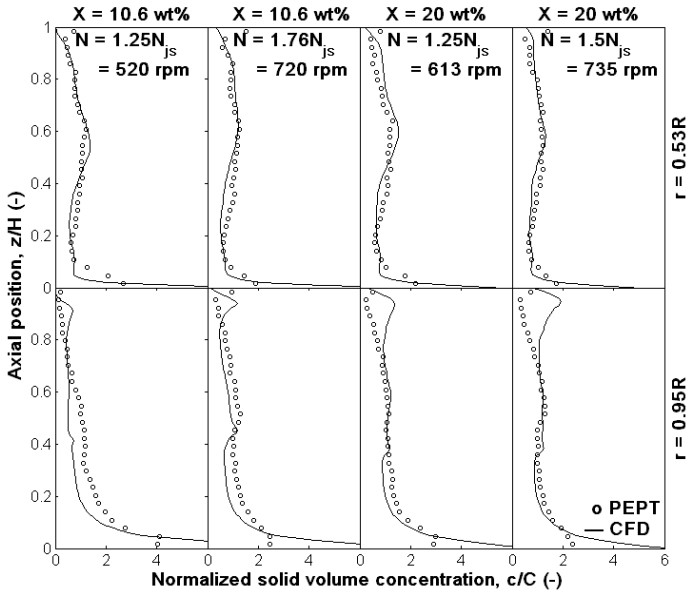

Figure 4.11. Azimuthally-averaged distributions of solid volume concentration in suspension at $N > N_{js}$ (d_p = 3 mm).

4.4.5. Uniformity of suspension

The degree of suspension uniformity can be assessed by a global uniformity index, ξ, defined, thus:

$$\xi = \frac{1}{\sigma^2 + 1} = \frac{1}{\frac{1}{N_C}\sum_{i=1}^{N_C}\left(\frac{c_i - C}{C}\right)^2 + 1} \tag{4.15}$$

where N_c is the total number of cells in the PEPT measurement (or CFD computational) grid and i is the cell number (Guida et al., 2009; 2010). ξ increases with the increase in the degree of uniformity of solid distribution within the vessel volume, and when $\xi = 1$ (i.e. $\sigma^2 = 0$) the solids are uniformly distributed within the vessel volume, i.e. the local solid concentration everywhere is equal to the average concentration in the vessel.

Values of the index ξ are reported in Fig. 4.12 for both systems of particles investigated (d_p = 1 and 3 mm). The results show that initially ξ increases sharply as N increases above N_{js}, but

the curve flattens out at high speeds and it becomes increasingly difficult to exceed $\xi \sim 0.9$. Even though N_{js} is the same for both particle sizes, the degree of uniformity is significantly better for the 1 mm particles at the same N throughout, as these are lighter, but both systems converge towards the same state of homogeneity ($\xi \sim 0.9$) as N approaches $2N_{js}$. The better homogeneity of the smaller particles is achieved at the same power dissipation as the larger 3 mm particles, as shown in Fig. 4.12. For both particle systems, the increased homogeneity achieved above N_{js} is obtained only at a huge power expense; it takes an increase of approximately seven folds in P/V to attain $\xi \sim 0.9$.

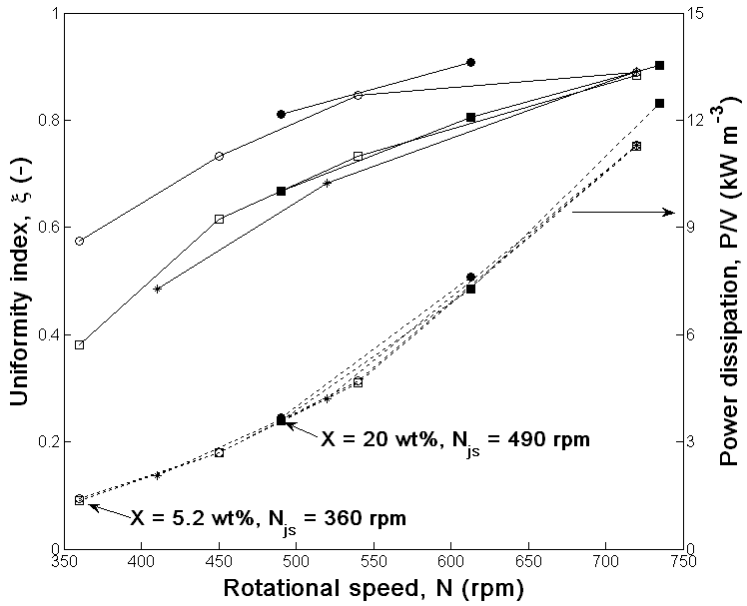

Figure 4.12. Variation of uniformity index and volumetric power consumption as a function of impeller speed for all conditions investigated (see Table 4.3):

—○— ξ; ····○···· P/V: d_p = 1 mm; X = 5.2 wt%;

—●— ξ; ····●···· P/V: d_p = 1 mm; X = 20 wt%;

—□— ξ; ····□···· P/V: d_p = 3 mm; X = 5.2 wt%;

—*— ξ; ····*···· P/V: d_p = 3 mm; X = 10.6 wt%;

—■— ξ; ····■···· P/V: d_p = 3 mm; X = 20 wt%.

It can also be deduced from the data in Fig. 4.12 that for a given particle diameter, ξ increases as a function of mean solid concentration when the suspensions are considered at the same hydrodynamic mixing regime, i.e. at their N_{js} speed or the same multiple of their N_{js}.

4.4.6. Effects of solids on liquid flow field

A number of earlier studies have reported large drop in the average liquid velocities in the presence of particles (Nouri and Whitelaw, 1992; Montante and Lee, 2000; Virdung and Rasmuson, 2003; Micheletti and Yianneskis, 2004). Some other studies, however, have reported little effect on the average velocity (Guiraud et al., 1997; Ljungqvist and Rasmuson, 2001; 2004; Unadkat et al., 2009; Pianko-Oprych et al., 2009; Gabriele et al., 2011). Where both the liquid and solid velocities have been measured, studies have been restricted to dilute suspensions because of the limits on transparency suffered by the laser techniques used.

In this study, the difference in liquid velocity with and without solids present is captured in Fig. 4.13 for $X = 20$ wt%. The axial and radial velocity profiles of the liquid with and without particles exhibit essentially the same trends but with some significant localised differences. With up to 10.6 wt% of solids, the effect on the liquid velocity field was minimal. Adding more solids, led to some significant reductions in liquid velocity near the impeller and along the wall of the vessel, affecting mainly the axial component u_z, as depicted in Fig. 4.13. The overall picture was similar at $N > N_{js}$.

Interestingly, the maximum total velocity for liquid being agitated alone is $\sim 0.55\,u_{tip}$ and occurs at $r/R = 0.47$ and $z/H = 0.17$. The presence of solids at all concentrations studied had no significant effect on this velocity or its position for both the 1 mm and 3 mm particle systems.

The effects of the solids presence on other parameters such as turbulent kinetic energy (TKE), energy dissipation rate (ε) and Kolmogorov length scale (λ) are also worthy of consideration. Some authors reported considerable suppression of turbulence due to the addition of a small amount of solids (0.02–2 vol%); for example, Micheletti and Yianneskis (2004) reported -50% in all areas of the vessel, and Unadkat et al. (2009) reported -21% in the discharge stream.

These turbulence quantities cannot be accurately obtained from the experimental PEPT data, but they can be estimated on the basis of the CFD results. Table 4.6 gives the volume-average values in the vessel $\bar{\varepsilon}$, $\bar{\lambda}$, and $\overline{TKE}$ for all cases investigated at N_{js} and above.

Table 4.6. Effects of solids presence on volume-average turbulent properties of the liquid phase.

		X = 0 wt%	X = 5.2 wt%		X = 10.6 wt%	X = 20 wt%	
	N(rpm)		d_p = 1 mm	d_p = 3 mm	d_p = 3 mm	d_p = 1 mm	d_p = 3 mm
$\bar{\varepsilon}$ (m^2 s^{-3})	N_{js} = 360	0.740	0.725	0.743	-	-	-
	N_{js} = 410	1.14	-	-	0.987	-	-
	N_{js} = 490	1.978	-	-	-	1.669	1.550
	720	6.46	6.03	6.05	-		
$\overline{TKE}$ (J kg^{-1})	N_{js} = 360	0.056	0.060	0.0626	-	-	-
	N_{js} = 410	0.077	-	-	0.072	-	-
	N_{js} =490	0.112	-	-	-	0.105	0.093
	720	0.260	0.251		-	0.253	-
$\bar{\lambda}$ (μm)	N_{js} = 360	32.30	32.30	32.20	-	-	-
	N_{js} = 410	29.2	-	-	30.4	-	-
	N_{js} = 490	25.30	-	-	-	26.40	26.90
	720	18.8	18.9	19.0	-		

At N_{js}, the 3-D distributions of TKE and λ do not seem to be significantly affected by the addition of solids at the concentrations used in this work. On the other hand, ε diminishes with increasing X. As shown in Table 4.6, for d_p = 1 mm, $\bar{\varepsilon}$ remains approximately the same at 5.2 wt% and drops by ~ 16% at 20 wt%. For d_p = 3 mm, $\bar{\varepsilon}$ also does not change at 5.2 wt%

and drops by ~ 15.5% at 10.6 wt% and by ~ 22% at 20 wt%. These effects can also be discerned in Fig. 4.14 by scrutinising the contours of ε in the 45 degree plane between two baffles.

Whilst these observations are generally in line with the previously reported experimental measurements of other authors such as Micheletti and Yianneskis (2004) and Unadkat et al. (2009), it should be noted that the turbulence data here are based on CFD calculations which have not been directly validated.

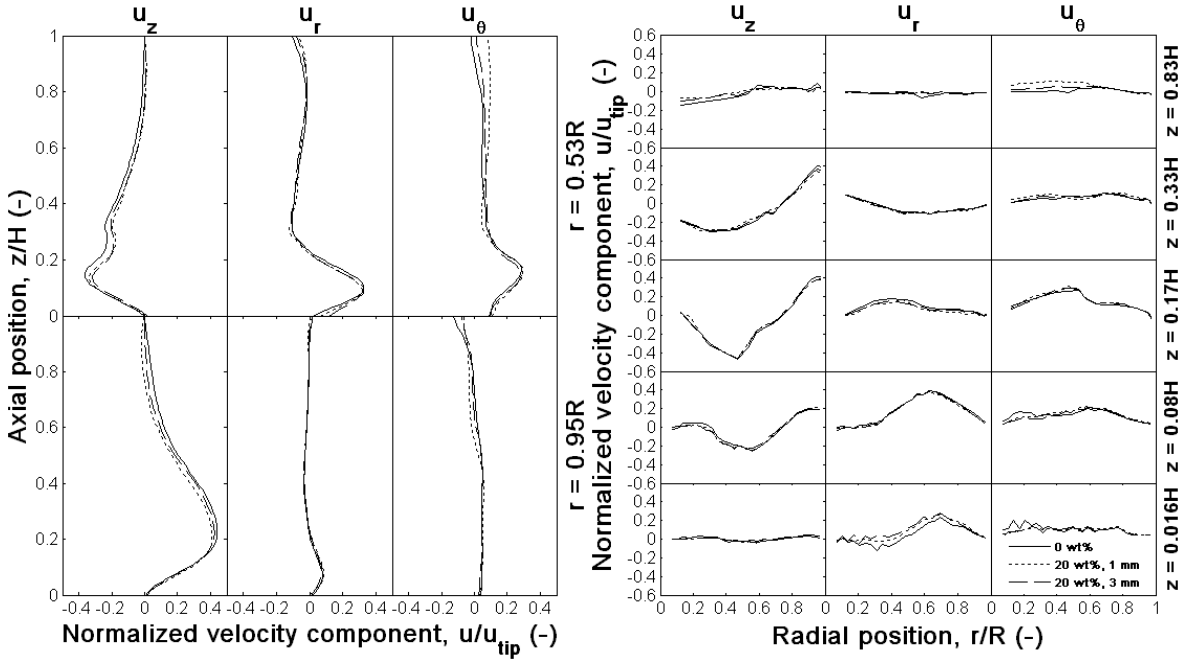

Figure 4.13. Effects of solids presence on the azimuthally-averaged velocity distributions of the liquid phase at N_{js}: d_p = 1 mm, 3 mm; X = 20 wt%; N_{js} = 490 rpm.

Finally, another parameter worthy of consideration is the characteristic integral length scale ℓ which is usually assumed to be equal to $W/2$, i.e. half the impeller blade width (Kresta and Wood, 1993). In these experiments ℓ would be 15 mm, so that $d_p / \ell = 0.067$ for the 1 mm particles and 0.20 for the 3 mm particles. It has been postulated (Gore and Crowe, 1991) that if $d_p / \ell < 0.1$ turbulence is suppressed and if $d_p / \ell > 0.1$ turbulence is enhanced, which

would suggest in this case that turbulence would be suppressed by the 1 mm particles and enhanced by the 3 mm particles. This argument does not agree with our findings as has also been reported by other workers (see for example, Unadkat et al., 2009).

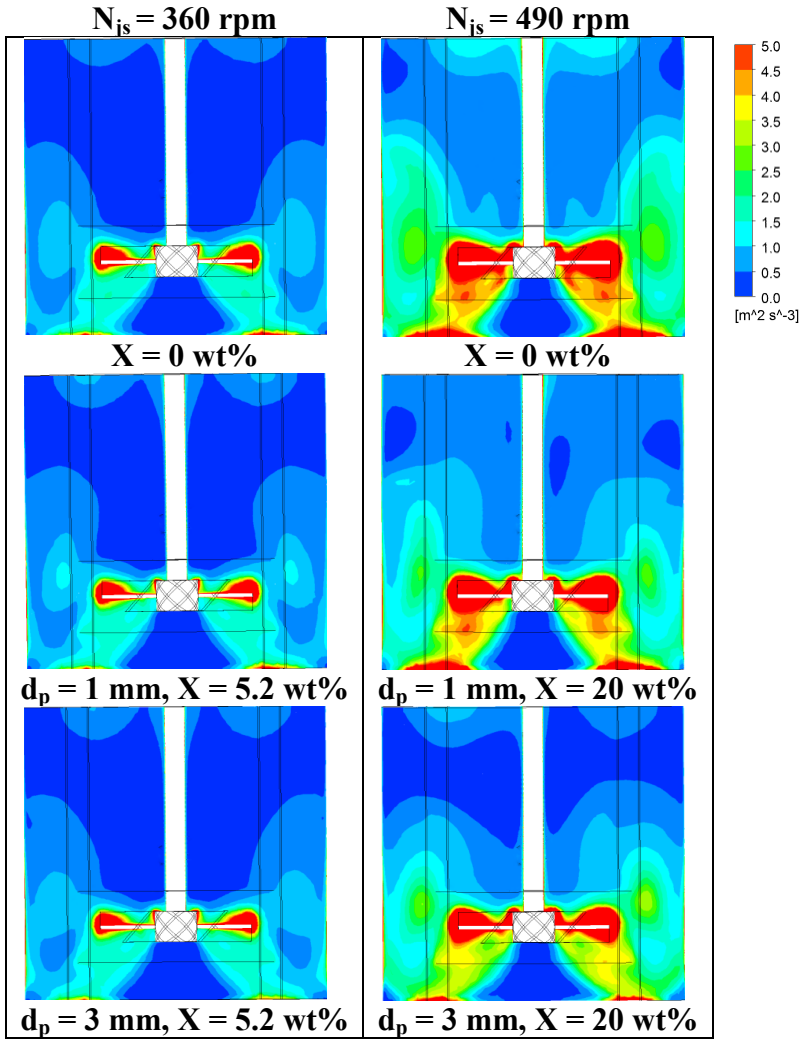

Figure 4.14. Contours of energy dissipation rate ε in the 45° plane between two baffles.

4.5. Effect of drag model

In comparison with particle settling velocities in still fluid, particle settling velocities in the prevailing turbulence in stirred vessels have been found to be significantly smaller in a number of studies, as reviewed by Brucato et al. (1998). The drag force coefficient $C_{D,still}$ Eq.

(4.16), derived from particle settling in still fluid has been reported to significantly overestimate the sedimentation of particles in turbulent fields (Brucato et al., 1998; Montante and Magelli, 2005). The drag coefficient has been found to be strongly affected by the free stream turbulence which has been reported to connect closely with the ratio between the particle diameter and the Kolmogoroff turbulent length scale, i.e. $\frac{d_p}{\lambda}$, therefore, is recommended to be included in the drag models in the CFD modelling of turbulent solid-liquid suspensions in stirred vessels. Some researchers have proposed the drag models that take into account the ratio, $\frac{d_p}{\lambda}$ in the correction factor to $C_{D,still}$.

The Brucato model, Eq. (4.17) (Brucato et al., 1998) was developed based on the experimental data of a Couette-Taylor flow field. Pinelli et al. (2001) proposed a correlation, Eq. (4.19) with the experimental settling velocities in a stirred tank of high aspect ratio agitated by multiple impellers. The proportionality constant in the modified Brucato model (Khopkar et al., 2006), Eq. (4.18) is 10 times smaller than that in the Brucato model, as suggested in their study that this proportionality constant should reduce with the increase in particle size and mean solid concentration in the systems.

$$C_{D,still} = \frac{24}{\mathrm{Re}}\left(1 + 0.15 \times \mathrm{Re}^{0.687}\right) \tag{4.16}$$

$$C_{D,turbl} = C_{D,still}\left[1 + 8.76 \times 10^{-4}\left(\frac{d_p}{\lambda}\right)^3\right] \tag{4.17}$$

$$C_{D,turbl} = C_{D,still}\left[1 + 8.76 \times 10^{-5}\left(\frac{d_p}{\lambda}\right)^3\right] \tag{4.18}$$

$$C_{D,turb2} = C_{D,still}\left[0.4\tanh\left(16\frac{\lambda}{d_p}-1\right)+0.6\right]^{-2} \tag{4.19}$$

However, these drag models were proposed based on the experimental data for very dilute systems (< 1 vol%), and have not been assessed for modelling the dense solid-liquid suspensions.

In this section, the CFD predicted flow fields of two phases and the solid distributions in the dense solid-liquid suspensions in stirred vessel using the modified Brucato model (equation (4.18)), Pinelli model (equation (4.19)) and the Gidaspow model (Eqs (4.7), (4.8)), were compared, and also validated with the reliable PEPT measurements.

Concerning the wide variations in the spatial distributions of turbulence throughout the stirred tank, the numerical local dissipation rate ε_{loc} was used to calculate the Kolmogoroff turbulent length scale λ, as defined by, $\lambda = \left(\frac{\gamma^3}{\varepsilon}\right)^{1/4}$ in the modified Brucato model and Pinelli model, where γ is the kinematic viscosity of the continuous phase.

The averaged dissipation rate ε_{ave} calculated from the experimental power input, i.e. $\varepsilon = \frac{P}{V\rho_l}$ was used in some work (Pinelli et al., 2001; Montante and Magelli, 2005; Khopkar et al., 2006), indicating that a uniform drag coefficient $C_{D,turb}$ was used throughout the vessel, while the local differences were ignored. On the other hand, the numerical local ε_{loc} was employed in the work of Tamburini et al. (2009, 2011), since using the average value to represent the local values has been referred to as one of the reasons for the discrepancy in the numerical study by other authors (Špidla et al., 2005).

The Gidaspow model is available in the commercial CFD code ANSYS CFX 12.0, while the other two models were implemented using the expression language feature in the ANSYS CFX 12.0.

4.5.1. Effect of drag models on velocity distributions

The three drag models mentioned above were used for predicting the suspensions of 3 mm particles at the solid concentration ranging from X = 5.2 wt% to the X = 40 wt%, at their 'just-suspended' speed N_{js}. The predicted velocity distributions for the both phases compared with the PEPT measurements are shown in Fig. 4.15 – 4.18, respectively. The salient features observed in the velocity profiles of the 1 mm particles, as discussed in section 4.4.1, were also observed in the case of the 3 mm particles.

The predicted velocity distributions of the liquid phase using the three drag models are identical and agree very well with the PEPT data at low solid concentration, X = 5.2 wt%. The drag model slightly affects the predicted radial and tangential velocity components, however, it has significant influence on the axial velocity component, u_z, as shown in Fig. 4.5. It can be seen that the predicted distributions of the axial velocity from the Pinelli and modified Brucato models are similar and agree better with the PEPT measurements compared with those from the Gidaspow model. The predicted solid falling down velocities in the upper part of stirred vessel using the Pinelli model and modified Brucato model are much smaller than that from the Gidaspow model, which could be attributed to taking into account the influence of the free stream turbulence in these two drag models.

At higher solid concentrations, the predicted velocities of the liquid phase are still slightly affected by different drag models, as shown in Fig. 4.16 – 4.18. The Pinelli model and modified Brucato model give good predictions of the axial velocities of solid phase in the

upper region of stirred vessel, meanwhile, the predicted solid axial velocities above the impeller using the Gidaspow model improve significantly with the increase in the solid mean concentration. This is consistent with the conclusion in the literature that the Gidaspow model is particularly useful for higher solid loadings in pipes (Eesa and Barigou, 2008; 2009) and in stirred vessels (Ochieng et al., 2008).

Similar observations can be made about impeller rotational speeds above N_{js}, and sample results for X = 20 wt%, N = 735 rpm are displayed in Fig. 4.19.

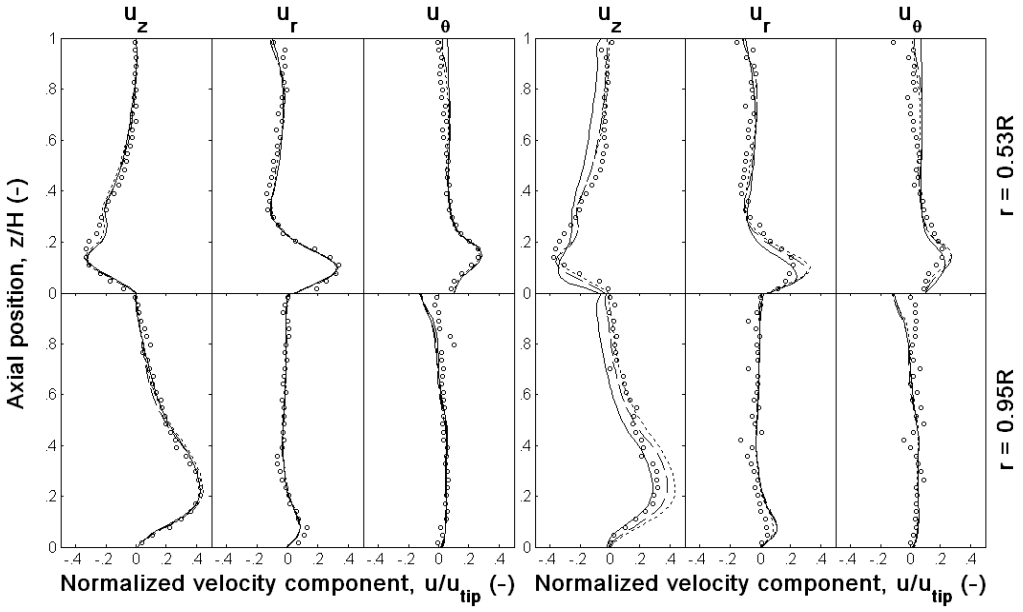

Figure 4.15. Azimuthally-averaged distributions of the velocity components of the liquid and solid phase in suspension at $N = N_{js}$ = 360 rpm, d_p = 3 mm, X = 5.2 wt%: — Gidaspow model; --- Pinelli model; ⋯ modified Brucato model; O PEPT.

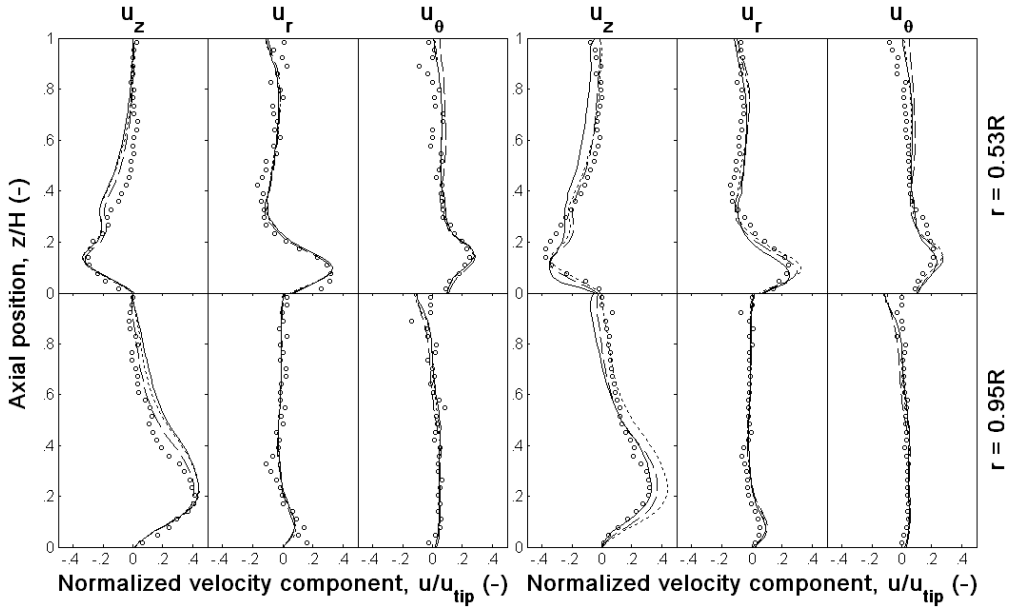

Figure 4.16. Azimuthally-averaged distributions of the velocity components of the liquid and solid phase in suspension at $N = N_{js} = 410$ rpm, $d_p = 3$ mm, $X = 10.6$ wt%: — Gidaspow model; --- Pinelli model; ⋯ modified Brucato model; O PEPT.

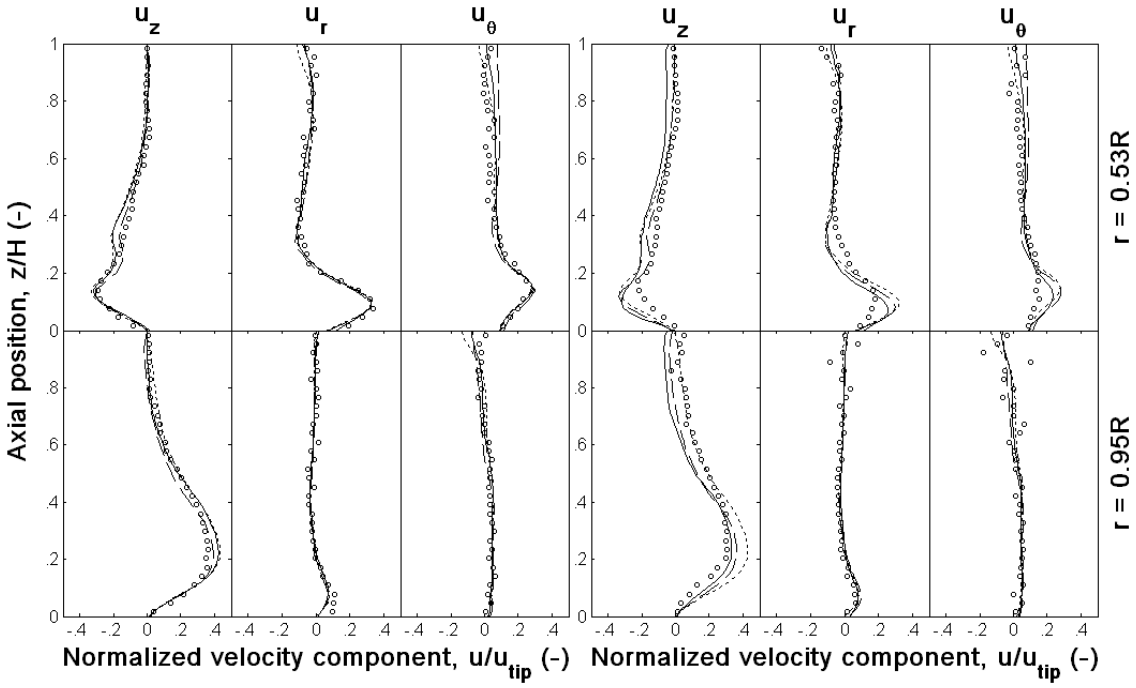

Figure 4.17. Azimuthally-averaged distributions of the velocity components of the liquid and solid phase in suspension at $N = N_{js} = 490$ rpm, $d_p = 3$ mm, $X = 20$ wt%: — Gidaspow model; --- Pinelli model; ⋯ modified Brucato model; O PEPT.

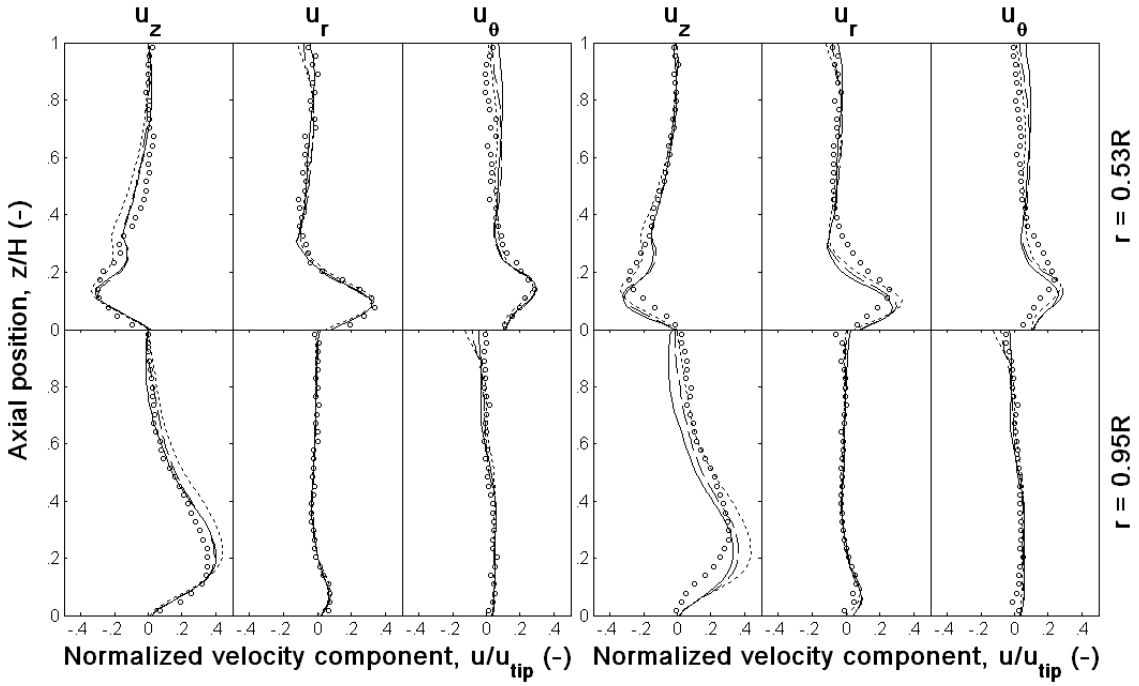

Figure 4.18. Azimuthally-averaged distributions of the velocity components of the liquid and solid phase in suspension at $N = N_{js} = 590$ rpm, $d_p = 3$ mm, $X = 40$ wt%: — Gidaspow model; --- Pinelli model; ⋯ modified Brucato model; O PEPT.

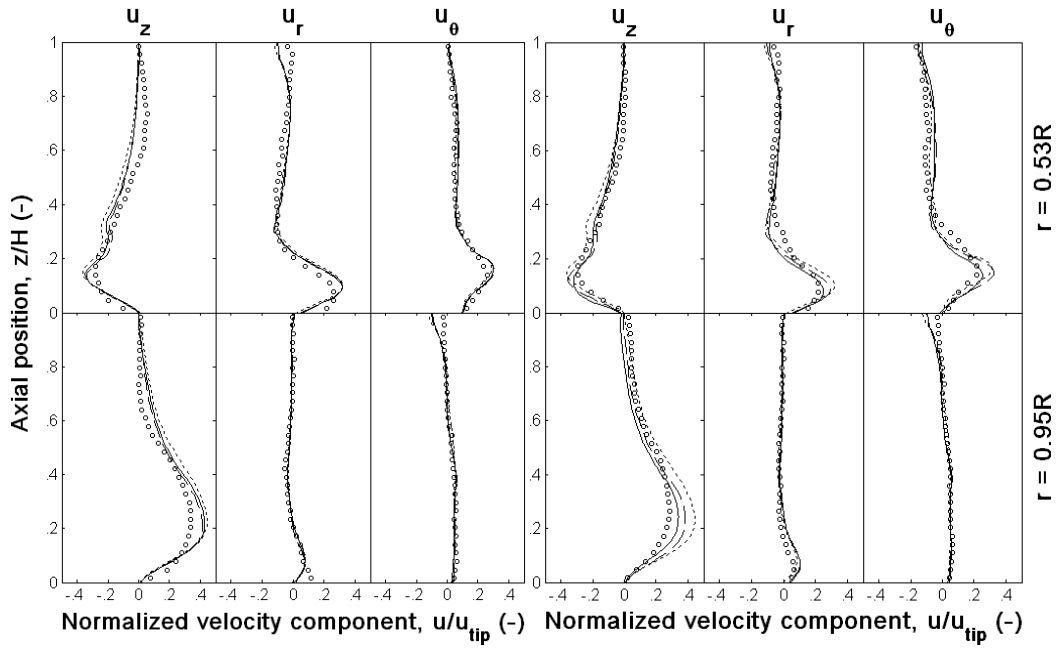

Figure 4.19. Azimuthally-averaged distributions of the velocity components of the liquid and solid phase in suspension at $N = 1.5N_{js} = 735$ rpm, $d_p = 3$ mm, $X = 20$ wt%: — Gidaspow model; --- Pinelli model; ⋯ modified Brucato model; O PEPT.

4.5.2 Effect of drag models on solid distribution

The azimuthally-averaged radial distributions of the solid phase under the 'just-suspended' condition are presented in Fig. 4.20. It can be readily seen that the drag model has significant effect on the solid distributions, especially in the central region underneath the impeller and in the upper part of the vessel. Similar to the observations noted for the 1 mm glass beads, the solid distributions close to the base (z = 0.016H and 0.08H) were significantly over-predicted by the Gidaspow model and the Pinelli model. On the contrary, the solid particles are significantly lifted up in this region using the modified Brucato model, which gave almost uniform solid distributions throughout the stirred tank.

This could be caused by the linearly increase in the drag coefficient $C_{D,turb}$ to the ratio d_p / λ in modified Brucato model, equation (4.14). Brucato et al. (1998) have stated that the constant factor, i.e. 8.76×10^{-4}, might depend on the particle size and even very small uncertainties might be amplified significantly, and this assumption was confirmed by Khopkar et al. (2006). Khopkar et al. have found that the solid suspension of submillimeter particles at moderate solid concentrations, was significantly overpredicted by the Brucato model, and this overestimation became more severe with the increase in the particle size. Consequently, the proportionality constant needs to reduce 10 times smaller to obtain good simulation results. Moreover, in their another study (Khopkar et al., 2005), they concluded that when the particle diameter is 4 mm in a gas-liquid system the constant factor in the Brucato model had to be reduced by about 100 times.

Concerning the solid distributions in the upper part of the stirred vessel (z > 0.83H), the predictions from the Gidaspow model agree better with the PEPT measurement, while the other two drag models overestimate the solid suspension in this region, which is more

pronounced with the modified Brucato model. The three drag models predict similar radial solid distributions just above ($z = 0.33H$) and below ($z = 0.17H$) the impeller.

At higher solid concentrations at N_{js}, the predictions with the Gidaspow model around the impeller and close to the base improve significantly with an increase in mean solid concentration. This improvement may be because, as mentioned above that as X increases, the solid phase behaves increasingly more like a continuum as assumed in the Eulerian model. Also, it may be because the effect of the solid concentration is taken into account in the Gidaspow model.

At impeller speeds above N_{js}, the drag models perform similarly to those obtained at N_{js}, as shown in Fig. 4.21. The CFD predictions of solid distribution improve somewhat with it, notably near the base, though accurately predicting the solid distributions close to tank base remains a challenge for all the three drag models.

Conclusion of which drag model give the best prediction cannot be drawn concerning the complex flow mechanisms of particle settling and particle lift-off and resuspension close to the tank base, the effects of various factors such as particle size and particle concentration are needed to be implemented in the CFD drag model. However, the currently available drag models either only consider the effect of solid concentration, like the Gidaspow model, or only take into account the influence of free stream turbulence such as the Pinelli model and modified Brucato model. Therefore, further fundamental knowledge is needed to provide insight into the parameters that affect the inter-phase drag coefficient, particular for relatively larger particles at high solid concentrations.

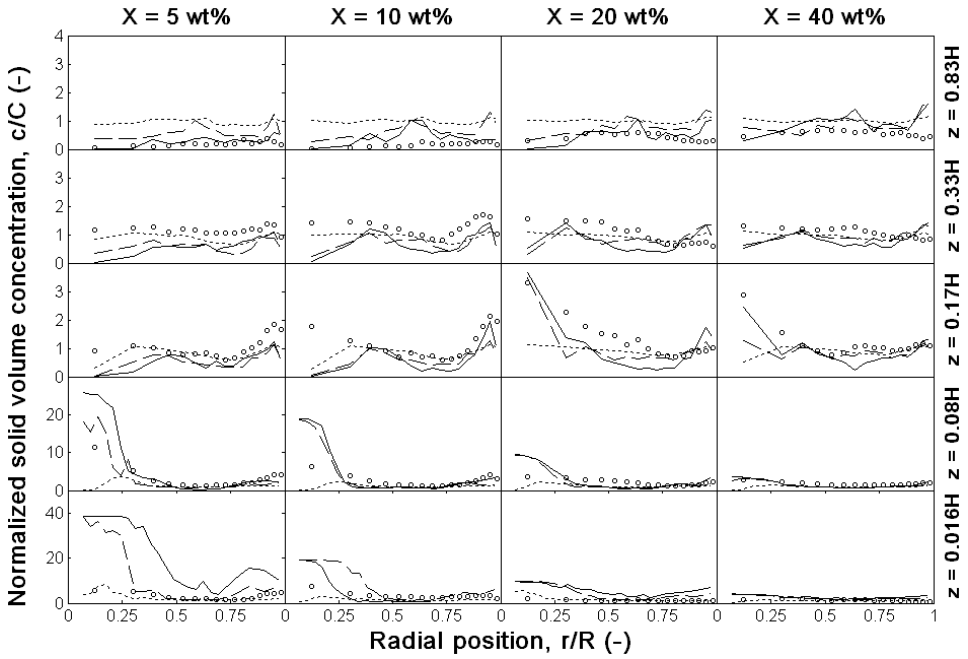

Figure 4.20. Azimuthally-averaged distributions of solid volume concentration in suspension at N_{js} (d_p = 3 mm): — Gidaspow model; --- Pinelli model; ⋯ modified Brucato model; O PEPT.

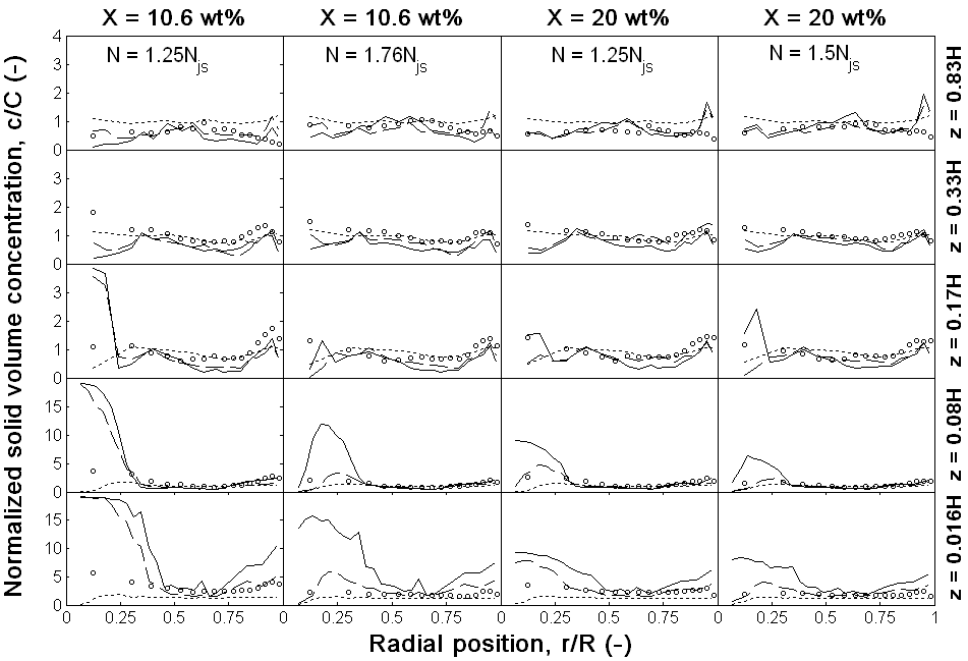

Figure 4.21. Azimuthally-averaged distributions of solid volume concentration in suspension at $N > N_{js}$ (d_p = 3 mm): — Gidaspow model; --- Pinelli model; ⋯ modified Brucato model; O PEPT.

4.6. Effects of non-drag forces

4.6.1. Effects of non-drag forces on the velocity distribution and solid distributions

The effects of non-drag forces such as the lift force and virtual mass force in Eq. (4.2), have been studied by some researchers and have been reported to have very little influence on the predicted flow field and solid concentration distributions (Ljungqvist and Rasmuson, 2001; Ochieng and Onyango, 2008). On the other hand, Fletcher and Brown (2009) reported that the effects of the non-drag forces were not clear, and the negligible effect that found in others' work was due to very low solids fractions in their studies. In this section, the effects of these non-drag forces on the flow fields of two phases as well as the solid distributions at low and high solid concentrations, at N_{js} and above it are investigated.

The representative sample results, i.e. the azimuthally averaged velocity distributions at the lowest and highest investigated solid concentrations (X = 5.2 and X = 40 wt%) at N_{js}, and at the highest investigated impeller speed, $N > N_{js}$, at X = 20 wt%, are displayed in Fig. 4.22-4.24, respectively. It can be seen that the non-drag forces have little effect on the flow fields of the both the liquid and solid phases.

Fig. 4.25 shows the solid concentration distributions under the above mentioned conditions and as expected, the solid concentration distributions are not affected by the non-drag forces.

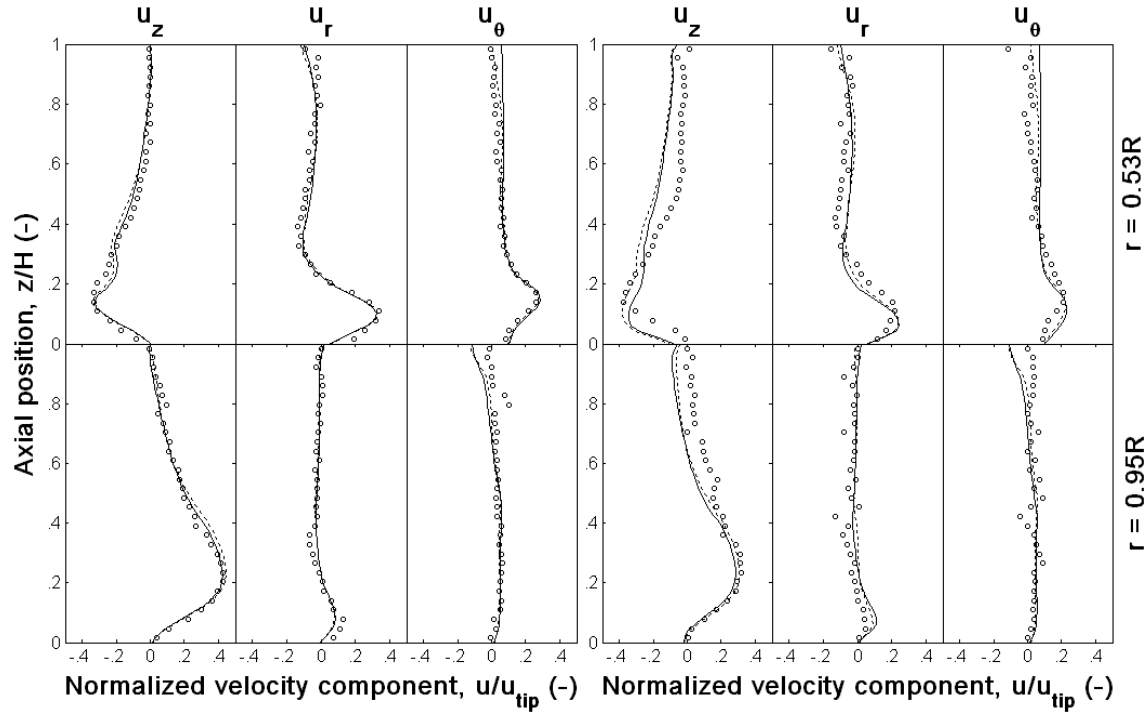

Figure 4.22. Azimuthally-averaged distributions of the velocity components of the liquid and solid phase in suspension at $N = N_{js}$ = 360 rpm, d_p = 3 mm, X = 5.2 wt%: — Gidaspow model only; ⋯ adding lift force and virtual mass force; O PEPT.

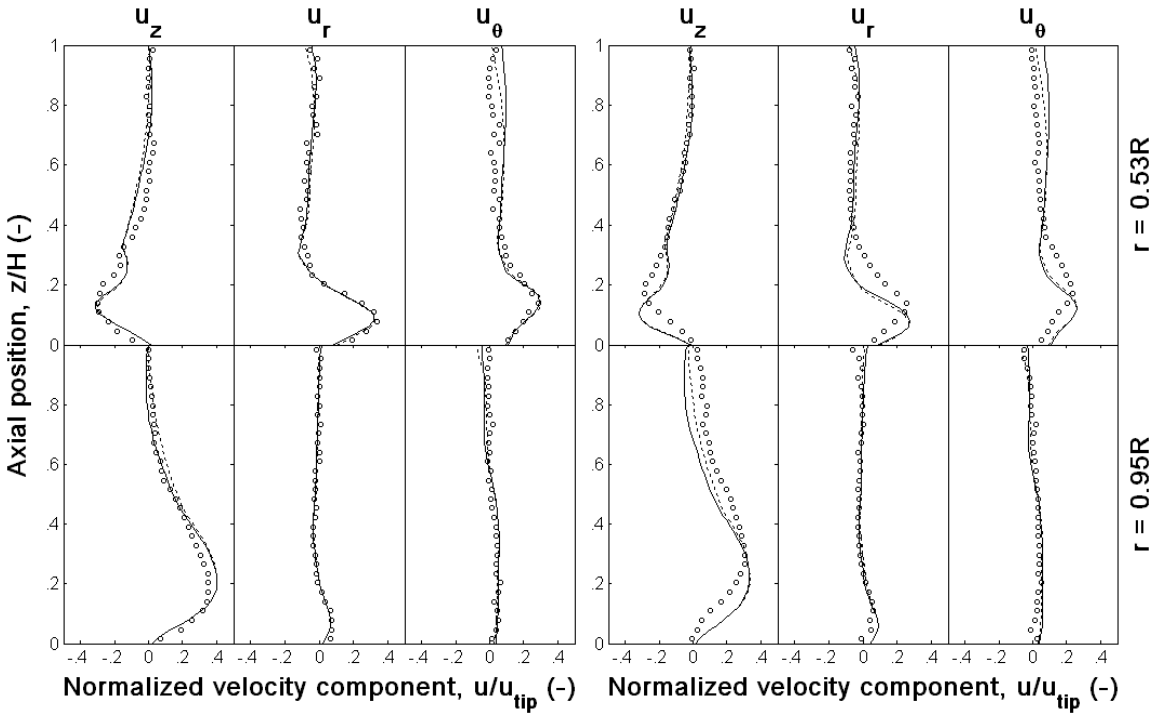

Figure 4.23. Azimuthally-averaged distributions of the velocity components of the liquid and solid phase in suspension at $N = N_{js}$ = 590 rpm, d_p = 3 mm, X = 40 wt%: — Gidaspow model only; ⋯ adding lift force and virtual mass force; O PEPT.

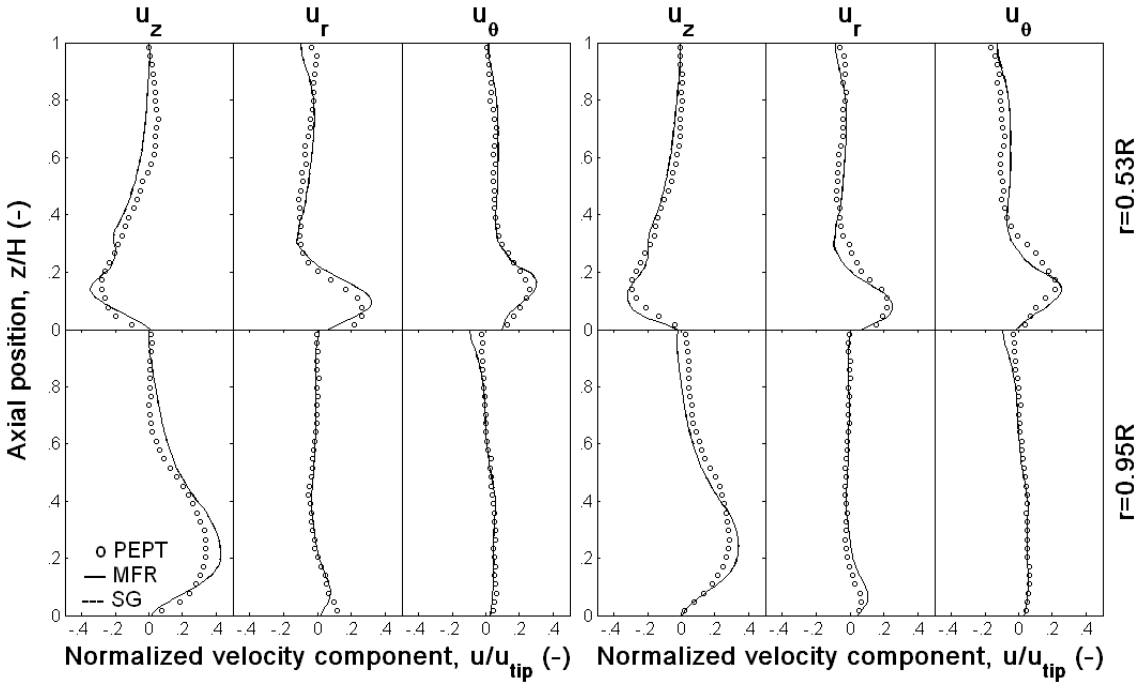

Figure 4.24. Azimuthally-averaged distributions of the velocity components of the liquid and solid phase in suspension at $N = 1.5N_{js} = 735$ rpm, $d_p = 3$ mm, $X = 20$ wt%: — Gidaspow model only; ⋯ adding lift force and virtual mass force; O PEPT.

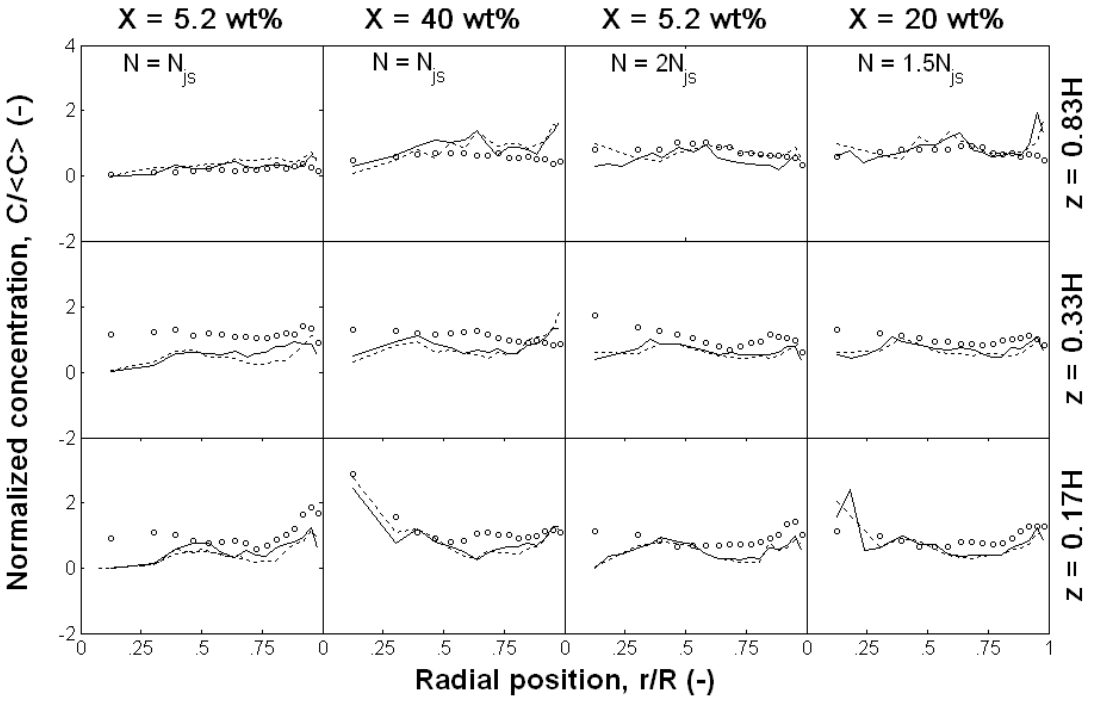

Figure 4.25. Azimuthally-averaged distributions of solid volume concentration in suspension, $d_p = 3$ mm: — Gidaspow model only; ⋯ adding lift force and virtual mass force; O PEPT.

4.7. Effects of "SG" and "MFR"

4.7.1. Effects of "SG" and "MFR" on the velocity distribution and solid distributions

The comparison of the modeling approaches, i.e. SG, MFR, and IO, dealing with the rotation of impeller, has been widely investigated for the single phase flow in previous literature (Brucato et al., 1998; Aubin et al., 2004; Montante and Magelli, 2005). The SG has been found to predict a better flow field in some studies (Brucato et al., 1998), while some researchers (Aubin et al., 2004) found a slight effect on the flow field. Solid-liquid systems, however, are seldom investigated. Montante and Magelli (2005) compared the SG and IO methods for a very dilute solid-suspension system.

The flow fields of the liquid phase and the solid phase using the 'MFR' and the 'SG' methods at the solid concentration, X = 5.2 wt% are shown in Fig. 4.26. Identical flow fields are predicted by these two modelling methods indicating little effects of the modelling approach that treats the impeller rotation. The predictions from the two approaches remain unanimous at rotational speed above N_{js}, and at higher solid concentrations, and for the sake of brevity, only two representative sample results, i.e. results at the highest investigated solid concentration, X = 40 wt% at N_{js}, and results at highest investigated impeller speed, $N > N_{js}$, X = 20 wt%, , displayed in Fig. 4.27 – 4.28, respectively.

The predicted azimuthally-averaged radial solid distributions from the two methods are shown in Fig. 4.29. It can be seen that the solid distributions are not affected, regardless of the mean solid concentration and impeller speed.

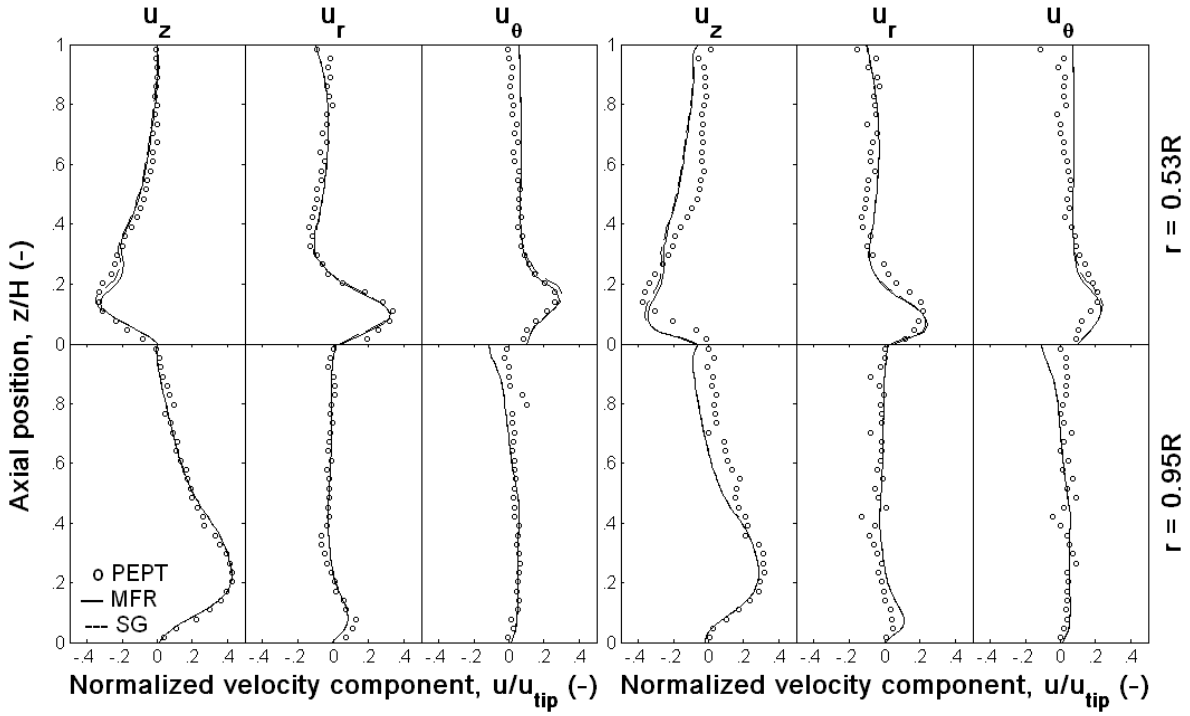

Figure 4.26. Azimuthally-averaged distributions of the velocity components of the liquid and solid phase in suspension at $N = N_{js} = 360$ rpm, $d_p = 3$ mm, $X = 5.2$ wt%.

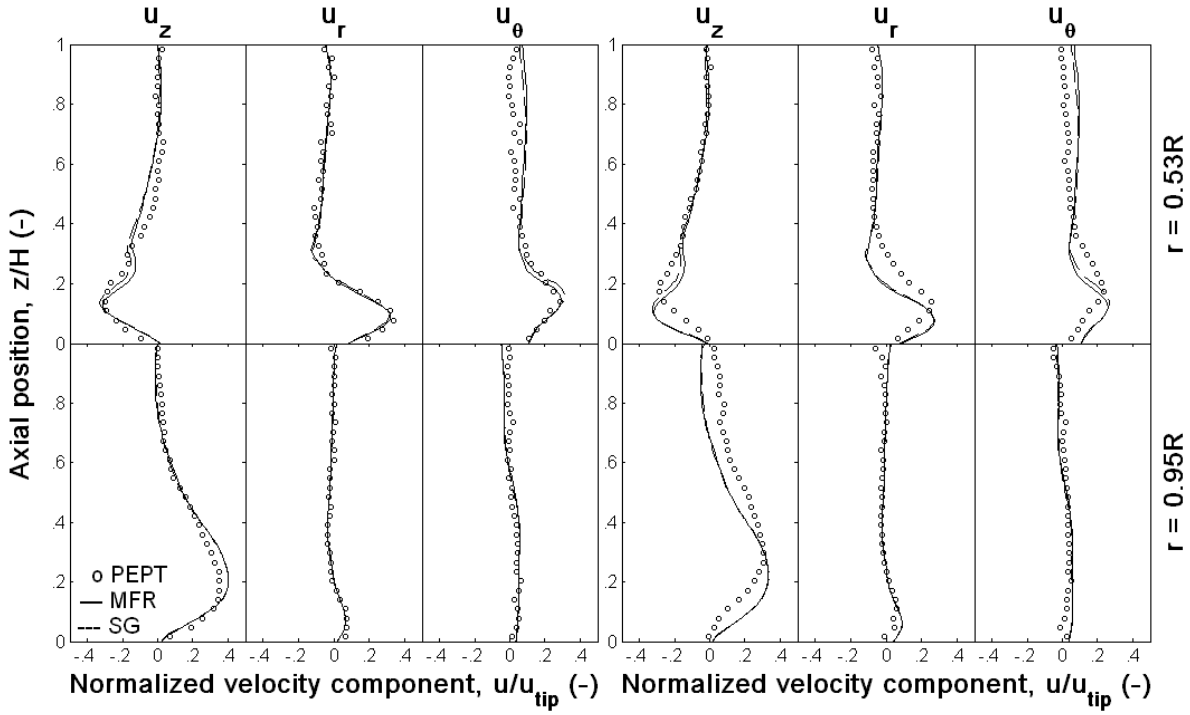

Figure 4.27. Azimuthally-averaged distributions of the velocity components of the liquid and solid phase in suspension at $N = N_{js} = 590$ rpm, $d_p = 3$ mm, $X = 40$ wt%.

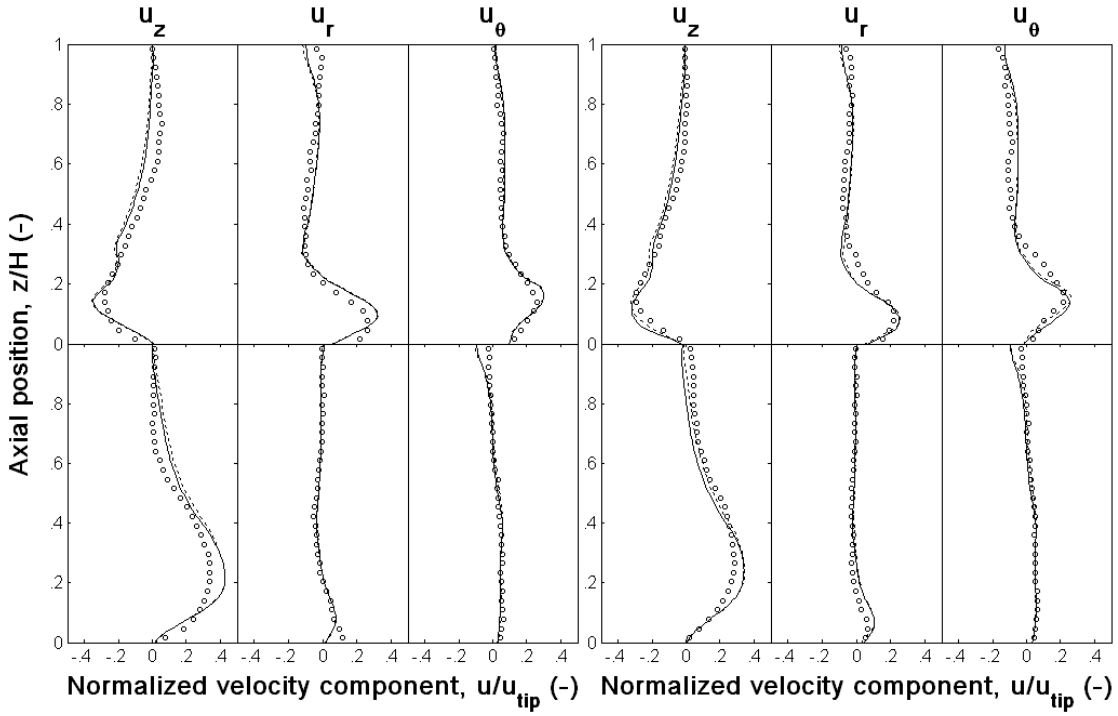

Figure 4.28. Azimuthally-averaged distributions of the velocity components of the liquid and solid phase in suspension at $N = 1.5N_{js} = 735$ rpm, $d_p = 3$ mm, $X = 20$ wt%.

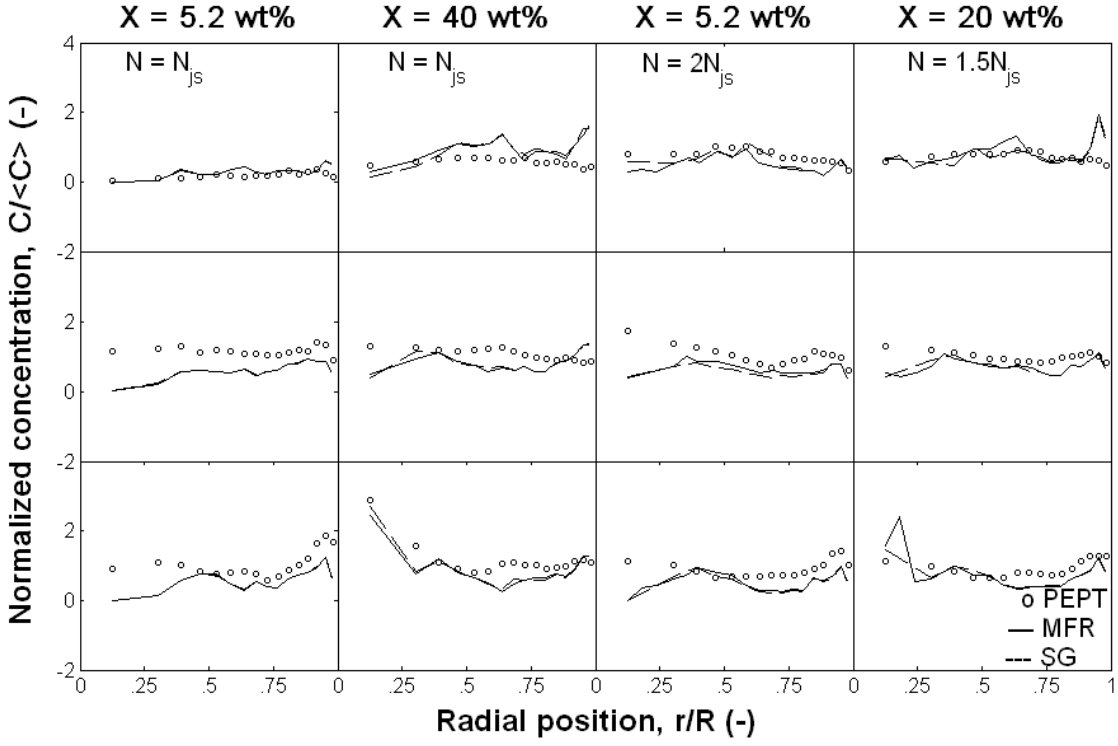

Figure 4.29. Azimuthally-averaged distributions of solid volume concentration in suspension ($d_p = 3$ mm).

4.8. Conclusions

The flow of dense solid-liquid suspensions in a mechanically agitated vessel has been successfully modelled by CFD. At both the 'just-suspended' state corresponding to N_{js} and at speeds above it, except for some limited localized errors, the two-phase velocity field generally agrees very well with measurements obtained by the accurate PEPT technique in all parts of the vessel including near the base and underneath the agitator where there is a considerable accumulation of solids. This has also led to accurate predictions of the two-phase flow number.

The spatial distribution of the solid phase is well predicted except close to the base of the vessel where large overestimations are registered. At impeller speeds above N_{js}, the suspension becomes more uniform and the CFD predictions improve somewhat, notably near the base. The relatively high solid presence coupled with the complexity of the flow at the bottom of the vessel, however, still prevent accurate prediction of the local solid concentration in this region, as the CFD model does not incorporate all of the physics of particle sedimentation and lift-off.

At the same power input, smaller particles are significantly better distributed than larger ones, and for both particle sizes studied, homogeneity improves with increasing solids concentration at the same hydrodynamic mixing regime. At speeds much above N_{js} (e.g. $N = 2N_{js}$), both particle systems converge towards a high state of homogeneity ($\xi \sim 0.9$), but this requires a seven time increase in power input.

At N_{js}, there are wide variations in the spatial distribution of the inter-phase slip velocity. The largest total slip velocities occur in the vicinity of the impeller, and because of the inertia of the particles they are of considerable magnitude, on the order of $\sim 0.10 u_{tip}$. Considering the

individual components of the slip velocity, the largest slip occurs in the axial direction. The volume-average slip velocity in the vessel measured by PEPT is considerably smaller than the measured settling velocity of the particles. Increasing the agitation speed up to $2N_{js}$, reduces the normalised slip velocities significantly. Such a reduction is essentially wholly related to reduction in the axial slip component given that particles are better suspended in a nearly homogeneous mixture. Note, however, that the absolute slip velocities are more or less unaffected by the increase in N.

At N_{js} and up to ~ 10 wt% solids, the effects of the solids presence on the liquid velocity field are minimal. At higher concentrations, however, some significant reductions in liquid velocity occur near the impeller and along the wall of the vessel, affecting mainly the axial component u_z. The effects are similar at $N > N_{js}$.

Results indicate that there is little impact on the distributions of turbulent kinetic energy and Kolmogorov length scale. At N_{js}, the eddy dissipation rate, however, is significantly suppressed but only at solid concentrations above ~ 5 wt%.

Identical flow fields and solid concentration distributions are predicted from the modelling approaches that deal with the impeller rotation, i.e. SG and MFR. Non-drag forces have little effect on the CFD predictions of solid-liquid systems. Drag models have a significant impact on the distributions of solid velocity and concentration, and need to be improved for the accurate solid-liquid suspensions of relatively larger particles at high solid concentrations.

Notation

c	local volume concentration of solids	-
C	mean volume concentration of solids	-

C_d	drag coefficient	-
d_p	particle diameter	m
D	impeller diameter	m
Fl	two-phase flow number (Q/ND^3)	-
$Fl^{(L)}$	liquid flow number ($Q^{(L)}/ND^3$)	-
$Fl^{(S)}$	solid flow number ($Q^{(S)}/ND^3$)	-
H	height of suspension	m
ℓ	integral length scale	m
N	impeller rotational speed	s^{-1}
N_{js}	minimum speed for particle suspension	s^{-1}
P	power consumption	W
Q	impeller pumping rate	$m^3\ s^{-1}$
r	radial distance	m
R	vessel radius	m
Re_{imp}	impeller Reynolds number (ND^2/ν)	-
s	slip velocity	$m\ s^{-1}$
T	vessel diameter	m
TKE	turbulent kinetic energy	$J\ kg^{-1}$
$\overline{TKE}$	volume-average turbulent kinetic energy	$J\ kg^{-1}$
u_{tip}	impeller tip speed	$m\ s^{-1}$
$u_r\ u_z\ u_\theta$	cylindrical velocity components	$m\ s^{-1}$
V	volume of stirred vessel	m^3
X	mean mass concentration of solids	-
z	vertical distance	m

Greek letters

ν	kinematic liquid viscosity	$m^2\ s^{-1}$
ξ	uniformity index	-
σ	standard deviation of normalised c	-
θ	azimuthal coordinate	rad
ε	energy dissipation rate	$m^2\ s^{-3}$

$\bar{\varepsilon}$	volume-average energy dissipation rate	$m^2\ s^{-3}$
λ	Kolmogrov length scale	m
$\bar{\lambda}$	volume-average Kolmogrov length scale	m

Chapter V

NUMERICAL MODELLING OF MULTI-COMPONENT HYDRODYNAMICS AND SPATIAL PHASE DISTRIBUTION IN MECHANICALLY AGITATED DENSE BINARY AND POLY SUSPENSIONS

Abstract

The mixing of dense (5-40 wt%) binary mixtures of glass particles in water has been studied in a stirred vessel at the 'just-suspended' speed and at speeds above it, using an Eulerian-Eulerian CFD model. For each phase component, numerical predictions are compared to 3-D distributions of local velocity components and solid concentration measured by an accurate technique of positron emission particle tracking. For the first time, it has been possible to conduct such a detailed 'pointwise' validation of a CFD model within opaque dense multi-component slurries of this type. Predictions of flow number and mean velocity profiles of all phase components are generally excellent. The spatial solids distribution is well predicted except near the base of the vessel and underneath the agitator where it is largely overestimated; however, predictions improve significantly with increasing solid concentration. Other phenomena and parameters such as particle slip velocities and homogeneity of suspension are analysed.

5.1. Introduction

Monodisperse solid-liquid suspensions have been reported in a number of mixing studies, both numerically and experimentally, though the majority of them are focused on dilute suspensions which have little practical relevance. However, suspensions of particles of different diameters in turbulent mixing in stirred vessels have been reported in very few works. Studies have found that smaller particles distribute more uniformly than larger particles (Altway et al., 2001; Špidla et al., 2005; Ochieng and Lewis, 2006).

Overall, therefore, the accuracy of CFD in the mixing of suspensions of solid particles of different sizes, i.e. binary or poly disperse, especially in dense suspensions has not been sufficiently studied and, in particular, little information exists on flow hydrodynamics. Hence, a detailed validation using detailed 'pointwise' measurements of 3-D velocities as well as the distribution of the phases and phase components, especially under conditions of moderate to high solid loadings, is needed in order to assess the capability of the numerical models and CFD codes available in these complex flows.

In this chapter, the flow of binary- and poly-disperse of coarse glass particles containing up to 40 wt% solids in water, is studied numerically by means of a CFD model in a mechanically agitated vessel under different regimes of particle suspension. Experimental results obtained using PEPT for binary suspensions at $N = N_{js}$ reported by Guida et al. (2011) together with new measurements of binary suspensions at $N > N_{js}$ and new measurements of poly-disperse at $N = N_{js}$ by the author are exploited for validation of a number of suspension characteristics, including most importantly the detailed 3-D velocity field of each phase component and its spatial phase distribution. The results are also analysed to infer for each phase component the

local time-average particle-fluid slip velocity, phase flow number and suspension uniformity. Finally, verification of the solids mass balance and mass continuity in the vessels is presented.

5.2. Experimental and modelling apparatus

The PEPT experimental set-up was similar to that used for measuring monodisperse systems reported in Chapter IV. A fully-baffled flat-base Perspex vessel of diameter $T = 288$ mm, fitted with four wall baffles of $0.1T$ spaced at 90° degrees was agitated by a down-pumping 6-blade 45º pitched-turbine (PBT) of diameter $D = T/2$, located $T/4$ from the tank base, as illustrated in Fig. 5.1. The height of the suspension was set at $H = T$. The solid particles used were spherical glass beads of density 2485 kg m^{-3}. The binary solid-liquid suspensions consist of two nearly-monomodal particle size fractions, ($d_p \sim 1$ mm; ~ 3 mm). Five nearly-monomodal particle size fractions, ($d_p \sim 1$ mm; 1.7 mm; 2.2 mm; 2.7 mm; 3 mm) were used to make poly disperse solid-liquid suspensions. The total solid mass concentration, X, varies from 0 to 40 wt%, and the fractions of different particle sizes were mixed in equal proportions, i.e., $X_1 = X_2 = 0.5X$ in binary and $X_1 = X_2 = X_3 = X_4 = X_5 = 0.2X$ in poly disperse systems. Experiments were conducted under different regimes of solid suspension corresponding to (i) $N = N_{js}$, the minimum speed for particle suspension; and (ii) speeds above N_{js} up to $2N_{js}$. The conditions of the PEPT experiments including those reported by Guida et al. (2011) and CFD simulations conducted are summarized in Table 5.1.

The 3-D trajectories of each component were resolved individually in distinct PEPT experiments. A neutrally-buoyant radioactive resin tracer of 600 μm diameter was used to track the liquid phase. A representative glass particle was taken from each particle size fraction and was radioactively labelled in a cyclotron and used to track the trajectories of the solid components, respectively. Based on the verification of ergodicity in a turbulent flow

system by Guida et al. (2010; 2011; 2012), every experiment was run for 30 minutes which is sufficiently long enough to obtain adequate data in every region of the stirred vessel.

5.3. Numerical modelling

Numerical simulations were performed using the commercial CFD code ANSYS CFX 12.0. The governing equations which form the basis of modelling the solid-liquid suspensions have been discussed in Chapter IV. Note that the equations for a binary suspension need to be extended to include a second solid component. The effects of the non-drag forces, i.e. lift force, $F_{lift,q}$, and the virtual mass force, $F_{vm,q}$ in the momentum equation (4.2) were negligible, as have been discussed in detail in Chapter IV and reported by others (Ljungqvist and Rasmuson, 2001; Sha et al., 2001), thus were omitted in the CFD modeling of the suspensions of binary disperse. The drag coefficient, C_D was estimated using the Gidaspow drag model (Gidaspow, 1994).

The Multiple Reference Frames (MFR) method was used to take into account the interaction between the stationary baffles and the rotating impeller blades in conjunction with the well-known mixture $k-\varepsilon$ turbulence model where the two phases are assumed to share the same k and ε (Montante and Magelli, 2005; Špidla et al., 2005). Consequently, the computational domain was divided into two regions, as shown in Fig. 4.1. The same meshing scheme with that used in Chapter IV was used because of the identical configuration of stirred tank used in this chapter.

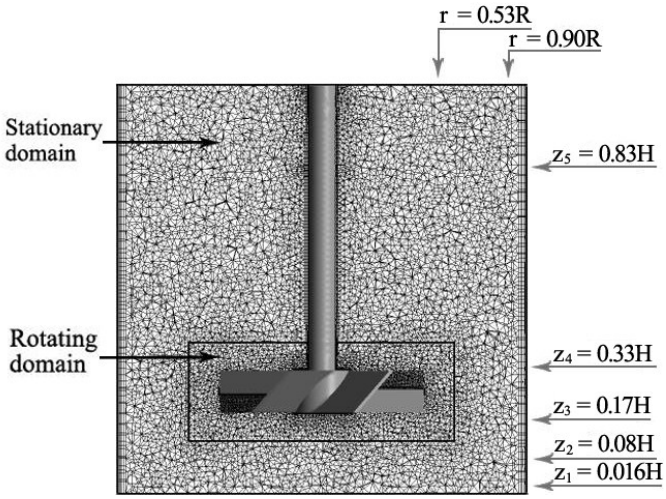

Figure 5.1. Computational grid section in the 45° plane between two baffles.

Table 5.1. Range of PEPT measurements and CFD simulations.

X (wt%)	C (vol%)	N (rpm) ($Re_{imp} \times 10^{-5}$)		
		$N = N_{js}$	$N > N_{js}$	
5	2.4	380 (1.51)*	570 (2.27)	760 (3.02)
10	4.9	450 (1.79)*	675 (2.68)	800 (3.18)
20	10.4	510 (2.03)*	765 (3.04)	-
40	23.6	610 (2.43)*	765 (3.04)	-

*PEPT measurements reported by Guida et al. (2011)

5.4. Results and discussion

5.4.1. Binary disperse

A detailed quantitative comparison between the CFD predictions and PEPT measurements was conducted at the positions depicted in Fig. 5.1. For the liquid phase and both components of the solid phase (i.e., 1 mm and 3 mm particles), the azimuthally-averaged distributions of the local velocity components (u_z, u_r, u_θ)were compared:

(i) axially along two radial positions: $r = 0.53R$, close to the tip of the impeller; and $r = 0.90R$, half the width of a baffle away from the tank wall; and

(ii) radially along five axial positions: $z = 0.016H$, close to the base of the vessel; $z = 0.08H$, approximately halfway between the base and the lower edge of the impeller; $z = 0.17H$, just under the lower edge of the impeller; $z = 0.33H$, just above the upper edge of the impeller; and $z = 0.83H$, in the upper part of the vessel. For ease of comparison, all the velocity plots presented have been normalized by the impeller tip speed ($u_{tip} = \pi DN$).

The azimuthally-averaged spatial distributions of the local solid concentration were also resolved by both PEPT and CFD, and compared at all these radial and axial locations. The solid concentration profiles presented have been normalized by the overall mean volume solid concentration (C).

5.4.1.1. Distribution of local velocity components

Azimuthally-averaged axial and radial distributions of the local velocity components (u_z, u_r, u_θ) at $N = N_{js}$ predicted by the CFD model compared with the equivalent distributions reported by Guida et al. (2011) are shown in Fig. 5.2 and Fig. 5.3, respectively, for the liquid phase and the two solid components (d_p = 1mm; 3 mm) at a solid concentration of 5 wt%. The mixture components exhibit similar velocity distributions where u_z is the predominant velocity component, which is consistent with the performance of a down-pumping mixed flow impeller. The radial distributions exhibit sharp variations in the impeller region ($z = 0.17H, 0.33H$), but are fairly flat in the upper parts of the vessel ($z = 0.83H$). Near the tank base, u_r is predominant as each component of the mixture is forced by the pumping action of the impeller to move towards the wall and is entrained in the single recirculation flow loop, thus, generated.

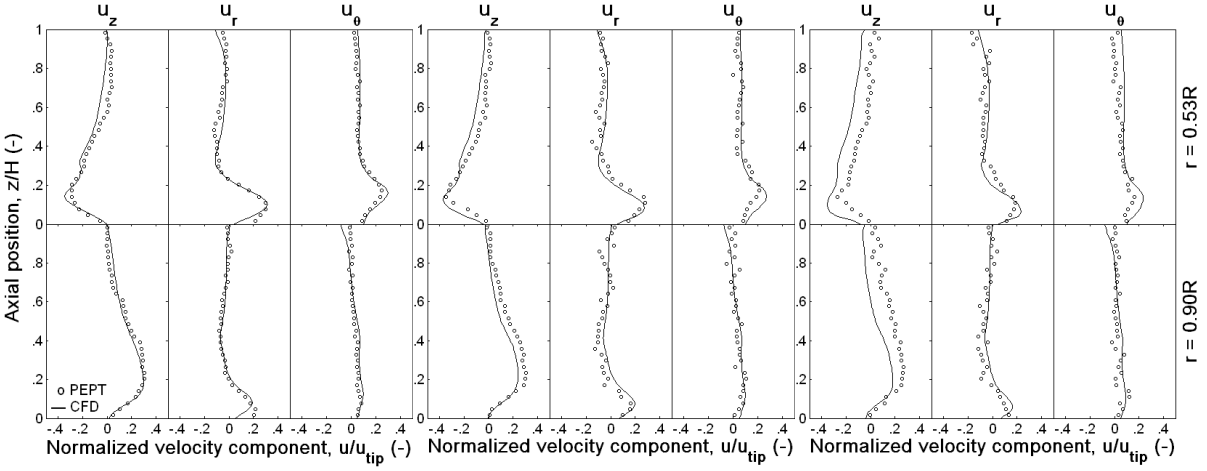

Liquid phase **d_p = 1 mm** **d_p = 3 mm**

Figure 5.2. Azimuthally-averaged axial distributions of the normalised velocity components of the liquid and solid components at N_{js}: X = 5 wt%; N_{js} = 380 rpm.

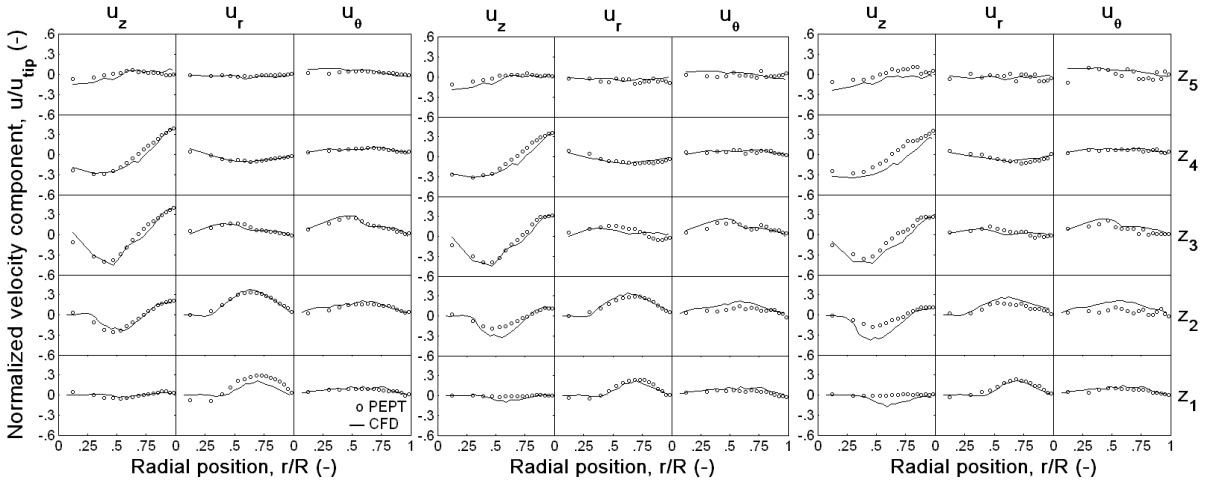

Liquid phase **d_p = 1 mm** **d_p = 3 mm**

Figure 5.3. Azimuthally-averaged radial distributions of the normalised velocity components of the liquid and solid components at N_{js}: X = 5 wt%; N_{js} = 380 rpm.

For the liquid phase and the 1 mm solids, all three velocity components are very well predicted by CFD throughout the vessel. For the 3 mm particles, however, there are some significant discrepancies between CFD and PEPT concerning the axial component u_z, which has also been found in the mono disperse (3 mm particles). This could be explained from two aspects: firstly, it is interesting to note that the number density of the 1 mm particles in the suspension is 27 times that of the 3 mm particles. It is perhaps plausible that as the number

density of the solids increases, the assumption of a continuum inherent in the Eulerian-Eulerian model becomes somewhat less unrealistic, which might explain why the accuracy of prediction is better for the smaller 1 mm particles; secondly, it could also be caused by the inadequacy of the current available drag models which do not take all the influenting factors into account, as discussed in detail in Chapter IV.

The numerically predicted axial velocity distributions at N_{js} for solid concentrations of 10 wt%, 20 wt% and 40 wt%, are compared to the experimental distributions (Guida et al., 2011) in Figures 5.4, 5.5 and 5.6, respectively. The distributions are similar to those observed at 5 wt% solids, as discussed in the next section.

With increasing solid concentration, the accuracy of prediction for the liquid phase and the 1 mm solids remains high. It is interesting, however, that for the 3 mm particles the numerical prediction improves significantly with X, becoming very good at X = 20 wt% and X = 40 wt%. Again, as X increases, the solid phase tends to behave increasingly more like a continuum, thus, possibly improving the suitability of the Eulerian-Eulerian model. As discussed in Chapter IV and reported by others (Eesa and Barigou, 2008, 2009; Ochieng and onyango, 2008) the Gidaspow drag model employed in this study was previously found to be particularly useful at higher solid loadings, which may have perhaps contributed the most to the improved accuracy of prediction at the higher solid concentrations. On the other hand, however, as solid concentration increases, particle-particle collisions are expected to increase which tends to complicate the physics of the flow to an unknown extent and, hence, it is difficult at present to suggest a completely satisfactory explanation.

Numerical simulations were also conducted to assess the capability of CFD to predict the solid suspension at $N >> N_{js}$. Sample results are shown in Fig. 5.7 for 10 wt% solids at N =

$2N_{js}$. Apart from some local discrepancies affecting especially the particles around the impeller discharge stream, the flow field of each mixture component is well predicted. At such a high rotational speed, the intensity of turbulence is extremely high, and it is well known that the standard k-ε model used here tends to significantly underestimate the turbulence kinetic energy and dissipation rate, especially near the tip of the impeller (Ranade et al., 2001; Aubin et al., 2004); this may explain the disparities observed near the impeller discharge. Similar results were obtained for the other solid concentrations.

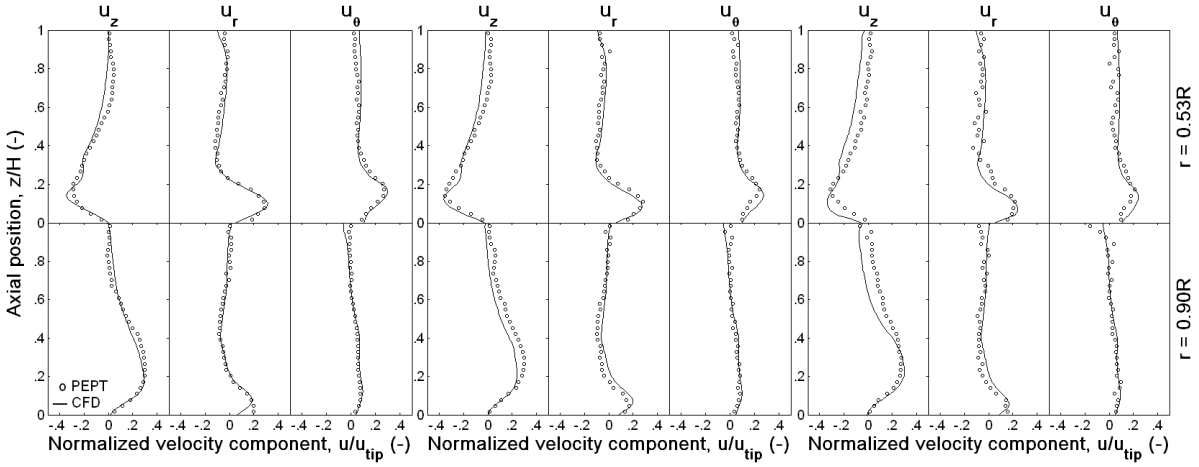

Liquid phase **d_p = 1 mm** **d_p = 3 mm**

Figure 5.4. Azimuthally-averaged axial distributions of the normalised velocity components of the liquid and solid components at N_{js}: X = 10 wt%; N_{js} = 450 rpm.

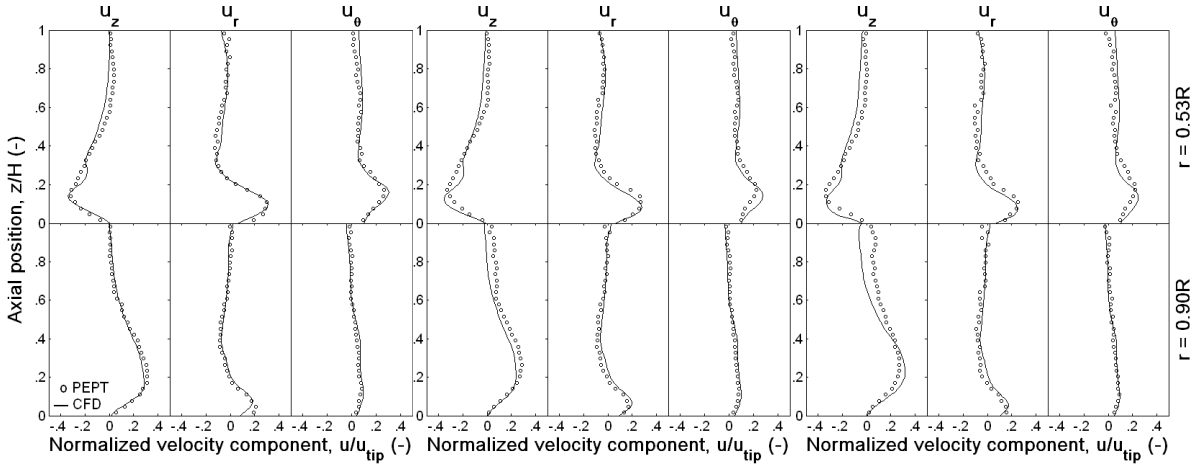

Liquid phase **d_p = 1** **d_p = 3 mm**

Figure 5.5. Azimuthally-averaged axial distributions of the normalised velocity components of the liquid and solid components at N_{js}: X = 20 wt%; N_{js} = 510 rpm.

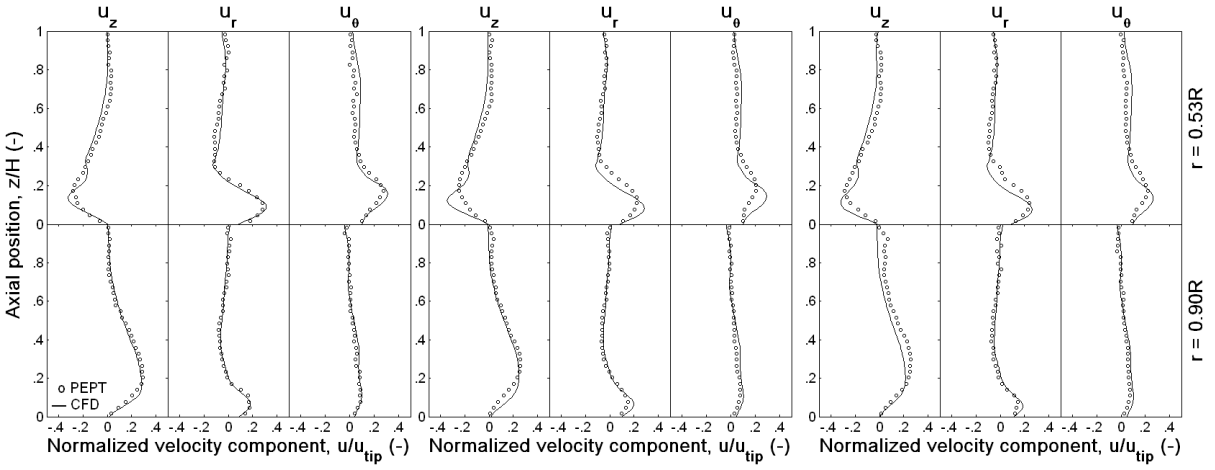

Liquid phase d_p **= 1 mm** d_p **= 3 mm**

Figure 5.6. Azimuthally-averaged axial distributions of the normalised velocity components of the liquid and solid components at N_{js}: X = 40 wt%; N_{js} = 610 rpm.

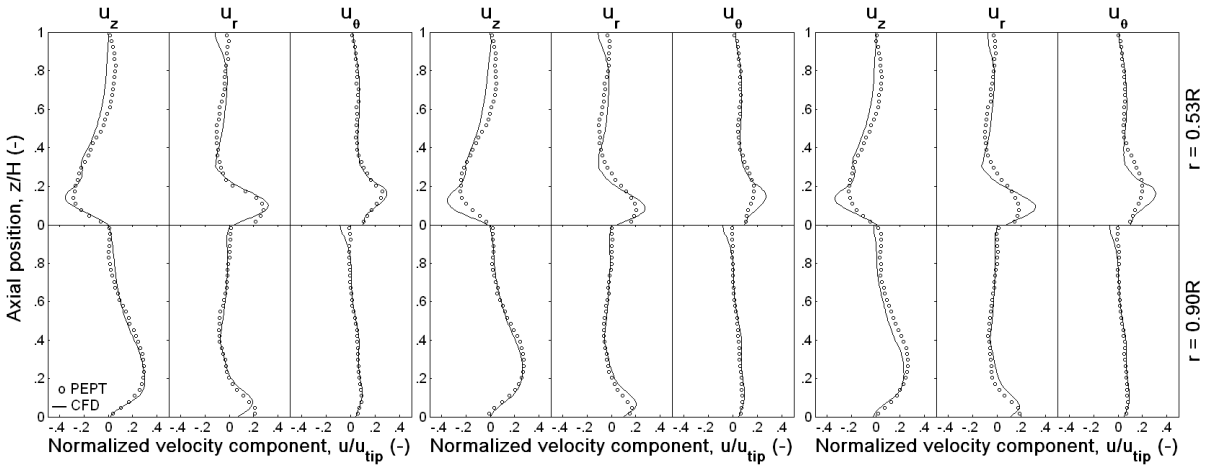

Liquid phase d_p **= 1 mm** d_p **= 3 mm**

Figure 5.7. Azimuthally-averaged axial distributions of the normalised velocity components of the liquid and solid components at $N = 2N_{js}$: X = 10 wt%; N = 800 rpm.

5.4.1.2. Reynolds number similarity

The flow structure at high Reynolds numbers presents similar characteristics, a phenomenon often referred to as Reynolds number similarity. In fully turbulent flow, viscosity effects vanish and dimensionless mean values such as velocities normalised by the impeller tip speed should be independent of Reynolds number. This similarity has been reported in Newtonian

and non-Newtonian liquids but does not seem to have been tested in multiphase flows of the type studied here (Van Der Molen and Van Mannen, 1978; Venneker et al., 2010). Results plotted in Fig. 5.8 show the azimuthally-averaged radial distributions of the normalised velocity components of the three mixture components at the four solid concentrations investigated. The values of the impeller Reynolds number ($Re_{imp} = ND^2/v$) are given in Table 5.1, and cover the range $1.5\times10^5 - 2.4\times10^5$ for $N = N_{js}$ (Guida et al., 2011). For the liquid phase, the Reynolds number similarity holds at all solid concentrations. For the solid components, some minor disparities are observed but the principle of similarity seems to hold too.

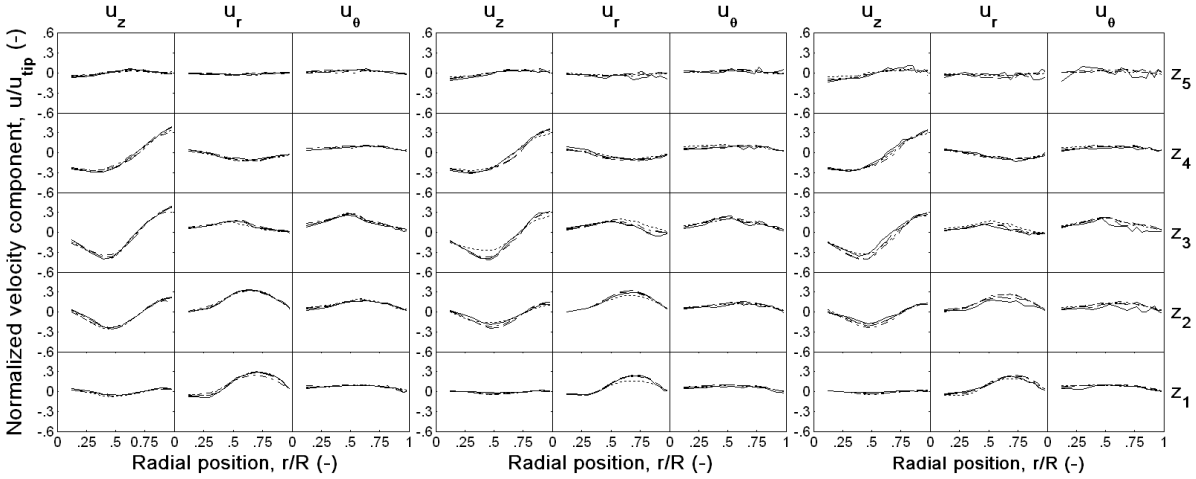

Liquid phase **d_p = 1 mm** **d_p = 3 mm**

Figure 5.8. Demonstration of Reynolds number similarity – Azimuthally-averaged radial distributions of the normalised velocity components of the three mixture components based on PEPT measurements: — X = 5 wt%; --- X = 10 wt%; -·-·-· X = 20 wt%; ⋯ X = 40 wt%; $N = N_{js}$; $Re_{imp} = 1.5\times10^5 - 2.4\times10^5$ (see Table 5.1).

5.4.1.3. Spatial distribution of solid components

The ability to predict the spatial phase distribution is of the utmost importance in modelling suspensions in stirred vessels because it impacts directly on the prediction of other important

phenomena such as heat and mass transfer. CFD predicted azimuthally-averaged axial and radial distributions of the two solid components at the 'just-suspended' state corresponding to N_{js} compared with the PEPT measurements (Guida et al. 2011) are displayed in Figs. 5.9 and 5.10, respectively. Overall, the agreement with experimental data is good, except near the base of the vessel and around the impeller. The solid distributions are largely overestimated near the base (z = 0.016H), and likewise they are largely underestimated just beneath and above the impeller (z = 0.17H, 0.33H); the errors are worse for the 3 mm particles. The worst CFD predictions occur at the lowest solid concentration of 5 wt%, but they improve significantly both axially and radially with an increase in solids loading, especially close to the tank base.

Particle lift-off from a bed of particles on the bottom of the vessel occurs as a result of the drag and lift forces exerted by the moving fluid. The flow near the base has been described as boundary layer flow which causes particles to be swept across the base of the vessel. Once small fillets of particles have been formed, particle lift-off is usually seen to be caused by sudden turbulent bursts originating in the turbulent bulk flow above. Fluid-particle interactions are dependent on the relative size of eddies and the particles. Eddies relatively large compared to the particles will tend to entrain them and are responsible for their suspension. Consequently, different agitator designs and configurations generate different convective flows and, thus, achieve different levels of solids suspension at the same power input. The complex nature of the flow field in a stirred vessel is such that there is no fundamental theory to describe the process of particle suspension. The CFD model does not incorporate all of the complex physics of particle sedimentation, particle lift-off, and particle-particle interactions and, hence, the difficulty in achieving accurate prediction of the local solid concentration near the base of the vessel.

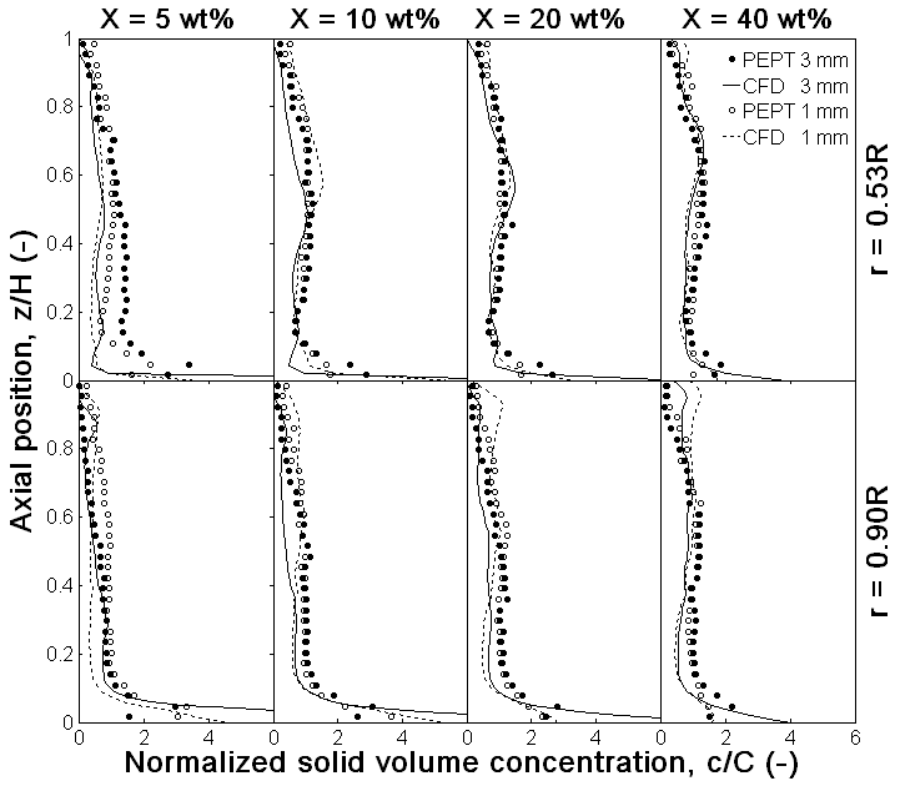

Figure 5.9. Azimuthally-averaged axial distributions of normalised solid volume concentration in suspension at N_{js}.

Considering the radial solid distributions at N_{js} shown in Fig. 5.10, the solids are nearly uniformly distributed except in the central region underneath the impeller where there is a substantial mound of accumulated solids. The axial solid distributions at N_{js} depicted in Fig. 5.9, also indicate a fairly uniform suspension in the upper part of the vessel, with the solid concentration reducing gradually upwards until it reaches zero close to the free surface. However, large concentration gradients are found in the lower part of the vessel ($z < 0.2H$). As discussed in more detail later, the homogeneity of the solid distribution at N_{js} improves when solid loading increases, and this feature is captured by CFD.

At impeller speeds above N_{js}, the uniformity of the suspension improves significantly, as shown in Fig. 5.11. The agreement between CFD predictions and PEPT measurements improves somewhat, but predictions remain rather poor near the base.

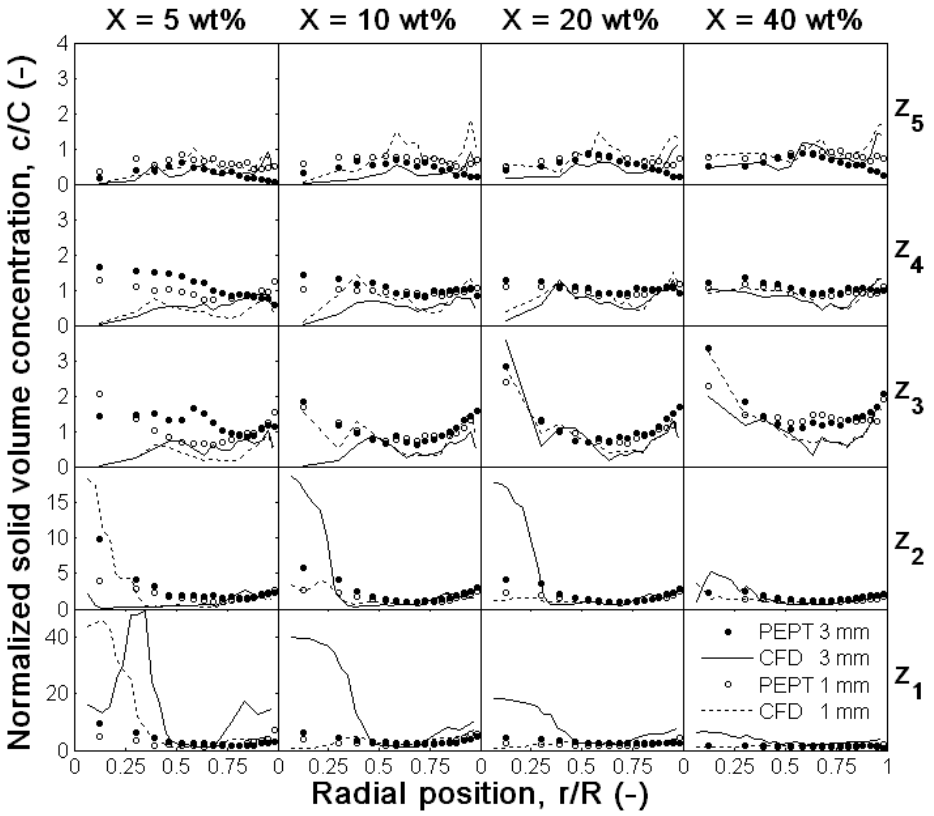

Figure 5.10. Azimuthally-averaged radial distributions of normalised solid volume concentration in suspension at N_{js}.

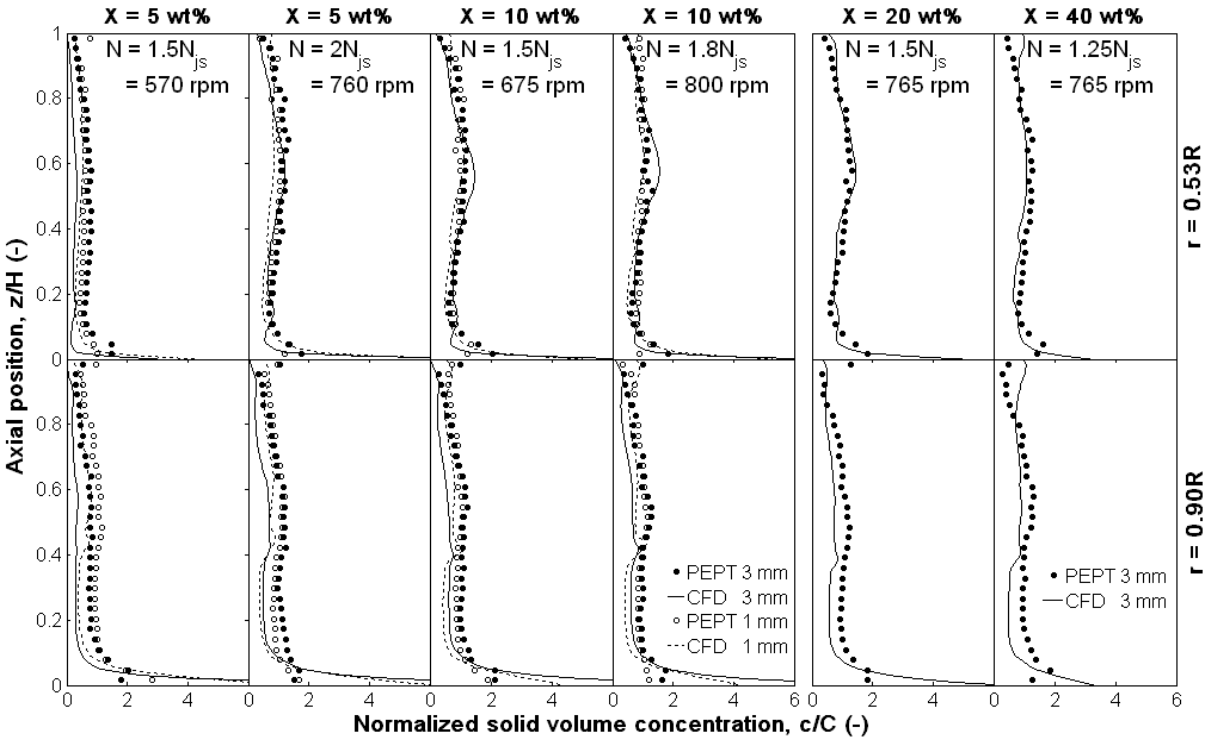

Figure 5.11. Azimuthally-averaged axial distributions of normalised solid volume concentration in suspension at $N > N_{js}$.

5.4.1.4. Impeller pumping capacity

The usual definition of the flow number used to estimate the pumping effectiveness of impellers in single-phase systems has been extended by Guida et al. (2011) to estimate the binary suspensions. These equations, as shown below, were used to assess the accuracy of the CFD predicted impeller pumping capacity in binary disperse systems agitated at $N = N_{js}$ and $N > N_{js}$ by comparing with the PEPT measurements.

The flow number is computed using:

for component 1 of the solid phase (d_p = 1 mm):

$$Fl^{(S1)} = \frac{Q^{(S1)}}{ND^3} = \frac{1}{ND^3} \int_{PBT} c_1 u_z^{(S1)} dS \tag{5.1}$$

for component 2 of the solid phase (d_p =3 mm):

$$Fl^{(S2)} = \frac{Q^{(S2)}}{ND^3} = \frac{1}{ND^3} \int_{PBT} c_2 u_z^{(S2)} dS \tag{5.2}$$

and for the liquid phase:

$$Fl^{(L)} = \frac{Q^{(L)}}{ND^3} = \frac{1}{ND^3} \int_{PBT} (1 - c_1 - c_2) u_z^{(L)} dS \tag{5.3}$$

The sum of $Q^{(L)}$, $Q^{(S1)}$ and $Q^{(S2)}$ represents the total volumetric discharge, Q, and introducing the total two-phase flow number, Fl, it follows that:

$$Fl = \frac{Q}{ND^3} = Fl^{(L)} + Fl^{(S1)} + Fl^{(S2)} \tag{5.4}$$

The computational CFD results are presented in Table 5.2 alongside the experimental PEPT values for ease of comparison.

The solid flow numbers $Fl^{(S1)}$ and $Fl^{(S2)}$ are only a small fraction of the liquid flow number $Fl^{(L)}$, but they increase proportionally to C. This is of course expected because in the calculation of the flow number, the flowrate of each phase (component) is weighted by its local volume concentration (see Eqs. (5.1), (5.2) and (5.3)). The experimentally measured values of $Fl^{(S1)}$ and $Fl^{(S2)}$ are approximately equal under all conditions investigated, meaning that both solid components (1 mm and 3 mm) are non-preferentially pumped by the PBT. The magnitude of $Fl^{(L)}$ reduces with increasing solid concentration, and so does the overall flow number Fl because of the higher proportion of heavy solids which are being pumped.

At low solid concentrations and low agitation speeds, $Fl^{(S1)}$ and $Fl^{(S2)}$ are largely underpredicted by CFD probably because of their small values which are more prone to

numerical error. Some of the discrepancy between $Fl_{PEPT}^{(s)}$ and $Fl_{CFD}^{(s)}$ is caused by the error in predicting the local particle concentration. However, the predictions improve greatly at higher mean solid concentrations or higher impeller speeds. The predictions of $Fl^{(L)}$ are very good throughout, and because of its dominance, the overall flow number Fl is also well predicted with an average error on the order of ~ 10%.

Table 5.2. Comparison of CFD predictions of flow number with PEPT measurements.

X (wt%)	N (rpm)	$Fl_{PEPT}^{(S1)}$	$Fl_{CFD}^{(S1)}$	$Fl_{PEPT}^{(S2)}$	$Fl_{CFD}^{(S2)}$	$Fl_{PEPT}^{(L)}$	$Fl_{CFD}^{(L)}$	Fl_{PEPT}	Fl_{CFD}	$\frac{Fl_{CFD}-Fl_{PEPT}}{Fl_{PEPT}}\times 100\%$
0	330*	-	-	-	-	0.870*	0.780	0.870*	0.780	-10.3
5	N_{js} = 380	0.0133*	0.0042	0.0118	0.0046	0.795*	0.766	0.8201*	0.7748	-5.5
	570	0.0115	0.0027	0.0113	0.0069	0.905	0.779	0.9278	0.7886	-15.0
	760	0.0087	0.0058	0.0094	0.0072	0.875	0.771	0.8931	0.7840	-12.2
10	N_{js} = 450	0.0221*	0.0100	0.0235	0.0174	0.755*	0.745	0.8006*	0.7724	-3.5
	675	0.0197	0.0135	0.0194	0.016	0.832	0.756	0.8711	0.7855	-9.83
	800	0.0179	0.0136	0.0163	0.0156	0.805	0.754	0.8392	0.7832	-6.67
20	N_{js} = 510	0.0489*	0.0336	0.0500	0.0382	0.783*	0.702	0.8819*	0.7738	-12.3
	765	0.0389	0.0318	-	0.0344	-	0.716	-	0.7822	-
40	N_{js} = 610	0.1080*	0.0820	0.0949	0.0883	0.565*	0.606	0.7679*	0.7763	1.09
	765	0.0852	0.0788	-	0.0830	-	0.618	-	0.7798	-

*PEPT measurements reported by Guida et al. (2011).

5.4.1.5. Distributions of particle-fluid slip velocities

Information on particle-fluid slip velocity is of real value to processing applications involving the transfer of heat or mass, such as in chemical reactions or the sterilisation of particulate food mixtures. A crude assumption often used in practice takes the free terminal settling velocity of the particle as a representative measure of its mean slip velocity (Atiemo-Obeng et al., 2004). In 3-D the magnitude of the local time-average slip velocity vector of a solid component can be estimated using PEPT (or CFD) data, thus:

$$u_s = \sqrt{\left(u_\theta^{(L)} - u_\theta^{(S)}\right)^2 + \left(u_r^{(L)} - u_r^{(S)}\right)^2 + \left(u_z^{(L)} - u_z^{(S)}\right)^2} \tag{5.5}$$

where the superscripts (L) and (S) refer to the liquid and solid phase, respectively.

Azimuthally-averaged distributions of the local time-average slip velocity, u_s, inferred from PEPT measurements at N_{js}, are presented in Fig. 5.12 at different heights in the vessel for all conditions investigated.

The difference between the slip velocity profiles of the two particle sizes shown in Fig. 5.12 can be measured by the root mean square value, thus:

$$\Delta_{rms} = \sqrt{\frac{1}{N_C}\sum_{i=1}^{N_C}\left(\frac{u_{s_1} - u_{s_2}}{u_{tip}}\right)^2} \tag{5.6}$$

Where, as before, subscripts 1 and 2 refer to the 1 mm and 3 mm solids, respectively.

At N_{js} and above it, the slip velocity varies considerably from point to point throughout the vessel. For example at 20 wt% solids at N_{js}, the slip velocity for both particle sizes is within the range 0.01-0.42 m s^{-1}. The minimum values tend to occur near the wall within a layer of fluid approximately one-baffle thick, whilst the maximum values tend to occur below the lower edge of the impeller, in the vicinity of the position (0.70R, 0.20H) corresponding approximately to the bottom of the circulation loop. These values are generally very different from the measured terminal settling velocities in stagnant fluid, i.e., u_∞ = 0.18 ms^{-1} and 0.36 ms^{-1} for the 1 mm and 3 mm particles, respectively. Even the global volume-average values of u_s (0.14 ms^{-1}; 0.18 ms^{-1}) are significantly different from the u_∞ values.

At N_{js} and at the lower solid concentrations, the larger particles with more inertia display considerably more slip than the smaller ones. This effect, however, reduces considerably at higher solid concentrations, as shown in the Δ_{rms} plot in Fig. 5.13, because at high concentrations particle-particle interactions become important and differences in velocity

reduce through particle collisions. The effect also reduces at speeds above N_{js}; again, because inter-particle interactions also gain importance at higher speeds.

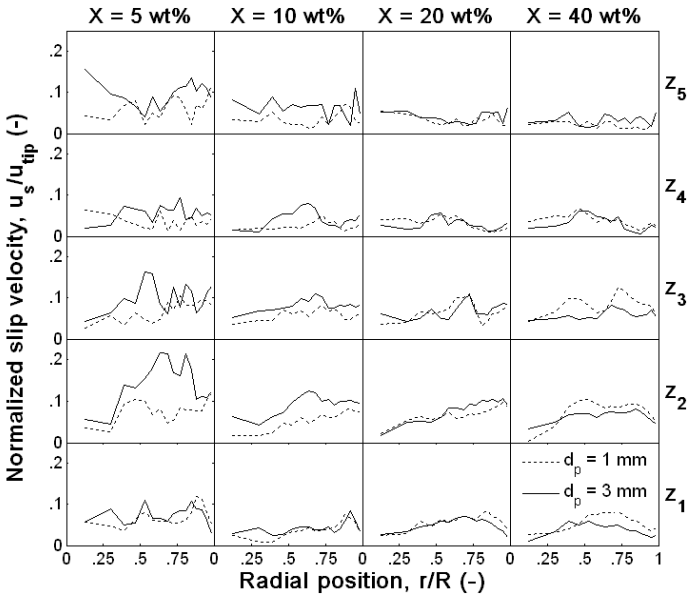

Figure 5.12. Azimuthally-averaged radial distributions of normalised time-average slip velocity based on PEPT measurements at different solid concentrations and agitation speeds.

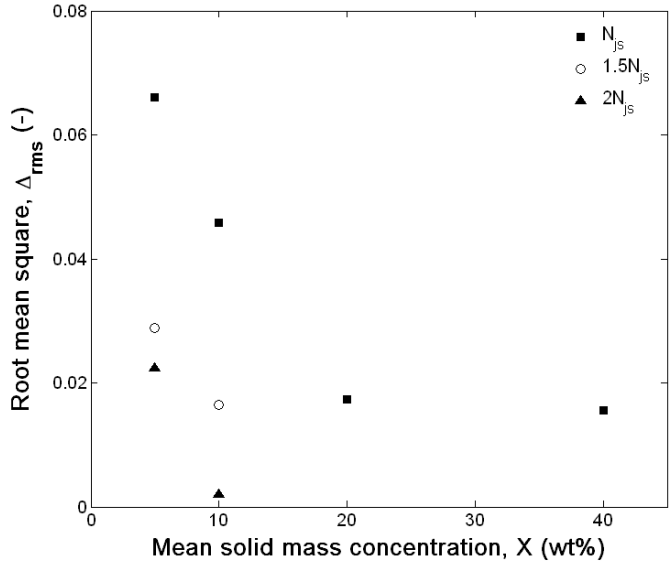

Figure 5.13. Measure of global difference in slip velocity between the two solid components in the vessel as a function of mean solid concentration.

5.4.1.6. Uniformity of suspension

5.4.1.6.1. Binary suspensions

The degree of suspension uniformity can be assessed by a global uniformity index, ξ, thus:

$$\xi = \frac{1}{\sigma^2 + 1} = \frac{1}{\frac{1}{n_c}\sum_{i=1}^{N_C}\left(\frac{c_i - C}{C}\right)^2 + 1} \tag{5.7}$$

where n_c is the total number of cells in the PEPT measurement (or CFD computational) grid and i is the cell number (Guida et al., 2009; 2010). ξ increases with the increase in the degree of uniformity of solid distribution within the vessel volume, and when $\xi = 1$ (i.e. $\sigma^2 = 0$) the solids are uniformly distributed within the vessel volume, i.e. the local solid concentration everywhere is equal to the average concentration in the vessel.

Results for the binary suspensions are plotted in Fig. 5.14. Generally, the 1 mm particles are better distributed than the 3 mm particles at all speeds except when $N >> N_{js}$. Initially ξ rises sharply as N increases above N_{js}, but a plateau is reached at high speeds and it becomes difficult to exceed $\xi \sim 0.9$, as it is hard to achieve perfect homogeneity below the impeller and near the free surface. This state of dispersion is reached at speeds significantly lower for the lighter 1 mm particles ($\sim 1.5N_{js}$) than for the 3 mm particles ($\sim 2N_{js}$).

It can also be inferred from the data in Fig. 5.14 that for a given particle size, ξ increases as a function of mean solid concentration when the suspensions are considered at the same hydrodynamic mixing regime, i.e., at their N_{js} speed or the same multiple of their respective N_{js} values. Note that the N_{js} values for the different solid concentrations investigated are displayed in Table 5.1. This seems to suggest that for a given state of suspension more concentrated suspensions will tend towards a homogeneous state simply by virtue of their increased solids loading ($C \rightarrow 1$).

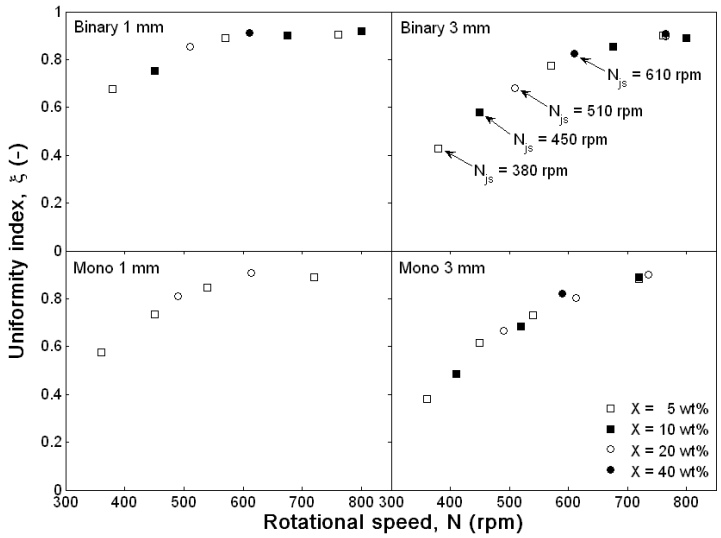

Figure 5.14. Variation of suspension uniformity index as a function of impeller speed for different particle sizes in binary- and mono-disperse suspensions.

5.4.1.6.2. Comparison of binary and mono-disperse suspensions

The suspensions of the same particles considered here but in a mono-disperse mode at the 'just-suspended' speed N_{js} and at speeds above it have been studied in Chapter IV. The spatial distributions of these particles obtained from PEPT measurements in the binary and mono-disperse modes are compared in Fig. 5.15. The distributions of the 1 mm particles do not show any significant difference at any solid concentration. The 3 mm particles, however, appear to be better distributed in the binary mixture than in the mono mixture at low to medium concentrations (5 wt% and 10 wt%), but this difference disappears at higher concentrations. Such an observation is at present difficult to explain. Compared to the binary suspension, however, significantly higher local solid concentrations are observed in the lower part of the vessel when the 3 mm particles are in a mono-disperse mode, as shown in Fig. 5.15. This maldistribution is confirmed by the uniformity index plots in Fig. 5.14 where the values of ξ for the binary suspension are significantly greater than for the mono suspension at the lower solid concentrations investigated.

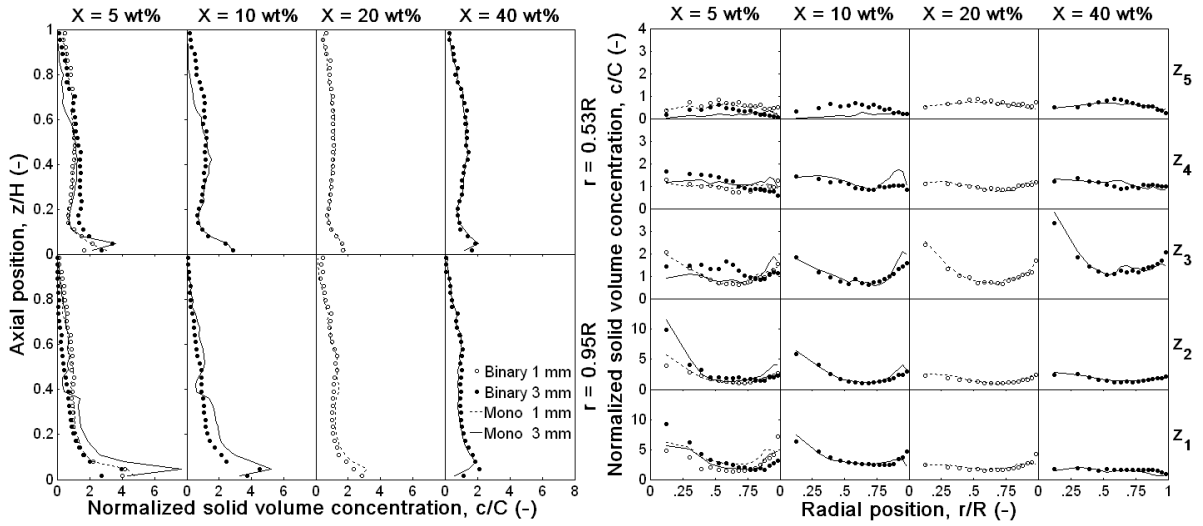

Figure 5.15. Comparison of azimuthally-averaged axial and radial distributions of normalised solid volume concentration based on PEPT measurements in binary- and mono-disperse suspensions at N_{js}.

5.4.1.7. Verification of mass continuity

An important tool for checking the accuracy and reliability of flow data is mass continuity. The net mass flux through a volume bounded by a closed surface S should be zero, thus:

$$\sum_S \mathbf{u}^{(j)} \cdot \Delta\mathbf{S} \cong 0 \tag{5.9}$$

Guida et al. (2011) applied the continuity test of PEPT measurements on two types of surfaces: 1) a closed cylindrical surface S_z with the same vertical axis, base and diameter as the tank but of a shorter height; 2) a lateral surface, S_r with the same vertical axis and height as the tank but with a smaller diameter. These two types of surfaces S_h and S_r were employed and the continuity test was applied to CFD predictions. Both the PEPT measurements (Guida et al. 2011) and CFD predictions are summarised in Fig. 5.16, showing a very good verification of the mass continuity as the velocity average across the given surface in each case is close to zero, generally less than $0.03u_{tip}$ for PEPT and even less for CFD.

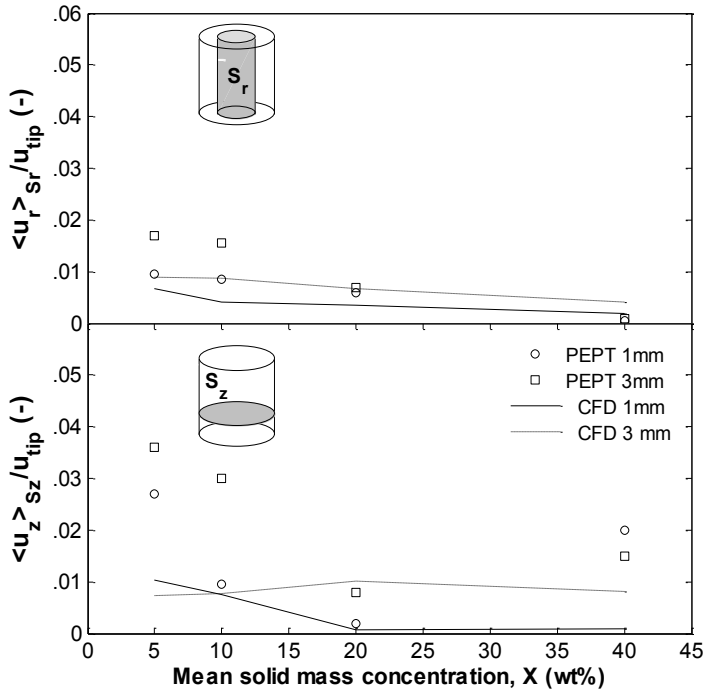

Figure 5.16. Normalised radial and axial velocities averaged on surfaces S_r (of diameter 0.5T) and S_h (0.3H off the base), respectively, showing excellent verification of mass continuity by both PEPT (Guida et al., 2011) and CFD.

5.4.2. Poly disperse

Study of the distribution behaviour of particles of different sizes in the binary disperse systems, as discussed in Section 5.4.1, shows that smaller particles are better distributed than bigger particles in the same suspension systems. Understanding the local particle size distribution, therefore, is of importance in the suspensions of multiple particle size fractions. CFD is being increasingly used in predicting solid-liquid suspensions, however, the majority of numerical studies have focused on the monodisperse systems (Sha et al., 2001; Montante and Magelli, 2005; Wadnerkar et al., 2012), while its capability of predicting hydrodynamics and particle size distributions in poly disperse systems has not been well investigated. In particular, little validation of the flow fields for both the liquid and solid phases as well as the solid distributions can be found in the literature. Lack of numerical research in this area is

either due to the significantly high requirements of computing resources or because the relevant experimental data use for validation is unavailable.

The detailed 3-D velocity fields of both the continuous and discrete phase, and the spatial phase distributions in suspensions of nearly-monomodal and nearly-spherical glass beads of five different sizes (d_p ~ 1 mm; ~ 1.7 mm; ~ 2.2 mm; ~ 2.7 mm; ~ 3 mm) having a density of 2485 kg m^{-3}, at a mean solid concentration ranging from X = 5 wt% to X = 40 wt%, were numerically simulated at the 'just-suspended' speed N_{js}. The five solid mixture components were mixed in equal proportions, i.e. $X_1 = X_2 = X_3 = X_4 = X_5 = 0.2X$. The numerical strategies are the same as those used for modelling the binary suspensions and the numerical results are compared to the PEPT measurements.

5.4.2.1. Distributions of local velocity components

The experimental and numerically predicted velocity distributions for the liquid and solid phases are compared in Fig. 5.17, for the six mixture components at the solid concentration of 5 wt%. It can be seen that all six mixture components present highly similar flow patterns, and the velocity distributions are very well predicted by CFD as the agreement with PEPT is very good. There are somewhat discrepancies between CFD and PEPT concerning the axial component u_z, which become more severe with increasing particle size. This has also been found in the mono- and binary-disperse of larger particles, as discussed in Chapter IV and Section 5.4.1. It has been reported that this is primarily caused by the significant reduction of the number density of particles with the increase in particle diameter that causes the assumption of a continuum inherent in the Eulerian-Eulerian model less realistic.

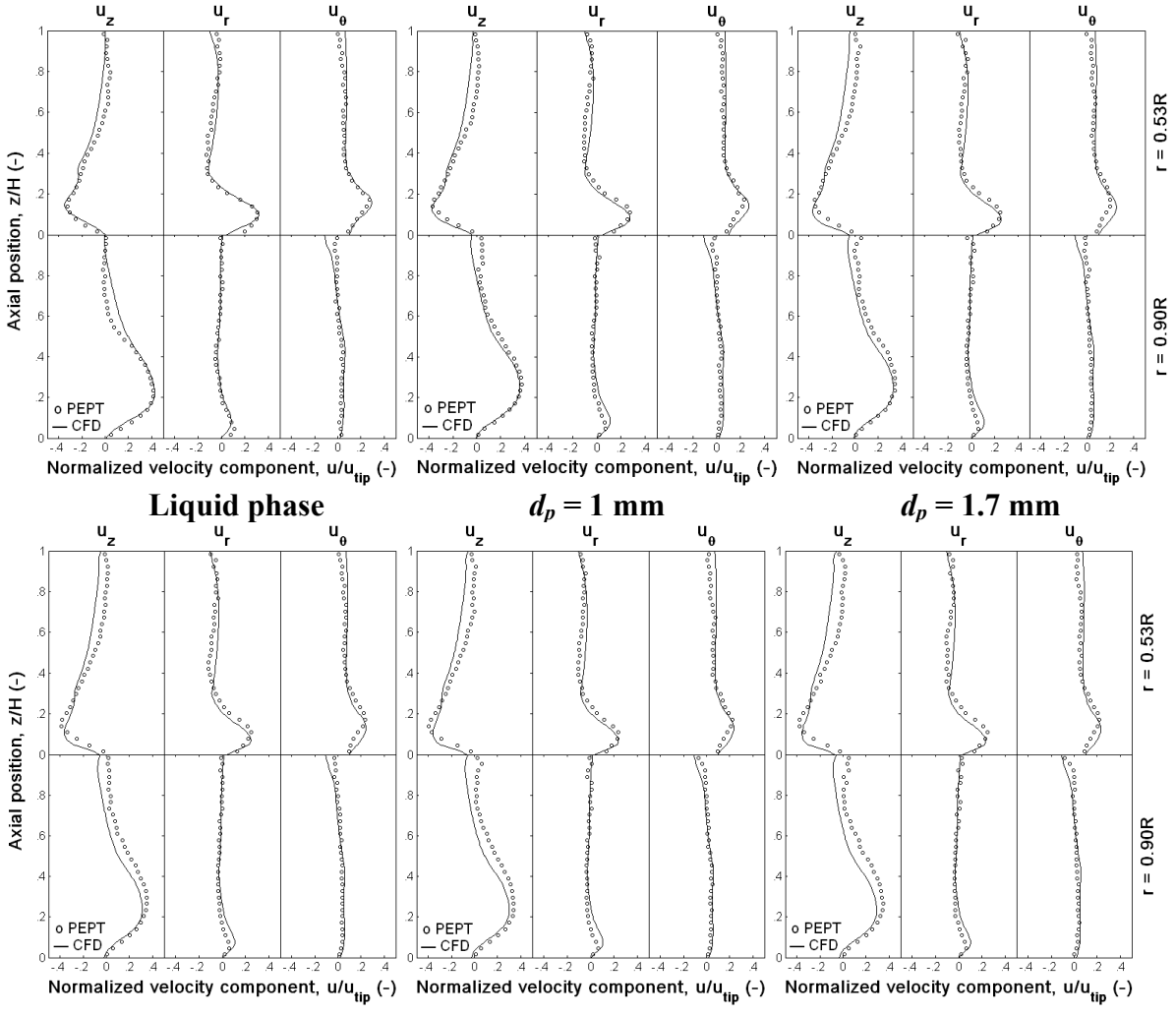

Figure 5.17. Azimuthally-averaged axial distributions of the normalised velocity components of the liquid and solid components at N_{js}: X = 5 wt%; N_{js} = 380 rpm.

The numerically predicted axial velocity distributions at N_{js} for solid concentrations of 10 wt%, 20 wt% and 40 wt%, are compared to the experimental distributions in Figures 5.18, 5.19 and 5.20, respectively. The distributions are similar to those observed at 5 wt% solids. This could be attributed to the Reynolds number similarity, as discussed in section 5.4.1.2. It can also be seen that the numerical predictions of the axial component u_z improves significantly with X, becoming very good at X = 20 wt% and X = 40 wt%. As X increases, the

solid phase tends to behave increasingly more like a continuum, thus, improving the suitability of the Eulerian-Eulerian model.

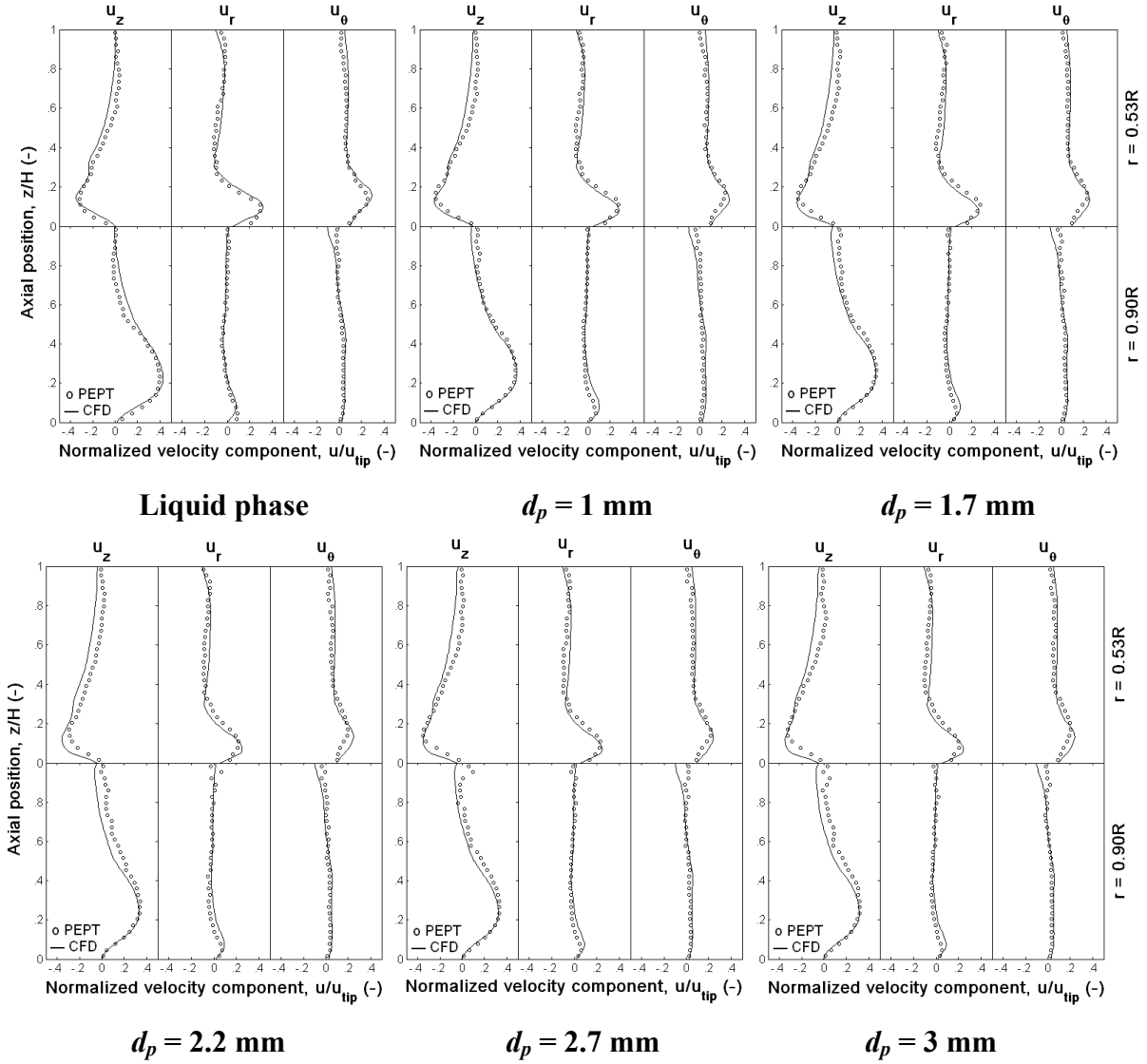

Liquid phase **d_p = 1 mm** **d_p = 1.7 mm**

d_p = 2.2 mm **d_p = 2.7 mm** **d_p = 3 mm**

Figure 5.18. Azimuthally-averaged axial distributions of the normalised velocity components of the liquid and solid components at N_{js}: X = 10 wt%; N_{js} = 450 rpm.

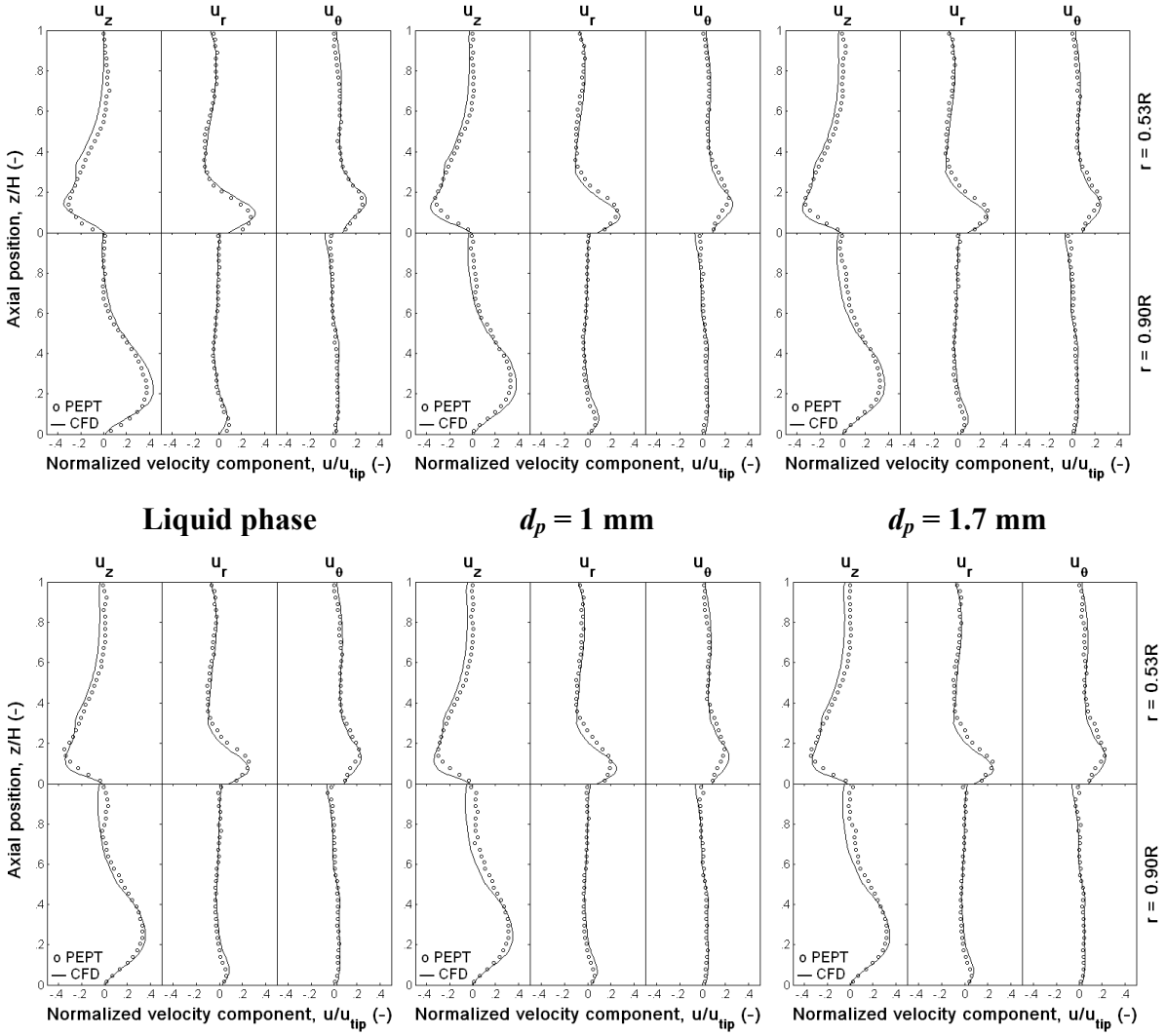

Liquid phase d_p **= 1 mm** d_p **= 1.7 mm**

d_p **= 2.2 mm** d_p **= 2.7 mm** d_p **= 3 mm**

Figure 5.19. Azimuthally-averaged axial distributions of the normalised velocity components of the liquid and solid components at N_{js}: X = 20 wt%; N_{js} = 510 rpm.

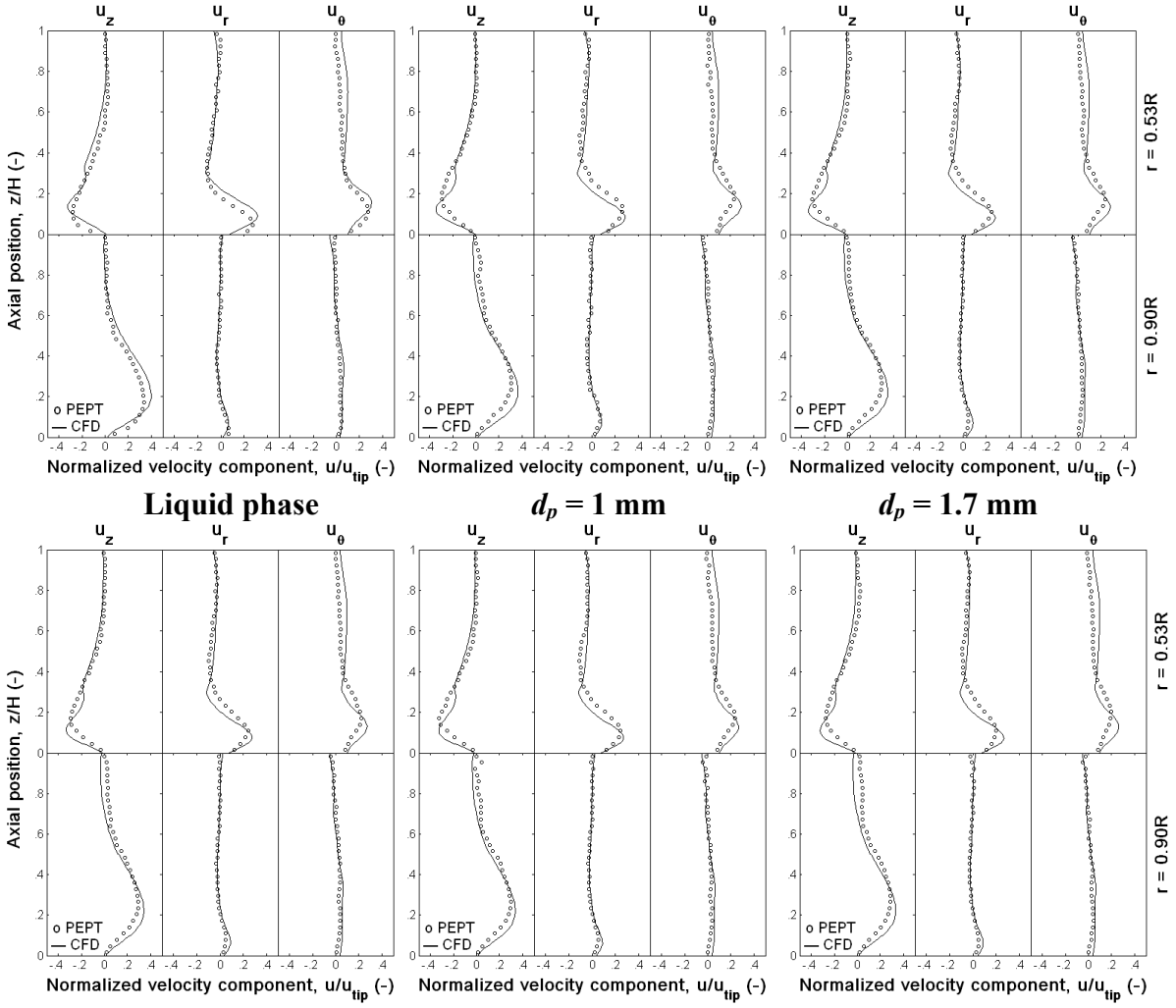

Figure 5.20. Azimuthally-averaged axial distributions of the normalised velocity components of the liquid and solid components at N_{js}: X = 40 wt%; N_{js} = 610 rpm.

5.4.2.2. Spatial distributions of solid components

The azimuthally-averaged radial distributions of the five size fractions at the 'just-suspended' state corresponding to N_{js} are displayed in Fig. 5.21, Fig. 5.22, Fig. 5.23 and Fig. 5.24, respectively. At low to medium concentrations (5 wt% and 10 wt%), the solid distributions just above ($z = 0.33H$) and below the impeller ($z = 0.17H$) are significantly underpredicted for all five size fractions by CFD modeling. In the upper region, away from the impeller, however, the agreement improves substantially and tends to be very good. This has also been

found in the mono-and binary-disperse systems, and has been discussed in detail in Chapter IV and Section 5.4.1.3. The numerical predictions of solid concentration distributions improve significantly with an increase in solids loading, becoming very good at $X = 40$ wt%.

For each solid concentration, the distributions of the five particle size fractions present high similarity. This seems to indicate that the particle size has little effect on the particle distributions in stirred vessel. In order to present this more clearly, the spatial distributions of the five solid components were investigated, and the maps of the azimuthally averaged solid concentrations, at $X = 5 – 40$ wt% are shown in Figure 5.25.

The stirred tank is divided into 5×10 square boxes containing the solid concentrations of the six mixture components. Each square box contains five bars, and from left to right, they represent $d_p = 1$ mm, 1.7 mm, 2.2 mm, 2.7 mm and 3 mm, respectively. The area of each bar is equal to the local volume of the corresponding solid component, and the white area is equal to the local liquid volume. The width of the colored bars in each map are equal, therefore, the height of each bar is proportional to the volume concentration of the corresponding solid component so that can be used for the investigation of particle size distributions.

A large proportion of solid particles, especially larger particles ($d_p \sim 2.7$ mm; ~ 3 mm), accumulated in the central region underneath the impeller at all concentrations studied. This effect is more pronounced at low solid concentration, $X = 5$ wt%, as the rest square boxes are nearly blank indicating few particles suspended in the bulk region of the stirred tank. A clear mound of solid accumulation can also be seen in the corner of the tank wall and tank base that has been known as the dead zone within a baffled tank.

The fraction of solid particles in the upper part of the stirred vessel increases significantly as the mean solid concentration increases, though the solid accumulation underneath the impeller

is still high. At X = 40 wt%, the spatial distributions of each particle size fraction in the stirred vessel are much more uniform.

A detailed comparison of the particle size distribution in each square box shows that the local volume concentration of each solid component is equivalent, except underneath the impeller where the accumulation of larger particles (d_p ~ 2.7 mm; ~ 3 mm) is more than the smaller particles (d_p ~ 1 mm). This effect, however, reduces significantly as the mean solid concentration increases, and at X = 40 wt%, the five particle size fractions are nearly equally distributed throughout the stirred tank. This could be attributed to an increase in the particle-particle interactions as the mean solid concentration increases.

The coloured bars that represent the azimuthally-averaged and vertically-averaged solid concentrations are drawn in the top square boxes. The right square boxes show the azimuthally-averaged and radially-averaged solid concentrations. There are considerable concentration gradients in the vertical direction, which is more pronounced at low to moderate X values, while the radial distributions of solid particles are fairly flat. The five particle size fractions are nearly equal in each of the top and right square boxes.

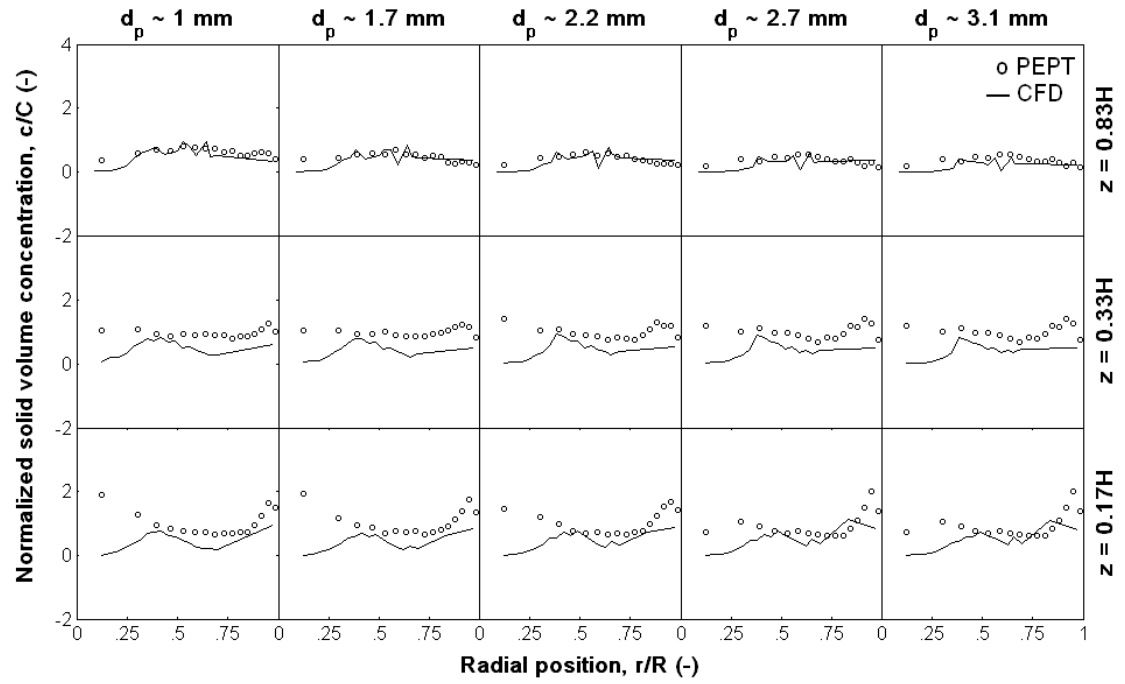

Figure 5.21. Azimuthally-averaged radial distributions of normalised solid volume concentration in suspension at N_{js}: X = 5 wt%; N_{js} = 380 rpm.

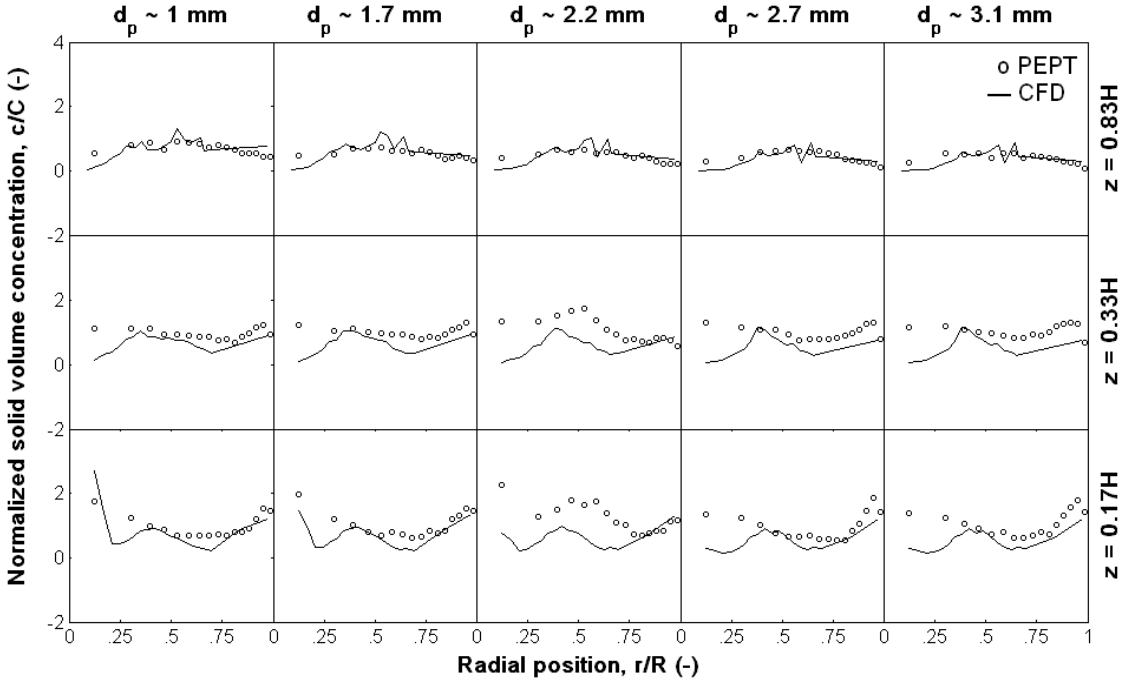

Figure 5.22. Azimuthally-averaged radial distributions of normalised solid volume concentration in suspension at N_{js}: X = 10 wt%; N_{js} = 450 rpm.

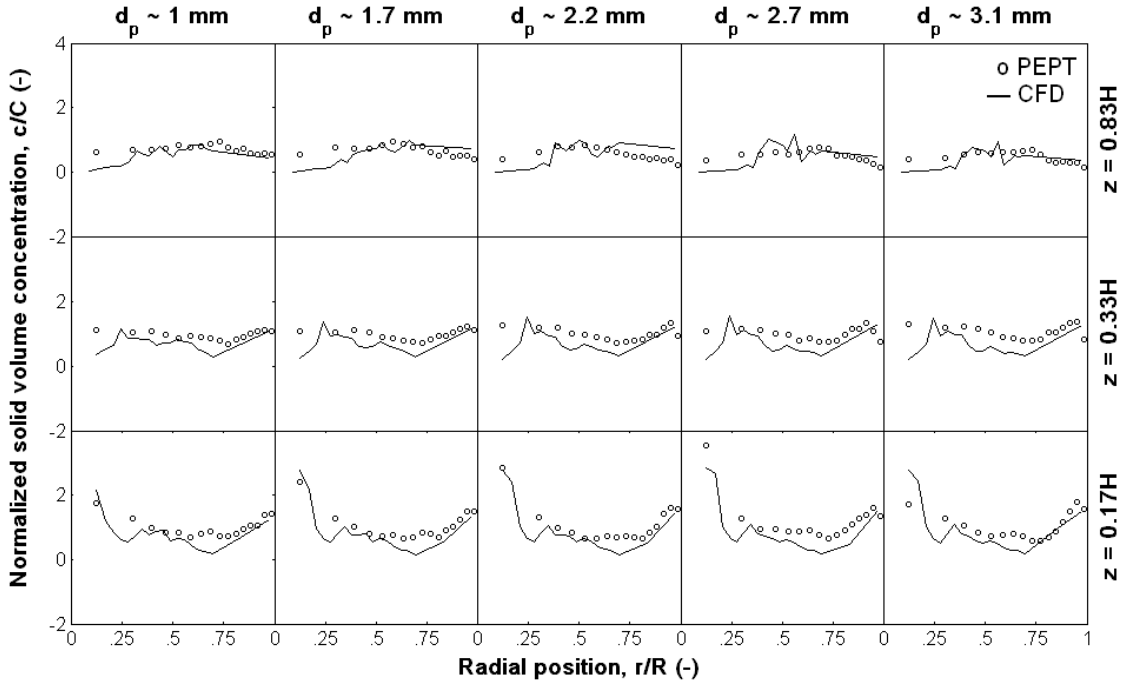

Figure 5.23. Azimuthally-averaged radial distributions of normalised solid volume concentration in suspension at N_{js}: X = 20 wt%; N_{js} = 510 rpm.

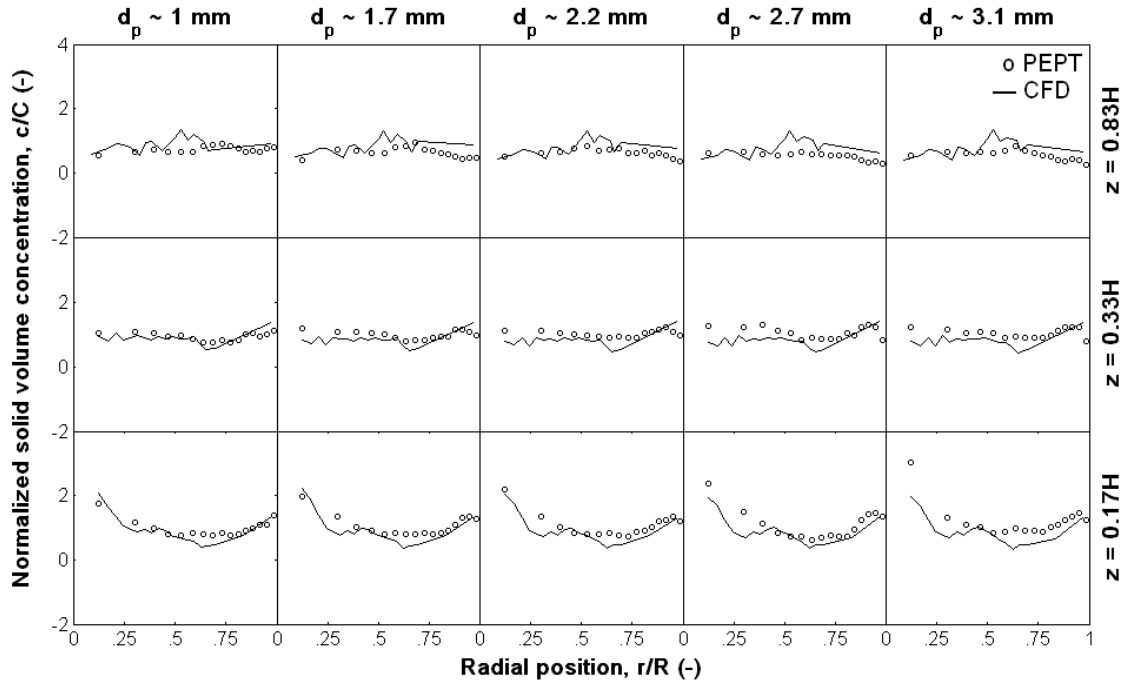

Figure 5.24. Azimuthally-averaged radial distributions of normalised solid volume concentration in suspension at N_{js}: X = 40 wt%; N_{js} = 610 rpm.

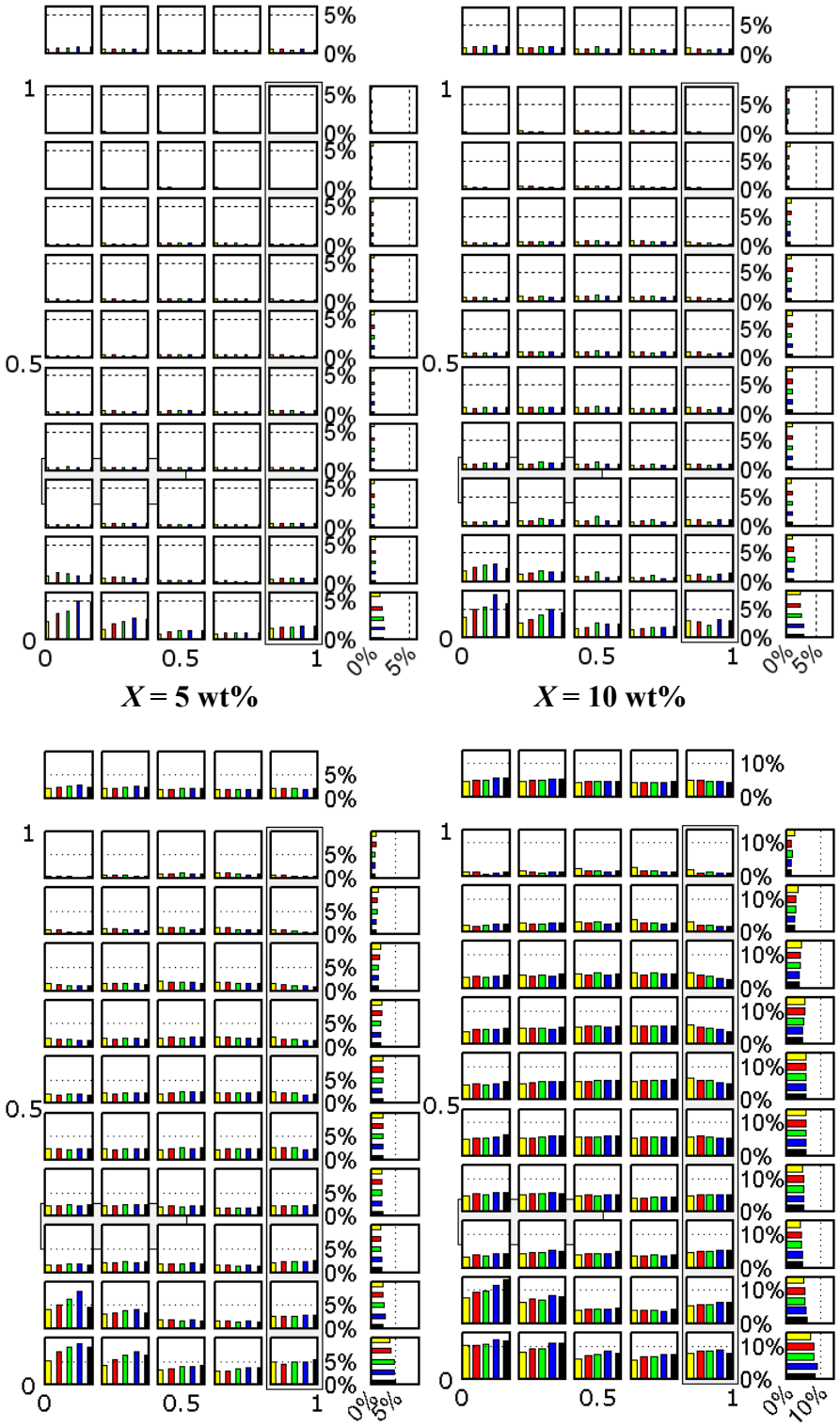

Figure 5.25. Azimuthally-averaged local volume concentration maps for the poly disperse systems at varying *X*: yellow, d_p ~ 1 mm; red, d_p ~ 1.7 mm; green, d_p ~ 2.2 mm; blue, d_p ~ 2.7 mm; black, d_p ~ 3 mm.

5.5. Conclusions

The three-component flow fields in mechanically agitated dense binary suspensions have been successfully modelled by CFD. The local velocity components of all the mixture components agree very well with PEPT measurements throughout the stirred vessel at N_{js} and at speeds above it. This has also led to accurate predictions of the flow numbers. Furthermore, the Reynolds number similarity was found to hold for all components of the two-phase flow under all conditions investigated.

The spatial distribution of the solid phase is well predicted except close to the base of the vessel and around the impeller where it is largely overestimated. However, the predictions improve significantly at higher solid concentrations as the Eulerian assumption of a continuum gains more significance. Generally, the smaller particles are better distributed than the larger ones except when $N >> N_{js}$. The uniformity of suspension improves sharply as N increases above N_{js}, but a plateau is reached at high speeds and it becomes difficult to reach 100% homogeneity, as it is hard to distribute particles below the impeller and near the free surface. In addition, uniformity increases as a function of mean solid concentration when suspensions are considered at the same hydrodynamic mixing regime, i.e. at their N_{js} speeds or the same multiple of their respective N_{js} values.

The local slip velocity varies widely within the vessel and is generally very different from the particle terminal settling velocity. At N_{js} and at lower solid concentrations, the larger particles with more inertia display considerably more inter-phase slip than the smaller particles.

This effect, however, reduces considerably with an increase in solid concentration and impeller speed as particle-particle interactions become important.

The dense poly suspensions in mechanically agitated stirred vessel have also been successfully modelled by CFD. The local velocity components of all the mixture components agree very well with PEPT measurements throughout the stirred vessel at N_{js}. The spatial distributions of the five particle size fractions present high similarity indicating little effect of particle size on the particle distributions in the stirred vessel.

Nomenclature

c	local volume concentration of solids	-
C	mean volume concentration of solids	-
d_p	particle diameter	m
D	impeller diameter	m
Fl	multiphase-phase flow number (Q/ND^3)	-
$Fl^{(L)}$	liquid flow number ($Q^{(L)}/ND^3$)	-
$Fl^{(S1)}$	1 mm solid flow number ($Q^{(S1)}/ND^3$)	-
$Fl^{(S2)}$	3 mm solid flow number ($Q^{(S2)}/ND^3$)	-
H	height of suspension	m
N	impeller rotational speed	s^{-1}
N_{js}	minimum speed for particle suspension	s^{-1}
Q	impeller pumping rate	$m^3\ s^{-1}$
r	radial distance	m
R	vessel radius	m
Re_{imp}	impeller Reynolds number (ND^2/v)	-
T	vessel diameter	m
u_s	slip velocity	$m\ s^{-1}$
u_∞	terminal settling velocity	$m\ s^{-1}$
u_{tip}	impeller tip speed	$m\ s^{-1}$
$u_r\ u_z\ u_\theta$	cylindrical velocity components	$m\ s^{-1}$
X	mean mass concentration of solids	-

z	vertical distance	m

Greek letters

v	kinematic liquid viscosity	$m^2\ s^{-1}$
ξ	uniformity index	-
σ	standard deviation of normalised c	-
θ	azimuthal coordinate	rad
Δ_{rms}	root mean square	

Chapter VI

NUMERICAL STUDY OF HERSCHEL-BULKLEY FLUID MIXING IN STIRRED VESSELS COMPARED WITH DIFFERENT TECHNOLOGICAL MEASUREMENTS

Abstract

Mixing of viscoplastic fluids in stirred vessels agitated by RDT, and by PBT in both the down- and up-pumping modes in the laminar and transitional regimes has been numerically investigated. The numerical results are compared to detailed distributions of velocity components measured by PIV and PEPT, and the CFD predicted cavern size and shape at various Reynolds numbers are compared with PLIF measurements reported by Adams and Barigou (2007). PEPT measurements are also carried out to obtain the cavern which is used for the validation of CFD modelling. Effects of impeller size, impeller bottom clearance, and the rheological parameters of viscoplastic fluids on the cavern shape and size as well as the velocity field within the cavern are investigated. It has been found that increasing impeller size performs better than increasing the impeller speed accounting for the cavern growth. Higher impeller position generates larger cavern volume in the PBTD mode, however, it has the opposite effect on the cavern size in the PBTU mode. The rheological parameters have significant effects on the cavern size, especially the apparent yield stress and the flow behaviour index. The positions of the interfaces connecting the rotating domain and the stationary domain have been found to affect the accuracy of CFD prediction of cavern size

and shape significantly. The cavern size and shape are not affected by impeller type at low Reynolds number due to the predominant tangential flow.

6.1. Introduction

Mixing of viscoplastic fluids (also termed yield stress fluids) in stirred vessels is commonly encountered in paint, cosmetic, catalyst, food and polymerization industries. Apart from the characteristic of viscosity varying with shear rate, viscoplastic fluids also exhibit an apparent yield stress, therefore, it is essential for the external forces to overcome the apparent yield stress for the viscoplastic fluids to flow, or they behave like solid. A number of difficult mixing problems with the mixing of viscoplastic fluids have been widely reported in literature (Amanullah et al., 1997; Arratia et al., 2006).

Cavern formation around the impeller is a unique characteristic of mixing of viscoplastic fluids in stirred vessels. The term cavern was first used by Wichterle and Wein (1975) to describe the mobile zone around the impeller. However, fluid mixing is merely constrained within the cavern, and there is no fluid motion beyond the cavern boundary due to the apparent yield stress. Poor mixing in the dead regions in stirred vessels is detrimental to mixing efficiency, therefore, these regions need to be well examined in order to eliminate these areas to improve mixing quality. Many studies have been carried out to relate the cavern size and shape to the key impact factors such as the power input and the apparent yield stress, and different mathematical models have been developed, e.g. cylindrical model (Elson and Cheesman, 1986; Elson, 1990; Nienow and Elson, 1988), spherical model (Solomon, 1981; Amanullah et al., 1998), and toroidal model (Amanullah et al., 1998; Wilkens et al., 2005). These models have been widely used to calculate the necessary power consumption for eliminating the dead zones.

Different experimental techniques have been used for investigating the cavern size and shape in the mixing of viscoplastic fluids. Simple photographic methods were used to visualize the cavern (Galindo and Nienow, 1992; Galindo et al., 1996). This method involves the injection of a dye solution and the visual observation of the process of its distribution. Adams and Barigou (2007) employed the optical PLIF technique to investigate the cavern size and shape at various Reynolds numbers. These optical measurements, however, require transparent systems, and could not be practically used in industry. ERT and PEPI can be used for opaque fluid mixing, and the cavern size and shape measured by these two techniques has been reported in the literature (Pakzad et al., 2008; Patel et al., 2013; Pakzad et al., 2013; Simmons et al., 2009).

However, the velocity distributions within the cavern, which are important to assess the mixing efficiency, have only been experimentally measured in very few works (Arratia et al., 2006; Ihejirika and Ein-Mozaffari, 2007; Ein-Mozaffari and Upreti, 2009) using ultrasonic Doppler velocimetry measurements.

As a powerful tool, CFD modelling has been employed in many studies to investigate the complex mixing of viscoplastic fluids in stirred vessels over the past several years. In order to use the CFD predictions confidently in practical applications, extensive validations need to be carried out. It has been discussed in Chapter III that CFD modelling of Newtonian fluid mixing in stirred vessels has been well validated in a number of studies, however, the validation of CFD modelling of mixing of viscoplastic fluids reported in the literature has been very limited and has relied mostly on global empirical data, like the power number (Prajapati and Ein-Mozaffari, 2009). The validation of CFD predicted velocity distributions

within the cavern is limited in literature (Moore and Cossor, 1995; Ihejirika and Ein-Mozaffari, 2007; Saeed et al., 2008; Ein-Mozaffari and Upreti, 2009).

In this chapter, mixing of viscoplastic fluids in mechanically agitated vessels is studied by CFD modelling. The CFD predicted cavern size and shape, the velocity distributions within the cavern, and the process of tracer distribution within the cavern are well validated by comparing with different experimental techniques. It should be noted that apart from PIV and PEPT measurements carried out by the author, the experimental data reported by Guida (2010) Adams and Barigou (2007) obtained from PEPT and PLIF measurements are also used to validate the CFD predictions in this study. Their work is marked with symbol * and ** in Table 6.1, respectively. The effects of impeller type, impeller size, impeller bottom clearance, and the rheological parameters on mixing of viscoplastic fluids are investigated experimentally and numerically.

6.2. Materials and methods

6.2.1. Mixing vessel and fluid rheology

Investigations on mixing of viscoplastic fluids were carried out in stirred vessels of two dimensions, as listed in Table 6.1. Both vessels were equipped with four baffles of width $0.1T$ and thickness $0.01T$. The liquid heights were set at $H = T$ in both vessels. Three six-bladed 45° down-pumping pitched-blade turbines (PBT) were employed, with geometrical parameters as listed in Table 6.1:

(i) the smallest impeller of $D = T/3$ and medium sized impeller of $D = T/2$, as displayed in Fig. 6.1 (a) and Fig. 6.1 (b), respectively, were used in the smaller vessel. The smallest impeller was used in the CFD modeling of cavern shape and size with increasing Reynolds number until the cavern reaches the tank wall, and these CFD predictions are compared with

PLIF and PEPT measurements reported by Adams and Barigou (2007) and Guida (2010), respectively;

(ii) the medium sized impeller was used in the CFD modeling of the cavern growing upward after reaching the tank wall until the fluid is in motion throughout the stirred vessel, and these CFD predictions are compared with the PEPT measurements. Moreover, the medium sized impeller was located at two positions, i.e. $T/3$ and $T/4$ from the tank bottom, to investigate the effect of impeller bottom clearance on the cavern size and velocity fields within cavern; and

(iii) the largest impeller was used in the larger vessel for the verification of both the PEPT measurements and CFD modeling of mixing of viscoplastic fluids by comparing with the velocity distributions obtained from the well-established PIV technique.

An aqueous solution of 0.1 wt% carbopol 940 (B. F. Goodrich Co.) was used to prepare the viscoplastic fluids. The initial carbopol solution with pH of ~ 3.0 does not perform as a viscoplastic fluid, and the pH of carbopol solution needs to be adjusted by properly adding aqueous sodium hydroxide (NaOH) for the liquid to exhibit apparent Herschel-Bulkley behavior. The adjustment process was examined using a pH meter with great caution since the rheology of the carbopol solution is very sensitive to the pH value (Curran et al., 2002). The rheological properties of fluid samples taken from the stirred tank were measured by a 2° 60 mm cone and plate geometry using a stress controlled rheometer (AR-1000, TA Instruments). The rheological properties of the viscoplastic fluids in the PEPT measurements are listed in Table 6.2. It should be noted that the pH value of the carbopol solution was altered after the carbopol solution was transferred to the mixing vessel to avoid the entrapment of air bubbles.

Table 6.1. Dimensions of stirred vessels used in PLIF, PIV, PEPT measurements and CFD simulations.

Stirred vessels	T (mm)	H (mm)	D (mm)	W (mm)	B (mm)
Smaller vessel*	150*	150*	50*	10*	15*
	150	150	75	10	15
Larger vessel	190	190	104	23	19

*PEPT and PLIF measurements are reported by Guida (2010) and Adams and Barigou (2007), respectively.

Table 6.2. Rheological parameters in PEPT measurements and CFD simulations.

Stirred vessels	Liquid	pH	τ_y (Pa)	k (Pa s^n)	n	N (rpm) (Re_{imp})
Smaller vessel	Carbopol*	4.6	-	-	-	200 (76.3)
	Carbopol**	4.6	2.63	0.54	0.56	(7.3)
	Carbopol**	4.6	1.41	0.37	0.57	(20.4)
	Carbopol**	4.6	1.29	0.35	0.57	(70.3)
	Carbopol**	4.6	1.56	0.45	0.55	(86.6)
	Carbopol**	4.6	1.97	0.37	0.58	(163.2)
	Solution 1	4.35	0.748	0.258	0.608	200 (223) 320 (455)
	Solution 2	4.56	1.697	0.431	0.589	200 (130) 320 (273)
Larger vessel	Carbopol solution in PEPT	4.6	1.24	0.23	0.69	65 (56)
						125 (159)
						180 (280)
	Carbopol solution in PIV	4.6	1.3	0.3	0.62	65 (52)
						125 (152)
						180 (273)

* PEPT and PLIF measurements reported by Guida (2010).
** PLIF measurements reported by Adams and Barigou (2007).

6.2.2. PEPT and PIV measurements

A neutrally-buoyant resin particle tracer (600 μm) labelled with ^{18}F by Ion exchange with water irradiated in a cyclotron was used to track the 3-D trajectories of mixing of viscoplastic fluids. Due to the less effective transportation of the particle tracer under the transitional regime caused by the lack of turbulence, the tracking time in each PEPT experiment was at least 60 min to ensure the runtime is long enough for the particle tracer to reach all areas

within the cavern. It should be noted that the more viscous the fluid, or the lower the Reynolds number, the longer the runtime required. More detailed descriptions of PEPT measurements have been reported in Chapter IV and Chapter V, and mixing of viscoplastic fluids measured by PEPT have also been reported by Adams (2009) and Guida (2010). PIV set-up for measuring the mixing of viscoplastic fluids in stirred vessels is similar to that for mixing of shear-thinning fluids in stirred vessels, and the detailed descriptions of PIV measurements have been reported in Chapter III.

6.3. Numerical modelling

The exact same configurations of the stirred vessels used in the experimental measurements were built using the DesignModeler in the ANSYS CFX package. The MFR approach which has been widely used in the CFD modeling of single phase mixing of viscoplastic fluids in stirred tanks (Pakzad et al. 2008; Saeed et al., 2007; Adams and Barigou, 2007) was employed to deal with the interaction between the stationary baffles and the rotating impeller blades for all conditions investigated. The rotating domain contains all the rotating elements (hub, blades and shaft) and the stationary domain contains the stationary parts (baffles, tank wall and base). The two domains are separated by three interfaces, a vertical cylindrical interface at r = 30 mm, and two horizontal interfaces at z = 40 mm and 60 mm from tank base when the smaller impeller was used, as displayed in Fig. 6.1(a), similarly, cylindrical interface at r = 50 mm, and two plane horizontal interfaces at z = 53 mm and 23 mm from the tank base when the medium impeller was used, as displayed in Fig. 6.1(b). The computational grid consisted of 723,920, and 805,440 non-uniformly distributed unstructured tetrahedral cells for the smaller stirred tank agitated by the smaller impeller and medium impeller, respectively, as illustrated in Fig.6.1 (a) and Fig.6.1 (b). A denser mesh is used in the rotating domain for

better accuracy, because this region is characterized by high velocity gradients. Inflated boundary layers were used on the tank bottom, walls, baffles, blades and shaft to cover the high velocity gradients in these regions of no slip. The detailed configuration and mesh information for the larger vessel agitated by the largest impeller is illustrated in Fig. 3.1 in Chapter III. Numerical simulations were performed using the commercial CFD code ANSYS CFX 12.0. Numerical convergence was assumed when the sum of all normalized residuals fell below 10^{-6} for all equations.

Due to the dependence of the viscosity of the viscoplastic fluids on the shear rate, an additional correlation that describes the relationship between the apparent viscosity and the shear rate needs to be solved simultaneously with the continuity and momentum equations. The Herschel-Bulkley model was used to describe the rheology of viscoplastic fluids in the CFD modelling, and the shear stress, τ, as a function of the shear rate, $\dot{\gamma}$, is given by

$$\begin{aligned} \tau &= \tau_y + k\dot{\gamma}^n \qquad for\, \tau > \tau_y \\ \dot{\gamma} &= 0 \qquad\qquad for\, \tau \le \tau_y \end{aligned} \tag{6.1}$$

thus,

$$\eta = \frac{\tau_y + k\dot{\gamma}^n}{\dot{\gamma}} \tag{6.2}$$

where τ_y is the yield stress, k is the fluid consistency coefficient and n is the flow behaviour index. Equation (6.2) was implemented into the CFD simulation using the expression language feature in the ANSYS CFX 12.0. All equations were solved using the finite volume method. It should be noted that the format of equation (6.2) cannot be used directly, since it is not suitable for the regions where the shear rate drops to zero. In order to avoid division by zero, a constant arbitrary value shear rate, 10^{-8}, was used if the shear rate dropped below this

value for calculating the apparent viscosity at $\dot{\gamma} = 0$. All simulations were conducted using the laminar model, which has been widely accepted to be suitable for modeling the transitional regime (Pakzad et al. 2008; Kelly and Gigas, 2003; Letellier et al., 2002; Zalc et al., 2001).

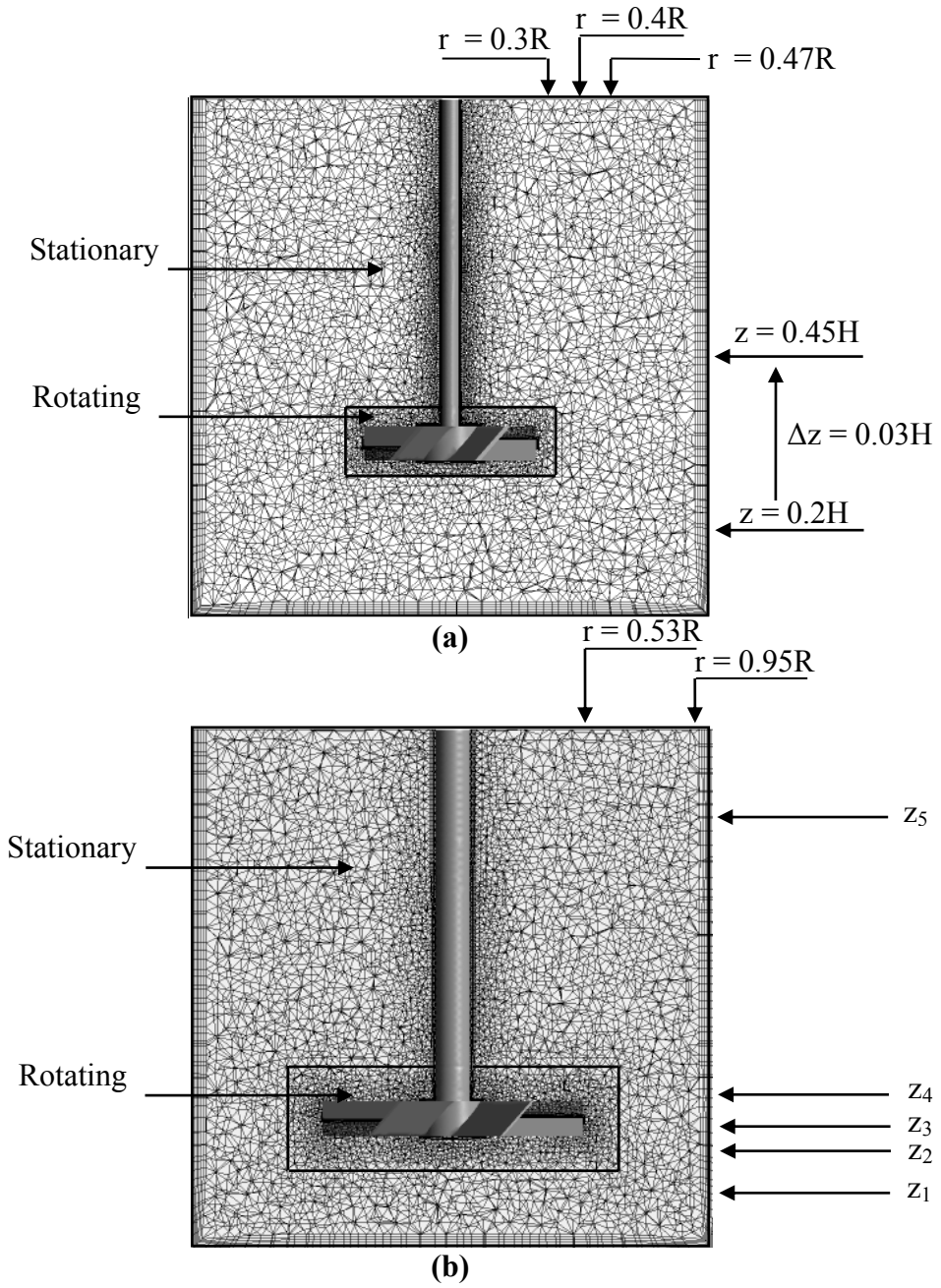

Figure 6.1. Computational grid section in the 45° plane between two baffles: (a) smaller tank with the smallest impeller; (b) smaller tank with the medium impeller.

6.4. Results and discussion

6.4.1. CFD predicted velocity field compared with PEPT

A detailed quantitative comparison between the CFD predictions and PEPT measurements was conducted at the positions depicted in Fig. 6.1(a). The azimuthally-averaged distributions of the local velocity components (u_z, u_r, u_θ) were compared:

(i) axially along three radial positions: $r = 0.3R$ which is within the impeller swept region, $r = 0.4R$ which is close to the tip of the impeller, and $r = 0.47R$; and

(ii) radially along nine axial positions: $z = 0.2H$, $z = 0.23H$, and $z = 0.27H$, below the impeller; $z = 0.3H$, $z = 0.33H$, and $z = 0.36H$, within the impeller blade width; $z = 0.39H$, $z = 0.42H$, and $z = 0.45H$, above the impeller. All the velocity plots presented have been normalized by the impeller tip speed ($u_{tip} = \pi DN$).

Fig. 6.2 illustrates the velocity field within the cavern around the impeller obtained on the basis of PEPT measurement at $N = 200$ rpm. The individual velocity components in the r, z, and θ directions are also displayed. These velocity vector plots from PEPT measurement were obtained by projecting the azimuthally-averaged 3D velocity onto the 2D plane. It can be seen that the fluid motion is constrained to a small flow loop close to the impeller, and the liquid flows predominantly in the tangential direction. The predominant tangential flow regardless of impeller type in the mixing of viscous non-Newtonian fluids in stirred vessels has been reported by some researchers (Elson, 1990; Moore and Cossor, 1995).

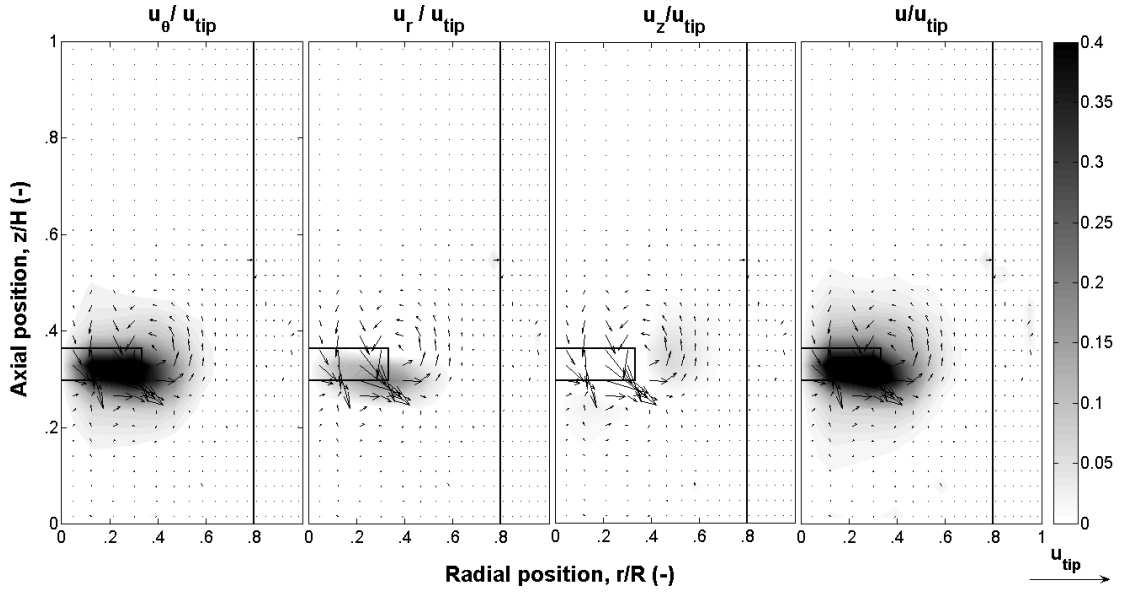

Figure 6.2. Azimuthally-averaged velocity field at N = 200 rpm (Re = 76.3) from PEPT measurement (Guida, 2010).

The experimental and numerically-predicted velocity distributions at positions shown in Fig. 6.1(a) are compared quantitatively in Fig.6.3. It can be seen that all three velocity components at various positions are very well predicted by CFD as the agreement with PEPT is overall excellent. Relatively a high discrepancy occurs for the local maximum value of tangential velocity, u_θ , at z = 0.36H (upper edge of the impeller blade), which was overestimated.

Concerning the axial profiles in Fig. 6.3(a), the noticeable velocities in the axial profiles are constrained in the impeller region, from $z \sim 0.2H$ to $z \sim 0.4H$. The three velocity components reduce significantly away from the impeller, especially the reduction in the axial velocity component, u_z. The magnitude of tangential component, u_θ ($u_\theta = 0.5\,u_{tip}$) at r = 0.3R is considerably bigger than the axial and radial components, u_z ($u_z = 0.2\,u_{tip}$) and u_r ($u_r = 0.17\,u_{tip}$) on the basis of PEPT measurement.

The radial velocity distributions at three horizontal planes within the impeller swept volume exhibit sharp variations, especially the tangential velocity, u_θ, as shown in Fig. 6.3(b). The maximum magnitude of $u_\theta = 0.5\,u_{tip}$, occurs in the center line of the impeller, i.e. $z = 0.33H$, which constitutes large portion of the total velocity u ($u = 0.55\,u_{tip}$) at $z = 0.33H$. In other two horizontal planes within the impeller swept volume, i.e. at $z = 0.36H$ (upper edge of the impeller blade) and $z = 0.3H$ (lower edge of the impeller blade), the total velocity u reduces to $u = 0.31\,u_{tip}$ and $u = 0.5\,u_{tip}$, respectively. The less reduction in the total velocity in the downward direction could be attributed to the liquid being discharged downward in the PBTD mode.

The radial velocity distributions at three horizontal levels below the impeller and three horizontal levels above the impeller are fairly flat, as shown in Fig. 6.3(c) and Fig. 6.3(d), respectively. All three velocity components reduce fast with the positions moving away from the impeller, and they are about zero at $z = 0.2H$ and $z = 0.45H$.

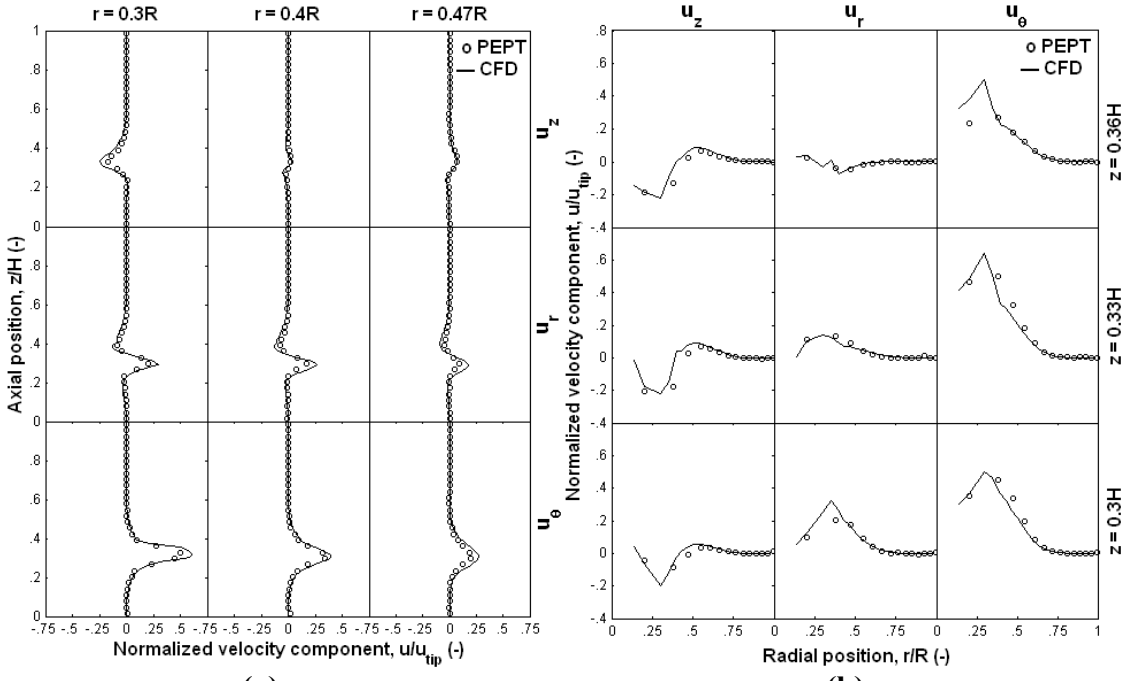

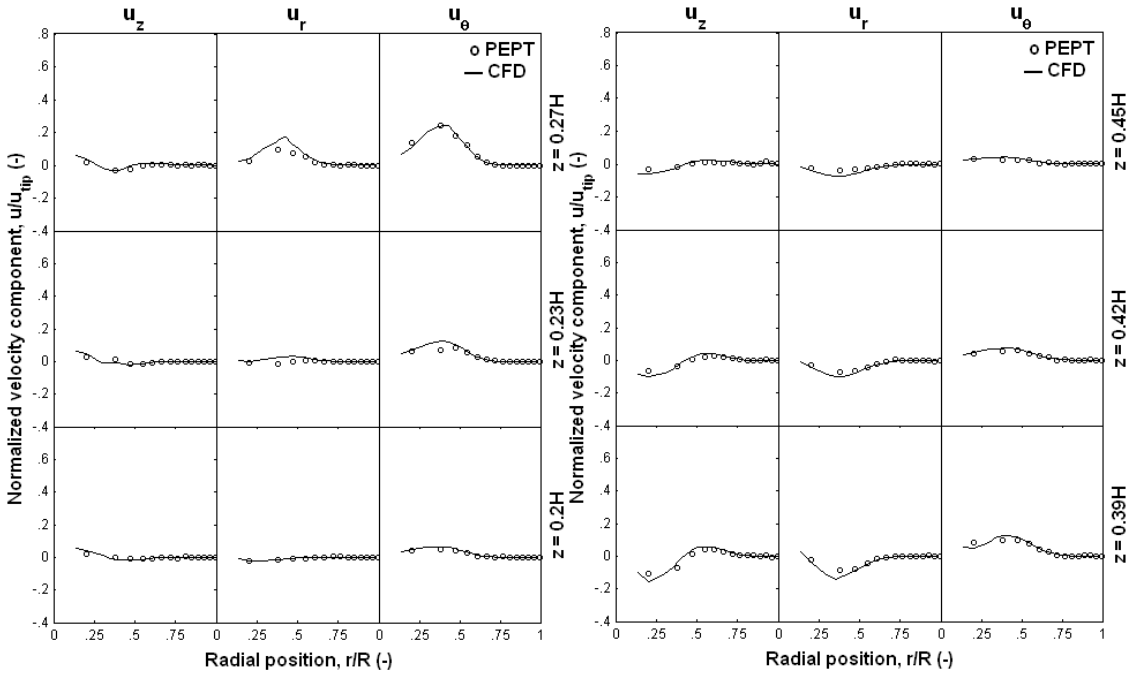

Figure 6.3. Azimuthally-averaged distributions of velocity components – CFD and PEPT compared: N = 200 rpm (Re = 76.3): (a) radial positions; (b) axial positions within the impeller blade width; (c) axial positions below the impeller; (d) axial positions above the impeller.

6.4.2. CFD predicted tracer distribution within cavern compared with PLIF

In this section, the tracer distribution inside the cavern against time is investigated. The well validated CFD predicted flow field in section 6.4.1 generated by PBTD at N = 200 rpm by comparing with PEPT measurement (Guida, 2010) was employed. A passive tracer was added in the flow field, and the tracer was created by a user scalar through under-defined functions in the CFX package. The transient simulation using the Sliding Grid (SG) method (Luo et al., 1993) was carried out, and an additional passive scalar transport, equation (6.3), was solved with the validated flow field being frozen. Bujalski et al. (2002 (a)) have found that solving the hydrodynamic equations simultaneously costs 10 times more computational resource than using the frozen flow field, but gives the same simulation results.

$$\frac{\partial}{\partial}(\rho Y_i)+\nabla\cdot(\rho u Y_i)=\nabla\cdot\left(\left(\Gamma_i+\frac{\mu_T}{Sc_T}\right)\nabla Y_i\right) \tag{6.3}$$

where, the Y_i and Γ_i are the mass fraction and molecular diffusion coefficient of species *i*, respectively. The Γ_i has been found to have negligible effect on the tracer distribution by some researchers (Montante and Magelli, 2005; Ihejirika and Ein-Mozaffari, 2007). Sc_T is the turbulent Schmidt Number and was set to the default value of 0.9. The tracer was set having the same properties as the bulk fluid. The simulation running time was set as 600 seconds to ensure that there is no change in the tracer concentration distribution throughout the volume. Because there is a high imbalance during the tracer injection, in order to resolve the tracer field accurately during the injection, small timestep of 0.01 was employed in the first 40 timesteps.

The tracer was injected at a point just above an impeller blade. It is worth noting that under the conditions of fluid mixing with the presence of a cavern, the tracer needs to be added inside the cavern rather than at random, or it will not distribute. The tracer distribution within the cavern against time obtained from the PLIF measurement (Guida, 2010) and CFD simulation, as shown in Fig. 6.4 and Fig. 6.5, respectively, are compared. The azimuthally-averaged 3-D caverns from these two sets of measurements were projected onto the 2D plane.

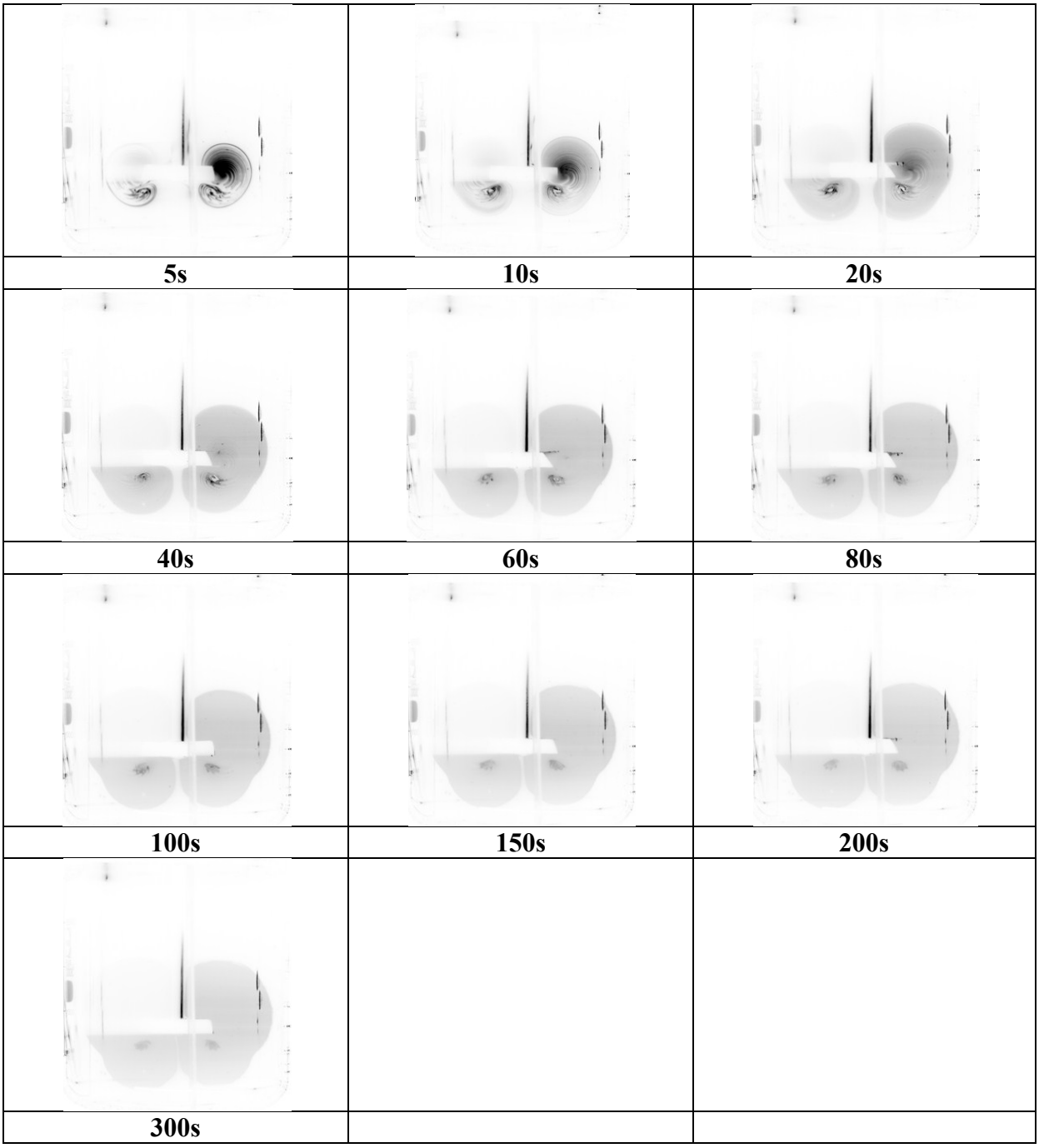

Figure 6.4. Distribution of tracer over time from PLIF measurement at N = 200 rpm (Re = 76.3) (Guida, 2010).

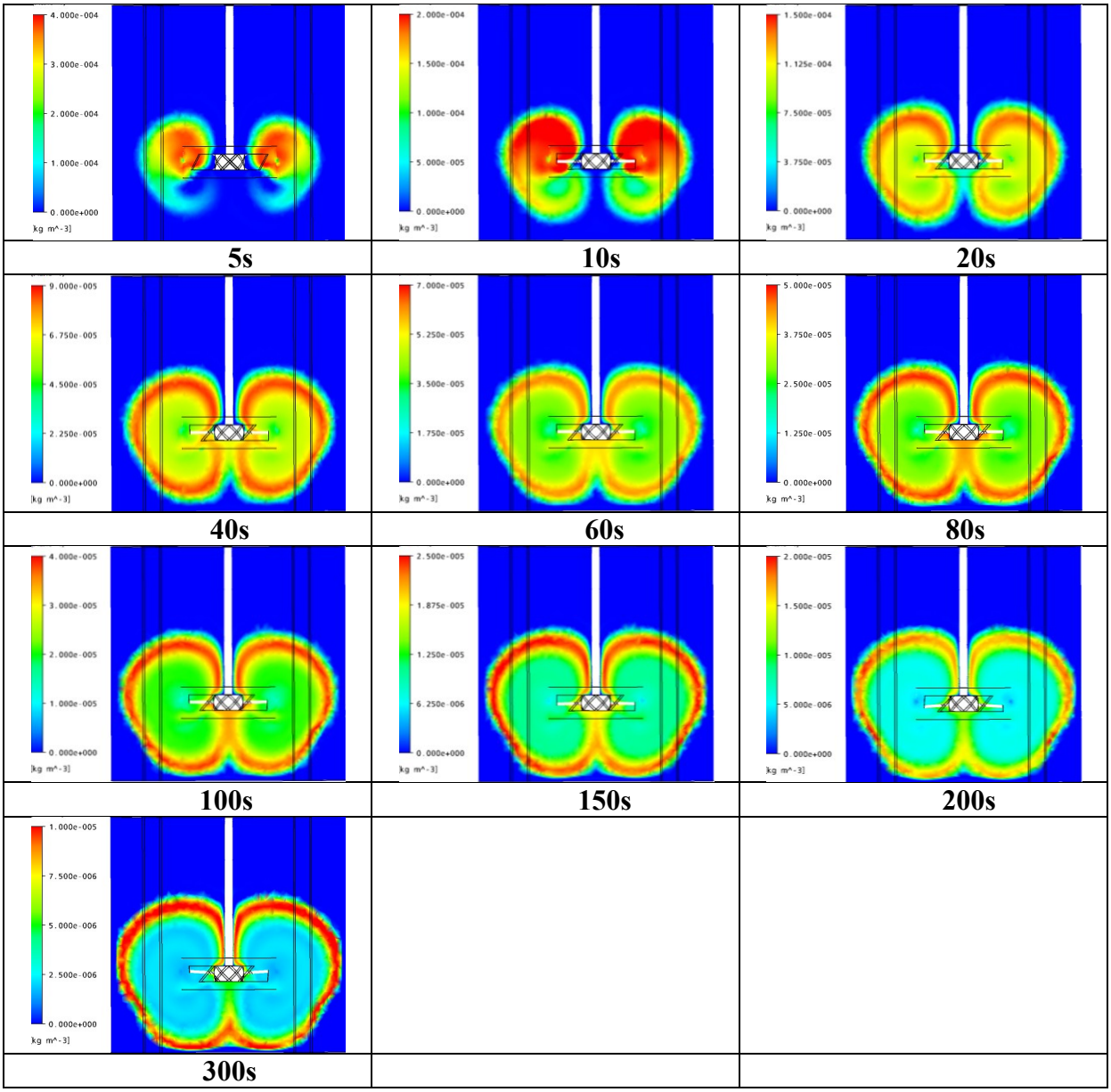

Figure 6.5. Distribution of tracer over time from CFD prediction at N = 200 rpm (Re = 76.3).

Initially (5 s to 40 s), the tracer distributes very rapidly, but the rate of distribution slows down dramatically after 40 s, which could be due to the poor mixing close to the cavern boundary. After 150s, the tracer stops distributing. The feature of the tracer distribution is well captured by the CFD simulation. The tracer distributes uniformly within the caver, except the tracer concentration varying dramatically close to the cavern boundary.

The area of tracer distribution at different time obtained from the PLIF measurements (Guida, 2010) and CFD simulations were calculated and normalized by the half tank region on the 2D plane, i.e. A_c/A_T, are compared in Fig. 6.6. The feature of the tracer distribution is well captured by the CFD simulation. The results show that initially A_c increases sharply with time, but the curves flattens out after ~100*s*.

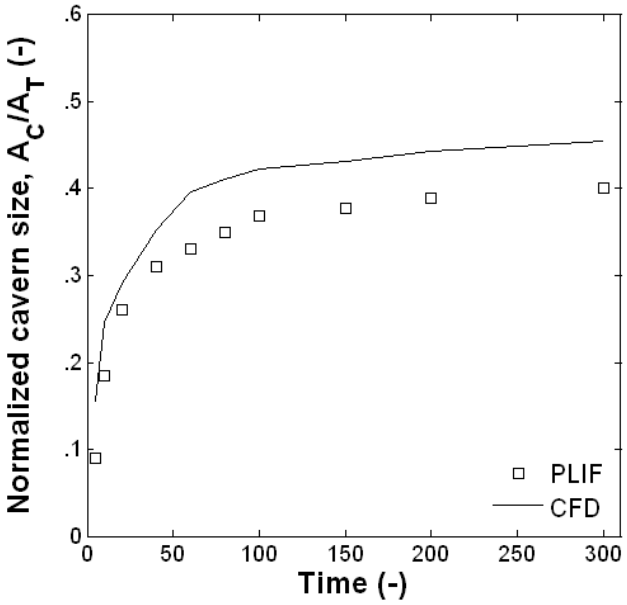

Figure 6.6. Cavern development over time.

6.4.3. Verification of PEPT and CFD methods by comparing with PIV measurements

The utility of PEPT in turbulent low viscosity Newtonian fluid flow has been verified by comparing with the PIV techniques in the work of Pianko-Oprych et al. (2009). The two sets of data have been found to agree very well, except minor discrepancies close to the impeller which may be due to the different methods of obtaining the data. The positron-emitting particle tracer which is of significant importance to the accuracy of the Lagrangian trajectory tracking is affected by the match of the tracer density and the liquid density, the tracer size

and its mechanical resistance. Ideally, the density of the radioactive tracer is the same as that of the tracked liquid phase, as reported in Chapter IV that in the solid-liquid suspensions the density of tap water was adjusted to 1150 kg m^{-3} by adding NaCl to make the PEPT particle tracer used to track the liquid phase neutrally buoyant. However, this approach is not feasible because the NaCl aqueous causes breakdown of carbopol structure. Therefore, it is necessary to examine the accuracy of PEPT measurements of mixing of viscoplastic fluids in stirred vessels. This study was carried out in the larger tank agitated by the largest PBT in down-pumping mode at Re = 56 – 273, as listed in Table 6.2.

The distributions of velocity components obtained from PIV and PEPT, and predicted by CFD modelling, at low to medium Reynolds numbers are compared in Fig. 6.7, 6.8, 6.9. It can be seen that the agreement between the three sets of data is good overall, and the large discrepancies occur to the local maximum underneath the impeller (z = 0.23H) at N = 180 rpm. It is worth noting that both the CFD predicted and PEPT measured velocities are azimuthally-averaged, while the PIV measurements are obtained in a vertical plane (85° which is on the windward side of the baffle), which could explain the discrepancies.

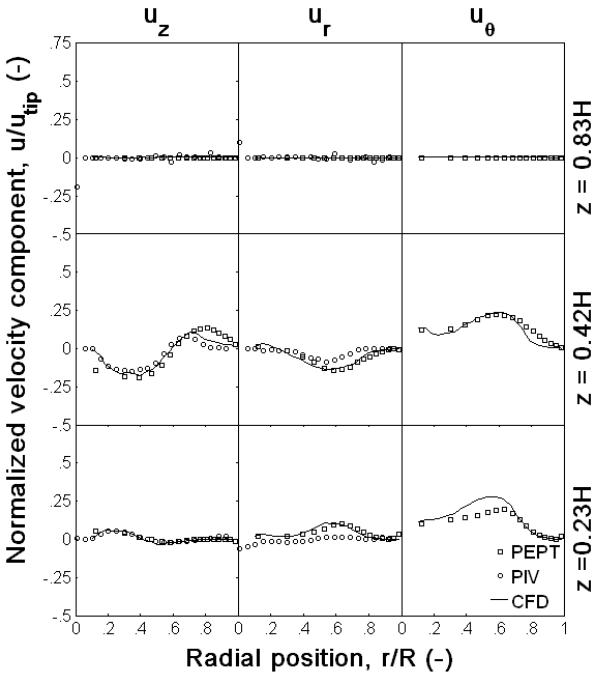

Figure 6.7. Comparison of velocity distributions from PEPT, PIV and CFD at N = 65 rpm (Re_{imp} = 52).

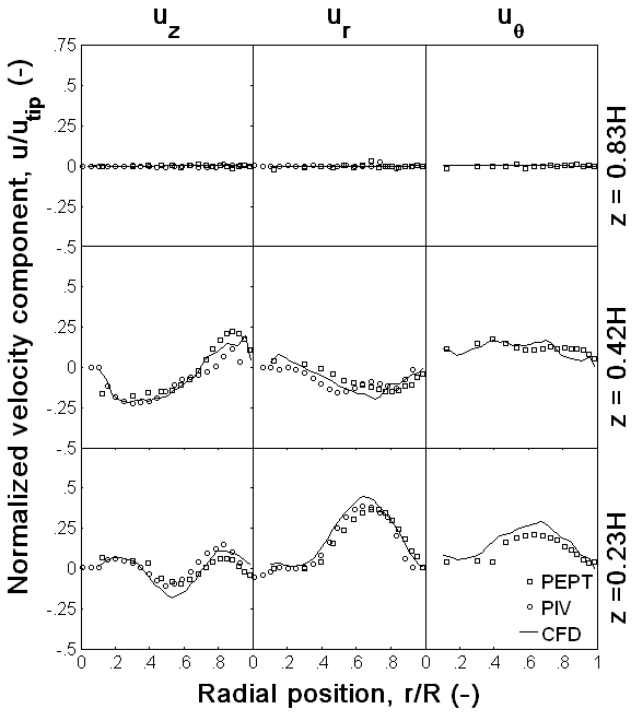

Figure 6.8. Comparison of velocity distributions from PEPT, PIV and CFD at N = 125 rpm (Re_{imp} = 152).

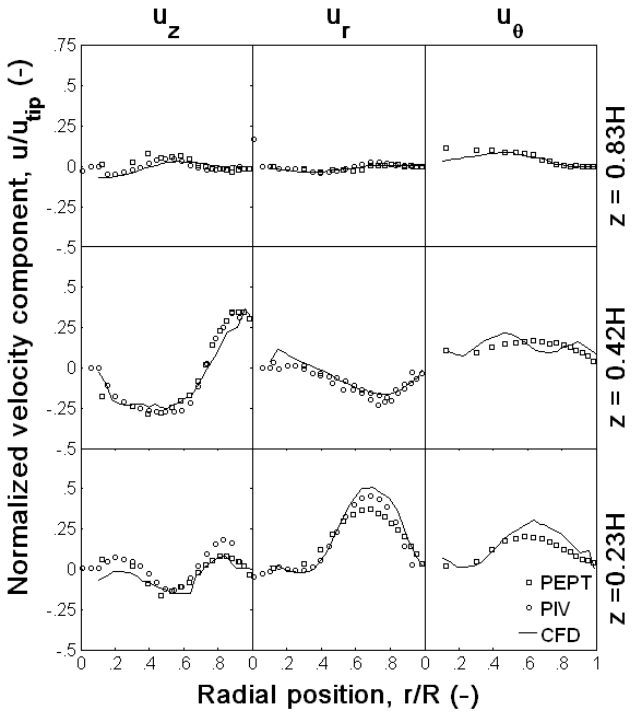

Figure 6.9. Comparison of velocity distributions from PEPT, PIV and CFD at N = 180 rpm (Re_{imp} = 280).

6.4.4. Effect of locations of interfaces between rotating and stationary domains on the CFD predicted cavern size and shape

It has been reported by some researchers that when the MFR method is used to take into account the interaction between the stationary baffles and the rotating impeller blades, the positions of the interface between these two domains play a very important role in the accuracy of the momentum transfer calculation between the two domains, especially the cylindrical interface. Setting the vertical cylindrical interface midway between the impeller blade tip and the baffles, as shown in Fig. 6.10(b), has been stated to be appropriate for modelling turbulent fluid flows in stirred vessels (Oshinowo et al., 2000; Bujalski et al., 2002 (a); Ein-Mozaffari and Upreti, 2009). However, little work has been carried out to investigate

the effect of locations of the interface on the CFD modelling of cavern formation in the mixing of viscoplastic fluids in the laminar and low transitional regimes.

In the numerical study of Adams and Barigou (2007), the rotating domain structure used in their work extends from the top surface to the plane of $z = 0.1T$ mm from the tank bottom, as shown in Fig. 6.10(a). It has been reported that severe deviations between the CFD simulated cavern size and shape with those from PLIF measurements occurred for higher *Re* values ($Re \geq 70.3$). Simulations using the same feature of the rotating domain employed in the work of Adams and Barigou (2007) in conjunction with the well validated CFD models discussed in section 6.4.1, were carried out. Similarly, deviations between CFD predicted caverns and PLIF measurements occurred for higher *Re* values. Therefore, the discrepancies in their studies may have been caused by the inappropriate arrangement of the interface between the rotating domain and stationary domain. The effect of the locations of the interface on the CFD modelling of cavern formation in the mixing of viscoplastic fluids is worth investigation.

The conventional approach, i.e. setting the radial position of the interface midway between the impeller blade tip and the baffles, as shown in Fig. 6.10(b), has also been attempted in this study, however, the caverns generated at low Reynolds numbers, i.e. $Re_{imp} = 7.3$ and $Re_{imp} = 20.4$ could not be well predicted, though caverns at higher Reynolds numbers were well predicted.

A smaller rotating domain was used in this study, as shown in Fig. 6.10(c) and Fig. 6.1(a). It has been discussed in section 6.4.1 and section 6.4.2 that the cavern size and shape as well as the flow field within cavern could be well predicted. Using the setting of interface in this study, the cavern size and shape with increasing Reynolds number in the range of 7.3 – 163.3 were predicted by CFD modelling. Fig. 6.11 shows the CFD predicted cavern shape and size

compared with the PLIF measurements (Adams and Barigou, 2007) at various Reynolds numbers. It can be seen that the caverns at different Reynolds numbers were well captured by CFD modelling. Three expressions used to determine the cavern boundary, as shown in Fig. 6.11 were discussed in more detail below.

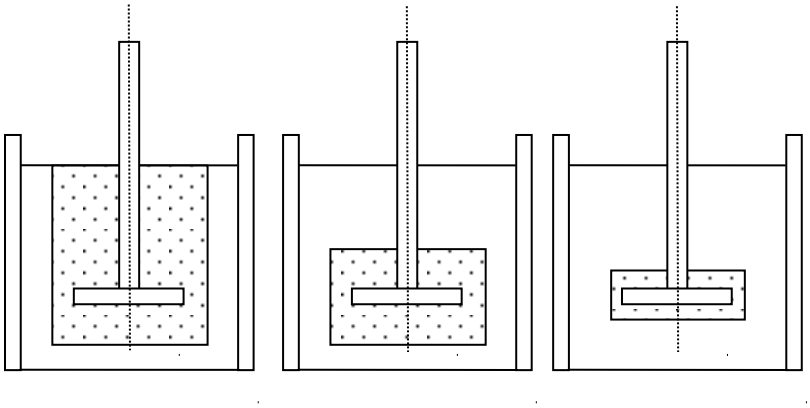

(a) **(b)** **(c)**

Figure 6.10. Different arrangements of the rotating domain and stationary domain in CFD modelling of a stirred vessel: (a) arrangement in the work of Adams and Barigou (2007); (b) conventional arrangement; (c) arrangement in present study.

The boundary of cavern in the mixing of viscoplastic material is composed of, in practice, the positions where the shear rate is zero, indicating the local shear stress is equal to the apparent yield stress, τ_y, according to equation (6.1). In order to obtain the cavern size predicted by CFD simulation, an appropriate expression is needed to describe the cavern boundary. Theoretically and numerically, different cavern boundary velocities have been employed to determine the cavern boundary (Amanullah et al. 1998; Adams and Barigou, 2007, 2008; Adams, 2009). Three expressions from literature were used to describe the cavern boundary velocity: 1): $u_\theta = 0.01 u_{tip}$ (Amanullah et al. 1998, Adams and Barigou, 2007); 2) $u_{rz} = 0.01 u_{tip}$ (Adams and Barigou, 2008); 3) $u = 5\times10^{-4}\ ms^{-1}$ (Arratia et al., 2006).

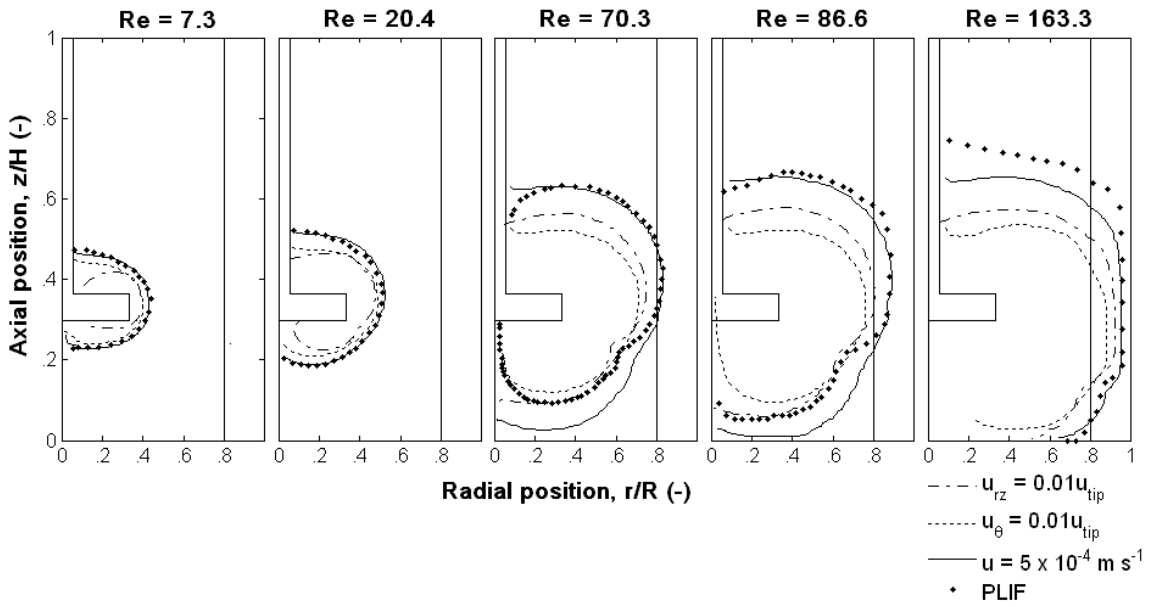

Figure 6.11. Comparison of cavern shape and size at different Reynolds numbers from PLIF measurement (Adams and Barigou, 2007) and CFD predictions using three definitions.

It can be seen from Fig. 6.11 that at lower Reynolds numbers (i.e. *Re* = 7.3 and *Re* = 20.4), the cavern shape is similar to spherical shape. Using $u = 5\times10^{-4}\ ms^{-1}$ and $u_{rz} = 0.01u_{tip}$ as the cavern boundary velocities, the predicted cavern size and shape agree very well with the PLIF measurement, whereas the cavern size is significantly underestimated using the $u_\theta = 0.01u_{tip}$.

Increasing the Reynolds number to *Re* = 70.3, two circulation loops develop inside the cavern, i.e. a larger flow loop above the impeller and a smaller one below it (Adams and Barigou, 2008). The boundary of the larger flow loop can be well predicted using $u = 5\times10^{-4}\ ms^{-1}$, and boundary of the smaller circulation loop below the impeller is well described using $u_{rz} = 0.01u_{tip}$. Both flow loops are underestimated using the $u_\theta = 0.01u_{tip}$.

The cavern reaches the tank wall and tank base at *Re* = 163.3, which is well captured by the CFD modelling, though the height of cavern was somewhat underpredicted using all the three definitions of the cavern boundary velocities.

In short, the accuracy of CFD modelling of cavern formation in the mixing of viscoplastic fluids in stirred vessels is affected significantly by the positions of the interfaces between the rotating domain and stationary domain, therefore, great care must be taken in setting the locations of the interfaces for simulating the cavern size and shape. The arrangement of interface shown in Fig. 6.10(c) gives the best predictions.

6.4.5. Effect of impeller type and rotating mode on the cavern size and shape

The impeller type determines the flow pattern and, hence, has significant influence on the mixing efficiency (Paul et al., 2004). Using the well validated CFD models discussed above, mixing of the viscoplastic fluid agitated by the RDT of $D = T/3$ and by PBT in the up-pumping mode was simulated. The CFD predicted cavern shape and size for the PBTU and RDT are shown in Fig. 6.12. At low Reynolds numbers (i.e. $Re = 7.3$ and $Re = 20.4$), the cavern size and shape of the viscoplastic fluid agitated by the RDT and in the PBTU mode are highly similar to that in the PBTD mode. This is consistent with the reports in the previous works that the tangential flow is predominant regardless of impeller type at low Reynolds numbers in the mixing of highly viscous non-Newtonian fluids in stirred vessels (Elson, 1990; Moore and Cossor, 1995). With increasing Reynolds number ($Re > 70.3$ in this study), the cavern shape and size for the RDT, PBTU and PBTD become significantly different, indicating the effect of impeller type.

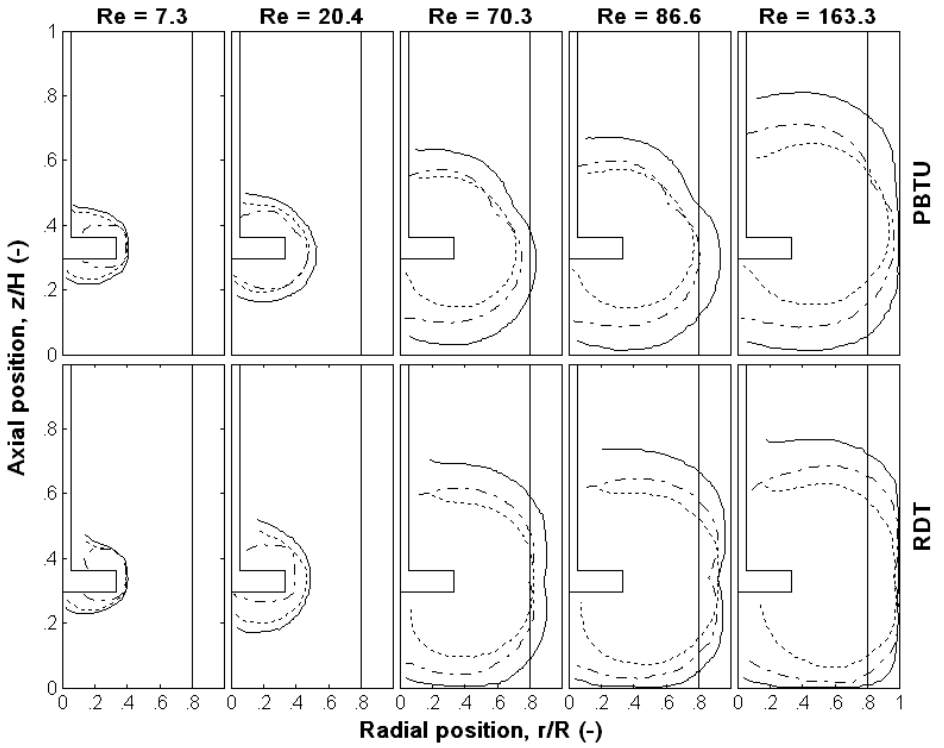

Figure 6.12. Cavern shape and size for PBTU and RDT from CFD predictions using the three definitions: --- $u_\theta = 0.01 u_{tip}$; -.-.- $u_{rz} = 0.01 u_{tip}$; — $\boldsymbol{u = 5\times10^{-4}\ ms^{-1}}$.

Similar to the mixing in the PBTD mode, two circulation loops are also generated in the PBTU mode at *Re* = 70.3, however, the positions of larger flow loops and smaller one were reversed, which is consistent with the findings in the experimental study of Adams and Barigou (2008). The cavern generated from the RDT is equally separated by the central line of the impeller because the fluid is discharged in the radial direction.

Similar to the cavern for the PBTD mode, the caverns for PBTU and RDT have also reached the tank wall and tank base at *Re* = 163.3 (*N* = 367 rpm). The PBTU and RDT perform better in developing the cavern upward at *Re* = 163.3. It can be seen that the cavern reaches a higher level (~ z = 0.80H) in the PBTU mode, whereas the height of cavern in the PBTD mode is, ~ z = 0.70H. This could be attributed to the fluid discharge direction, i.e. being discharge upward in the PBTU mode, while downward in the PBTD mode.

6.4.6. Cavern upward growth for PBTD, PBTU and RDT

Due to the detrimental effect of the dead zone outside the cavern on the mixing efficiency, it is necessary to investigate the growth of cavern in the upper part of the stirred vessel once it reaches the tank wall in order to completely eliminate the poor mixing area. Fig. 6.13 shows the CFD predicted caverns at three higher impeller rotation speeds after the cavern reaches the tank wall, i.e. N = 500 rpm, N = 600 rpm, and N = 800 rpm.

The cavern size in the PBTU and RDT modes at the same Reynolds number is similar. The cavern grows upward significantly with the impeller speed, and reaches the top free surface at N = 600 rpm for PBTU and RDT. However, the growth of the cavern in the PBTD mode is constrained after the upper boundary reaches a certain level ($\sim z = 0.7H$), and hardly develops upward even at much higher impeller speed of N = 800 rpm. The difficulty of the cavern growing upward in the PBTD mode may be caused by the fluid being discharged downward. Therefore, the impeller type and rotating mode (i.e. up or down-pumping) have significant effects on the cavern growth upward in stirred vessels at higher Reynolds number.

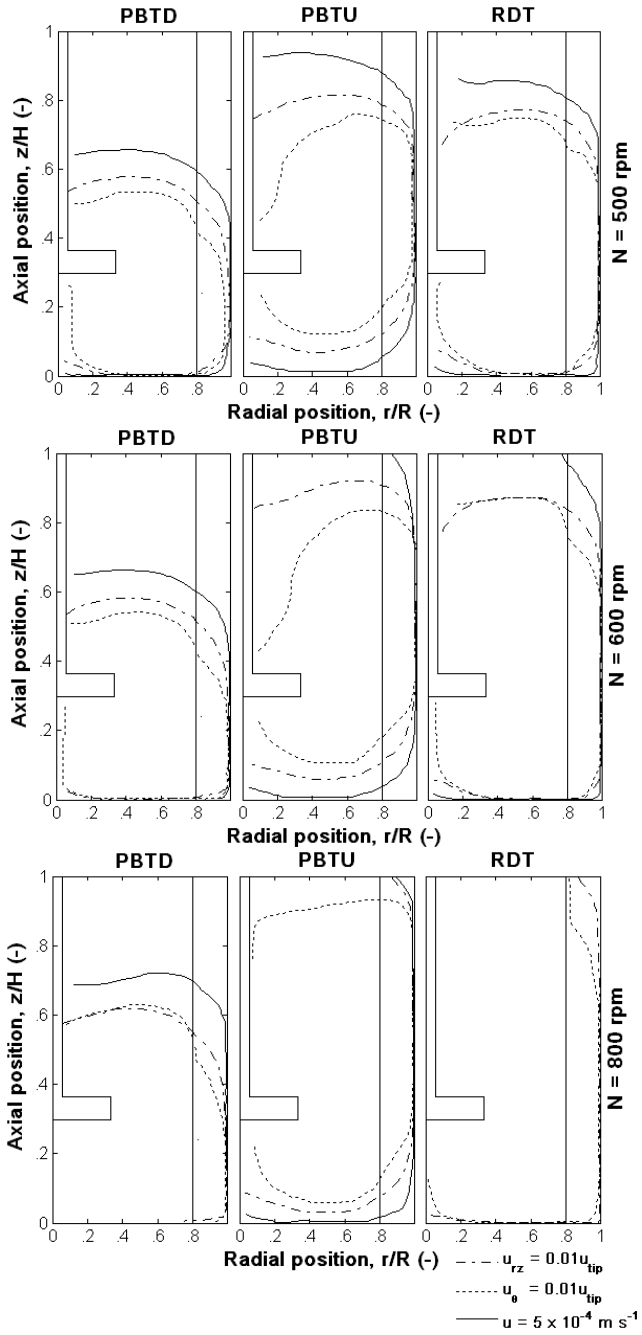

Figure 6.13. Cavern growth upward under PBTD, PBTU and RDT rotating modes.

6.4.7. Effects of impeller size on the cavern size and shape

Cavern size can be increased either by increasing impeller speed, as discussed in section 6.4.4, or by increasing impeller size. As both methods require more power input, and in order to

examine which method performs better, the power consumption of generating the same cavern size using the two methods was compared.

A viscoplastic fluid of same rheology as that used in section 6.4.1 (i.e. 0.1 wt% carbopol solutions with pH value of pH = 4.6) was used, and the cavern generated by a PBT of $D = T/2$ at $C = T/4$ in down-pumping mode at impeller speed of $N = 200$ rpm measured by PEPT is shown in Fig. 6.14 (a). A much bigger cavern is generated in comparison with that generated by the PBT at $C = T/3$, as shown in Fig. 6.14 (c), in down-pumping mode at impeller speed of $N = 200$ rpm.

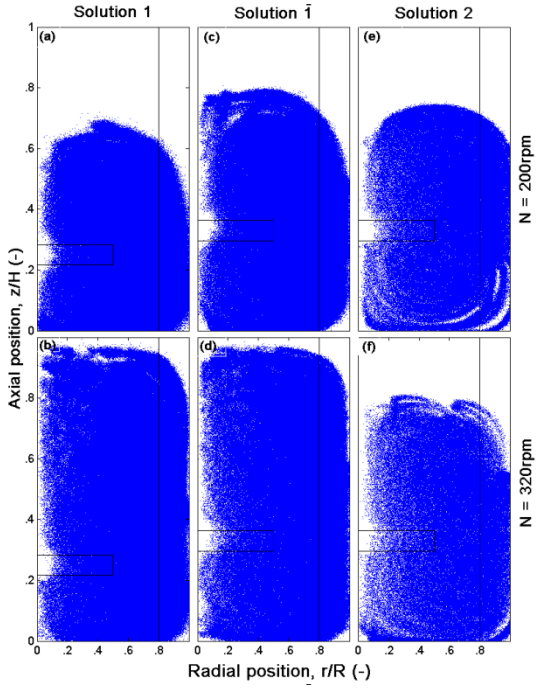

Figure 6.14. Effects of rheological properties and impeller bottom clearance on the cavern size and shape generated by PBT of $D = T/2$ in the down-pumping mode and measured by PEPT.

Moreover, the cavern generated by the PBT of $D = T/2$ in down-pumping mode at $N = 200$ rpm (Fig. 6.14 (a)) is also bigger in comparison with that generated by the PBT of $D = T/3$ in down-pumping mode at much higher impeller speed of $N = 800$ rpm, as shown in Fig. 6.13.

Considering the volumetric power input, P/V, in these two cases, P/V = 0.04 W/m^3 for using bigger PBT at N = 200 rpm, while P/V = 0.88 W/m^3 for using smaller PBT at N = 800 rpm from the CFD predictions. Therefore, to increase cavern size, it is more effective to use a larger impeller than increasing impeller speed.

6.4.8. Effects of rheological parameters on the cavern size and shape

The rheological parameters of non-Newtonian fluids play an important role in the fluid mixing. The effect of flow index, n, on the flow behaviour of shear thinning fluids has been presented by Ameur and Bouzit (2012), and they found that the three velocity components increased with the flow index. The study of Ihejirika and Ein-Mozaffari (2007) showed that the cavern reduces significantly with an increase in yield stress. In this section, the effects of three rheological properties of the viscoplastic fluid, i.e. yield stress, τ_y, flow behaviour index n and fluid consistency coefficient, k, on the cavern shape and size were investigated.

The pH value has been found to have significant effect on the rheological properties of carbopol solutions (Curran et al., 2002). Carbopol solutions with different rheological parameters were prepared by changing the pH value and were used to investigate the effects of rheological properties on the cavern size and shape. For the sake of clarity, the carbopol solution of pH = 4.35 is called solution 1, and carbopol solution of pH = 4.6 is called solution 2 in the following sections. The rheological properties are listed in Table 6.2.

Cavern formation in solution 1 agitated by a PBT of $D = T/2$ in the down-pumping mode at impeller clearance of $C = T/3$ is illustrated in Fig. 6.14 (c), (d). Cavern formation in solution 2 agitated by the PBT of $D = T/2$ in the down-pumping mode at impeller clearance of $C = T/3$ is illustrated Fig. 6.14 (e), (f). The cavern size and shape are obtained by plotting the tracer positions from PEPT measurements in a 2D plane. It can be seen that the caverns in solution

1 are significantly larger than those in solution 2 at the same impeller speed. The cavern height is $z = 0.80H$ in solution 1, which reduces to $z = 0.70H$ in solution 2 at $N = 200$ rpm. Solution 1 is in motion throughout the stirred vessel at $N = 320$ rpm, while the dead zone still exists in the upper part of stirred vessel in solution 2 at $N = 320$ rpm. The carbopol solution becomes thicker with the increase in pH value and hence, solution 2 is more viscous that solution 1, with rheological properties as listed in Table 6.2. Therefore, higher shear stress is required for solution 2 to start to flow.

Using the well validated CFD approaches and models as discussed in section 6.4.1 and section 6.4.2, parametric studies could be conveniently carried out. A constant impeller speed of $N = 200$ rpm was used and two rheological parameters were kept constant when the effect of one parameter was investigated. The cavern boundary was defined by $u_{rz} = 0.01\, u_{tip}$.

Concerning the effect of the yield stress, τ_y, the cavern size reduces sharply, from $A_C = 0.22A_T$ to $A_C = 0.04A_T$ with the yield stress increasing from $\tau_y = 2$ Pa to $\tau_y = 10$ Pa, indicating the significant effect of the yield stress on the cavern size, as shown in Fig. 6.15.

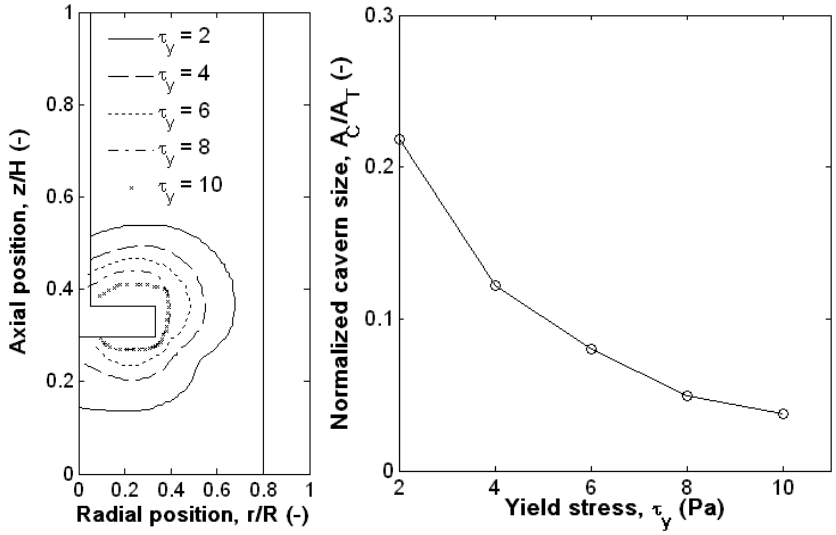

Figure 6.15. Effect of yield stress on the cavern shape and size.

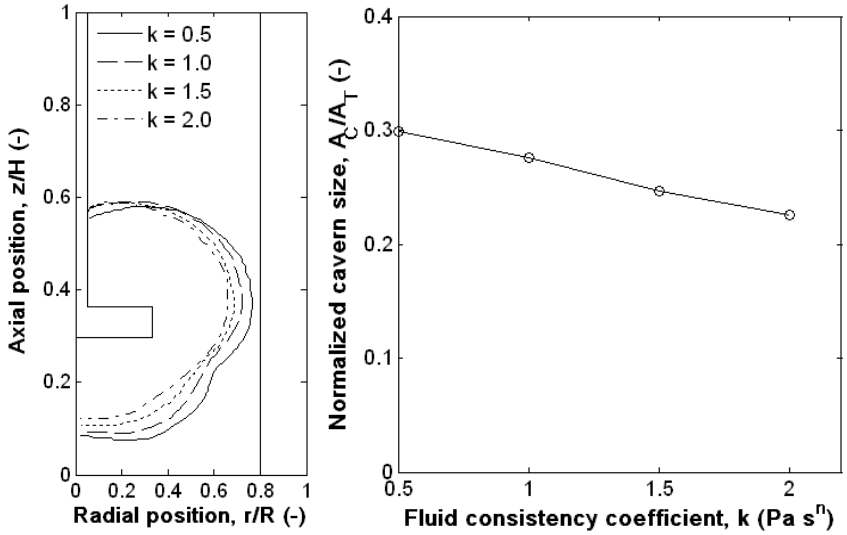

Figure 6.16. Effect of flow consistency coefficent on the cavern shape and size.

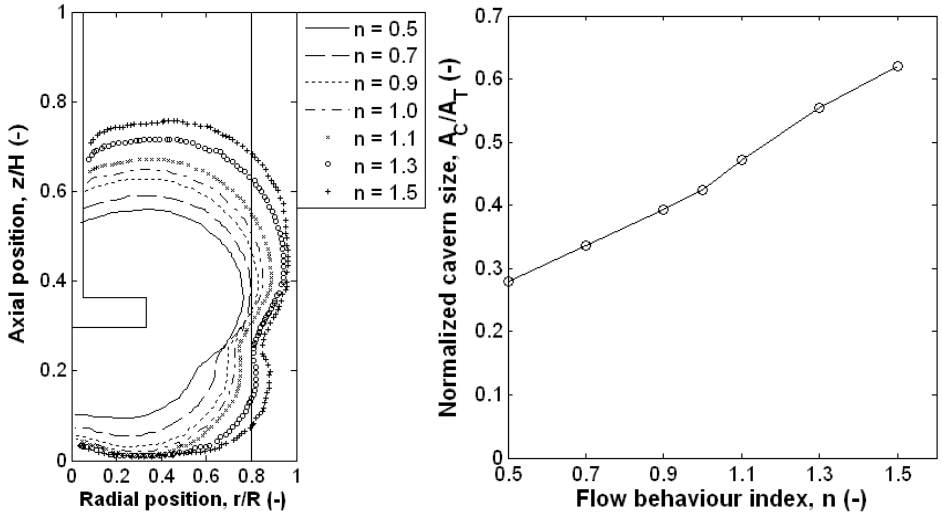

Figure 6.17. Effect of flow behavior index on the cavern shape and size.

The cavern size is also reduced with an increase in k, as shown in Fig. 6.16, however, its influence is much less compared with that of yield stress. The apparent viscosity reduces with the shear rate as $n < 1$, whereas the apparent viscosity increases with the shear rate as $n > 1$. The cavern size varies significantly with different flow behaviour index n. Fig. 6.17 shows that the cavern grows from $A_C = 0.28A_T$ to $A_C = 0.62A_T$ with the flow behaviour index n increasing from 0.5 to 1.5. This may be due to that the shear stress increases with increasing

n, given the constant mean shear rate base on the well-known Metzer and Otto correlation (Metzner and Otto, 1957), i.e. $\dot{\gamma} = k_s N$. Therefore, the region where the shear stress could overcome the apparent yield stress for the fluid flow becomes larger.

6.4.9. Effects of impeller bottom clearance on the cavern size and shape

Studies of the effect of the impeller bottom clearance on the mixing of various fluids agitated by different types of impellers have shown that moving the impeller from the standard position ($T/3$) to higher positions ($T/2$) can generate better flow pattern (Jaworski et al., 1991; Kresta and Wood, 1993; Fangary et al., 2000; Ochieng et al., 2008). Concerning the effect of impeller bottom clearance on the mixing of viscoplastic fluids, larger caverns were generated by increasing impeller bottom clearance (Ameur et al., 2011; Derksen, 2009; Ein-Mozaffari and Upreti, 2009).

Caverns generated by PBT of $D = T/2$ in the down-pumping mode at impeller bottom clearances of $C = T/3$ and $C = T/4$ at $N = 200$ rpm are shown in Fig. 6.14 (a), (c). Larger cavern is generated at higher impeller position of $C = T/3$, and the cavern reaches the height of $z = 0.80H$ and $z = 0.65H$ for $C = T/3$ and $C = T/4$, respectively.

In order to investigate the effect of the impeller bottom clearance on the cavern size and shape for different impellers and in different rotating modes (e.g. RDT, PBTD, and PBTU) was investigated. CFD simulations of cavern formation from PBTD, PBTU and RDT at impeller bottom clearance of $C = T/2$ at impeller speed of $N = 500$ rpm were carried out, and the simulations were compared with those at impeller bottom clearance of $C = T/2$ at impeller speed of $N = 500$ rpm as shown in Fig. 6.18. This reason for choosing the impeller speed of $N = 500$ rpm is that the cavern from all three rotating modes have not reached the liquid free

surface at this speed so that the effect of impeller bottom clearance on the cavern size could be conveniently compared.

As expected, increasing the impeller clearance significantly enhance the cavern upward growth in the PBTD and RDT modes. The cavern in the PBTD mode, without affecting the cavern reaching the tank base, has reached the height of $z = 0.85H$, which is even bigger than that at higher impeller speed of $N = 800$ rpm at $C = 0.33T$, as shown in Fig. 6.13. The cavern in RDT has reached the top free surface at lower impeller speed at $C = 0.5T$ compared with that at $C = 0.33T$. However, in PBTU mode, at $C = 0.5T$, the cavern cannot reach the tank bottom, though has also reached the top surface. This can be attributed to the fluid being discharged upward. Therefore, the impeller clearance needs to be taken into account when choosing different agitation regime.

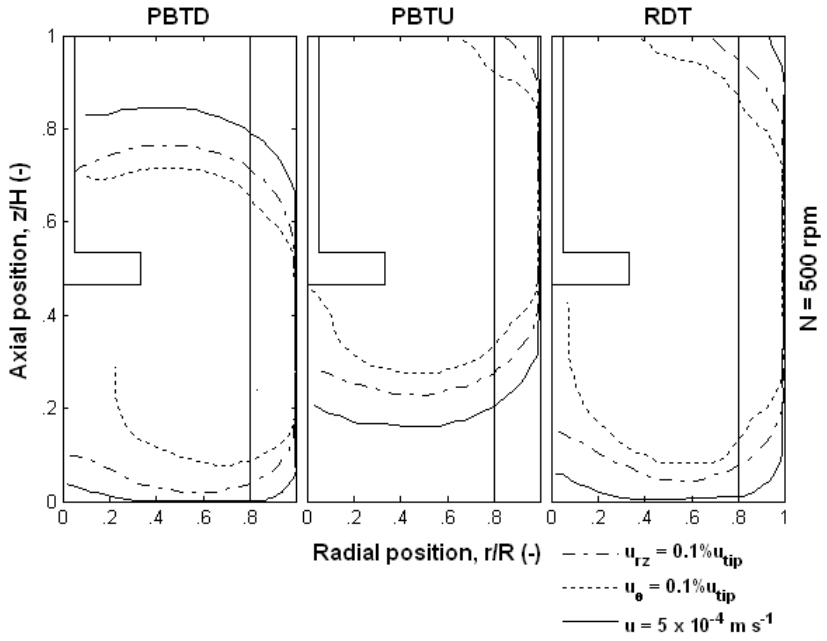

Figure 6.18. CFD predicted cavern shape and size under PBTU and RDT rotating modes: $C = 0.5T$.

6.4.10. Effects of impeller bottom clearance on the flow field within cavern

Fig. 6.19 shows the corresponding velocity fields from the PEPT measurement inside the cavern, as shown in Fig. 6.14. The typical flow pattern created by the down-pumping PBT is illustrated. The size of the flow loop is significantly affected by the impeller rotational speed, for example, the bottom of circulation loop in solution 1 at $C = T/4$ is at $\sim 0.1H$ at $N = 200$ rpm, which has reached the tank bottom at $N = 320$ rpm.

Though having significant effect on the cavern size, as discussed above in section 6.4.9, the impeller bottom clearance, however, has little effect on the size of the flow loop and the flow velocity, as shown in Fig. 6.19. The flow loop generated at $C = T/3$ in the same carbopol solution is almost a copy of that generated at $C = T/4$. When the impeller is set at higher position, in addition to the primary anti-clockwise flow loop, a clockwise secondary flow loop can also be observed beneath the primary anti-clockwise flow loop, which becomes stronger at high impeller speed of $N = 320$ rpm. The primary flow loop in the case of $C = T/3$ cannot reach the tank base due to high impeller position.

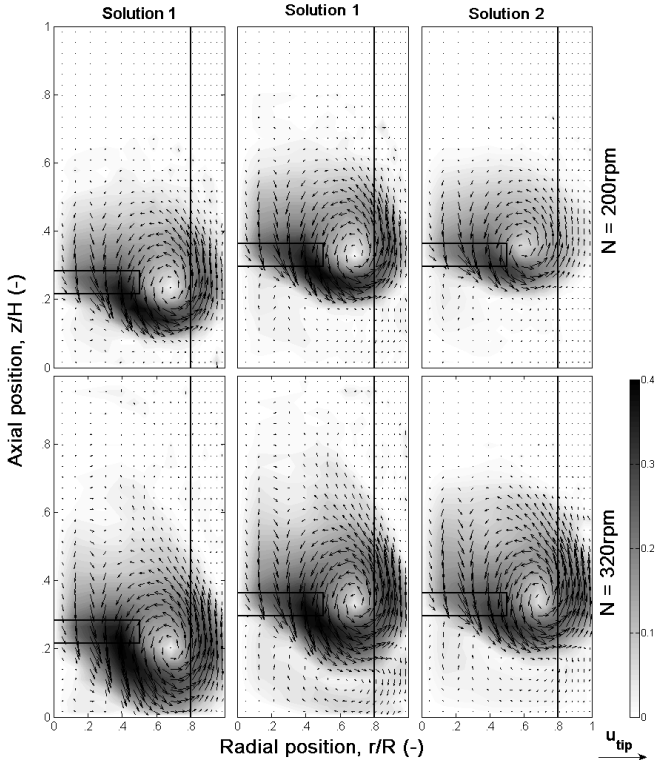

Figure 6.19. Azimuthally-averaged velocity fields from PEPT measurement.

The effect of impeller speed (or Reynolds number) on the discharge angle of mixing of shear-thinning fluids in stirred vessels has been discussed in detail in Chapter III. The effect of impeller speed on the discharge angle of mixing of viscoplastic fluids is also shown apparently in Fig. 6.19. The discharge angle measured from the horizontal plane increases with the increase in the Reynolds number, for example, the discharge angles of solution 1 are 48^{o} and 62^{o}, at N = 200 rpm and N = 320 rpm, respectively. The impeller clearance, however, has little effect of on the discharge angle.

6.4.11. Ability of CFD modelling to capture the effects of different stirred tank configurations on the mixing of viscoplastic fluids

Fig. 6.20 shows the CFD predicted cavern size and shape, and compared with the PEPT measurements shown in Fig. 6.14. The effects of different stirred tank configurations on the cavern size and shape are well simulated by the CFD modelling.

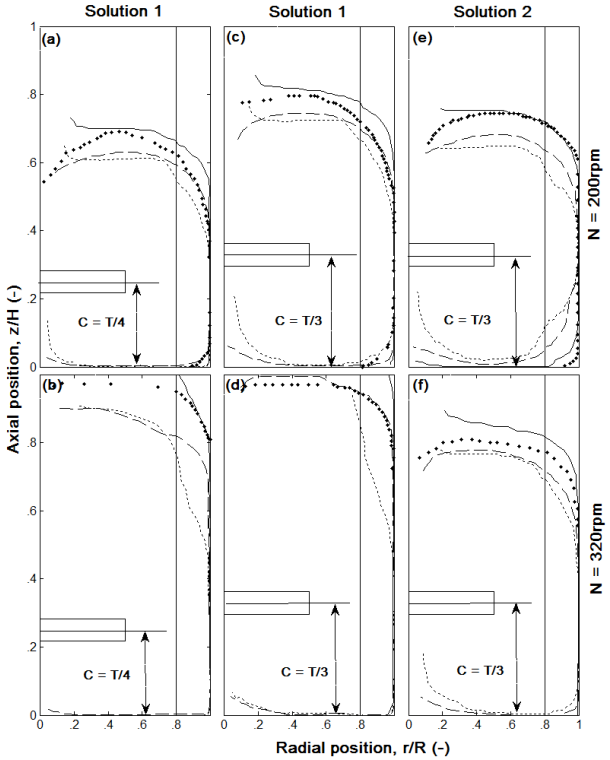

Figure 6.20. Comparison of cavern size and shape from PEPT measurement and CFD prediction: - - -, $u_{rz} = 0.01 u_{tip}$; ·····, $u_{\theta} = 0.01 u_{tip}$; —, $u = 5 \times 10^{-4}$; ♦ PEPT measurement.

Fig. 6.21 shows the azimuthally-averaged distributions of the local velocity components u_z, u_r, u_θ, respectively, in solution 1 and solution 2 agitated at two impeller speeds of N = 200 rpm and N = 320 rpm, and at impeller bottom clearance of $C = T/3$. The detailed quantitative comparison between the CFD and PEPT data were radially along five axial positions: z = 0.14H, approximately halfway between the base and the lower edge of the impeller; z = 0.27H, just under the lower edge of the impeller; z = 0.33H, centre line of the impeller; z = 0.39H, just above the upper edge of the impeller; and z = 0.83H, in the upper part of the vessel. All the velocity plots presented have been normalized by the impeller tip speed ($u_{tip} = \pi DN$).

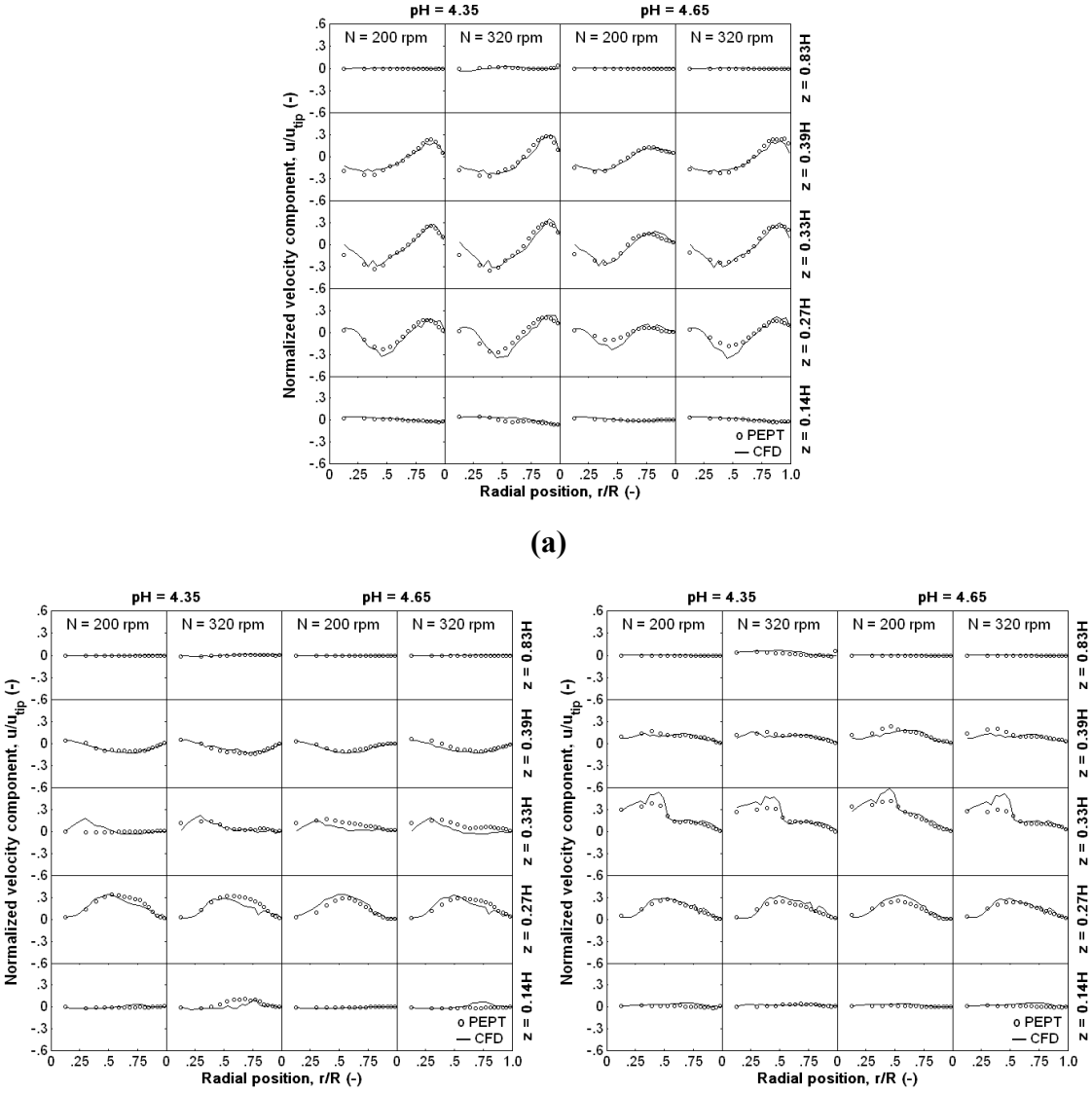

(a)

(b) **(c)**

Figure 6.21. Azimuthally-averaged radial velocity profiles of radial velocity components: (a) u_z; (b) u_r; (c) u_θ.

The agreement between the CFD predicted three velocity components and those from the PEPT measurements are very good throughout the stirred vessel, indicating the high accuracy of using the CFD modelling to predict the mixing feature of viscoplastic fluids, also confirming that using the laminar model is suitable for modeling the transitional regimes up to Re = 455.

The local maximum magnitude of u_z at the impeller discharge plane ($z = 0.27H$) in solution 1, is $0.20\,u_{tip}$ to $0.30\,u_{tip}$ at $N = 200$rpm and $N = 320$rpm, respectively. The values at the impeller discharge plane ($z = 0.27H$) in solution 2, however, reduce to $0.10\,u_{tip}$ to $0.20\,u_{tip}$ at $N = 200$rpm and $N = 320$rpm, respectively. Far away from the impeller ($z = 0.14H$ and $z = 0.83H$), the three velocity components u_z, u_r, u_θ become nearly zero.

The values of u_θ are much smaller than u_z and u_r, except in the center line of the impeller ($z = 0.33H$), and the maximum value of u_θ occurs at the impeller tip. However, u_θ decreases sharply away from the impeller.

6.4.12. Power number

The power number, P_o, is inversely proportional to Reynolds number in the laminar regime, but changes slightly with *Re* in the turbulent regime, which has been reported in the literature (Lee et al., 1957; Galindo and Nienow, 1993; Pakzad et al., 2007). The power number, P_o calculated from CFD simulations (based on torque), as a function of Reynolds number for the PBTD, PBTU and RDT is shown in Fig. 6.22. It shows that the power numbers of impellers in down- and up-pumping modes are practically the same for all Reynolds numbers. The power number for the RDT are the same with that for the PBT in the laminar regime, but the power number becomes about 2 times bigger than that for the PBT in the transitional regime. CFD predicts that the power number of all three agitating regimes decreases approximately linearly when the flow is in laminar and low transitional regimes, after *Re* reaches about *Re* = 200, P_o only changes slightly with further increasing Reynolds number. In addition, CFD also predicts that the power numbers at *Re* = 1000 are very similar to those in the fully turbulent regime (Hemrajani and Tatterson, 2004).

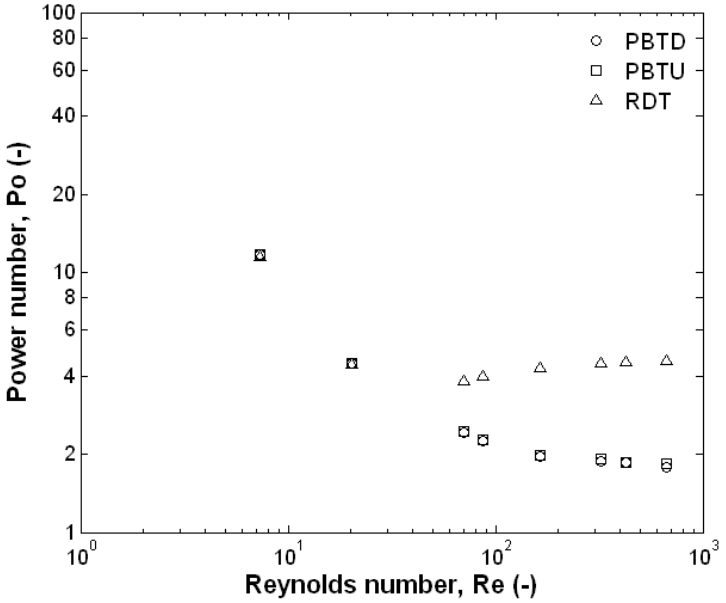

Figure 6.22. Power number as a function of Reynolds number.

6.5. Conclusion

Detailed investigation on the cavern formation and the hydrodynamics within the cavern in the mixing of viscoplastic fluids in stirred vessels was carried out both numerically and experimentally. Numerical results are compared to detailed distributions of velocity components obtained by PIV and PEPT measurements, and very good agreements confirm the capability of CFD simulation for predicting the mixing of viscoplastic fluids in stirred vessels. The mixing features of viscoplastic fluids in various agitating conditions are well captured using the MFR approach in conjunction with the laminar model.

The predicted cavern size and shape at different Reynolds numbers are in good agreement with the PLIF measurements. At low Reynolds numbers the cavern size and shape are not affected by either impeller type or impeller pumping direction, which may be attributed to the predominant tangential flow. Two flow loops develop with increasing Reynolds number, the smaller flow loop below the impeller in the PBTD mode can be well depicted using u_{rz}=0.01

u_{tip} as the boundary velocity, and the larger flow loop can be well depicted using $u = 5\times10^{-4}$ $m\ s^{-1}$ as the boundary velocity, while all velocities underestimate the cavern height once the cavern reaches the tank wall and base. The cavern size is underestimated using $u_\theta = 0.01\,u_{tip}$ as the boundary velocity.

The location of the interfaces between the rotating domain and stationary domain has significant influence in the CFD prediction of cavern size and shape, therefore, great care must be taken for the arrangement of the rotating domain. Tracer distributes within the cavern very fast initially, but the distribution speed slows down dramatically after 40, and distribution stops after 150s.

The yield stress τ_y and the flow behaviour n have significant but reverse effects on the cavern size, while the fluid consistency coefficient, k has little effect.

The cavern is constrained to grow upward in the PBTD mode, and using a bigger impeller cost much less power consumption compared with that by increasing the impeller rotating speed, meanwhile, replacing the impeller from $C = T/3$ to $C = T/2$ could also significantly enhance the cavern size in the PBTD mode, which, however, has opposite effect for the PBTU mode, and the cavern could not reach the tank base at $C = T/2$.

PEPT technique for measuring the velocity field in the mixing of viscoplastic fluids was validated by comparing the velocity data with those obtained from PIV and CFD.

Notation

C	impeller bottom clearance	-
D	impeller diameter	m

H	height of suspension	m
N	impeller rotational speed	s^{-1}
P	power consumption	W
P_0	power number	-
r	radial distance	m
R	vessel radius	m
Re_{imp}	impeller Reynolds number (ND^2/v)	-
T	vessel diameter	m
u_{tip}	impeller tip speed	m s^{-1}
$u_r\ u_z\ u_\theta$	cylindrical velocity components	m s^{-1}
V	volume of stirred vessel	m^3
z	vertical distance	m

Greek letters

v	kinematic liquid viscosity	$m^2\ s^{-1}$

Chapter VII

EXPERIMENTAL AND NUMERICAL MODELLING OF SOLID SUSPENSIONS IN VISCOPLASTIC FLUIDS

Abstract

Suspensions of monodisperse coarse glass particles of 1 mm diameter in viscoplastic fluids were experimentally investigated and numerically simulated at the 'just-suspended' speed N_{js}, in a vessel agitated by a down-pumping 6-blade 45º pitched-turbine (PBT). The mean solid concentration was in the range of 2.4–21.6 wt% (1 – 10 vol%). The normalized axial velocity u_z of the liquid phase is significantly enhanced with the presence of solid particles, particularly in the impeller discharge stream. At N_{js}, the spatial distribution of the inter-phase slip velocity varies in a wide range, and the largest total slip velocities occur in the circulation loop. The normalized slip velocity decreases significantly at high solid concentration, X = 21.6 wt%. At N_{js}, the distribution of solid particles in viscoplastic fluids is more uniform than solid suspensions in water under the same regimes of agitation.

The numerical results and PEPT measurements are compared in the detailed 3-D distributions of the three velocity components of both phases and the solid concentration. The mean velocity profiles for both phases are well predicted, though a discrepancy occurs close to the tip of the impeller which may be due to the inadequacy of using the laminar model for modelling transitional flow. The spatial solid distributions are also well predicted, except in the central region underneath the impeller where they are largely overestimated.

7.1. Introduction

Solid-liquid suspensions have drawn considerable attention because of their wide use in industry. The majority of previous works has mainly focused on investigating dilute solid suspensions in water under highly turbulent flow regime. Both experimental and numerical studies on dense solid suspensions in water in highly turbulent flow have been discussed in detail in Chapter IV and Chapter V. However, little information could be found in the literature concerning solid particles suspended in non-Newtonian fluids in stirred vessels, though they are also widely encountered in industry, for example, fruit particles in yoghurt, petroleum and mining processes.

Viscoplastic fluids, as an important type of non-Newtonian fluids which exhibit complex rheology, have been described in detail in Chapter II. The mixing characteristics of single-phase viscoplastic fluids in stirred vessels have been reported in Chapter VI. Due to the viscosity dependence on shear rate and apparent yield stress of viscoplastic fluids, the flow mechanism of solid motion in viscoplastic fluids is expected to be significantly different with solid suspensions in water under the highly turbulent flow regime. Solid motion in viscoplastic fluids in stirred vessels is not only affected by gravity force, but also the apparent yield stress of viscoplastic fluids, so that the interactions between the liquid phase and solid particles become much more complicated. For example, because of the apparent yield stress, solid particles can be trapped in local positions if the gravity force acting on the particles does not exceed the apparent yield stress. As a consequence, a wide range of challenges in this area have not been addressed. Also the lack of suitable techniques results in various difficulties in investigating solid suspensions in viscoplastic fluids.

Relatively simple experimental and numerical studies concerning solid motion in non-Newtonian fluids have been carried out. The motion of a single solid particle in non-Newtonian fluids has been reported to be significantly different with that in turbulent Newtonian flows. The settling velocity of a single spherical particle in a non-Newtonian fluid has been studied extensively, as summarized by Wilson and Horsley (2004). Recently, experiments have been conducted to investigate the interactions between two particles falling in non-Newtonian fluids with one above the other (Horsley et al., 2004; Merkak et al., 2006), and the studies showed that the second particle had a greater terminal fall velocity due to the trail of the first particle. The sedimentation of one sphere particle and two falling spherical particles in a Bingham liquid has been numerically investigated by Prashant and Derksen (2011). They have found that the terminal velocity is affected by the separation distance, and the terminal velocity of two spheres becomes higher than that of a single sphere settling under the same conditions with the decrease in their separation distance. The present understanding of the motion of only one or two particles in complex non-Newtonian fluids has shed light on the effect of the rheological properties of non-Newtonian fluids on solid suspensions. The previous studies, however, only provide limited practical information for industrial process applications. Therefore, studies on the solid suspensions in non-Newtonian fluids at certain solid concentrations are necessary.

As discussed in Chapter IV and V, the just complete suspension (impeller speed of N_{js},) is a critical state which could satisfy the requirement in most industrial applications. Solid suspensions in highly turbulent Newtonian fluid flows have been numerously investigated and reported, and have been reviewed most recently by Jafari et al. (2012). Few studies have been attempted to determine the just suspended speed for solid suspensions in non-Newtonian fluids. In the studies of Kushalkar and Pangarkar (1995), the values of N_{js}, for solid

suspensions in CMC solutions of different rheologies, at the mean solid concentration of 0.5 wt% were investigated, and they found that the values of N_{js} are higher than those for solid suspensions in water.

Little information about the 3-D distribution of the phase velocities and solid concentration can be found in the literature, though this detailed information can provide a better and more efficient basis for design. Attempt at understanding the detailed local information of solid suspensions in Bingham liquids has been made numerically by Derksen (2009) using a lattice-Boltzman method. However, due to the lack of experimental data for the solid suspensions in viscoplastic liquids in stirred vessels, a one-dimensional single phase planar channel flow was performed instead for the validation of the CFD predictions. Confidence in using these predictions may be compromised, however, because of the significant difference between the flow mechanics of solid suspensions in a viscoplastic fluid in stirred tank and one-dimensional single phase planar channel flow.

In this chapter, the PEPT technique which has been successfully used to measure solid-liquid suspensions in water under turbulent flow regime, as presented in Chapter IV and Chapter V, is used to measure the distributions of the three velocity components of both the liquid and solid phases as well as the solid concentration at the just suspended speed N_{js} for the solid suspension in viscoplastic fluids. Numerical studies are also carried out by means of CFD modelling, and detailed quantitative comparisons between the two sets of data are conducted.

7.2. Materials and methods

7.2.1. Mixing vessel and solid-liquid systems

A flat-bottomed cylindrical glass tank of diameter T = 150 mm was used in the PEPT measurements. The vessel was fitted with four wall baffles of 0.1T spaced at 90° degrees and

was agitated by a down-pumping 6-blade 45º pitched-turbine (PBT) of diameter $D = T/2$, located $T/4$ from the tank base. The height of the suspension in the vessel was set at $H = T$. Nearly-monomodal and nearly-spherical glass beads (d_p = 1.00-1.25 mm) of ρ = 2485 kg m^{-3} were used. The mean solid mass concentration, X, varies in the range 2.4 – 21.6 wt% (equivalent volume concentration range, C of 1 – 10 vol%).

An aqueous solution of 0.1 wt% carbopol 940 (B. F. Goodrich Co.) was used to prepare the viscoplastic fluids. Detailed information about the preparation process has been reported in Chapter VI. It needs to be noted that the pH value of the carbopol solutions was altered to ~ 4.3 in the PEPT experiments in this chapter for two reasons: firstly, the liquid should exhibit Herschel-Bulkley behaviour, secondly, the solid particles could settle down to the tank base and are not trapped on the top free surface caused by too high value of apparent yield stress. The pH value of the carbopol solutions was altered after the carbopol solution was transferred to the mixing vessel to avoid the entrapment of air bubbles. The rheological properties of the fluid samples taken from the stirred tank were measured by a 2° 60 mm cone and plate geometry using a stress controlled rheometer (AR-1000, TA Instruments). The rheological properties are listed in Table 7.1.

Table 7.1. Rheological parameters and experimental conditions for solid-liquid suspension

X (wt%)	C (vol%)	τ_y (Pa)	k (Pa s^n)	n	N_{js} (rpm) (Re_{imp})
2.4	1	0.63	0.23	0.6	495 (965)
11.5	5	0.63	0.23	0.6	600 (1,268)
21.6	10	0.63	0.23	0.6	750 (1,754)

7.2.2. Positron emission particle tracking

A detailed PEPT measurement has been described in Chapter IV and Chapter V. It is noted that due to the less effective transportation of particle tracer under the transitional regime, a longer run time is necessary for the particle tracer to reach all regions of stirred vessel. The

tracking time in each PEPT measurement of solid suspensions in viscoplastic fluids was at least 60 min, longer than the runtime, ~30 min for the solid-liquid suspensions under highly turbulent flows.

PEPT measurements were conducted at N_{js}, which was visually determined in the transparent vessels based on the well-known Zwietering criterion, i.e. no particle remains stationary on the bottom of the tank for longer than 1-2 s (Zwietering, 1958). The range of PEPT experiments and CFD studies conducted are summarized in Table 7.1.

7.3. Numerical modelling

The basic governing equations for solid-liquid suspensions, i.e. the continuity and momentum equations in the CFD modelling have been reported in Chapter IV, i.e. Eqs. (4.1), (4.2). The multi-fluid Eulerian-Eulerian model was used, whereby the liquid and solid phases were both treated as continua, and the momentum transfer between the two phases was calculated using the Gidaspow drag model (Gidaspow, 1994), i.e. Eqs. (4.4), (4.5) in Chapter IV. As mentioned in Chapter VI that due to the dependence of the viscosity of the viscoplastic fluid on the shear rate, an additional correlation that describes the relationship between the apparent viscosity and shear rate needs to be solved simultaneously with the continuity and momentum equations. The Herschel-Bulkley model, i.e. Eqs. (6.1), (6.2) was implemented into the CFD simulation using the expression language feature in the ANSYS CFX 12.0.

The MFR approach which has been widely used in the CFD modeling of single phase viscoplstic fluid mixing in stirred tank (Pakzad et al. 2008; Saeed et al., 2008; Adams and Barigou, 2007), was employed to deal with the interaction between the stationary baffles and the rotating impeller blades. The rotating domain containing all the rotating elements (hub, blades and shaft) and the stationary domain containing the stationary parts (baffles, tank wall

and base) are displayed in Fig. 7.1. The computational grid consisted of 805,440 non-uniformly distributed unstructured tetrahedral cells based on the mesh independence study, as illustrated in Fig. 7.1. A denser mesh is used in the rotating domain for better accuracy, because this region is characterized by high velocity gradients. Inflated boundary layers were used on the tank bottom, walls, baffles, blades and shaft to cover the high velocity gradients in these regions of no slip. The numerical simulations were performed using the commercial CFD code ANSYS CFX 12.0. Numerical convergence was assumed when the sum of all normalized residuals fell below 10^{-6} for all equations.

The Reynolds number varies from 965 to 1,754, i.e. within transitional regimes. All simulations were conducted using the laminar model in this chapter, which has been widely accepted to be suitable for modeling the transitional regimes (Pakzad et al. 2007; Kelly and Gigas, 2003; Letellier et al., 2002; Zalc et al., 2001).

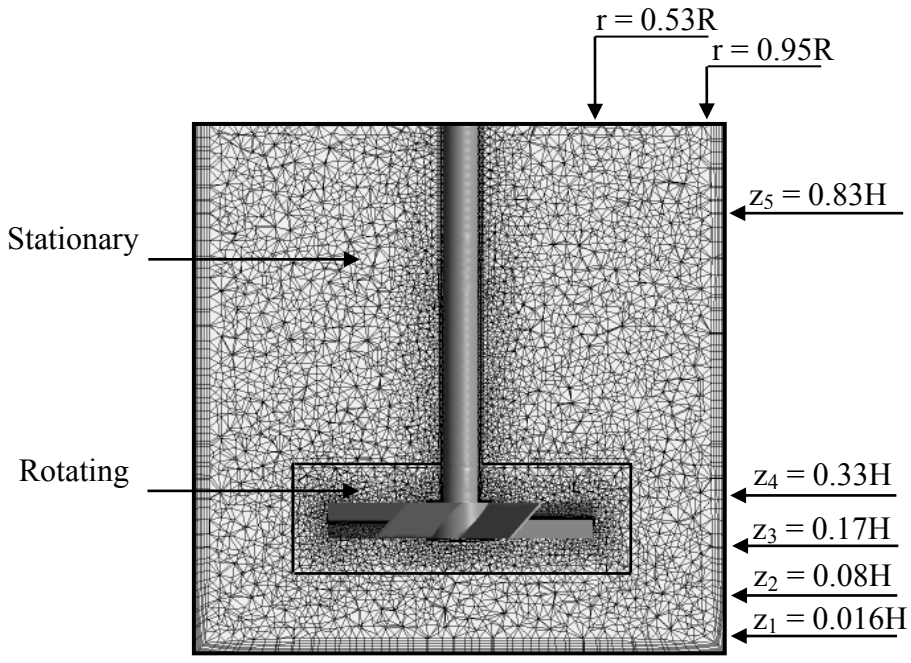

Figure 7.1. Computational grid section in the 45° plane between two baffles.

7.4. Results and discussion

7.4.1. Velocity distributions

Fig. 7.2 shows the vector maps of the normalized azimuthally-averaged velocities of the agitated liquid and solid phases from PEPT measurement, at the just suspense speeds of N_{js}. It shows the typical single flow loop generated by a down-pumping PBT. The fluid velocities of both phases under all investigated conditions relatively high in the typical circulation loop generated by the down-pumping PBT, however, fluid velocities reduce significantly outside of the flow loops and in the loop eyes.

The velocity vector map of the mixing of viscoplastic fluid without the presence of solid particles at N = 495 rpm which is equal to the impeller speed of N_{js} at X = 2.4 wt%, is also shown in Fig. 7.2 for the sake of qualitatively presenting the effect of the solid particles on the flow field of the liquid phase. Comparing the flow fields of the liquid phase with and without the presence of solid particles (i.e. X = 2.4 wt% and X = 0 wt%, respectively) at the same impeller speed of N = 495 rpm, a bigger circulation loop of the liquid phase is observed with the presence of solid particles at X = 2.4 wt% than that at X = 0 wt%. The colour of the velocity vector map represents the magnitude of the total velocity, i.e. $u = \sqrt{u_z^2 + u_r^2 + u_\theta^2}$. It can be observed that the colour of the circulation loop of the liquid phase with the solids presence is darker, in particular, within the impeller region and along the tank wall, indicating higher flow velocity. Therefore, adding solid particles could significantly enhance both the fluid circulation loop and the fluid velocity of viscoplastic fluids.

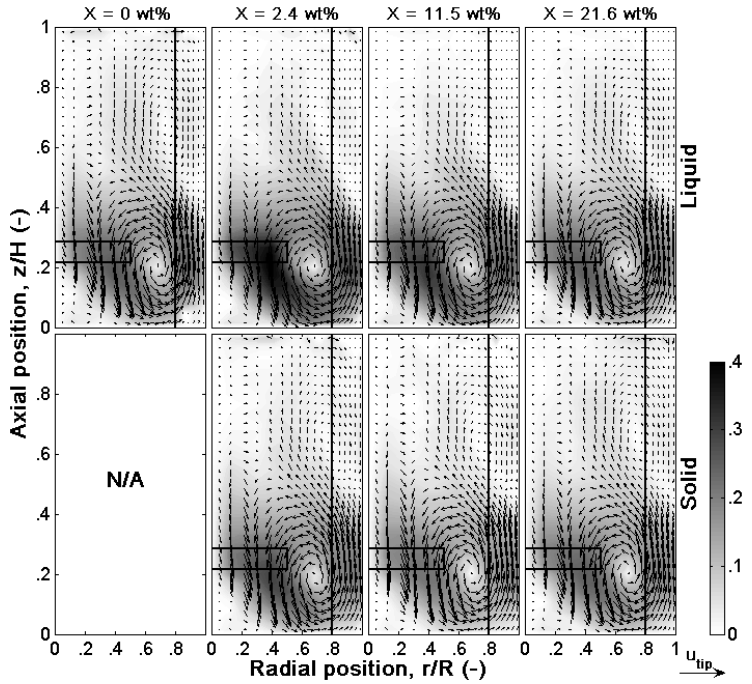

Figure 7.2. Azimuthally-averaged velocity maps of the liquid and solid phases at varying X and $N = N_{js}$.

Considering the liquid flow fields at higher solid concentrations, i.e. X = 11.5 wt% and X = 21.6 wt%, the circulation loops are also larger than that of X = 0 wt%. However, in comparison with that at X = 2.4 wt%, the diminution of the normalized velocity at higher solid concentrations can be observed. The diminution of the normalized velocity with increasing mean solid concentration can also be observed for the solid phase. Similar damping trend for both phases has also been reported for solid suspensions in water (Guida et al., 2010). This trend should be analysed together with the detailed solid concentration distributions (as discussed in section 7.4.4), because the local hydrodynamics of both phases and the local solid concentration are closely related and affected by each other.

Comparing the flow fields of the liquid phase with those of the solid phase at solid concentrations investigated, it can be found that the fluid velocity of the liquid phase is higher than that of the solid phase, especially in the impeller discharge stream and at X = 2.4 wt%.

For solid suspensions in water, however, it has been reported in Chapter IV that the solid particles lead the flow in the impeller discharge stream. The different observations between solid suspension in viscoplastic fluids and solid suspension in water could be attributed to the different rheological properties of the continuous phase, which has a significant effect on the inter-phase interactions.

7.4.2. Effect of the presence of solid phase on the flow field of the liquid phase

The effect of solid particles on the flow velocity of liquid phase which is usually water has been reported in a number of earlier studies. The conclusions from these studies are in contrast. For example, the large drop in liquid velocities in the presence of particles have been reported in some studies (Nouri and Whitelaw, 1992; Montante and Lee, 2000; Virdung and Rasmuson, 2003; Micheletti and Yianneskis, 2004), however, some other studies reported little effect (Guiraud et al., 1997; Ljungqvist and Rasmuson, 2001; 2004; Unadkat et al., 2009; Pianko-Oprych et al., 2009). These contrary findings may be due to the complex interactions between the two phases. There has so far no published studies concerning the effect of solid particles on the viscoplastic fluid flow, to the author's knowledge.

Fig. 7.3 shows the azimuthally-averaged three velocity components (u_z, u_r, u_θ) of the liquid phase with and without solid presence at the same impeller speed of N = 495 rpm. Significant localised differences can be seen near the impeller and along the wall of the vessel, which is more pronounced for the axial velocity, u_z. However, all three velocity components (u_z, u_r, u_θ) of the liquid phase in the upper part of the vessel ($z = 0.83H$) are slightly affected by the solid particles.

Considering the individual component of the liquid velocity, the tangential component, u_θ, is slightly affected by solid particles throughout the stirred vessel. Close to the tank base, all of the fluid has to flow in the radial direction towards the tank wall, therefore, the effect of the solid particle is more pronounced for the radial component, u_r, which is enhanced in the presence of particles. In the vicinity of impeller ($z_3 = 0.17H$, just below the impeller and $z_4 = 0.33H$, just above the impeller), the axial component, u_z, is mainly affected, and is increased significantly by the addition of solid particles.

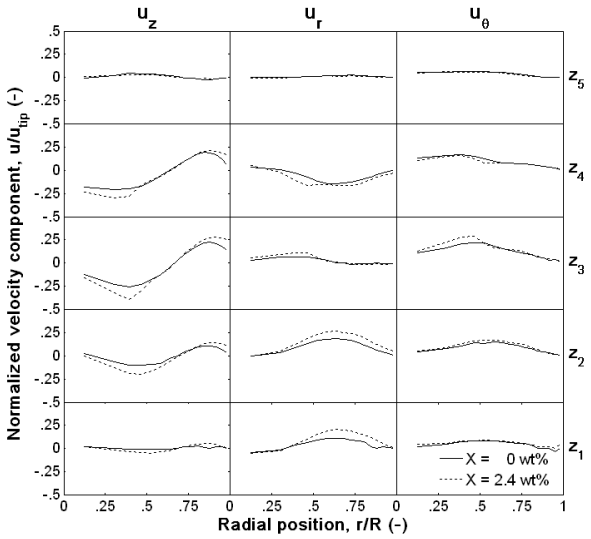

Figure 7.3. Effect of solid phase on the velocity distribution of the liquid phase at N_{js}.

As reported in Chapter IV that the effect of solids on the velocity field of water was not negligible with solid concentration up to X = 10.6 wt%, and the effect become apparent by adding more solids, affecting mainly the axial component u_z near the impeller and along the wall of the stirred vessel. For solid suspensions in viscoplastic fluids, however, the effect of solid particles has found to be considerable on the flow field of viscoplastic fluids flow at very low concentration, X = 2.4 wt%.

7.4.3. Flow number

The flow number of solid suspensions in water has been discussed in detail in Chapter IV and Chapter V. Based on the same calculation method and using Eqs. (4.9) and (4.10), the flow number of solid suspensions in viscoplastic fluids was calculated by integrating along the lower horizontal edge of the impeller blade the axial velocity profile weighted by the local phase volume concentration, i.e. by c for the solid phase and by (1-c) for the liquid phase. The solid flow number, $Fl^{(S)}$, as illustrated in Fig. 7.4 increases proportionally to C. The liquid flow number, $Fl^{(L)}$, on the other hand, reduces almost linearly with the increase in solid mean concentration. The two-phase flow number, Fl, decreases at similar rate to the $Fl^{(L)}$, because the solid flow number $Fl^{(S)}$ is only a small fraction and cannot compensate the significant reduction of $Fl^{(L)}$. Fl reduces by ~ 26% when X rises from 2.4 wt% to 21.6 wt%.

At zero solid concentration (i.e. single-phase viscoplastic fluid), Fl is ~ 0.65, which is smaller than that reported for mixing of water, ~ 0.87 in Chapter IV. The flow number of non-Newtonian fluids has been found to be a function of the rheological properties of the fluid. Reductions in the impeller flow number for agitating various non-Newtonian fluids including shear-thinning and viscoplastic fluids in comparison with the flow number for water, have been reported in the previous literature (Jaworski and Nienow, 1993; Ein-Mozaffari et al. 2007a; Saeed et al., 2008).

Because of the concern of the radial discharge contribution, the radial flow from the side edge of the impeller blades was calculated by integrating the radial velocity on the cylindrical surface around the impeller tip by equation,

$$Fl = \frac{Q}{ND_3} = \frac{1}{ND^3} \int_{PBT} cu_r dS \tag{7.1}$$

However, the values of the radial flow rate for both phases was found to be one order of magnitude lower than the axial flow rate indicating small radial contribution, therefore, the radial discharge was not taken into account.

The significant increase in the liquid flow number $Fl^{(L)}$ to a value of ~ 0.85 at X = 2.4 wt% could be attributed to the significant increase in the liquid velocities in the discharge stream of the impeller resulting from the presence of solid particles.

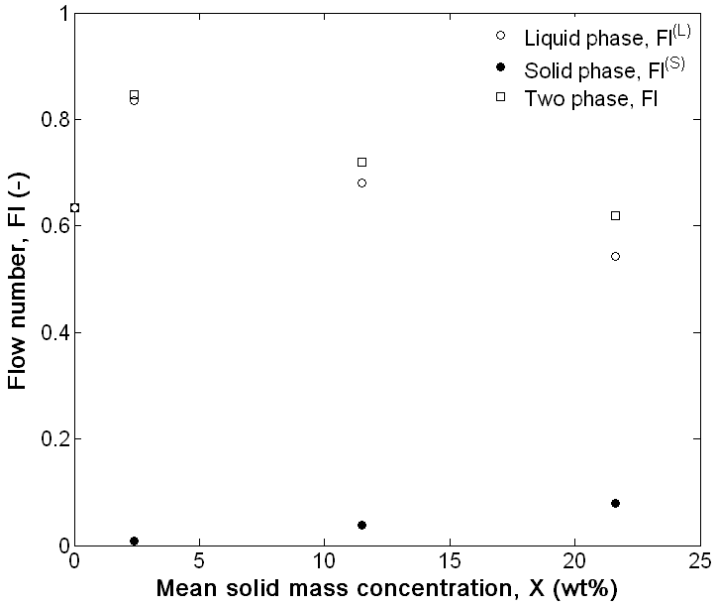

Figure 7.4. Effect of the mean mass concentration of the solid phase on the flow number.

7.4.4. Particle-fluid slip

On the basis of PEPT measurements, the spatial distributions of the normalised total local time-average slip velocity, s for all solid concentrations investigated, at their N_{js} speeds, and estimated using equation (4.8) are depicted in Fig. 7.5. The individual slip components in the r, z, and θ directions, i.e. s_z, s_r, and s_θ are also displayed.

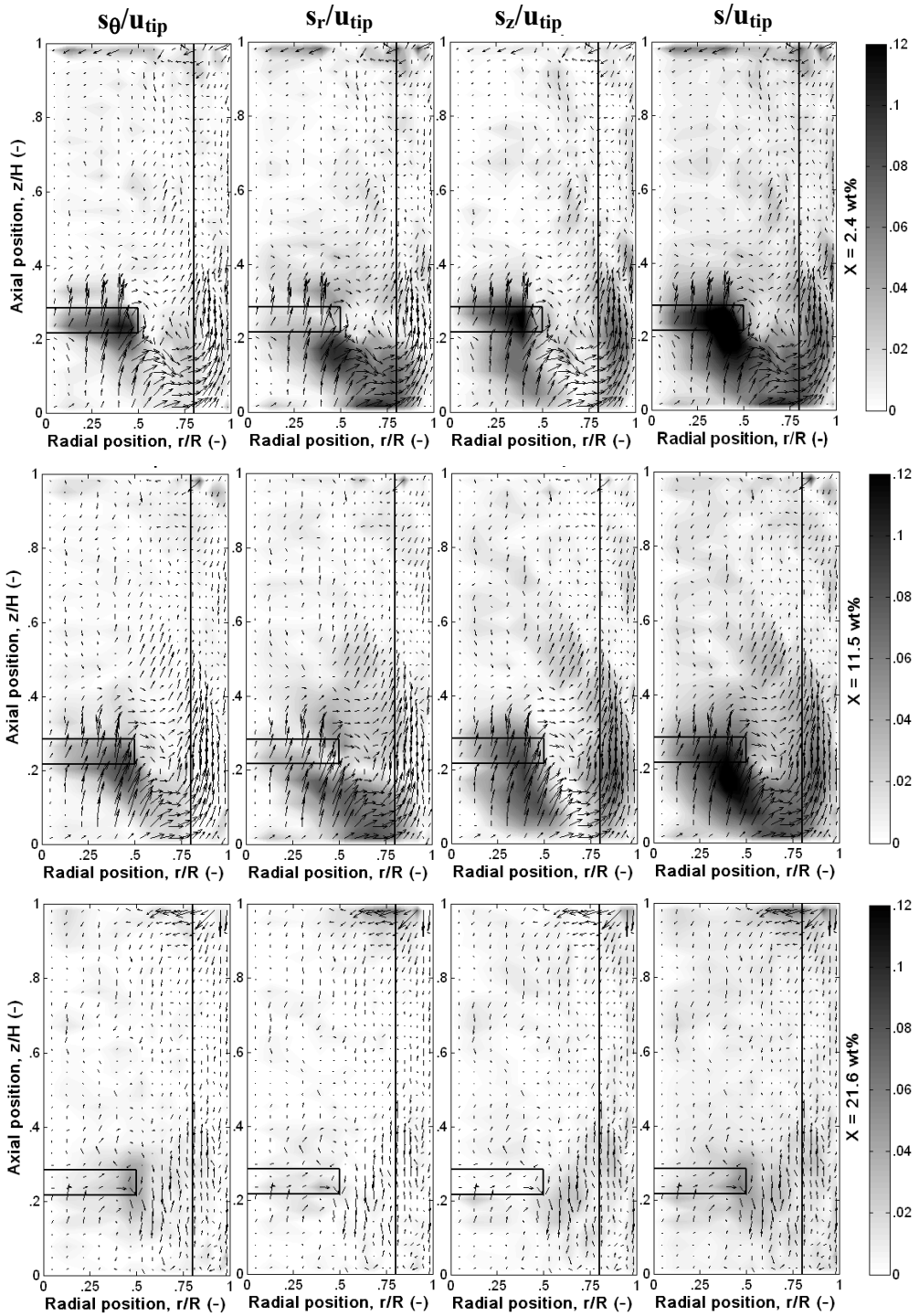

Figure 7.5. Azimuthally-averaged maps of time-averaged slip velocity from PEPT measurements.

At low to moderate X values, there are wide variations in the spatial distributions of s. The largest total slip velocities occur in the discharge region of the impeller and are of the order of

$\sim 0.12\,u_{tip}$. Considering the individual components of the slip velocity vector, the largest axial slip and radial slip occur in the in the impeller discharge region and at the bottom of the circulation loop, respectively, whereas, the largest slip in the tangential direction is observed in the vicinity of impeller blades. Away from the circulation loop, in the upper part of the stirred vessel, the slip velocity drops significantly.

The distributions and magnitudes of the normalized slip velocity, s, at X = 2.4 wt% and X = 11.5 wt% present qualitative similarity. However, the normalised slip velocity reduces significantly at high solid concentration of 21.6 wt%. As mentioned in section 7.4.1, this variation may be closely related to the solid concentration distribution, which is discussed in more detail below in the following section.

7.4.5. Solid distributions

The contours of the azimuthally-averaged spatial distributions of the local solid concentration in viscoplastic fluids at various solid concentrations investigated here, and at their corresponding N_{js} speeds, normalised by the overall mean volume solid concentration (C) are shown in Fig. 7.6. At X = 2.4 wt%, solid particles accumulate in the central region underneath the impeller and at the tank base. The solid concentration above the impeller reduces gradually upwards until it reaches zero close to the surface. Radially, the solids are nearly uniformly distributed.

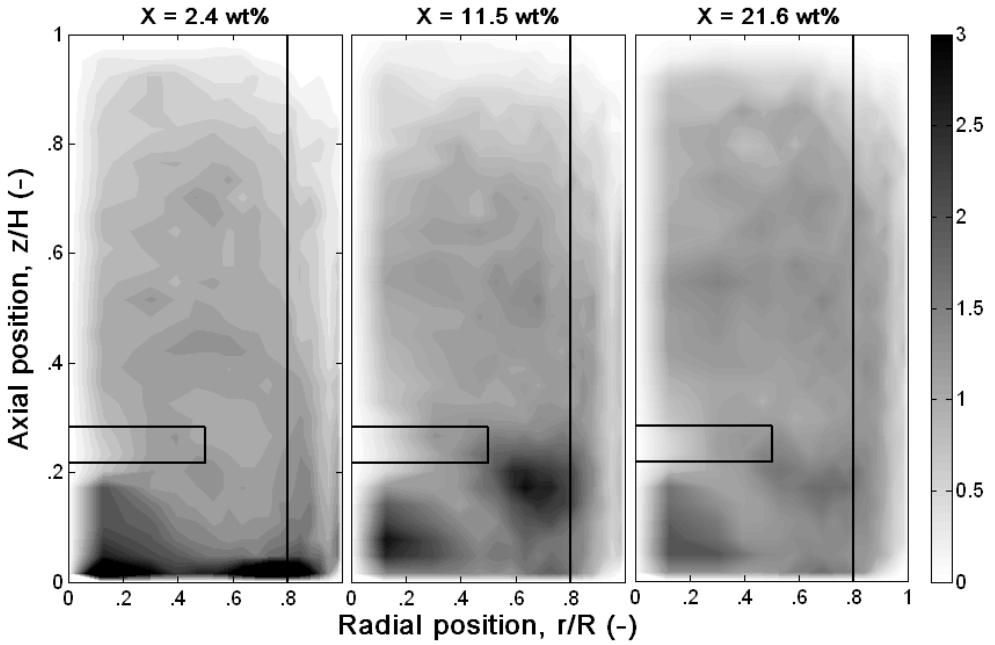

Figure 7.6. Normalized azimuthally-averaged maps of spatial distribution of the local solid concentration at varying X and $N = N_{js}$.

Increasing the mean solid concentration, at X = 11.5 wt%, the solid particles are significantly lifted up from the tank base, though a certain amount of particles remain in the central region underneath the impeller and trapped in the center of flow loop. The solid concentration distributions become nearly uniform at X = 21.6 wt%.

In comparison with the solid distributions in water under the just suspended condition, as discussed in Chapter IV, where there are considerable concentration gradients in the axial direction in the stirred vessel, the solid distributions in viscoplastic fluids are more uniform in the bulk region of the stirred tank. This could be attributed to the apparent yield stress of viscoplastic fluids which is capable of hindering the falling of solid particles.

7.4.6. Uniformity of suspension

As discussed in Chapter IV, the degree of suspension uniformity can be assessed by a global uniformity index, ξ, which is defined as,

$$\xi = \frac{1}{\sigma^2 + 1} = \frac{1}{\frac{1}{N_C}\sum_{i=1}^{N_C}\left(\frac{c_i - C}{C}\right)^2 + 1} \tag{7.2}$$

where N_c is the total number of cells in the PEPT measurement (or CFD computational) grid and i is the cell number (Guida et al., 2009; 2010). ξ increases with the increase in the degree of uniformity of solid distributions within the vessel volume, and when $\xi = 1$ (i.e. $\sigma^2 = 0$) the solids are uniformly distributed within the vessel volume, i.e. the local solid concentration everywhere is equal to the average concentration in the vessel.

Fig. 7.7 shows the values of ξ at various solid concentrations. It can be seen that ξ increases sharply as a function of the mean solid concentration when the suspensions are considered at the same hydrodynamic mixing regime, i.e. at their N_{js} speeds. This indicates that more concentrated suspensions tend to achieve significantly more homogeneous state.

The values of ξ in Fig. 7.7 are much higher compared with those for the solid distributions in water, as shown in Fig. 4.12. This, again, proves that solid particles are more uniformly distributed in viscoplastic fluids than in water under the just suspended regime of agitation.

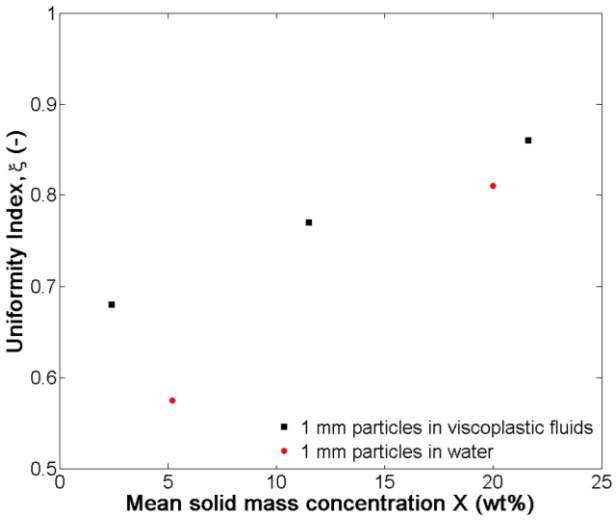

Figure 7.7. Variation of the suspension uniformity index as a function of the mean solid mass concentration.

7.4.7. Mass continuity

Mass continuity is defined as the mass flowing into a closed volume is equal to the mass flowing out of it. It has been used by Guida et al. (2010; 2011) for validating the accuracy and reliability of the PEPT measurements for the solid suspension in turbulent water flows.

Similarly, the mass continuity was analysed in this section to verify the flow data of both phases from the PEPT measurements. The ideal mass continuity require the net mass flux through a volume bounded by a closed surface S be zero. The mass continuity was calculated on two surfaces using the equation,

$$\sum_{S} u \cdot \Delta S \cong 0 \tag{7.3}$$

Two cylindrical closed surfaces were used, one comprising the same vertical axis, base and diameter as the tank but with a shorter height, and the other comprising the same vertical axis and height as the tank but with a smaller diameter, as shown in Fig. 7.8. It can be seen that the calculations are smaller than $0.02u_{tip}$ indicating a high degree of the accuracy of the flow data from the PEPT measurements.

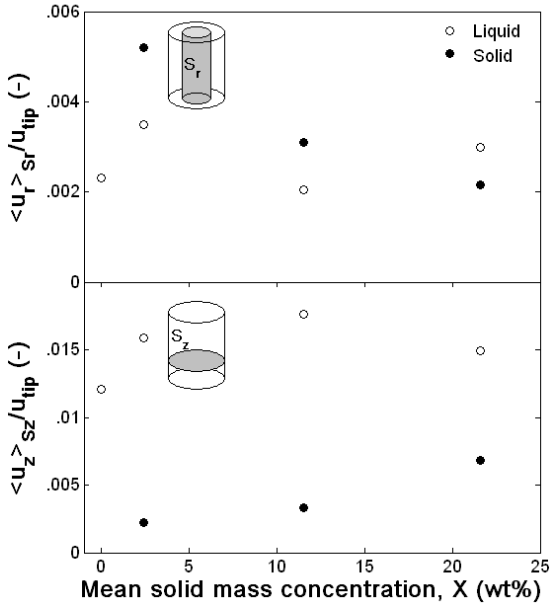

Figure 7.8. Normalized radial and axial velocities averaged on surface S_r (of diameter 0.53T) and S_z (0.2H off the base), respectively.

7.4.8. Comparison of velocity distributions from CFD and PEPT

A detailed quantitative comparison between the CFD predictions and PEPT data was conducted at the positions depicted in Fig. 7.1. For both liquid and solid phases, the azimuthally-averaged distributions of the local velocity components (u_z , u_r , u_θ) were compared:

(i) axially along two radial positions: r = 0.53R, close to the tip of the impeller; and r = 0.95R, close to the tank wall; and

(ii) radially along five axial positions: z_1 = 0.016H, close to the base of the vessel; z_2 = 0.08H, approximately halfway between the base and the lower edge of the impeller; z_3 = 0.17H, just under the lower edge of the impeller; z_4 = 0.33H, just above the upper edge of the impeller; and z_5 = 0.83H, in the upper part of the vessel. All the velocity plots presented have been normalized by the impeller tip speed ($u_{tip} = \pi DN$).

The azimuthally-averaged spatial distributions of the local solid concentration were also resolved both by PEPT and CFD, and compared at these two radial and five axial locations. The solid concentration profiles presented have been normalized by the overall mean volume solid concentration (C).

The detailed quantitative comparisons of the azimuthally-averaged axial and radial velocity distributions measured by PEPT and predicted by CFD modelling, are shown in Fig. 7.9 and Fig. 7.10, respectively, for the liquid phase and solid phase at a solid concentration of 2.4 wt%. Similar observations can be made about the liquid velocity distributions and the particle velocity distributions throughout the stirred vessel. Both the axial and radial distributions exhibit sharp variations of all three velocity components around the impeller, i.e. $r = 0.53R$, $z = 0.17H$, $z = 0.33H$. Close to the tank wall, at $r = 0.95R$, the axial velocity component, u_z also shows a sharp belly shape, because here the fluid has to flow upward due to the effect of the baffles, as shown in Fig. 7.2. In the regions close to the impeller and tank wall, the fluid viscosity reduces significantly due to the local high shear rate, therefore, better mixing occurs in these regions in comparison with mixing in other regions of the stirred vessel. The velocities of both phases reduce fast upward as the axial profiles show that all the three velocity components have dropped to about zero at $z \sim 0.5H$. This could be attributed to the significant effect of the apparent yield stress.

The velocity distributions of both phases are well predicted by CFD, particularly in the radial direction. However, the local maxima of u_z close the impeller tip ($r = 0.53R$) and tank wall ($r = 0.95R$) are greatly overestimated by CFD modelling, for example, the maximum deviation of the velocity of solid phase at $r = 0.95R$, is about $\sim 0.15\,u_{tip}$. Such a significant error could be attributed to inaccuracy of using the laminar model in these regions, as discussed in section

7.4.1 that the flow velocity is relatively high in these regions. The laminar flow model has been commonly used for modelling the low transitional flow by other researchers (Zalc et al., 2001; Letellier et al., 2002; Kelly and Gigas, 2003; Alliet-Gaubert et al., 2006; Ein-Mozaffari and Upreti, 2009), but the suitability of using the laminar flow model for relatively high transitional flow, like in this work (Re_{imp} listed in Table 7.1), has not been examined. The SST model which has been stated to perform more appropriately for the transitional flows at higher Re_{imp} by Bakker et al. (2009) was attempted in this work, but no improvement was obtained, therefore, the results from the SST model are not shown for the sake of brevity. The agreement between the PEPT measurements and the CFD predictions is fairly good away from the impeller where the fluid flow falls into the laminar or low transition regime, thus good predictions are obtained using the laminar model.

Comparing the local maximum of the axial velocity component of the solid particles to that of the liquid near the tank wall, the upward moving particles lag the upward moving fluid. This is similar to the solid suspended behaviour in water which has been reported by other workers (Guiraus et al., 1997; Ljungqvist and Rasmuson, 2001). In the impeller discharge region, the liquids are discharged downwards at a significantly higher velocity than the solid particles, for example, $u_z \sim 0.40\, u_{tip}$ compared to $\sim 0.30\, u_{tip}$ at $z = 0.17H$, on the basis of the PEPT measurements. Above the impeller ($z = 0.33H$) where all of the fluids return to the impeller, the liquid also leads the downward flow. This has been observed qualitatively in Fig. 7.2.

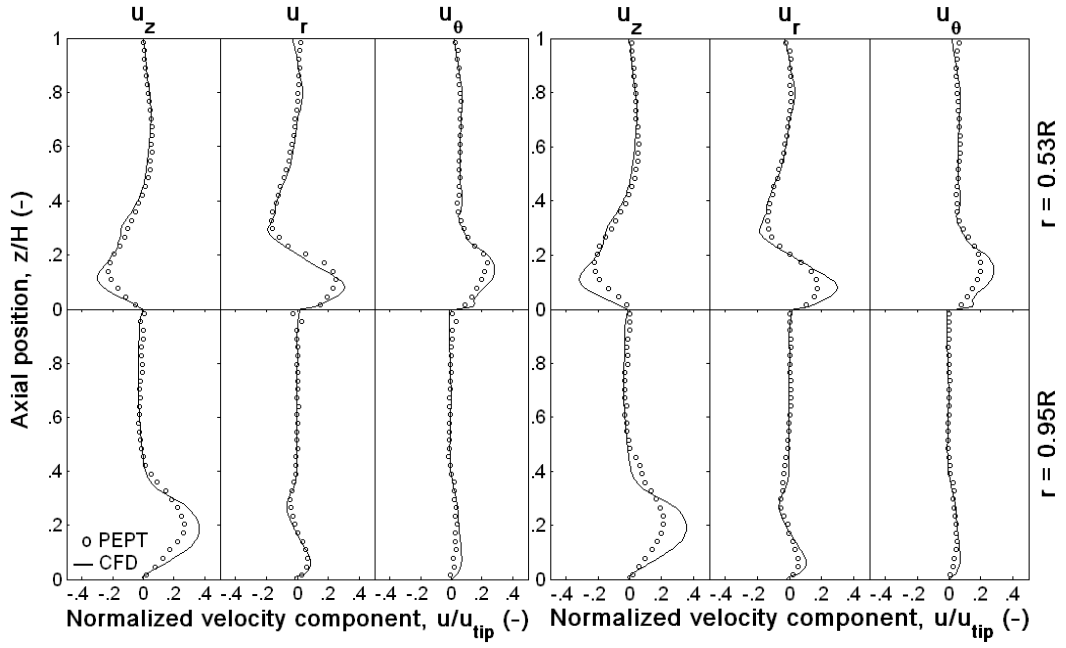

Liquid phase **Solid phase**

Figure 7.9. Azimuthally-averaged axial distributions of the velocity components of the liquid and solid components at N_{js}: X = 2.4 wt%; N_{js} = 495 rpm (Re_{imp} = 965).

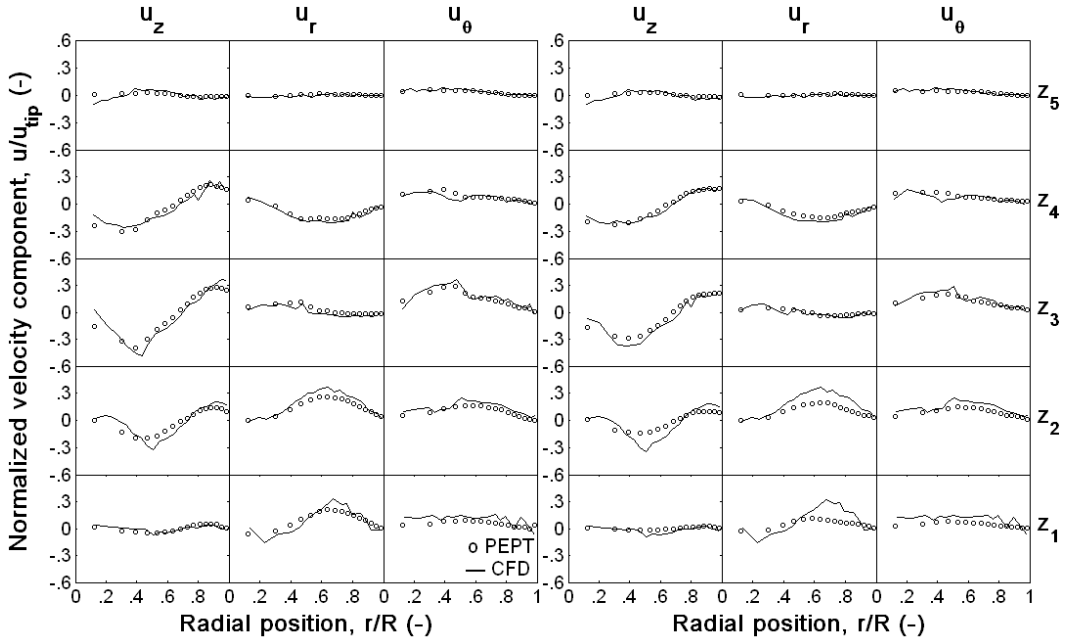

Liquid phase **Solid phase**

Figure 7.10. Azimuthally-averaged radial distributions of the velocity components of the liquid and solid components at N_{js}: X = 2.4 wt%; N_{js} = 495 rpm (Re_{imp} = 965).

Detailed comparisons of the azimuthally-averaged velocity distributions at N_{js}, at solid concentrations of 11.5 wt% and 21.6 wt%, obtained from PEPT and CFD, are shown in Fig. 7.11–7.14, respectively. These distributions are similar to those observed at 2.4 wt% solids. As expected, the discrepancies between PEPT data and CFD predictions become more serious with the increase in Reynolds number which may be due to the inadequacy of the laminar model, as mentioned above.

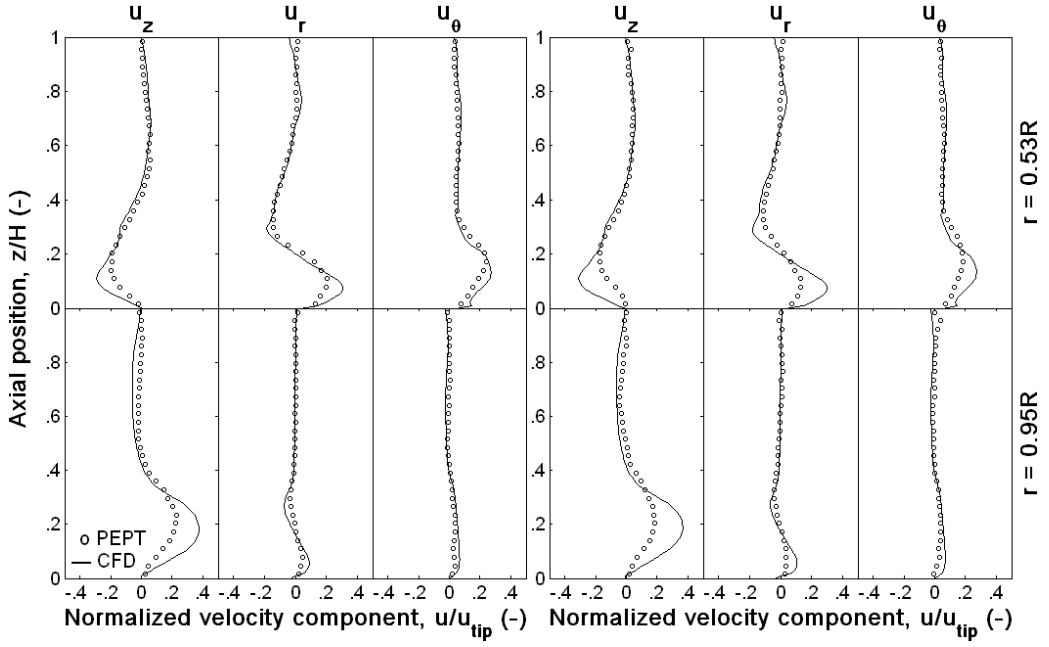

Figure 7.11. Azimuthally-averaged axial distributions of the velocity components of the liquid and solid components at N_{js}: X = 11.5 wt%; N_{js} = 600 rpm (Re_{imp} = 1,268).

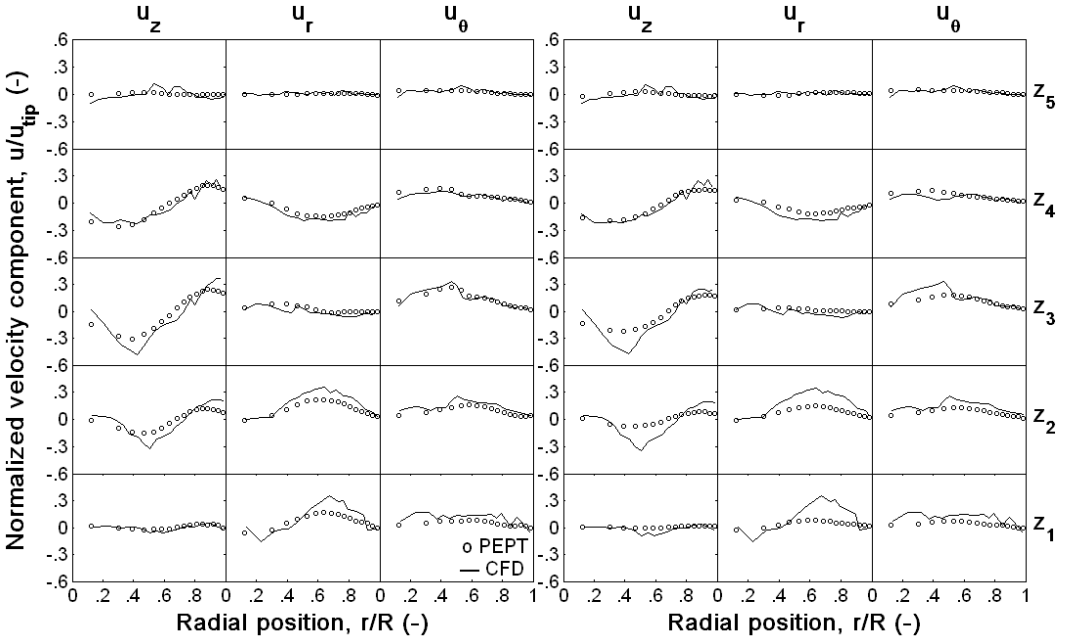

Liquid phase **Solid phase**

Figure 7.12. Azimuthally-averaged radial distributions of the velocity components of the liquid and solid components at N_{js}: X = 11.5 wt%; N_{js} = 600 rpm (Re_{imp} = 1,268).

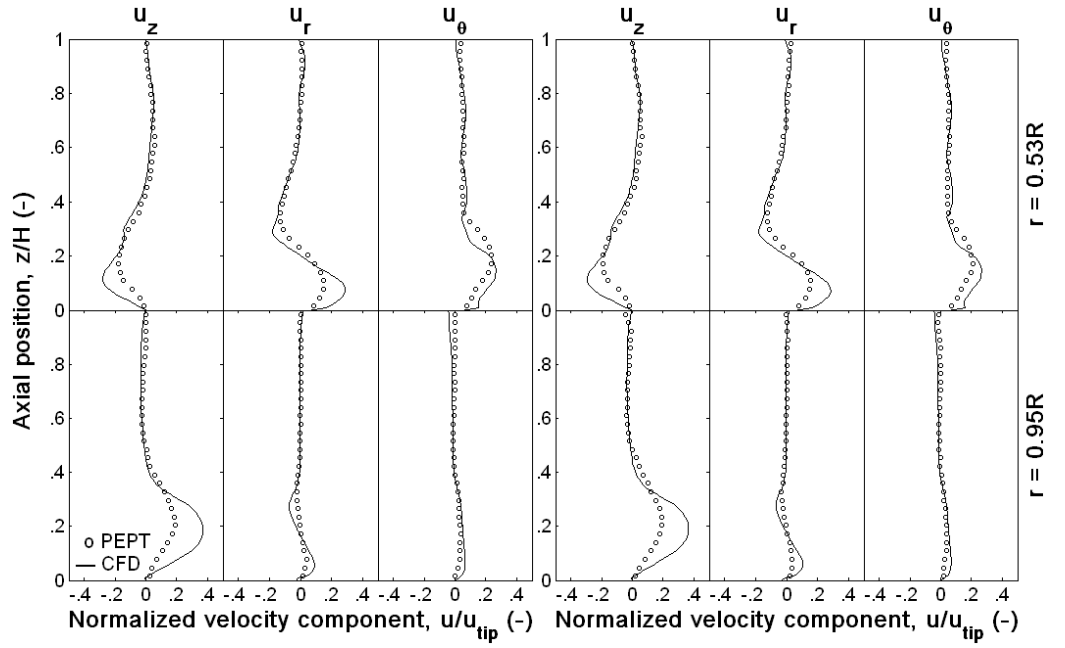

Liquid phase **Solid phase**

Figure 7.13. Azimuthally-averaged axial distributions of the velocity components of the liquid and solid components at N_{js}: X = 21.6 wt%; N_{js} = 750 rpm (Re_{imp} = 1,754).

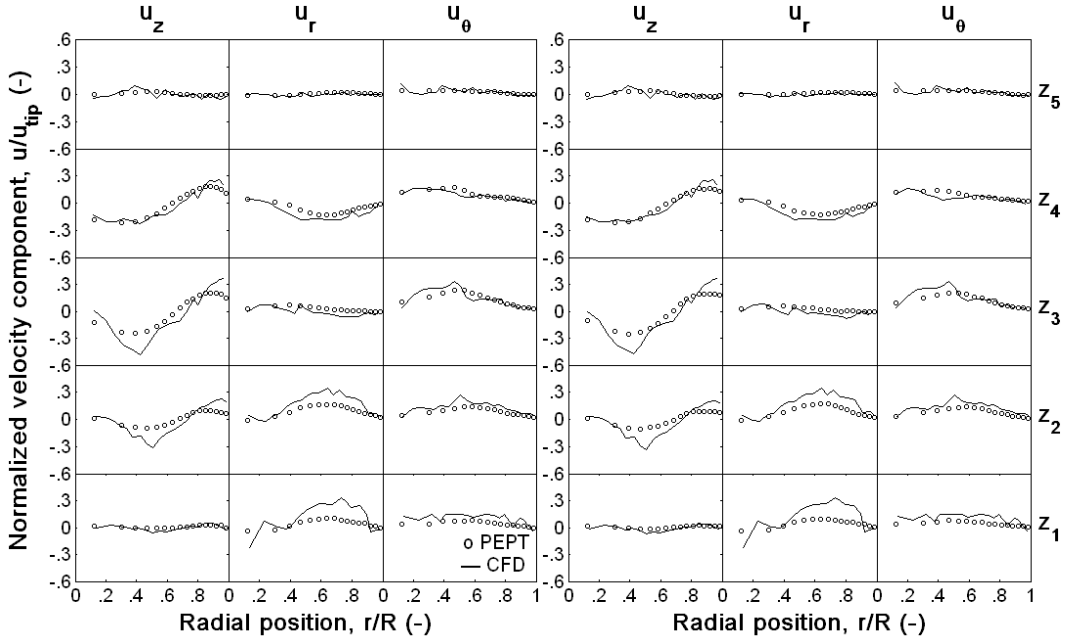

Figure 7.14. Azimuthally-averaged radial distributions of the velocity components of the liquid and solid components at N_{js}: X = 21.6 wt%; N_{js} = 750 rpm (Re_{imp} = 1,754).

In comparison with solid suspensions in turbulent water flow, the axial velocity, u_z, of both phases in solid suspensions in viscoplastic fluids, reaches the local maxima at a distance from the tank wall ($r \sim 0.8R$), as shown in the radial profiles for all solid concentrations investigated, i.e. Fig. 7.10, Fig. 7.12 and Fig. 7.14. However, for solid suspensions in turbulent water flow, it has been reported in Chapter IV that all fluids flowing upward near the wall reach the local maxima at the tank wall ($r \sim R$). Again, the difference could be attributed to the different rheological properties of the continuous phases. The local maxima of both phases in solid suspensions in viscoplastic fluids occurring away from the tank wall could be caused by the apparent yield stress of viscoplastic fluids.

7.4.10. Comparison of solid distributions from CFD and PEPT

The quantitative detailed azimuthally-averaged radial distributions of solid concentrations obtained from the CFD predictions and PEPT measurements are shown in Fig. 7.15. Overall,

the agreement between the PEPT measurements and the CFD predictions is good, except near the tank base ($z = 0.016H$) and in the centre below the impeller where the solid concentration is seriously overpredicted in the CFD modelling. However, the predictions near the impeller and close to the base improve significantly with an increase in mean solid concentration.

In the upper region, away from the impeller, the agreement improves substantially and tends to be very good. The solid distributions at $z = 0.33H$ and $z = 0.83H$ are nearly the same, ~ $0.8C$, based on the PEPT measurement. This quantitatively confirms that the solid above the impeller ($z > 0.33H$) are nearly uniformly distributed.

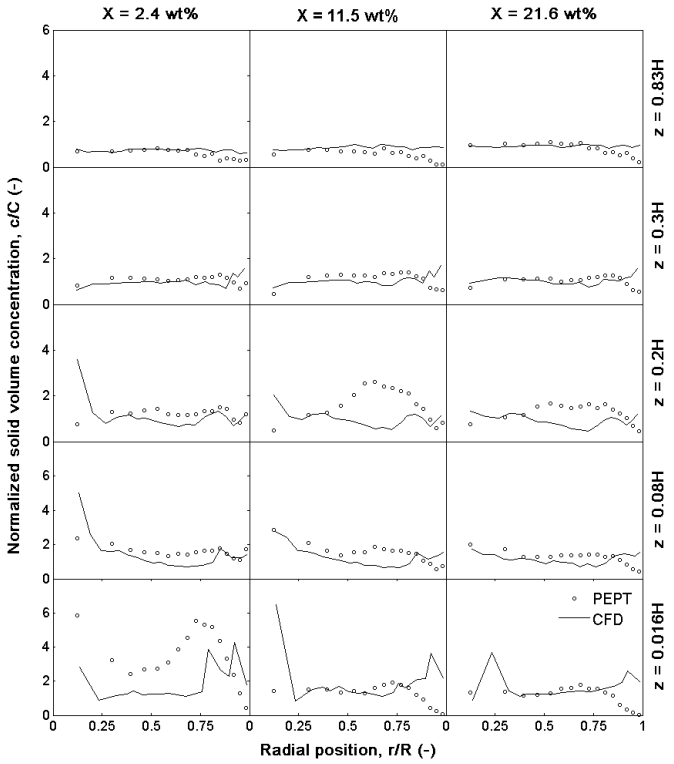

Figure 7.15. Radial profiles of azimuthally-averaged solid volume concentration.

Moreover, Fig. 7.15 quantitatively confirms the observations shown in Fig. 7.6 that there is a clear mound of accumulated solids close to tank bottom ($z = 0.016H$) at low solid concentration, $X = 2.4$ wt%, which are ~ 6 times greater than the mean concentration. However, the solid concentration in this region reduces significantly to ~ C as X increases to

11.5 wt% and 21.6 wt%. Moreover, at X = 21.6 wt%, the solid distributions at different height levels are nearly the same, implying the nearly uniform solid distributions throughout the stirred vessel.

7.4.10. Numerical study of the effect of solids on mixing of viscoplastic fluids with higher apparent yield stress

In order to investigate solid suspensions in viscoplastic fluids with higher apparent yield stress, rheological parameters of the viscoplastic fluid (Solution 2) in Chapter VI were used, i.e. $\tau_y = 1.697$, k = 0.431, and n = 0.589. Figure 7.16 – 7.18 show the azimuthally-averaged velocity distributions of solid phase in viscoplastic fluids with low and relatively high apparent yield stress, at solid concentrations of 2.4 wt%, 11.5 wt% and 21.6 wt%, respectively. It can be seen that the flow fields of solid phase are identical. Solid distributions in these two viscoplastic fluids are also identical, as shown in Fig. 7.19. The little effect of liquid rheology may be caused by the high shear rate because of the high speeds investigated.

Therefore, a smaller impeller speed of N = 200rpm was employed. Fig. 7.20 compares the flow fields of the liquid phase with and without the presence of solid particles (i.e. X = 0 wt%, X = 2.4 wt% and X = 11.5 wt%) at the same impeller speed of N = 200 rpm. Identical velocity profiles are presented. Little effect of solid particles on the flow velocity of viscoplastic fluids with relatively high apparent yield stress may be because solid particles could not move freely due to the apparent yield stress. Solid particles being trapped in local positions can be seen from Fig. 7.21. In the higher region of the stirred tank ($z = z_5$) where the velocity is zero, the solid concentration is equal to the mean solid concentration, i.e. $c = C$. At high speeds, i.e. N_{js} at X = 2.4 wt% and X = 11.5 wt%, due to the reduction of the apparent viscosity in the upper part of the stirred tank ($z = z_5$), solid particles move downwards which results in fewer

particles suspended at high speeds than low impeller speeds. This is similary to that reported by Derksen (2009). However, it can be seen that more particles are lifted from tank base at higher speed.

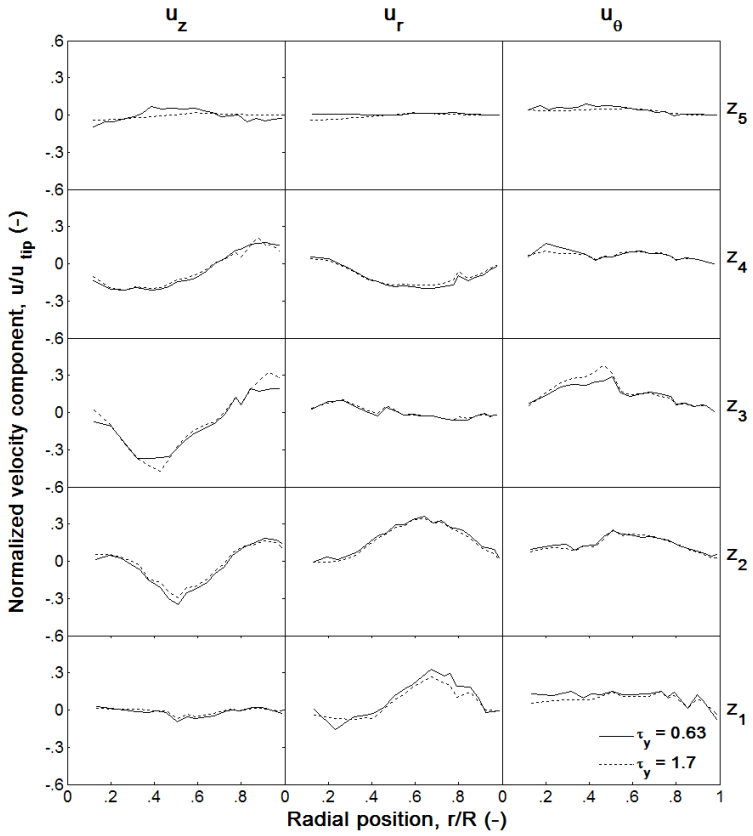

Figure 7.16. Azimuthally-averaged radial distributions of the velocity components of the liquid and solid components at N_{js}: X = 2.4 wt%; N_{js} = 495 rpm.

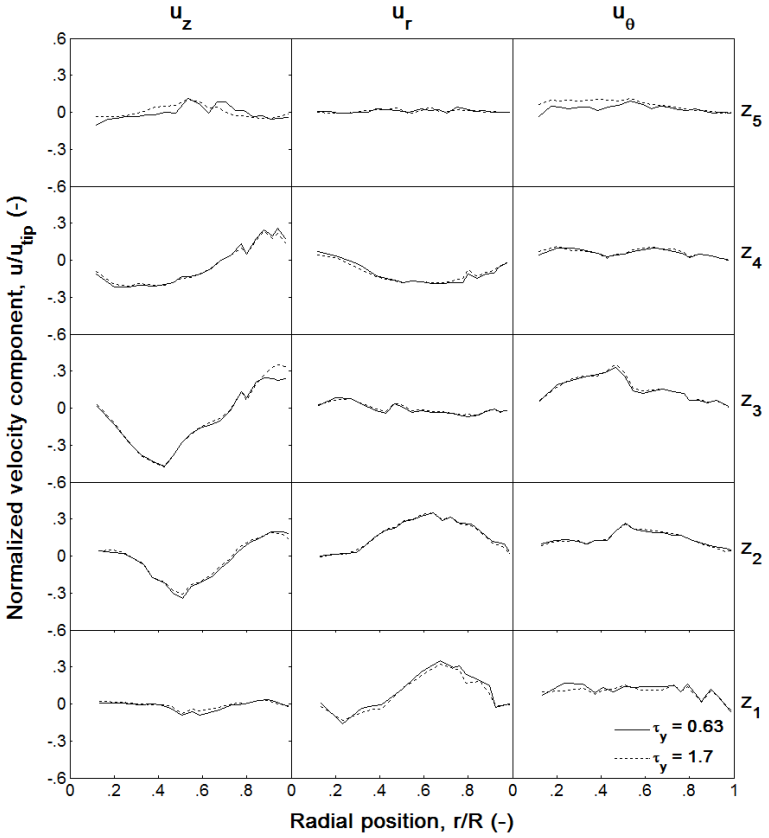

Figure 7.17. Azimuthally-averaged radial distributions of the velocity components of the liquid and solid components at N_{js}: X = 11.5 wt%; N_{js} = 600 rpm.

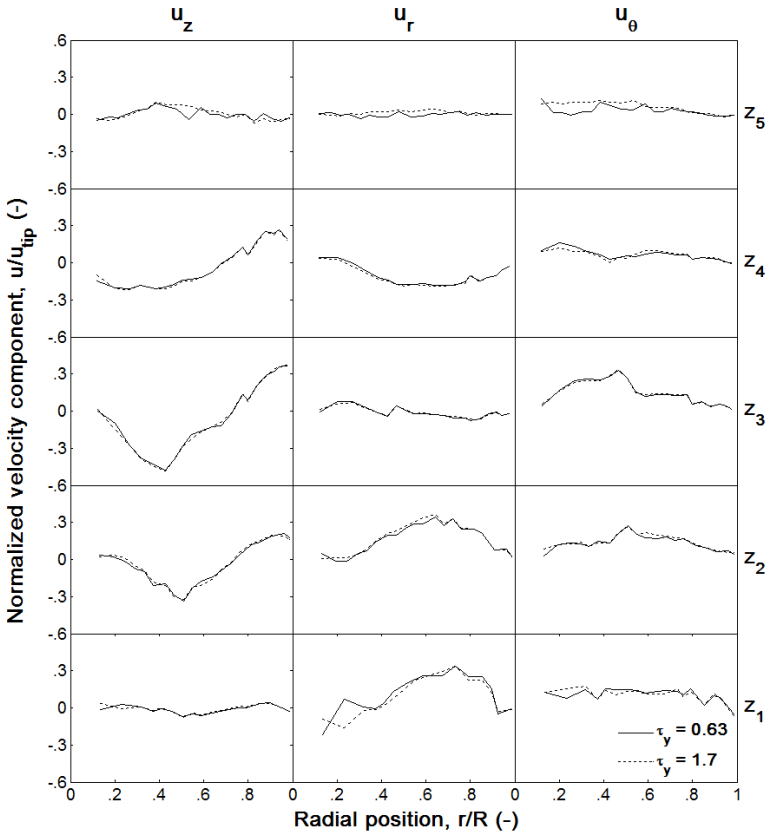

Figure 7.18. Azimuthally-averaged radial distributions of the velocity components of the liquid and solid components at N_{js}: X = 21.6 wt%; N_{js} = 750 rpm.

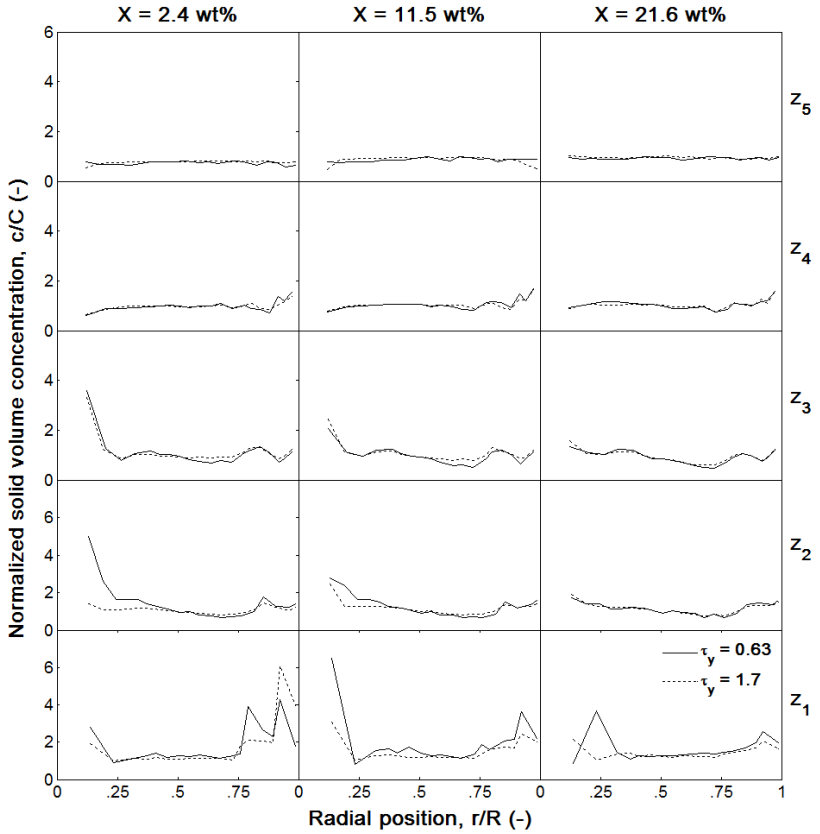

Figure 7.19. Comparison of azimuthally-averaged radial distributions of solid volume concentration in different viscopalstic fluids.

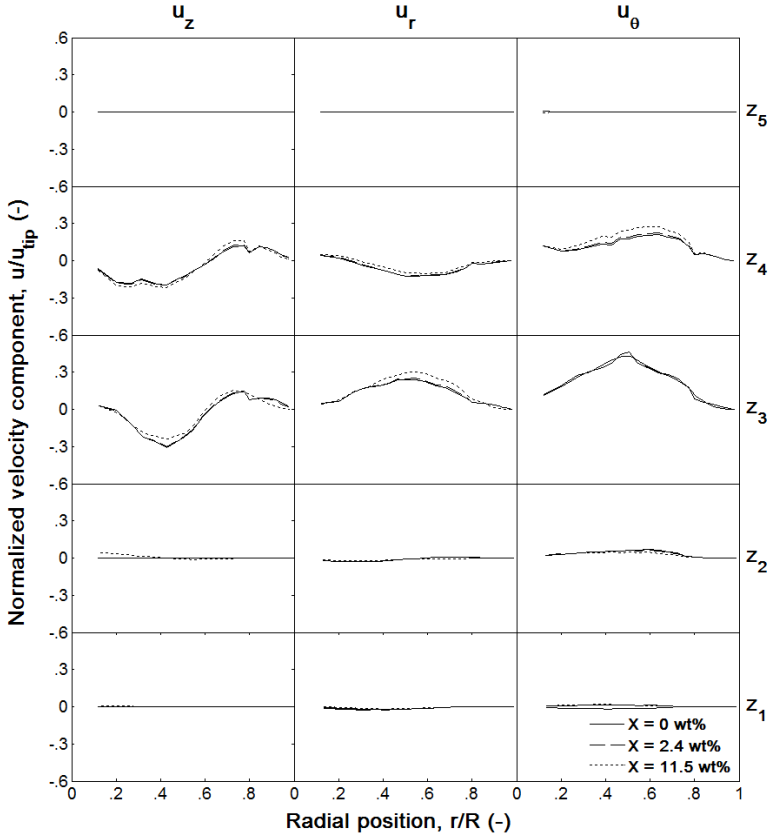

Figure 7.20. Comparison of azimuthally-averaged radial distributions of liquid velocity with and without presence of solids at N = 200 rpm.

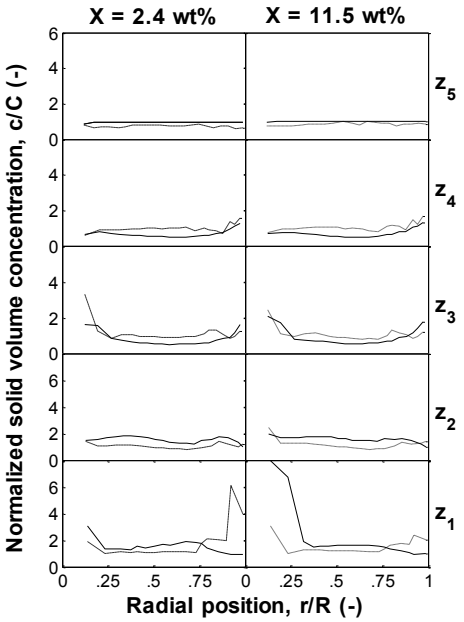

Figure 7.21. Comparison of azimuthally-averaged radial distributions of solid concentration with and without presence of solids: – N = 200 rpm; --- $N = N_{js}$ = 495 rpm; ⋯ $N = N_{js}$ = 600 rpm.

7.5. Conclusions

Solid suspensions in viscoplastic fluids in a mechanically agitated vessel have been investigated experimentally by PEPT and numerically by the CFD modeling, at the 'just-suspended' state corresponding to N_{js}.

The flow field of viscoplastic fluid is significantly enhanced by the presence of solids near the impeller and along the wall of the vessel, especially for the axial component u_z. In the upper part of the vessel, however, the liquid velocities are slightly affected by the solid particles. The tangential component, u_θ, is slightly affected by solid particles throughout the stirred vessel. Near the tank base, the radial component u_r, is increased in the presence of solid particles.

The impeller flow number for single phase mixing of viscoplastic fluids is ~ 0.65, which is smaller than that for water, is ~ 0.87. The flow number, *Fl*, increases significantly with the presence of solids at X = 2.4 wt% which could be due to the significant increase in the liquid velocities. However, *Fl* reduces significantly with further increasing the solid concentration.

At low to moderate X values, there are wide variations in the spatial distribution of the inter-phase slip velocity at N_{js}, with the largest total slip velocities being mainly restricted to the circulation loop. By increasing the mean solid concentration up to X = 21.6 wt%, however, the normalised slip velocities are reduced significantly.

The mass continuity calculated using the velocity data obtained from PEPT measurements on two closed surfaces for both phases has successfully verified the accuracy of the PEPT measurements for the solid suspensions in viscoplastic fluids.

The agreement between the predicted velocity fields of both the liquid and solid phases and the measurements obtained by PEPT is generally good in the bulk regions of stirred vessel including near the base where there is a considerable accumulation of solids. However, some localized errors occur in the regions with high flow intensity such as the impeller tip and near the wall where the axial component, u_z, exhibits a local maximum. Such discrepancies could be attributed to the inadequacy of using the laminar model for modelling regions with high flow velocity in stirred vessels.

The spatial distributions of the solid phase are well predicted by CFD modeling, except close to the base of the vessel where solid concentration is overestimated due to the complex mechanics of particle settling and particle lift-off in this region. Because the apparent yield stress of viscoplastic fluids could hinder the settling of solid particles, solid particles are more uniformly distributed in viscoplastic fluids in the bulk region of the stirred tank than solid

distributions in water. Under the same hydrodynamic mixing regime, e.g. at N_{js} in this study, the degree of homogeneity increases significantly with increasing solids concentration.

Notation

c	local volume concentration of solids	-
C	mean volume concentration of solids	-
d_p	particle diameter	m
D	impeller diameter	m
Fl	two-phase flow number (Q/ND^3)	-
$Fl^{(L)}$	liquid flow number ($Q^{(L)}/ND^3$)	-
$Fl^{(S)}$	solid flow number ($Q^{(S)}/ND^3$)	-
H	height of suspension	m
N	impeller rotational speed	s^{-1}
N_{js}	minimum speed for particle suspension	s^{-1}
r	radial distance	m
R	vessel radius	m
Re_{imp}	impeller Reynolds number (ND^2/v)	-
s	slip velocity	m s^{-1}
T	vessel diameter	m
u_{tip}	impeller tip speed	m s^{-1}
$u_r\ u_z\ u_\theta$	cylindrical velocity components	m s^{-1}
X	mean mass concentration of solids	-
z	vertical distance	m

Greek letters

ξ	uniformity index	-
σ	standard deviation of normalised c	-
θ	azimuthal coordinate	rad

Chapter VIII

CONCLUSIONS AND FUTURE WORK

8.1. Conclusions

Complex characteristics of mixing of various fluids under different regimes (laminar, transitional, and turbulent regimes) in stirred vessels agitated by various impellers were investigated by CFD modelling. As a cost-effective and powerful tool for investigating fluid flow, CFD modelling has been used in more and more areas. However, due to the simple assumptions of CFD models, it is always necessary to carry out detailed validation in order to use the CFD predictions confidently.

CFD modelling is capable of investigating complicated fluid mixing in stirred vessels, like dense solid-liquid suspensions and opaque non-Newtonian fluid mixing. However, due to the lack of experimental data, the CFD approach and models have not been well assessed on simulating such complex mixing systems. In this thesis, CFD predictions of mixing various fluids in stirred vessels were well validated by comparing with different experimental techniques. The conclusions of both numerical and experimental studies are summarised here.

8.1.1. CFD modelling of mixing of Newtonian and shear-thinning fluids

Both the highly turbulent and transitional flow fields of Newtonian and non-Newtonian fluids have been well predicted by CFD modeling. For highly turbulent water flow, both azimuthally-averaged velocities and velocities at various angular positions have been validated by comparing with PIV and PEPT measurements.

For mixing of shear-thinning fluid flow under transitional regime, the mixing efficiency has been found to be affected by both the fluid rheology and the configuration of stirred tank. The mixing performance of impeller has also been found to be affected by the fluid rheology. Therefore, the effect of fluid rheology needs to be taken into account for proper design of stirred vessel configuration.

8.1.2. CFD modelling of solid-liquid suspensions

The ability of CFD modeling of hydrodynamics and phase distributions in dense solid-liquid suspensions in a mechanically agitated vessel at both the 'just-suspended' state ($N = N_{js}$) and at speeds above it ($N > N_{js}$) have been assessed. The two-phase velocity field has been successfully predicted by CFD. Though the spatial distributions of the solid phase underneath the agitator and close to the base of the vessel at low solid concentration at N_{js} are overestimated, CFD predictions improve significantly with the increase in solid mean concentration and impeller rotational speed. This may be attributed to the insufficiency of the drag model which has a significant impact on the distributions of solid velocity and concentration. In order to accurately predict distributions of relatively larger particles at high solid concentrations, more impact factors needs to be taken into account in the drag model. The method dealing with the impeller rotation, i.e. SG and MFR, and non-drag forces have little effect on the solid-liquid suspensions in stirred vessels.

8.1.3. CFD modelling of mixing of viscoplastic fluids

CFD predicted cavern size and shape at different Reynolds numbers are in good agreement with the PLIF and PEPT measurements. CFD predicted hydrodynamics within the cavern are in good agreement with the PIV and PEPT measurements. The process of tracer distribution within the cavern has been well captured by comparing with the PLIF measurements.

The location of the interfaces between the rotating domain and the stationary domain has significant influence in the CFD prediction of cavern size and shape, therefore, great care must be taken for the arrangement of the rotating domain.

Replacing the impeller from $C = T/3$ to $C = T/2$ could significantly enhance the cavern size in the PBTD mode, which, however, has opposite effect for the PBTU mode where the cavern could not reach the tank base at $C = T/2$.

The yield stress τ_y and the flow behaviour n have significant but reverse effects on the cavern size, while the fluid consistency coefficient, k has little effect.

8.1.4. CFD modelling of mixing of solid suspension in viscoplastic fluids

The velocity distributions of both the liquid and solid phases have been generally well predicted by CFD modeling by comparing with PEPT measurements, except those in the regions with high flow intensity such as the impeller tip and near the wall. Such discrepancies could be attributed to the inadequacy of using the laminar model for modelling the fluid flow in relatively high transitional regime. The spatial distributions of the solid phase is well predicted by CFD modeling, except close to the base of the vessel where solid concentration is overestimated due to the complex mechanics of particle settling and particle lift-off in this region and the inadequacy of drag models.

Because of the apparent yield stress, solid particles in viscoplastic fluids are more uniformly distributed in the bulk region of the stirred tank than in water.

The flow field of viscoplastic fluids is significantly enhanced by the presence of solids near the impeller and along the wall of the vessel, especially for the axial component. In the upper part of the vessel, however, the liquid velocities are slight affected by the solid particles.

8.2. Suggestions for future work

In this work, the capability of CFD modelling of fluid mixing in stirred vessels has been discussed in detail. Simulation results have been well validated in comparison with different experimental measurements. Both the advantage and inadequacy of CFD modelling of fluid flow in stirred vessels have been presented.

For solid-liquid suspensions, the complexity of solid suspensions at N_{js} has been discussed and different CFD approaches and CFD models have been compared for modelling solid-liquid suspensions in stirred vessels. The drag model has been found to play an important role in predicting solid concentration distribution, and the inadequacy of the current drag model has been discussed. Effects of impact factors on the momentum transfer between liquid and solid particles are suggested to be further investigated and included in the drag model. Apart from the inadequacy of drag model for predicting solid distribution accurately, different treatments of raw data might also contribute to the discrepancy between CFD modelling and PEPT measurement. In the PEPT measurement, the stirred tank is divided into cells with the same volume which causes the cells in the tank center to have much larger radius than those close to the tank wall. Therefore, the gradient of solid concentration in the radial direction below the impeller could not be measured accurately by PEPT. In order to improve the measurement of solid concentration distributions in this region, treatment of PEPT raw data by dividing the stirred tank into cells with the same radius is worth being assessed and compared with the current treatment of PEPT raw data.

In this work, the particle size in concentrated solid-liquid suspensions is within the range of 1 – 3 mm. Due to the wide use of particles of microns in industries, suspensions of particle of microns at high solid concentrations are worth being investigated using PEPT measurement,

meanwhile, the capability of CFD modelling of suspensions of particles of microns in liquid can be assessed in comparison with the PEPT measurement.

In this work, lifting up of solid particles from tank bottome has been investigated using particle of density of 2485 kg m^{-3}. Drawdown of floating particles such as polypropylene in stirred vessels has drawn much less attention though they are widely used in industries. The critical just drawdown impeller speed, N_{jd}, has been investigated by researchers, however, the flow field and solid concentration distributions of floating particles in liquid have not been well studied. PEPT meausurements on flow fields and solid concentration distribution in solid-liquid systems with floating particles are suggested to be carried out, and the ability of CFD modelling of draw-down and distribution of floating particles in liquid can then be assessed by comparing with PEPT measurements.

Flow fields and solid distributions of solid suspensions in high viscosity non-Newtonian fluids have been investigated in this work. More conditions for these kinds of systems such as particles of different size and density, non-Newtonian fluids of different rheology are worth being investigated both experimentally and numerically.

REFERENCES

Adams, L.W. and Barigou, M. (2007), CFD analysis of caverns and pseudo-caverns developed during mixing of non-Newtonian fluids, Chemical Engineering Research and Design, **85** (A5), 598-604.

Adams, L., Chiti, F., Guida, A., Jaffer, S., Nienow, A.W. and Barigou, M. (2008), Positron emission particle tracking caverns formed during mixing of an industrial slurry, Proceedings of International Symposium on Mixing in Industrial Processes VI, Niagara on the Lake, Niagara Falls, Ontario, Canada, Aug, 17-21.

Adams, L.W. (2009), Experimental and computational study of non-turbulent flow regimes and cavern formation of non-Newtonian fluids in a stirred tank, Ph.D. Thesis, University of Birmingham.

Abujelala, M. T. and Lilley, D. G. (1984), Limitations and empirical extensions of the k-ε model as applied to turbulent confined swirling flow, Chemical Engineering Communication, **31**, 223-236.

Altway, A., Setyawan, H., Margono and Winardi, S. (2001), Effect of particle size on simulation of three-dimensional solid dispersion in stirred tank. Chemical Engineering Research Design, **79** (8), 1011-1016.

Amanullah, A., Hjorth, S.A. and Nienow, A.W. (1997), Cavern sizes generated in highly shear thinning viscous fluids by SCABA 3 SHP1 impeller, Transactions IChemE, **75** (C), 232-238.

Amanullah, A., Hjorth, S.A. and Nienow, A.W. (1998), A new mathematical model to predict cavern diameters in highly shear thinning, power law liquids using axial flow impellers, Chemical Engineering Science, **53** (3), 455-469.

Ameur, H., Bouzit, M. and Helmaoui, M. (2011), Numerical study of fluid flow and power consumption in a stirred vessel with a SCABA 6SRGT impeller, Chemical Process Engineering, **32** (4), 351-366.

Ameur, H. and Bouzit, M. (2012), Mixing in shear thinning fluids, Brazilian Journal Chemical Engineering, **29** (2), 349-358.

Armenate, P.M. and Chou, C-C (1996), Velocity profiles in a baffled vessel with single or double pitched blade turbine, AIChE Journal, **42** (1), 42-54.

Armenante, P. M. and Nagamine, E. U. (1998), Effect of low off-bottom impeller clearance on the minimum agitation speed for complete suspension of solid in stirred tanks. Chemical Engineering Science, **53**, 1757-1775.

Arratia, P. E., Kukura, J., Lacombe, J. and Muzzio, F. J. (2006), Mixing of shear-thinning fluids with yield stress in stirred tanks, AIChE Journal, **52** (7), 2310-2322.

Atiemo-Obeng, V. A., Penney, R. W. and Aremenante, P. (2004), Solid-liquid mixing, in: Paul, E. L., Atiemo-Obeng, V. A., and Kresta, S. M. (Eds), Handbook of industrial mixing: Science and practice, Wiley-Interscience: Hoboken, NJ. Chapter 10, 543-584.

Aubin, J., Naude, I., Bertrand, J. and Xuereb, C. (2000), Blending of Newtonian and shear-thinning fluids in a tank stirred with a helical screw agitator, Chemical Engineering Research and Design, Trans IChenE, **78** (A8), 1105-1114.

Aubin, J., Fletcher, D. F. and Xuereb, C. (2004), Modeling turbulent flow in stirred tank with CFD: the influence of the modelin approach, turbulence model and numerical scheme, Experimental Thermal and Fluid Science, **28**, 431-445.

Alvarez-Hernández, M.M., Shinbrot, T., Zalc, J. and Muzzio, F.J. (2002), Practical chaotic mixing, Chemical Engineering Science, **57** (17), 3794-3753.

Barigou, M., Chiti, F., Pianko-Oprych, P., Guida, A., Adams, L.; Fan, X., Parker, D. J. and Nienow, A. W. (2009), Using Positron Emission Particle Tracking (PEPT) to study mixing in stirred vessels: validation and tackling unsolved problems in opaque systems. Journal of Chemical Engineering of Japan, **42**, 829-846.

Bakker, A. (1992), Hydrodynamics of stirred gas-liquid dispersions, Ph.D. Thesis, Delft University of Technology, the Netherlands.

Bakker, A., Myers, K.J., Ward, R.W. and Lee, C.K. (1996), The laminar and turbulent flow pattern of a pitch blade turbine, Chemical Engineering Research and Design, *74* (A), 485-491.

Bakker, A., Haidari, A.H. and Oshinowo, L.M. (2001), Realize greater benefits from CFD, Fluid/Solid Handling, AIChE's CEP magazine, March 2001, 45-53.

Bakker, A. and Van den Akker, H.E.A. (1994), A computational model for the gas-liquid flow in stirred reactors, Chemical Engineering Research and Design, Trans IChemE, **72** (A4), 573-582.

Baldi, S. and Yianneskis, M. (2003), On the direct measurement of turbulence energy dissipation in stirred vessels with PIV, Industrial & Engineering Chemistry Research, **42**, 7006-7016.

Barresi, A.A. and Baldi, G. (1987), Solid dispersion in an agitated vessel, Chemical Engineering Science, **42** (12), 2949-2956.

Barrue, H., Bertrand, J., Cristol, B. and Xuereb, C. (2001), Eulerian simulation of dense solid-liquid suspension in multi-stage stirred vessel, Journal of Chemical Engineering of Japan, **34** (5), 585-594.

Bohnet, M. and Niesmak, G. (1980), Distribution of solids in stirred suspensions, German Chemical Engineering, **3**, 57-65.

Bouillard, J.X., Lyczkowski, R.W. and Gidaspow, D. (1989), Porosity distribution in a fluidized bed with an immersed obstacle, AIChE Journal, **35** (6), 908-923.

Brito-de la Fuente E., Choplin, L. and Tanguy, P. A. (1997), Mixing with helical ribbon impellers: effect of highly shear thinning behaviour and impeller geometry, Transaction IChemE, **75** (A), 45-52.

Brucato, A., Ciofalo, M., Grisafi, F. and Micale, G. (1994), Complete numerical simulation of flow fields in baffled stirred vessels: The inner-outer approach, IChemE Symposium Series, **136**, 155-162.

Brucato, A., Grisafi, F. and Montante, G. (1998), Particle drag coefficients in turbulent fluids, Chemical Engineering Science, **53** (18), 3295-3314.

Brucato, A., Ciofalo, M., Grisafi, F. and Micale, G. (1998), Numerical prediction of flow fields in baffled stirred vessels: a comparison of alternative modelling approaches, Chemical Engineering, Science, **53**, 3653-3684.

Brunazzi, E., Galletti, C., Paglianti, A. and Pintus, S. (2004), An impedance probe for the measurements of flow characteristics and mixing properties in stirred slurry reactors, Chemical Engineering Research and Design, **82** (A9), 1250-1257.

Bujalski, W., Jaworski, Z. and Nienow, A.W. (2002 (a)), CFD study of homogenization with dual Rushton turbines-comparison with experimental results, Part II: the multiple reference frame, Chemical Engineering Research and Design, **80** (A), 97-104.

Chiti, F. (2007), Lagrangian studies of turbulent mixing in a vessel agitated by a Rushton turbine: Positron Emission Particle Tracking (PEPT) and Computational Fluid Dynamics (CFD), Ph.D. Thesis, University of Birmingham.

Chtourou, W., Ammar, M., Driss, Z. and Abid, M.S. (2011), Effect of the turbulence models on Rushton turbine generated flow in a stirred vessel, Central European Journal of Engineering, **1** (4), 380-389.

Chung, K.H.K (2008), Mixing in high throughput experimentation reactors, Ph.D. Thesis, University of Birmingham.

Chung, K.H.K., Barigou, M. and Simmons, M.J.H. (2007), Reconstruction of 3-D flow field inside miniature stirred vessels using a 2-D PIV technique, Chemical Engineering Research and Design, **85** (A5), 560-567.

Coroneo, M., Montante, G., Paglianti, A. and Magelli, F. (2011), CFD prediction of fluid flow and mixing in stirred tanks: Numerical issues about the RANS simulations, Computers and Chemical Engineering, **35**, 1959-1968.

Costes, J. and Couderc, J.P. (1998), Study by laser Doppler anemometry of the turbulent flow induced by a Rushton turbine in a stirred tank: influence of the size of units-I. Mean flow and turbulence, Chemical Engineering Science, **43**, 2751-2764.

Couerbe, G., Fletcher, D., Xuereb, C. and Poux, M. (2008), Impact of thixotropy on flow patterns induced in a stirred tank: numerical and experimental studies, Chemical Engineering Research and Design, **86** (6), 545-553.

Curran, S.J., Hayes, R.E., Afacan, A., Williams, M.C. and Tanguy, P.A. (2002), Properties of carbopol solutions as models for yield-stress fluids, Journal of Food Science, **67** (1), 176-180.

Cutter, L.A. (1966), Turbulence: The filtering approach, Journal of Fluid Mechanics, **238**, 325-336.

Decker, S. and Sommerfeld, M. (1996), Calculations of two-phase flows in agitated vessels using the Euler/Lagrange approach, Institution of Chemical Engineers, Symposium, **140**, 71-82.

Deglon, D. A. and Meyer, C. J. (2006), CFD modeling of stirred tanks: numerical considerations, Minerals Engineering, **19** (10), 1056-1068.

Derksen, J. J. (2003), Numerical simulation of solids suspension in a stirred tank, AIChE Journal, **49** (11), 2700-2714.

Derksen, J.J. (2009), Solid particle mobility in agitated bingham liquids, Industrial & Engineering Chemistry Research, **48** (4), 2266-2274.

Doucet, J., Bertrand, F. and Chaouki, J. (2008), A measure of mixing from Lagrangian tracking and its application to granular and fluid flow systems. Chemical Engineering Research and Design, **86**, 1313-1321.

Dyster, K.N., Koutsakos, E., Jaworski, Z. and Nienow, A.W. (1993), A LDA study of the radial discharge velocities generated by a Rushton turbine: Newtonian fluids, Chemical Engineering Research and Design, **71**, 11-23.

Edwards, M.F. (1997), Laminar flow and distributive mixing, in: Harnby, N., Edwards, M.F., Nienow, A.W. (Eds), Mixing in the process industries, Butterworth-Heinemann: Oxford. Chapter 11, 200-224.

Eesa, M. and Barigou, M. (2008), Horizontal laminar flow of coarse nearly-neutrally buoyant particles in non-Newtonian conveying fluids: CFD and PEPT experiments compared; International Journal of Multiphase Flow, **34** (11), 997–1007.

Eesa, M. and Barigou, M. (2009), CFD investigation of the pipe transport of coarse solids in laminar power law fluids, Chemical Engineering Science, **64** (2), 322-333.

Eggels, J.G. (1996), Direct and large-eddy simulations of turbulent flow using the lattice – Boltzmann scheme, International Journal of Heat and Fluid Flow, **17**, 307-323.

Ein-Mozaffari, F., Upreti, S.R. (2009), Using ultrasonic Doppler velocimetry and CFD modelling to investigate the mixing of non-Newtonian fluid possessing yield stress, Chemical Engineering Research and Design, **87**, 515-523.

Elson, T. P. and Cheesman, D. J. (1986), X-Ray studies of cavern sizes and mixing performance with fluids possessing a yield stress, Chemical Engineering Science, **41** (10), 2555-2562.

Elson, T.P. (1990), The growth of cavern formed around rotating impellers during the mixing of a yield stress fluid, Chemical Engineering Communication, **96**, 303-319.

Escudié, R., Bouyer, D. and Liné, A. (2004), Characterization of trailing vortices generated by a Rushton turbine, AIChE Journal, **50** (1), 75-86.

Escudié, R. and Liné, A. (2006), Analysis of turbulence anisotropy in a mixing tank, Chemical Engineering Science, **61** (9), 2771-2779.

Fan, L., Mao, Z.Sh. and Wang, Y.D. (2005), Numerical simulation of turbulent solid-liquid two-phase flow and orientation of slender particles in a stirred tank, Chemical Engineering Science, **60** (24), 7045-7056.

Fangary, Y.S., Seville, J.P.K. and Barigou, M. (1999), Flow studies in stirred tanks by positron emission particle tracking (PEPT), Institution of Chemical Engineers Symposium Series, **146**, 23-24.

Fangary, Y.S., Barigou, M., Seville, J.P.K. and Parker, D.J. (2000), Fluid trajectories in a stirred vessel of non-Newtonian liquid using Positron Emission Particle Tracking, Chemical Engineering Science, **55** (24), 5969-5979.

Fangary, Y.S., Barigou, M., Seville, J.P.K. and Parker, D.J. (2002), A Lagrangian study of solids suspension in a stirred vessel by Positron Emission Particle Tracking (PEPT), Chemical Engineering Technology, **25** (5), 521-528.

Fishwick, R.P., Winterbottom, J.M. and Stitt, E.H. (2003), Explaining mass transfer observations in multiphase stiffed reactors: particle-liquid slip velocity measurements using PEPT, Catalysis Today, **79** (1-4), 195-202.

Fishwick, R., Winterottom, M., Parker, D., Fan, X. and Stitt, E.H. (2005), The use of positron emission particle tracking in the study of multiphase stirred tank reactor hydrodynamics, The Canadian Journal of Chemical Engineering, **83** (1), 97-103.

Fletcher, D. F. and Brown, G. J. (2009), Numercal simulation of solid suspension via mechanical agitation: effect of the modelling approach, turbulence model and hindered settling drag law, International Journal of Computational Fluid Dynamics, **23** (2), 173-187.

Gabriele, A., Nienow, A.W. and Simmons, M.J.H. (2009), Use of angle resolved PIV to estimate local specific energy dissipation rates for up- and down-pumping pitched blade agitators in a stirred tank, Chemical Engineering Science, **64**, 126-143.

Gabriele, A., Tsoligkas, A.N., Kings, I.N., Simmons, M.J.H. (2011), Use of PIV to measure turbulence modeluation in a high throughput stirred vessel with the addition of high stokes

number particles for both up- and down-pumping configurations, Chemical Engineering Science, 66, 5862-5874.

Galindo, E. and Nienow, A. W. (1992), Mixing of highly viscous simulated Xanthan fermentation broths with the Lightinin A-315 impeller, Biotechnology Progress, **8**, 233-239.

Galindo, E. and Nienow, A. W. (1993), Performance of the SCABA 6 SRGT agitator in mixing of simulated xanthan gum broths, Chemical Engineering and Technology, **16**, 102-108.

Galindo, E., Argüiello, M.A., Velasco, D., Albiter, V. and Martínez, A. (1996), A comparison of cavern development in mixing of yield stress fluid by Rushton and Intermig impellers, Chemical Engineering Technology, **19**, 315-323.

Gidaspow, D. (1994), Multiphase flow and fluidization: Continuum and kinetic theory description, Academic Press, New York.

Godfrey, J.C. and Zhu, Z.M. (1994), Measurement of particle-liquid profiles in agitated tank, AIChE Symposium Series, **90**, 181-185.

Gore, R.A. and Crowe, C.T. (1991), Modulation of turbulence by a dispersed phase, Journal of Fluids Engineering - ASME, **113** (2), 304–307.

Gosman, A.D., Lekakou, C., Politis, S., Issa, R.I. and Looney, M.K. (1992), Multidimensional modeling of turbulent two-phase flows in stirred vessels, AIChE Journal, **38** (12), 1946-1956.

Guha, D., Ramachandran, P.A. and Dudukovic, M.P. (2007), Flow field of suspended solids in a stirred tank reactor by Lagrangian tracking, Chemical Engineering Science, **62** (22), 6143-6154.

Guha, D., Ramachandran, P.A., Dudukovic, M.P. and Derksen, J.J. (2008), Evaluation of large eddy simulation and Euler-Euler CFD models for solids flow dynamics in a stirred tank reactor, AIChE Journal, **54** (3), 766-778.

Guida, A. (2010), Positron emission particle tracking applied to solid-liquid mixing in mechanically agitated vessels, Ph.D. Thesis, University of Birmingham.

Guida, A., X. Fan, D.J. Parker, A., Nienow, A.W. and Barigou, M. (2009), Positron emission particle tracking in a mechanically agitated solid-liquid suspension of coarse particles, Transaction IChemE, Part A, Chemical Engineering Research Design, **87** (4), 421-429.

Guida, A., Nienow, A.W. and Barigou, M. (2010), PEPT measurements of solid-liquid flow field and spatial phase distribution in concentrated monodisperse stirred suspensions, Chemical Engineering Science, **65** (6), 1905-1914.

Guida, A., Nienow, A. W. and Barigou, M. (2011), Mixing of dense binary suspensions: multi-component hydrodynamics and spatial phase distribution by PEPT, AIChE Journal, **57** (9), 2302-2315.

Guida, A. and Barigou, M. (2012), Lagrangian tools for the analysis of mixing in single- and multi-phase flow systems, AIChE Journal, **58** (1), 31-45.

Guillard, F., Trägärdh, C. and Fuchs, L. (2000), A study of turbulent mixing in a turbine-agitated tank using a fluorescence technique, Experiments in Fluids, **28**, 225-235.

Gunyol, O. and Mudde, R. F. (2009), Computational study of hydrohynamics of a standard stirred tank reactor and a large-scale multi-impeller fermenter, International Journal for Multiscale Computational Engineering, **7** (6), 559-576.

Günkel, A.A., Patel, R.P. and Weber, M.E. (1971), An experimental study of the steady and unsteady flow characteristics of stirred reactors, Industrial & Engineering Chemistry Fundamentals, **10** (4), 627-631.

Guiraud, P., Costes, J. and Bertrand, J. (1997), Local measurements of fluid and particle velocities in a stirred suspension, Chemical Engineerig Journal, **68** (2-3), 75-86.

Hartmann, H., Derksen, J.J., Montavon, C., Pearson, J., Hamill, I.S. and Van den Akker, H.E.A. (2004 (b)), Assessment of large eddy and RANS stirred simulations by means of LDA, Chemical Engineering Science, **59**, 2419-2432.

Hemrajani, R.R. and Tatterson, G.B. (2004), Mechanically stirred vessels, in: Paul, E.L., Atiemo-Obeng, V.A., Kresta, S.M. (Eds), Handbook of industrial mixing: Science and practice, Wiley, New York. Chapter 6, 345-390.

Hinsch, K.D. (2002), Holographic particle image velocimetry, Measurements Science and Technology, **13**, 61-72.

Hockey, R.M. and Nouri, J.M. (1996), Turbulent flow in a baffled vessels stirred by a 60° pitched blade impeller, Chemical Engineering Science, **51**, 4405-4421.

Holmes, D. B., Voncken, R. M. and Dekker, J. A. (1964), Fluid flow in turbine-stirred, baffled tanks-I: Circulation time, Chemical Engineering Science, **19** (3), 201-208.

Hosseini, S., Patel, D., Ein-Mozaffari, F. and Mehrvar, M. (2010), Study of solid-liquid mixing in agitated tanks through computational fluid dynamics modeling, Industrial & Engineering Chemistry Research, **49** (9), 4426-4435.

Ibrahim, S. and Nienow, A.W. (2010), The effect of viscosity on particle suspension in an aerated stirred vessel with different impellers and bases, Chemical Engineering Communications, **197**, 434-454.

Ihejirika, I. and Ein-Mozaffari, F. (2007), Using CFD and ultrasonic velocimetry to study the mixing of pseudoplastic fluids with a helical ribbon impeller, Chemical Engineering Technology, **30** (5), 606-614.

Jafari, R., Chaouki, J. and Tanguy, P.A. (2012), A comprehensive review of just suspended speed in liquid-solid and gas-liquid-solid stirred tank reactors, International Journal of Chemical Reactor Engineering, **10**, Review R1, 1-32.

Jahangiri, M. (2005), A laser Doppler anemometry study of the Rushton turbine velocity profile for mixing of polymeric liquids, Iranian Polymer Journal, **14** (6), 521-530.

Javed, K.H., Mahmud, T. and Zhu, J.M. (2006), Numerical simulation of turbulent batch mixing in a vessel agitated by a Rushton turbine, Chemical Engineering and Processing, **45**, 99-112.

Jaworski, Z., Wyszynski, M.L., Moore, I.P.T. and Nienow, A.W. (1997), Sliding mesh computational fluid dynamics-a predictive tool in stirred tank design, Proceedings Institution of Mechanical Engineers, Part E, Journal of Process Mechanical Engineering, **211** (3), 149-156.

Jaworski, Z., Bujalski, W., Otomo, N. and Nienow, A.W. (2000), CFD study of homogenization with dual Rushton turbines-Comparison with experimental results, Part I: Initial studies, Chemical Engineering Research and Design, **78** (A), 327-333.

Jaworski, Z., Nienow, A.W., Koutsakos, E., Dyster, K. and Bujalski, W. (1991), An LDA study of turbulent flow in a baffled vessel agitated by a pitched blade turbine, Chemical Engineering Research and Design, **64** (A4), 313-320.

Jaworski, Z. and Nienow, A.W. (1994), LDA measurements of flow fields with hydrofoil impellers in fluids with different rheological properties, Proceedings of the 8th European Conference on Mixing, Cambridge, IChemE Symposium, **136**, 105-112.

Jaworski, Z., Wyszynski, M.L., Dyster, K.N., Mishra, V.P. and Nienow, A.W. (1998), A study of an up and a down pumping wide blade hydrofoil impeller: II. CFD analysis, Canadian Journal of Chemical Engineering, **76**, 866-876.

Jaworski, Z. and Zakrzewska, B. (2002), Modelling of the turbulent wall jet generated by a pitched blade turbine impeller: the effect of turbulence model, Transaction IChemE, **80** (A), 846-854.

Jenne, M. and Reuss, M. (1999), A critical assessment on the use of k-ε turbulence models for simulation of the turbulent liquid flow induced by a Rushton-turbine in baffled stirred-tank reactor, Chemical Engineering Science, **54** (17), 3921-3941.

Kushalkar, K.B. and Pangarkar, V.G. (1995), Particle-liquid mass transfer in three-phase mechanically agitated contactors: power law fluids, Industrial & Engineering Chemistry Research, **34** (7), 2485-2492.

Kasat, G. R. and Pandit, A. B. (2005), Review on mixing characteristics in solid-liquid and solid-liquid-gas reactor vessels. The Canadian Journal of Chemical Engineering, **83**, 618-643.

Kasat, G.R., Khopkar, A.R., Ranade, V.V. and Pandit, A.B. (2008), CFD simulation of liquid-phase mixing in solid-liquid stirred reactor. Chemical Engineering Science, **63** (15), 3877-3885.

Kelly, W. and Gigas, B. (2003), Using CFD to predict the behaviour of power law fluids near axial-flow impellers operating in the transitional flow regime, Chemical Engineering Science, **58**, 2124-2152.

Kemoun, A., Lusseyran, F., Mahouast, M. and Mallet, J. (1994), Experimental determination of the complete Reynolds stress tensor in fluid agitated by a Rushton turbine, IChemE Symposium, **136**, 399-406.

Khan, F. R., Rielly, C. D. and Hargrave, G. D. (2004), A multi-block approach to obtain angle-resolved PIV measurements of the mean flow and turbulence fields in a stirred vessel, Chemical Engineering Technology, **27** (3), 264-269.

Khan, F.R., Rielly, C.D. and Brown, D.A.R. (2006), Angle-resolved stereo-PIV measurements close to a down-pumping pitched-blade turbine, Chemical Engineering Science, **61** (9), 2799-2806.

Khazam, O. and Kresta, S.M. (2008), Mechanisms of solids drawdown in stirred tanks, The Canadian Journal of Chemical Engineering, **86** (4), 622-634.

Khopkar, A. R., Rammohan, A. R., Ranade, V. V. and Dudukovic, M. P. (2005), Gas-liquid flow generated by a Rushton turbine in stirred vessel: CARPT/CT measurements and CFD simulations, Chemical Engineering Science, **60**, 2215-2229.

Khopkar, A.R., Kasat, G.R., Pandit, A.B. and Ranade, V.V. (2006), Computational fluid dynamics simulation of the solid suspension in a stirred slurry reactor, Industrial & Engineering Chemistry Research, **45**, 4416,4428.

Koutsakos, E., Nienow, A.W. and Dyster, K.N. (1990), Laser anemometry study of shear thinning fluids agitated by a Rushton turbine, IChemE Symposium Series, **121**, 51-73.

Kresta, S.M. and Wood, P.E. (1993), The flow field produced by a pitched blade turbine: characterization of the turbulence and estimation of the dissipation rate, Chemical Engineering Science, **48** (10), 1761–1774.

Kukura, J., Arratia, P.C., Szalai, E.S., Bittorf, K.J. and Muzzio, F.J. (2002), Understanding pharmaceutical flows, Pharmaceutical Technology, 48-72.

Kumaresan, T. and Joshi, J. B. (2006), Effect of impeller design on the flow pattern and mixing in stirred tanks, Chemical Engineering Journal, **115**, 173-193.

Lamberto, D.J., Alvarez, M.M. and Muzzio, F.J. (1999), Experimental and computational investigation of the laminar flow structure in a stirred tank, Chemical Engineering Science, **54**, 919.

Lamarque, N., Zoppé, Lebaigue, O., Dolias, Y., Bertrand, M. and Ducros, F. (2010), Large-eddy simulation of the turbulent free-surface flow in an unbaffled stirred tank reactor, Chemical Engineering Science, **27** (11), 1969-1978.

Lamberto, D.J., Alvarez, M.M. and Muzzio, F.J. (2001), Computational analysis of regular and chaotic mixing in a stirred tank reactor, Chemical Engineering Science, **56**, 4887-4899.

Launder, B.E. and Spalding, D.B. (1974), The numerical computation of turbulent flows, Computer Methods for Applied Mechanics & Engineering, **3**, 269-289.

Lee, K.C. and Yianneskis, M. (1997), A liquid crystal thermographic technique for the measurement of mixing characteristics in stirred vessels, Chemical Engineering Research Design, **75** (A8), 746-754.

Lee, K. C. and Yianneskis, M. (1998), Turbulence properties of the impeller stream of a Rushton turbine, AIChE Journal, **44**, 13-24.

Letellier, B., Xuereb, C., Swaels, P., Hobbes, P. and Bertrand, J. (2002), Scale-up in laminar and transient regimes of a multi-stage stirrer, a CFD approach, Chemical Engineering Science, **57**, 4617-4632.

Li, M., White, G., Wilkinson, D. and Roberts, K.J. (2005), Scale up study of retreat curve impeller stirred tanks using LDA measurements and CFD simulation, Chemical Engineering Journal, **108**, 81-90.

Lightnin company (http://www.lightninmixers.com).

Ljungqvist, M. and Rasmuson, A. (2001), Numerical simulation of the two-phase flow in an axially stirred vessel, Transactions IChemE, **79** (A), 533-546.

Ljungqvist, M. and Rasmuson A. (2004), The two-phase flow in an axially stirred vessel investigated using Phase-Doppler Anemometry, The Canadian Journal of Chemical Engineering, **82** (2), 275-288.

Luo, J.Y., Gosman, A. D., Issa, R. I., Middleton, J. C. and Fitzgerald, M. K. (1993), Full flow field computation of mixing in baffled stirred vessels, Chemical Engineering Research and Design, **71**, 342-344.

Luo, J.Y., Issa, R. I. and Gosman, A. D. (1994), Prediction of impeller-induced flows in mixing vessels usin multiple frames of references, IChemE Symposium Series, **136**, 549-556.

Marshall, E. M. and Bakker, A. (2004), Computational fluid mixing, In E. L. Paul. V. A. Atiemo-Obeng, S, M. Kresta (Eds.). Handbook of industrial mixing, pp, 257-344. Hoboken, NJ: Wiley-Interscience.

Mavros, P. (2001), Flow visualization in stirred tanks, a review of experimental techniques, Transactions of the Institution of Chemical Engineer, **79** (A), 113-127.

Mersmann, A., Werner, F., Maurere, S. and Bartosch, K. (1998), Theoretical prediction of the minimum stirrer speed in mechanically agitated suspensions, Chemical Engineering Process, **37** (6), 503-510.

Metzner, A.B. and Otto, R.E. (1957), Agitation of non-Newtonian fluids, AIChE Journal, **3** (1), 3-10.

Metzner, A. B., Feehs, R. H., Ramos, H. L., Otto, R. E. and Tuthill, J. D. (1961), Agitation of viscous Newtonian and non-Newtonian fluids, AIChE Journal, **7** (1), 3-9.

Micale, G., Brucato, A., Grisafi, F. and Ciofalo, M. (1999), Prediction of flow fields in a dual-impeller stirred vessel, AIChE Journal, **45**, 445-464.

Micale, G., Montante, G., Grisafi, F., Brucato, A. and Godfrey, J. (2000), CFD simulation of particle distribution in stirred vessels, Transactions IChemE, **78** (A), 435-444.

Micale, G., Grisafi, F., Rizzuti, L. and Brucato, A. (2004), CFD simulation of particle suspension height in stirred vessels, Chemical Engineering Research Design, **82** (9), 1204-1213.

Micheletti, M. and Yianneskis, M. (2004), Study of fluid velocity characteristics in stirred solid-liquid suspensions with a refractive index matching technique, Proceedings of the Institution of Mechanical Engineers, **218**, 191-204.

Montante, G. and Lee K.C. (2000), Liquid and solid particle mean flow and turbulence levels in stirred vessel with low impeller clearance, IChemE Symposium Series, **146**, 305-316.

Montante, G., Lee, K. C., Brucato, A. and Yianneskis, M. (1999), Double to single loop flow pattern transition in stirred vessels, The Canadian Journal of Chemical Engineering, **77**, 649-659.

Montante, G., Micale, G., Brucato, A. and Magelli, F. (2000), CFD simulation of particle distribution in a multiple-impeller high-aspect-ratio stirred vessel, 10th European Conference on Mixing, Van den Akker, H.E.A., Derksen, J.J., Eds., Delf, July 2-5, Elsevier, Amsterdam, the Netherlands, 125-132.

Montante, G., Micale, G., Magelli, F. and Brucato, A. (2001), Experiments and CFD predictions of solid particle distribution in a vessel agitated with four pitched blade turbines, Chemical Engineering Research Design, **79** (8), 1005-1010.

Montante, G., Pinelli, D. and Magelli, F. (2002), Diagnosis of solid distribution in vessels stirred with multiple PBTs and comparison of two modeling approaches, The Canadian Journal of Chemical Engineering, **8**, 1-9.

Montante, G. and Magelli, F. (2005), Modelling of solids distribution in stirred tanks: analysis of simulation strategies and comparison with experimental data, International Journal of Computational Fluid Dynamics, **19** (3), 253-262.

Montante, G. and Magelli, F. (2007), Mixed solids distribution in stirred vessels: experiments and computational fluid dynamics simulations, Industrial & Engineering Chemistry Research, **46** (9), 2885-2891.

Montante G., Occulti, M.H., Magelli, F. and Paglianti, A. (2010), PIV measurements of mean flow and turbulence modulation in dilute solid-liquid stirred tanks, 15th International Symposium on Applications of Laser Techniques to Fluid Mechanics, Lisbon, Portugal, 1-8.

Montante, G., Paglianti, A. and Magelli, F. (2012), Analysis of dilute solid-liquid suspensions in turbulent stirred tanks, Chemical Engineering Research and Design, **90** (10), 1448-1456.

Montante, G., Micale, G., Magelli, F. and Brucato, A. (2000), CFD simulation of particle distribution in an unbaffled high-aspect-ratio stirred vessel, International Congress of Chemical and Process Engineering CHISA, Praha, 27-31.

Moore, I. P. T., Cossor, G. and Baker, M. R. (1995), Velocity distribution in a stirred tank containing a yield stress fluid, Chemical Engineering Science, **50** (15), 2467-2481.

Murthy, B. N. And Joshi, J. B. (2008), Assessment of standard k-ε, RMS and LES turbulence models in a baffled stirred vessel agitated by various impeller designs, Chemical Engineering Science, **63**, 5468-5495.

Ng, K., Fentiman, N.J., Lee, K.C. and Yianneskis, M. (1998), Assessment of sliding mesh CFD predictions and LDA measurements of the flow in a tank stirred by a Rushton impeller, Transactions of the Institute of Chemical Engineers, **76** (A), 737-747.

Nienow, A. W. (1968), Suspension of solid particles in turbine agitated baffled vessels, Chemical Engineering Science, **23**, 1453-1459.

Nienow, A.W. and Elson, T.P. (1988), Aspects of mixing in rheologically complex fluids, Chemical Engineering Research and Design, **66**, 5-51.

Nienow, A.W. (1997a), On impeller circulation and mixing effectiveness in the turbulent flow regime, Chemical Engineering Science, **52** (15), 2557-2565.

Nienow, A.W. (1997b), The suspension of solids particles, in: Harnby, N., Edwards, M.F., Nienow, A.W. (Eds), Mixing in the process industries, Butterworth-Heinemann: Oxford. Chapter 16, 364-394.

Nouri, J. M. and Whitelaw, J. H. (1992), Particle velocity characteristics of dilute to moderately dense suspension flows in stirred reactors, International Journal of Multiphase Flow, **18** (1), 21-33.

Ochieng, A. and Lewis, A.E. (2006), Nickel solids concentration distribution in a stirred tank, Minerals Engineering, **19** (2), 180-189.

Ochieng, A. and Onyango, M.S. (2008), Drag models, solids concentration and velocity distribution in a stirred tank, Powder Technology, **181** (1), 1-8.

Ochieng, A., Onyango, M.S., Kumar, A., Kiriamiti, K. and Musonged, P. (2008), Mixing in a tank stirred by a Rushton turbine at a low clearance, Chemical Engineering and Processing, **47**, 842-851.

Oshinowo, L.M. and Bakker, A. (2002), CFD modeling of solids suspensions in stirred tanks, Symposium on Computational Modeling of Metals, Minerals and Materials, TMS Annual Meeting, Seattle, WA, pp 17-21.

Oshinowo, L., Jaworski, Z., Dyster, K.N., Marshall, E. and Nienow, A.W (2000), Predicting the tangential velocity field in stirred tanks using the multiple reference frames (MRF) model with validation by LDA measurements, 10th European Conference on Mixing, Delft, 281-288.

Pakzad, L., Ein-Mozaffari, F. and Chan, P. (2007), Using computational fluid dynamics modelling to study the mixing of pseudoplastic fluids with a Scaba 6SRGT impeller, Chemical Engineering and Processing, **47**, 2218-2227.

Pakzad, L., Ein-Mozaffari, F. and Chan, P. (2008), Using electrical resistance tomography and computational fluid dynamics modelling to study the formation of cavern in the mixing of pseudoplastic fluids possessing yield stress, Chemical Engineering Science, **63**, 2508-2522.

Pakzad, L., Ein-Mozaffari, F., Upreti, S.R. and Lohi, A. (2013), Characterisation of the mixing of non-Newtonian fluids with a Scaba 6SRGT impeller throughout ERT and CFD, The Canadian Journal of Chemical Engineering, 90-100.

Parker, D.J., Broadbent, C.J., Fowles, P., Hawkesworth, M.R. and Mcneil, P. (1993), Positron Emission Particle Tracking-A technique for studying flow within engineering equipment, Nuclear Instruments and Methods in Physics Research Section A, **326** (3), 592-607.

Parker, D.J., Forster, R.N., Fowles, P. and Takhar, P.S. (2002), Positron Emission Particle Tracking using the new Birmingham positron camera, Nuclear Instruments and Methods in Physics Research Section A, **477** (1-3), 540-545.

Paul, E. L., Atiemo-Obeng, V. A. and Kresta, S. M. (2004), Hand book of industrial mixing: Science and practice, Wiley-Interscience: Hoboken, NJ.

Peixoto, S. M. C., Nunhez, J. R. and Duarte, C. G. (2000), Characterizing the flow of stirred vessels with anchor type impellers, Brazillian Journal Chemical Engineering, **17**, 925-936.

Patel, D., Ein-Mozaffari, F. and Mehrvar, M. (2011), Dynamic performance of continuous-flow mixing of psedudoplastic fluids exhibiting yield stress in stirred reactors, Industrial & Engineering Chemistry Research, **50**,9377-9389.

Patel, D., Ein-Mozaffari and F., Mehrvar, M. (2013), Using tomography to characterize the mixing of non-Newtonian fluids with a maxblend impeller, Chemical Engineering Technology, **36** (4), 687-695.

Pianko-Oprych, P., Nienow, A.W. and Barigou, M. (2009), Positron emission particle tracking (PEPT) compared to particle image velocimetry (PIV) for studying the flow generated by a pitched-blade turbine in single phase and multi-phase systems, Chemical Engineering Science, **64** (23), 4955–4968.

Pinelli, D., Nocentini, M. and Magelli, F. (2001), Solids distribution in stirred slurry reactors: influence of some mixer configurations and limits to the applicability of a simple model for predictions, Chemical Engineering Communication, **00**, 1-18.

Prajapati, P. and Ein-Mozaffari, F. (2009), CFD investigation of the mixing of yield-pseudoplastic fluid with anchor impeller, Chemical Engineering, Tecnology, **32** (8), 1211-1218.

Rammohan, A.R., Kemoun, A., Al-Dahhan, M.H. and Dudukovic, M.P. (2001), A Lagrangian description of flows in stirred tanks via computer-automated radioactive particle tracking (CARPT), Chemical Engineering Science, **56** (8), 2629-2639.

Rammohan, A. R. (2002), Characteriztion of single and multiphase flows in stirred tank reactors, D. Sc. Thesis, Washington University in St., Louis, St. Louis.

Ranade, V. V. and Joshi, J. B. (1989), Flow generated by pitched blade turbines. I. Measurements using laser doppler anemometer, Chemical Engineering Communication, **81**, 197-224.

Ranade, V.V., Mishra, V.P., Saraph, V.S., Deshpande, G.B. and Joshi, J.B. (1992), Comparison of axial flow impellers using LDA, Industrial & Engineering Chemistry Research, **31**, 2370-2379.

Ranade, V. V., Perrard, M., Le Sauze, N., Xuereb, C. and Bertrand, J. (2001), Trailing vortices of Rushton turbine: PIV measurements and CFD simulations with snapshot approach. Trans IChemE, Part A, Chemical Engineering Research and Design, **79** (1), 3-12.

Revstedt, J., Fuchs, L., Kovács, T. and Trägärdh, C. (2000), Influence of impeller type on the flow structure in a stirred reactor, AIChE Journal, **46** (12), 2373-2382.

Rushton, J., Costich, E. and Everett, H. (1950), Power characteristics of mixing impellers, Chemical Process Engineering, **46** (9), 467-476.

Roy, S., Acharya, S. and Cloeter, M. D. (2010), Flow structure and the effect of macro-instabilities in a pitched-blade stirred tank, Chemical Engineering Science, **65**, 3009-3024.

Rutherford, K., Mahmoudi, S.M.S., Lee, K.C. and Yianneskis, M. (1996), The influence of Rushton impeller blade and disk thickness on the mixing characteristics of stirred vessels, Chemical Engineering Research and Design, **74** (A), 369-378.

Saeed, S., Ein-Mozaffari, F. and Upreti, S.R. (2008), Using computational fluid dynamics to study the dynamic behaviour of the continous mixing of Herschel-Bulkley fluids, Industrial & Engineering Chemistry Research, **47**, 7465-7475.

Sano, Y. and Usui, H. (1985), Interrelations among mixing time, power number and discharge flow rate number in baffled mixing vessels, Journal of Chemical Engineering of Japan, **18** (1), 47-52.

Sardeshpande, M.V., Juvekar, V.A. and Ranade, V.V. (2011), Solid suspension in stirred tanks: UVP measurements and CFD simulations, The Canadian Journal of Chemical Engineering, **89**, 1112-1121.

Sardeshpande, M. V. and Ranade, V. V. (2012), Computational fluid dynamics modelling of solid suspension in stirred tanks, Current Science, **102** (10),1-14.

Sbrizzai, F., Lavezzo, V., Verzicco, R., Campolo, M. and Soldati, A. (2006), Direct numerical simulation of turbulent particle dispersion in an unbaffled stirred tank reactor, Chemical Engineering Science, **61** (9), 2843-2851.

Schäfer, M., Yianneskis, M., Wächter, P., Durst, F., 1998, Trailing vortices around a 45° Pithced-blade impeller, AIChE Journal, **44** (6), 1233-1246.

Serra, A., Campolo, M. and Soldati, A. (2001), Time-dependent finite-volume simulation of the turbulent flow in a free-surface CSTR, Chemical Engineering Science, **56** (8), 2715-2720.

Sha, Z., Oinas, P., Louhi-Kultanen, M., Yang, G. and Palosaari, S. (2001), Application of CFD simulation to suspension crystallization-factors affecting size-dependent classification. Powder Technology, **121** (1), 20-25.

Shamlou, P.A. and Koutsakos, E. (1989), Solids suspension and distribution in liquids under turbulent agitation, Chemical Engineering Science, **44** (3), 529-542.

Shan, X., Yu, G., Yang, Ch., Mao, Z.Sh. and Zhang, W. (2008), Numerical simulation of liquid-solid flow in an Unbaffled stirred tank with a pitched-blade turbine down flow, Industrial & Engineering Chemistry Research, **47**, 2926-2940.

Sharp, K. V. and Adrian, R. J. (2001), PIV study of small-scale flow structure around a Rushton turbine, Fluid Mechanics and Transport Phenomena, **47** (4), 766-778.

Sheng, J., Meng, H. and Fox, R.O. (1998), Validation of CFD simulations of a stirred tank using particle image velocimetry data, The Canadian Journal of Chemical Engineering, **76**, 611-625.

Schetz, J.A. and Fuhs, A.E. (1996), Handbook of fluid dynamics and fluid machinery, Volume 1, Fundamentals of Fluid Mechanics, John Wiley & Sons.

Simmons, M.J.H., Edwards, I., Hall, J.F., Fan, X., Parker, D.J. and Stitt, E.H. (2009), Techniques for visualization of cavern boundaries in opaque industrial mixing systems, AIChE Journal, **55** (11), 2765-2772.

Smith, J.M. (1990), Industrial needs for mixing research, Chemical Engineering Research and Design, **68** (1), 3-6.

Solomon, J., Elson, T.P. and Nienow, A.W. (1981), Cavern sizes in agitated fluids with a yield stress, Chemical Engineering Communications, **11**, 143-164.

Sommerfeld, M. and Decker, S. (2004), State of the art and future trends in CFD simulations of stirred vessel hydrodynamics, Chemical Engineering Technology, **27** (3), 215-224.

Špidla, M., Sinevič, V., Jahoda, M. and Machoň, V. (2005), Solid particle distribution of moderately concentrated suspensions in a pilot plant stirred vessel, Chemical Engineering Journal, **113** (1), 73-82.

Szalai, E.S., Arratia, P., Johnson, K. and Muzzio, F.J. (2004), Mixing analysis in a tank stirred with Ekato Intermid®impellers, Chemical Engineering Science, **59**, 3793-3805.

Taghavi, M., Zadghaffari, R., Moghaddas, J. and Moghaddas, Y. (2011), Experimental and CFD investigation of power consumption in a dual Rushton turbine stirred tank, Chemical Engineering Research and Design, **89**, 280-290.

Tamburini, A., Cipollina, A., Micale, G., Ciofalo, M. and Brucato, A. (2009), Dense solid-liquid off-bottom suspension dynamics: simulation and experiment. Chemical Engineering Research and Design, **87** (4), 587-597.

Tamburini, A., Cipollina, A., Micale, G., Brucato, A. and Ciofalo, M. (2011), CFD simulations of dense solid-liquid suspensions in baffled stirred tanks: Prediction of suspension curves, Chemical Engineering Journal, **178** (15), 324-341.

Thakur, R. K., Vial, Ch., Djelveh, G. and Labbafi, M. (2004), Mixing of complex fluids with flat-bladed impellers: effect of impeller geometry and highly shear-thinning behaviour, Chemical Engineering and Processing, **43**, 1211-1222.

Thomas, D.G. (1965), A note on the viscosity of Newtonian suspensions of uniform spherical particles, Journal of Colloid Science, **20**, 267-277.

Torré, J-P, Fletcher, D.F., Lasuye, T and Xuereb, C. (2006), CFD modelling of partially baffled agitated vessels with free surfaces, Fifth International Conference on CFD in the Process Industries, CSIRO, Melbourne, Australia.

Unadkat, H., Rielly, C.D. and Hargrave, G.K. (2009), Application of fluorescent PIV and digital image analysis to measure turbulence properties of solid-liquid stirred suspensions, Chemical Engineering Research and Design, **87** (4), 573-586.

Utomo, A.T. (2009), Flow patterns and energy dissipation rates in batch rotor-stator mixers, Ph.D. Thesis, University of Birmingham.

Van Wachem, B.G.M. and Almstedt, A.E. (2003), Methods for multiphase computational fluid dynamics, Chemical Engineering Journal, **96** (1-3), 81–98.

Van Der Molen, K. and Van Mannen, H. R. E. (1978), Laser-Doppler measurements of the turbulent flow in stirred vessels to establish scaling rules, Chemical Engineering Science, **33** (9), 1161-1168.

Venneker, B. (1999), Turbulent flow and gas dispersion in stirred vessels with pseudoplastic liquids, Ph.D. Thesis, University of Delft.

Venneker, B.C.H., Derksen, J.J. and Van den Akker, H.E.A. (2010), Turbulent flow of shear-thinning liquids in stirred tanks-the effects of Reynolds number and flow index, Chemical Engineering Research and Design, **88**, 827-843.

Versteeg, H.K. and Malalasekera, W. (1996), Introduction to computational fluid dynamics: the finite volume method, Addison-Wesley.

Verzicco, R., Fatica, M., Iaccarino, G. and Orlandi, P. (2004), Flow in an impeller-stirred tank using an immersed-boundary method, AIChE Journal, **50** (6), 1109-1118.

Virdung, T., Rasmuson, A. (2003), PIV measurements of solid-liquid mixing at elevated concentrations, 11th European Conference on Mixing, Bamberg, Germany, 129-136.

Wadnerkar, D., Utikar, R. P., Tade, M. O. and Pareek, V. K. (2012), CFD simulation of solid-liquid stirred tanks, Advanced Powder Technology, **23**, 445-453.

Wang, M., Dorward, A., Vlaev, D. and Mann, R. (2007), Measurements of gas-liquid mixing in a stirred vessel using electrical resistance tomography (ERT), Chemical Engineering Journal, **77**, 93-98.

Wichterle, K. and Wein, O. (1975), Agitation of concentrated suspensions, 5th Congress CHISA, Prague, Czechoslovakia.

Wilkens, R.J., Miller, J.D., Plummer, J.R., Dietz, D.C. and Myers, K.J. (2005), New techniques for measuring and modelling cavern dimensions in a Bingham plastic fluid, Chemical Engineering Science, **60**, 5269-5275.

Wu, H. and Patterson, G. K. (1989), Laser-Doppler measurements of turbulent-flow parameters in a stirred mixer, Chemical Engineering Science, **44** (10), 2207-2221.

Wu, J. and Pullum, L. (2001), Impeller geometry effects on velocity and solid suspension, Transaction IChemE, **79** (A), 989-997.

Yamazaki, H., Tojo, K. and Miyanami, K.1986, Concentration profiles of solids suspended in a stirred tank, Powder Technology, **48**, 205-216.

Yeoh, S.L., Papadakis, G. and Yianneskis, M. 2004 (a), Numerical simulation of turbulent flow characteristics in a stirred vessel using the LES and RANS approaches with the sliding/deforming mesh methodology, Chemical Engineering Research and Design, **82** (A7), 834-848.

Yeoh, S.L., Papadakis, G., Lee, K.C. and Yianneskis, M. 2004 (b), Large eddy simulation of turbulent flow in a Rushton impeller stirred reactor with sliding-deforming mesh methodology, Chemical Engineering and Technology, **27** (3), 257-263.

Yianneskis, M., Popiolek, Z. and Whitelaw, J. H. (1987), An experimental study of the steady and unsteady flow characteristics of stirred reactors, Journal of Fluid Mechanics, 175,537-555.

Zalc, J. M., Alvarez, M. M., Muzzio, F. J. and Arik, B. E. (2001), Extensive validation of computed laminar flow in a stirred tank with three Rushton turbines, AIChE Journal, **47** (10), 2145-2154.

Zhang, X. and Ahmadi, G. (2005), Eulerian-Lagrangian simulations of liquid-gas-solid flows in three-phase slurry reactors, Chemical Engineering Science, **60**, 5091-5106.

Zhou, G. and Kresta, S. M. (1996), Impact of geometry on the maximum turbulence energy dissipation rate for various impellers, AIChE Journal, **42**, 2476-2490.

Zwietering, T.N. (1958), Suspending of solid particles in liquid by agitators, Chemical Engineering Science, **8** (3-4), 244-253.